

# Probing compact objects with gravitational waves

Bounding dark charges on black holes and exploring  
gravitomagnetic tides on neutron stars

Probing compact objects with gravitational waves

Pawan Kumar Gupta

Pawan Kumar Gupta

---

# **Probing compact objects with gravitational waves**

Bounding dark charges on black holes and exploring  
gravitomagnetic tides on neutron stars

---

**Pawan Kumar Gupta**

---

ISBN :

DOI : <https://doi.org/10.33540/1919>

Printed by :

Copyright © 2023 Pawan Kumar Gupta



**Utrecht  
University**



This work originates as part of the research program of the Foundation for Fundamental Research on Matter (FOM), and falls as of April 1, 2017 under the responsibility of the Foundation for Nederlandse Wetenschappelijk Onderzoek Instituten (NWO-I), which is part of the Dutch Research Council (NWO).

# **Probing compact objects with gravitational waves**

Bounding dark charges on black holes and exploring  
gravitomagnetic tides on neutron stars

## **Onderzoek van compacte objecten met gravitatiegolven**

Het begrenzen van donkere ladingen op zwarte gaten  
en het onderzoeken van gravitomagnetische getijden  
op neutronensterren  
(met een samenvatting in het Nederlands)

Proefschrift

ter verkrijging van de graad van doctor aan de Universiteit Utrecht op gezag van de  
rector magnificus, prof.dr. H.R.B.M. Kummeling, ingevolge het besluit van het college  
voor promoties in het openbaar te verdedigen op maandag 9 oktober 2023 des middags  
te 4.15 uur

door

**Pawan Kumar Gupta**  
geboren op 5 juli 1994  
te Laxmipur Ekdanga, India

---

**Promotor**

Prof. dr. C.F.F. van den Broeck

**Copromotor**

Dr. Tanja Hinderer

**Beoordelingscommissie**

Prof. dr. Jo van den Brand

Prof. dr. Vitor Cardoso

Dr. Elisa Chisari

Prof. dr. Andreas Freise

Prof. dr. R.J.M. Snellings

# Dedication

In loving memory of my Great Grandfathers: Late Shri Ram Lal Gupta and Late Shri Vindheshwari Gupta



# Preface

## Gravitational waves

Our story begins after the discovery of special relativity, which suggests that causal effects should travel at most at the speed of light. With this thought in mind, imagine the sudden disappearance of the sun from our solar system. What would happen to the motion of the planets? According to Newtonian theory, the planets would fly away in a tangential direction to their orbit instantaneously. However, this prediction does not seem to respect the causal effect of special relativity. To address this issue, in 1915, Albert Einstein introduced the theory of general relativity, which is based on the foundation of special relativity.

General relativity is a theory of gravitation that describes gravity as a curvature of spacetime. Massive objects distort the spacetime curvature which affects the motion of other objects in the vicinity. In other words, the geometry of spacetime is not flat but rather curved in the presence of matter. In 1916, Albert Einstein predicted the existence of gravitational waves which are the ripples in the spacetime [1]. In 1974, the first indirect evidence of gravitational waves comes from discovery of a binary neutron star (BNS) system known as Hulse–Taylor binary [2].

In 2015, the Advanced Laser Interferometer Gravitational-wave Observatory (Advanced LIGO) [3] made the first direct detection of gravitational waves signal from a binary black hole. This signal is referred to as GW150914, which was emitted by a binary black hole with masses of  $36 M_{\odot}$  and  $29 M_{\odot}$  at a distance of 1.4 billion light-years [4]. In 2017, the first gravitational wave signal from a binary neutron star merger, GW170817 [5], was detected by both Advanced LIGO and Advanced Virgo [6].

The detection of gravitational waves from compact binary mergers has opened up a unique avenue for gaining insight into gravity, particle physics, cosmology, and astrophysics. Specifically, the study of gravitational waves from compact binary mergers enables tests of general relativity in the highly dynamic and strong-field regimes [7–11].

## Outline

This thesis is divided into three parts. In Part I, we provide a general introduction to gravitational waves, tidal effects for neutron stars, and the analysis of gravitational wave signals. In Part II, we describe the bounding of dark charges on binary black holes using gravitational waves. In Part III, we model the gravitomagnetic tidal effects for binary



---

neutron stars and study their impact on the measurability of tidal deformability and neutron star equation of state for third-generation gravitational wave detectors.

## Part I

In Chapter 1, we briefly introduce general relativity, gravitational waves, and the waveform model for a compact binary system. In Chapter 2, we discuss the detection and parameter estimation of gravitational wave signals from a compact binary system. In Chapter 3, we review the electric tidal effects and oscillation modes for neutron stars in the framework of general relativity.

## Part II

Most of the matter in the Universe is made of dark matter, whose evidence comes from many independent observations [12–15]. The first strong evidence comes from the velocities of galaxies in clusters, which was proposed by Zwicky [16], and other strong evidence comes from galactic rotation curves [17]. A galactic rotation curve tells us about the density distribution of dark matter in the galaxy, but it does not tell us anything about the nature of dark matter. The Bullet Cluster gives us information that the dark matter appears to be relatively collisionless [18]. The cosmic microwave background power spectrum tells us that dark matter is non-baryonic [19].

There are several dark matter candidates have been proposed, such as weakly interacting massive particles (WIMPs), axions, sterile neutrinos, primordial black holes, dark charges, and others [20, 21]. Ongoing experiments such as XENON, Large Hadron Collider (LHC) and others are actively searching for evidence of dark matter particles [22, 23]. All dark matter observations have been done only through its gravitational interactions, which hints that dark matter could be hidden, i.e., neutral under all standard model gauge interactions [24], but charged under an exact  $U(1)$  gauge symmetry of the hidden sector. This type of dark matter is known as minicharged dark matter which satisfies the criteria for a dark matter candidate [25], and we explore its possibility on binary black holes in Chapter 4.

## Part III

Gravitational waves from inspiraling binary neutron stars encode unique information on the matter at supra-nuclear densities in their interiors [26–31]. Understanding the properties of matter at such extreme density remains an important frontier in subatomic physics [32, 33]. Among the most interesting imprints of matter on the gravitational waves during a binary inspiral are signatures of tidal effects [34–36]. Tidal effects comprise a rich set of phenomena associated with the excitation of the stars’ quasi-normal modes [37–42]. The mode excitation can be either resonant or adiabatic, depending on the rate of variations in the tidal fields due to the spacetime curvature produced by the orbiting companion compared to the characteristic mode frequency. The excitation of quasi-normal modes is most commonly considered for the ringdown signals in black hole binaries, where the merger excites a broad spectrum of quasi-normal modes of the remnant which damp away due to gravitational radiation. Neutron stars have a much richer

---

mode spectrum than black holes due to the presence of matter. Several classes of neutron star modes have sufficiently low frequencies to become individually excited during a binary inspiral. This opens the possibility for a detailed, spectroscopic characterization of the ground-state matter in neutron-star interiors from gravitational waves emitted during their inspiral, provided that the modes have sufficiently large tidal coupling strengths to lead to a noticeable effect. The fundamental modes typically have the largest tidal couplings. They are an example of gravitoelectric phenomena associated with tidal deformability, a parameter that is measurable in the gravitational-wave signals [26, 27, 43]. There are also several other interesting classes of modes predominantly connected with gravitoelectric tides [41].

In Chapter 5, we develop a relativistic effective action to incorporate the effects of gravitomagnetic tidal effects of neutron stars in waveform models. In Chapter 6, we present a waveform model for a binary neutron stars incorporating gravitomagnetic adiabatic and modes effects of neutron stars for gravitational waves data analysis and explore their effects on measurements of tidal deformability parameters, using Cosmic Explorer as a case study. In Chapter 7, we explore how third-generation gravitational waves detector like Einstein Telescope can accurately determine the equation of state of neutron stars using resonant r-modes (gravitomagnetic  $\ell = m = 2$  mode) in binary neutron star inspirals.

---

# Acknowledgement

Ph.D. life is an intense and challenging but also rewarding journey. It demands not only technical expertise but, more importantly, emotional resilience. As a result, this journey has been life-changing in many ways and I would like to thank people who helped me to make it possible.

I would like to thank Chris for giving me this Ph.D. position. I am thankful for his guidance, expertise, valuable insights, and comments on this thesis.

I would like to thank Tanja Hinderer for giving me the opportunity to work with you and for being my co-supervisor. I learned a lot from you on how to become a better physicist and be precise about physics. I am very grateful that you always had time for me when I needed and you always encouraged me to ask questions. Thank you so much for all the positivity and motivation throughout this Ph.D.

I would like to thank Jan Steinhoff for giving me the opportunity to work with you. Although you were not an official co-supervisor I have considered you as one. Thank you so much for giving me time when I needed and I learned a lot from you as a physicist.

I would like to thank Badri Krishnan for giving me the opportunity to work with you. Thank you so much for all the help academic and non-academic throughout this Ph.D.

Coming from India to live in Amsterdam was not easy for me but I would like to thank Archisman Ghosh who organized Indian traditional festivals that made me feel at home.

Benjamin Lion, Thank you so much for offering the apartment to share and for all the fun adventures that we did together. You are the most open-minded and complete personality person I have met in my life and learned a lot from you. Thank you so much for all your help which helped me finish this Ph.D.

Jasper Roosmale Nepveu, Thank you for all the physics discussions and fun activities. It was great fun to play foosball with you although you won most of the time. Thank you for playing chess and losing to me.

---

Muriel Pérez, thank you so much for the mathematical discussion on symplectic geometry and information geometry and other fun adventures.

Maricke Flierman, you are a very kind and happy person and I am so glad to become friends with you. Thank you so much for all the help throughout this Ph.D. and fun activities like outdoor running, spinning class, and bench press (my favorite) in the gym. Thank you so much for being my paranymp.

Pieter Braat, Thank you so much for your positivity and motivation during thesis writing. I enjoyed your spinning class as an instructor and bench press in the gym.

Avanish Basdew-Sharma, thank you so much for all the coffee chats and discussions about Indian politics (haha). Thank you for inviting me for Christmas dinners at your place, and thanks to your parents for offering a delicious meal that made me feel at home. Thank you so much for being my paranymp.

I would like to thank my college friends Shraddha Agrawal and Siddharth Dhanpal for all the motivation and support thought out my Ph.D.

Khun Sang Phukon and Soumen Roy, thank you so much for all the support and for looking me after like elder brothers. I enjoyed all the delicious meals that you cooked and all the fun adventures that we did together.

Swapnil Shankar, thank you so much for all the fun adventure we did together.

I would like to thank everyone at Nikhef and Utrecht for nice time: Anna Green, Antonella Bianchi, Jon Perry, Pooya Saffarieh, Enzo Tapia, Enrico Porcelli, Michele Valentini, Jesse Dongen, Valeriia Lukashenko, Amit Reza, Haris Maliyamveetil, Harsh Narola, Chinmay Kalaghatgi, Soumen Koley, Johanna Lömker, Bouke Jung, Jhilik Majumdar, Justin Janquart, Anna Puecher, Peter Pang, Peter Gaemers, Marjolein Nuland and others whose name I may have missed.

Doing a Ph.D. in Physics in the Netherlands seems like a dream galaxy far away for me as growing up in a small village in India. This would not be possible without continuous support from my family. I would like to thank my family for *not plucking my wings and letting me fly*, and supporting this flight. My grandfather Late Shri Sripat Gupta, thank you so much for enriching my curiosity and for all the encouragement. Unfortunately, I lost you during this Ph.D., if you were here I know you would have been the proudest person of me.

# Contents

<b>List of Figures</b>	<b>xiv</b>
<b>List of Tables</b>	<b>xx</b>
<b>List of Acronyms</b>	<b>xxi</b>
<b>Conventions and notations</b>	<b>xxiv</b>
<b>1 Gravitational waves</b>	<b>3</b>
1.1 Overview of General Relativity . . . . .	3
1.2 Linearised General Relativity . . . . .	5
1.2.1 Background Lorentz transformations . . . . .	5
1.2.2 Gauge transformations . . . . .	5
1.2.3 Weak-field Einstein equations . . . . .	6
1.3 Plane wave solution . . . . .	7
1.3.1 Transverse-traceless gauge . . . . .	7
1.4 Effect of gravitational waves on matter . . . . .	9
1.5 The generation of gravitational waves . . . . .	11
1.5.1 Binary system in circular orbit . . . . .	12
1.6 Waveform . . . . .	13
1.6.1 Post-Newtonian approximations . . . . .	14
1.6.2 TaylorF2 waveform . . . . .	16
1.6.3 Phenomenological IMRPhenomPv2 waveform . . . . .	18
1.7 Dark charged binary black holes . . . . .	21
1.7.1 Binary black holes . . . . .	21
1.7.2 Dark charges on binary black holes . . . . .	21
<b>2 Detection and parameter estimation of gravitational waves</b>	<b>23</b>
2.1 Detection of gravitational waves . . . . .	23
2.1.1 Gravitational waves strain induced in interferometric detectors . . . . .	25
2.2 Signal extraction . . . . .	26
2.2.1 Characterization of noise . . . . .	27
2.2.2 Matched filtering . . . . .	28
2.3 Parameter estimation framework . . . . .	30

2.3.1	Bayesian framework . . . . .	30
2.3.2	Fisher matrix framework . . . . .	31
2.4	Markov Chain Monte Carlo (MCMC) . . . . .	32
2.5	Nested sampling . . . . .	34
<b>3</b>	<b>Neutron stars</b>	<b>37</b>
3.1	TOV equations . . . . .	37
3.1.1	Uncertainties in the neutron star equation of state . . . . .	40
3.2	Tidal effects for neutron stars . . . . .	41
3.3	Oscillation modes . . . . .	44
3.4	Approximate-universal relations . . . . .	46
3.5	Binary neutron stars . . . . .	47
<b>4</b>	<b>Bounding dark charges on binary black holes using gravitational waves</b>	<b>51</b>
4.1	Introduction . . . . .	51
4.2	Waveform model and analysis framework . . . . .	52
4.3	Simulations . . . . .	54
4.4	Analysis of selected binary black hole signals . . . . .	61
4.5	Summary and conclusions . . . . .	62
<b>5</b>	<b>Relativistic effective action of dynamical gravitomagnetic tides for slowly rotating neutron stars</b>	<b>67</b>
5.1	Introduction . . . . .	67
5.2	Dynamical magnetic tides of rotating stars . . . . .	69
5.2.1	Metric of a slowly rotating neutron star . . . . .	69
5.2.2	Fluid perturbation in the corotating frame . . . . .	70
5.2.3	Magnetic tidal Lagrangian for slow rotation . . . . .	72
5.2.4	Gravitomagnetic mode frequency . . . . .	73
5.2.5	Lagrangian in the symmetric tracefree basis . . . . .	74
5.2.6	Effective Lagrangian . . . . .	76
5.3	Relativistic effective action . . . . .	77
5.3.1	Spherical symmetry and dynamical variables . . . . .	77
5.3.2	Coordinate invariance and external fields . . . . .	78
5.3.3	Final set of building blocks for the action . . . . .	79
5.3.4	Symmetry restrictions on the possible couplings . . . . .	79
5.3.5	Power counting . . . . .	80
5.3.6	Relativistic action in the corotating frame . . . . .	81
5.3.7	Relativistic action in the coordinate frame . . . . .	82
5.4	Matching the coefficients . . . . .	83
5.4.1	Matching the static Love number . . . . .	84
5.4.2	Matching the irrotational Love number . . . . .	85
5.4.3	Matching the mode frequency . . . . .	86
5.5	Tidal response and Love operator . . . . .	87
5.5.1	The response function . . . . .	87
5.5.2	Time-domain response and Love operator . . . . .	88
5.5.3	Asymptotic limits of the response function in the inertial frame . . . . .	90

5.6	Summary and discussion . . . . .	90
5.7	Conclusions . . . . .	93
<b>6</b>	<b>Effect of dynamical gravitomagnetic tides on measurability of tidal parameters for binary neutron stars using gravitational waves</b>	<b>95</b>
6.1	Introduction . . . . .	95
6.2	Effective Gravitomagnetic Love number . . . . .	97
6.2.1	Definition of gravitomagnetic Love numbers . . . . .	97
6.2.2	Application to a binary system . . . . .	99
6.2.3	Features of the effective response . . . . .	101
6.3	Effective waveform model with adiabatic and resonance effects . . . . .	102
6.4	Results . . . . .	104
6.4.1	Setup and parameter choices for case studies . . . . .	105
6.4.2	Consistency checks . . . . .	105
6.4.3	Physical effects . . . . .	108
6.4.4	Measurement accuracy for different spins . . . . .	114
6.5	Discussion . . . . .	119
6.6	Conclusion . . . . .	122
<b>7</b>	<b>Determining the equation of state of neutron stars with Einstein Telescope using tidal effects and r-mode excitations from a population of binary inspirals</b>	<b>125</b>
7.1	Introduction . . . . .	125
7.2	Resonant r-modes: Frequencies, phase shifts, and universal relations . . .	126
7.2.1	Universal relation for the r-mode frequencies . . . . .	127
7.2.2	Universal relation for the r-mode overlap . . . . .	127
7.3	Setup of the analyses . . . . .	128
7.3.1	Waveform model . . . . .	128
7.3.2	Spectral parametrization of the EOS . . . . .	130
7.3.3	Analysis framework . . . . .	131
7.4	Results . . . . .	133
7.4.1	Analysis of a GW170817-like signal . . . . .	133
7.4.2	EOS reconstruction with Einstein Telescope . . . . .	134
7.5	Summary and conclusions . . . . .	136
<b>8</b>	<b>Summary and conclusions</b>	<b>143</b>
<b>A</b>	<b>Appendix</b>	<b>147</b>
A.1	Useful formulas . . . . .	147
A.2	Tensor Virial theorem . . . . .	148
A.3	PN coefficients of the phase in Einstein-Maxwell theory . . . . .	150
	<b>Public summary</b>	<b>151</b>
	<b>Openbare samenvatting</b>	<b>153</b>
	<b>CV</b>	<b>156</b>



<b>Bibliography</b>	<b>157</b>
---------------------	------------

# List of Figures

1.1	Effect of the GW polarizations $h_+$ and $h_\times$ on a ring of test masses (blue lines). The wave is always traveling in the $z$ direction. The solid circles show the original configuration of the test masses before the arrival of oscillatory gravitational wave and the dashed circles and ellipses show the new position of the test masses during the quarter cycles ( $\omega t = 0, \pi/2, \pi, 3\pi/2$ ) of oscillatory gravitational wave. . . . .	10
1.2	A binary system with masses $m_1$ and $m_2$ , separated by distance $l_0$ orbiting around their center of mass with an inclination angle $\iota$ and orbital frequency $\omega_{orb}$ . The inclination angle $\iota$ is defined as the angle between the orbital angular momentum $\omega_{orb}$ and the line of sight to the observer along $z$ . . . . .	12
1.3	The three phases of gravitational waves from a binary system and techniques to model these.[46] . . . . .	14
2.1	Aerial views of three of the existing GW detectors: LIGO Hanford Observatory, Washington USA (left), the LIGO Livingston Observatory, Louisiana USA (centre) and the Virgo detector, Italy (right). . . . .	23
2.2	Artist's Impression of the future next-generation detector Einstein Telescope by Marco Kraan (Nikhef) . . . . .	24
2.3	The detector's response is characterized by the antenna pattern function for the $+$ polarization(left) and $\times$ polarization (right) (here $\psi = 0$ ). . . . .	25
2.4	PSDs of the Advanced LIGO–Advanced Virgo network. There are high-amplitude narrow-band spectral lines which originate from a variety of sources including the mirror suspensions, the AC electrical supply, or sinusoidal motion imparted on the mirrors for data calibration [102]. . . . .	26
2.5	ASDs of the ET-D, CE (proposed future facilities), Advanced LIGO and Virgo at design. ET-D is basically a factor $\sim 10$ more sensitive in a wide frequency range, and has much better sensitivity at low frequencies than Advanced LIGO and Virgo at design. CE is slightly more sensitive in a wide frequency range and less sensitive at lower frequencies compared to ET-D. . . . .	27
2.6	Metropolis-Hastings MCMC . . . . .	33

2.7	Left panel shows the likelihood $\mathcal{L}(\theta)$ of a two-dimensional problem and right panel shows the transformed the likelihood $\mathcal{L}(X)$ as function of prior volumes $X_i$ using Eq. (2.37) [106]. Evidence $\mathcal{Z}$ is easier to evaluate with the likelihood $\mathcal{L}(X)$ as it is one dimensional integral shown in Eq. (2.39).	35
3.1	Examples of proposed nuclear equations of state: WFF1, H4, AP4 and SLy. The saturation density of nuclei is $\rho_{nuc} = 2.8 \times 10^{14} \text{g/cm}^3$ . The termination of EOS at high density is an artefact of the tabulated data set for given EOS.	39
3.2	Mass radius after solving the TOV equations for WFF1, H4, AP4 and SLy. Each point along a curve is obtained by solving TOV equations with a different central pressure configuration and the central density increases from right to left. TOV equations also describes relativistic hydrostatic equilibrium of a star, as a result, when there is no hydrostatic relativistic equilibrium for a given high central density, the curves terminate, while termination of low central density is due to numerical reason of TOV solver in LALSuite [108].	40
3.3	Tidal Love number $k_2$ for WFF1, H4, AP4 and SLy EOS. Each point along a curve is obtained by solving Eq. (3.19) with TOV equations Eq. (3.10) for a different central pressure configuration and the central density increases from left to right.	42
3.4	Dimensionless tidal Love number $\Lambda$ for WFF1, H4, AP4 and SLy EOS which is directly constrained by GW measurements.	43
3.5	Classification of electric type oscillation modes of Newtonian stars. For $f$ -modes and $p$ -modes pressure is the restoring force while for $g$ -modes buoyancy is restoring force.	46
3.6	PDFs for the tidal deformability parameters $\Lambda_1$ and $\Lambda_2$ for low-spin priors. The dashed and solid lines are 50% and 90% credible regions respectively. The black curves are the tidal parameters for the EOS models using the masses estimated with TaylorF2 model [117]. This is data for the first binary neutron star inspiral event GW170817 and that $\Lambda_1$ and $\Lambda_2$ correspond to the two bodies in the binary.	48
4.1	Histograms for $\ln B_{\text{NC}}^{\text{C}}$ for 67 choices of masses and spins with ranges as detailed in the main text, and the five different choices of $(\sigma_1, \sigma_2)$ indicated in the legend.	54
4.2	Posterior distributions for an injection with $(m_1, m_2) = (13.87, 6.36) M_{\odot}$ at an SNR of 12.52, and $(\sigma_1, \sigma_2) = (0, 0)$ . The left panel shows a corner plot for the posterior distributions of $ \sigma_1 $ and $ \sigma_2 $ (with the contours enclosing respectively 68%, 95%, and 99.7% of probability), while the right one is the posterior for $\xi =  \sigma_1 - \sigma_2 $ . Here and in the analogous figures below, orange lines indicate the injected parameters.	55
4.3	Same as in Fig. 4.2 but for $(\sigma_1, \sigma_2) = (0.05, -0.05)$ .	56
4.4	Same as in Fig. 4.2 but for $(\sigma_1, \sigma_2) = (0.5, 0)$ .	57
4.5	Same as in Fig. 4.2 but for $(\sigma_1, \sigma_2) = (0.5, -0.5)$ .	58
4.6	Same as in Fig. 4.2 but for $(\sigma_1, \sigma_2) = (0.5, 0.5)$ .	59

4.7	Corner plots for the posteriors of $ \sigma_1 $ , $ \sigma_2 $ , for the events of Table 4.2. . . . .	64
4.8	Posterior densities for $\xi =  \sigma_1 - \sigma_2 $ , for the events of Table 4.2. The solid lines indicate 68% confidence levels, the dashed lines 90% confidence levels. . . . .	65
5.1	Classification of magnetic type oscillation modes of Newtonian stars. For r-modes Coriolis force is the restoring force. . . . .	74
6.1	<i>CE noise spectral density and various mode resonances</i> for the two bodies and varying spins $\chi$ . Green and purple symbols refer to the NS with mass $m_1 = 1.5M_\odot$ with lower and higher spin respectively, while red and brown symbols are the corresponding values for the companion of mass $m_2 = 1.3M_\odot$ . Diamond shapes denote the modes with azimuthal number $m = 1$ , triangles those with $m = 2$ . . . . .	106
6.2	<i>Posterior probability distribution of <math>\tilde{\Lambda}</math> for SNR 1800 with the PNTidal waveform model (without gravitomagnetic effects) used for injection and recovery.</i> The label 4D refers to a reduced parameter space of the tidal deformabilities $\tilde{\Lambda}$ , $\delta\tilde{\Lambda}$ and the time and phase of coalescence $t_c, \phi_c$ with all other parameters fixed, while 8D also includes the sampling of the mass and spin parameters for each body. The results from the Fisher matrix (orange curve) agree well with the corresponding Bayesian analysis (blue curve), with both centered on the injected value (vertical line). The green curve shows the broadening of the distribution when doubling the dimensionality of the parameter space sampled. The shaded tails of the curves indicate regions outside the 90% credible interval. For the parameter $\delta\tilde{\Lambda}$ , both the 4D and 8D posteriors are essentially flat in this case. . . . .	107
6.3	<i>Shifts in the posterior distribution for <math>\tilde{\Lambda}</math> due to adiabatic and resonant gravitomagnetic effects.</i> This case study is for SNR 1800, aligned spins $\chi = 0.005$ and sampling only on $(\tilde{\Lambda}, t_c, \phi_c)$ with all other parameters fixed. We inject with a waveform that includes all effects PNTidal <sup>modes</sup> <sub>asym</sub> and recover with the same waveform (green curve) and those that include only the resonance jumps (blue curve) and only the adiabatic effects (orange curve). In this case the contribution from the adiabatic effects is dominant; omitting them (as for the results shown by the blue curve) leads to the largest shifts in the distribution. . . . .	108
6.4	<i>Posterior distributions of the tidal parameters for nonspinning NSs at SNR 1800.</i> The injection neglected gravitomagnetic tides, and the blue curve illustrates the recovery with the same waveform. The effect of gravitomagnetic tides, which are purely adiabatic in this case, is indicated by the orange curve. In the two-dimensional representation in the lower-left panel, the contours correspond to the one and two sigma confidence levels. . . . .	109
6.5	<i>Gravitomagnetic effects for aligned spins of <math>\chi_{1,2} = 0.005</math> and SNR 1800.</i> The blue curve corresponds to using the same waveform for injection and recovery. Comparing this with the orange curve indicates the changes due to gravitomagnetic tides from both the $m = 1$ mode resonances and the adiabatic effects, which lead to a shift in the distribution of $\tilde{\Lambda}$ and a slight change in the shape of the $\delta\tilde{\Lambda}$ posterior. . . . .	110

6.6	<i>Gravitomagnetic effects for aligned spins of <math>\chi_{1,2} = 0.01</math> and SNR 1800.</i> The blue curve corresponds to using the same waveform for injection and recovery, the orange curve indicates the effect of gravitomagnetic tides from both the $m = 1$ mode resonances and the adiabatic effects. Significant shifts in $\tilde{\Lambda}$ and a peaked shape of the distribution of $\delta\tilde{\Lambda}$ are clearly visible in this case. This is also illustrated by the two-dimensional representation of the error ellipses in the lower left panel. . . . .	111
6.7	<i>Effects of various gravitomagnetic contributions on the parameter recovery for aligned spins.</i> The results are for the systems with SNR 1800 and spins of $\chi = 0.005$ (upper panels) and $\chi = 0.01$ (lower panels). Green curves correspond to recovering with the same full model as used for the injection, blue curves include only the mode resonances, while orange curves indicate the adiabatic effects. We see that the conclusions about the impact of the resonance and adiabatic effect is opposite for the lower and higher spins: for low spins, adiabatic effects are most important for reducing the bias in $\tilde{\Lambda}$ , while resonances give the dominant contribution to the measurability of $\delta\tilde{\Lambda}$ . For high spins, the largest reduction in the bias in $\tilde{\Lambda}$ is due to the resonances, while the impact on $\delta\tilde{\Lambda}$ is comparable between resonance and adiabatic effects. . . . .	112
6.8	<i>Gravitomagnetic effects for spin orientations <math>\psi = \pi/3</math> and magnitudes <math>\chi = 0.005</math> at SNR 1800.</i> The blue curve corresponds to using the same waveform for injection and recovery. Comparing this with the orange curve indicates the changes due to gravitomagnetic tides from both the $m = 2$ mode resonances and the adiabatic effects, which lead to a shift in the distribution of $\tilde{\Lambda}$ and a more peaked shape of the $\delta\tilde{\Lambda}$ posterior. . . . .	113
6.9	<i>Gravitomagnetic effects for spin orientations <math>\psi = \pi/3</math> and magnitudes <math>\chi_{1,2} = 0.01</math> at SNR 1800.</i> The blue curve corresponds to using the same waveform for injection and recovery. Comparing this with the orange curve indicates the changes due to gravitomagnetic tides from both the $m = 2$ mode resonances and the adiabatic effects, which lead to a substantial shift in the distribution of $\tilde{\Lambda}$ and clear peak in the $\delta\tilde{\Lambda}$ posterior. . . . .	114
6.10	<i>Effects of various gravitomagnetic contributions on the parameter recovery for misaligned spins.</i> The results are for the systems with SNR 1800 and spin orientations of $\psi = \pi/3$ with $\chi = 0.005$ (upper panels) and $\chi = 0.01$ (lower panels). Green curves correspond to recovering with the same full model as the injection, blue curves include only the mode resonances, while orange curves indicate the adiabatic effects. We see that in both cases the mode resonances play a larger role for reducing biases than the adiabatic effects. . . . .	115
6.11	<i>Effect of the spin magnitude on inferred tidal parameters for aligned spins and SNR of 1800.</i> The injection and recovery both use the same model $\text{PNTidal}_{\text{asym}}^{\text{modes}}$ with corresponding spin magnitudes, as indicated in the legend. Increasing the spin magnitude has very little impact on the width of the posterior in $\tilde{\Lambda}$ but significantly affects that of $\delta\tilde{\Lambda}$ , where a higher spin leads to tighter bounds. . . . .	116

6.12	Accumulation of information encoded in integrands $\text{Abs} \left( \frac{\partial \tilde{h}^*}{\partial \theta_i} \frac{\partial \tilde{h}}{\partial \theta_i} * \frac{1}{S_n(f)} \right)$ (normalized to its maximum value) for $\theta_i = \tilde{\Lambda}$ (left panel) and $\theta_i = \delta \tilde{\Lambda}$ (right panel) as a function of frequency for the injected value of aligned spins $\{0.0, 0.005, 0.01\}$ , $\tilde{\Lambda} = 519.38$ and $\delta \tilde{\Lambda} = 48.37$ . “SNR” denotes the integrands $\text{Abs} \left( \frac{\tilde{h}^* \tilde{h}}{S_n(f)} \right)$ , “electric” denotes only adiabatic gravitoelectric tidal contribution in (6.25a) and “Mag. all” denotes adiabatic and resonant gravitomagnetic tidal contribution in (6.25a). . . . .	117
6.13	<i>Effect of the spin magnitude on inferred tidal parameters for inclined spins at <math>60^\circ</math> and SNR of 1800.</i> The injection and recovery both use the full model $\text{PNTidal}_{\text{asym}}^{\text{modes}}$ with varying spin magnitudes as indicated in the legend. Increasing the spin magnitude from a finite value to a higher one has very little impact on the width of the posteriors in this case. . . . .	118
6.14	<i>Fisher matrix results for systems with SNR 400 for different spins.</i> The injection and recovery both use the model $\text{PNTidal}_{\text{asym}}^{\text{modes}}$ with the corresponding spin magnitude indicated in the legend. <i>Left panel:</i> aligned spins, <i>right panel:</i> spin inclinations of $60^\circ$ . Same as Figs. 6.11 and 6.13 except for lower SNR. . . . .	120
7.1	Top panel: values of $\kappa$ and corresponding tidal deformabilities $\Lambda$ computed for a variety of EOSs and compactnesses listed in [172] (green dots), and the fit for $\kappa(\Lambda)$ of Eq. 7.7. Bottom panel: fitting residuals. . . . .	128
7.2	Shown is pressure versus density for a GW170817-like signal whose EOS is FPS (the red curve), with a 90% credible region (orange). This is compared with the 90% credible region that was actually obtained for GW170817 (black curves) [118]. Vertical lines indicate a few multiples of the nuclear saturation density, $\rho_{\text{sat}}$ . . . . .	134
7.3	Combined posterior probability distributions for the EOS parameters from the 20 loudest sources in ET, the red shows the injected EOS parameters. EOS parameters are more constrained, when r-modes are included than without r-modes. . . . .	137
7.4	90% credible regions for pressure versus density from the loudest source, the 5 loudest sources, and the 20 loudest sources in ET, in the case where r-modes are included. . . . .	138
7.5	Left panel: The improvement in the measurement of pressure at twice the nuclear saturation density; shown is the evolution of medians (the dots) and 90% credible intervals when going from 1 source to 20 sources, where the blue includes r-modes while the orange does not. From left to right, sources are being added in order of decreasing SNR. Right: The individual and combined probability distributions for pressure. . . . .	138
7.6	Similar plot as the Fig. 7.3, but for an analysis in which the neutron star rotation frequencies were taken to be larger by a factor 3. . . . .	139
7.7	Similar plot as the Fig. 7.4, but for an analysis in which the neutron star rotation frequencies were taken to be larger by a factor 3. . . . .	140
7.8	Similar plot as the Fig. 7.4, but for an analysis in which the neutron star rotation frequencies were taken to be larger by a factor 3. . . . .	140



# List of Tables

3.1	Numerical coefficients for the fitting formula of the I-Love, I-Q, and Q-Love relations given in Eq. (3.34) [115]. . . . .	47
4.1	Values of $\ln B_{\text{NC}}^{\text{C}}$ for different injected values of $(\sigma_1, \sigma_2)$ , in the case of an injection with $(m_1, m_2) = (13.87, 6.36) M_{\odot}$ and an SNR of 12.52, for which PDFs are shown in Figs. 4.2-4.6. . . . .	60
4.2	The GWTC-2 events analyzed, with their log Bayes factors for charges versus no charges. . . . .	62
6.1	Recovered mean and 90% credible intervals of $\tilde{\Lambda}(\delta\tilde{\Lambda})$ for SNR 1800 and 400. The injected values are $\tilde{\Lambda} = 519$ and $\delta\tilde{\Lambda} = 48$ . The spin magnitude $\chi$ on each NS increases from top to bottom, and we recall that in the aligned spin case $\psi = 0$ only the $m = 1$ modes pass through resonance, for $\psi = \pi/3$ it is only the $m = 2$ modes, and in the nonspinning case the resonances are absent. . . . .	119
7.1	The widths of the 90% credible intervals for the pressure at different densities, for our GW170817-like analysis, and for ET with different numbers of sources. In the case of ET, the numbers in brackets are without r-modes.	135
7.2	Similar results to the ones in Table 7.1, but for an analysis in which the neutron star rotation frequencies were taken to be larger by a factor 3. . .	136





# List of Acronyms

<b>ASD</b>	Amplitude spectral density
<b>BBH</b>	Binary black hole
<b>BH</b>	Black hole
<b>BNS</b>	Binary neutron star
<b>CE</b>	Cosmic Explorer
<b>CI</b>	Confidence interval
<b>EOS</b>	Equation of state
<b>ET</b>	Einstein telescope
<b>GR</b>	General relativity
<b>GW</b>	Gravitational wave
<b>GWTC</b>	Gravitational wave Transient Catalog
<b>IMR</b>	Inspiral-merger-ringdown
<b>ISCO</b>	Innermost stable circular orbit
<b>LIGO</b>	Laser Interferometer Gravitational-wave Observatory
<b>LISA</b>	Laser Interferometer Space Antenna
<b>MCMC</b>	Markov chain Monte Carlo
<b>NS</b>	Neutron star

**O3** Third observation run

**PDF** Probability density function

**PN** Post Newtonian

**PSD** Power spectral density

**SNR** Signal-to-noise ratio

**TOV** Tolman-Oppenheimer-Volkoff

**TT** Traceless transverse

**QNM** Quasi-normal mode

# Conventions and notations

We use the Einstein summation convention, in which repeated indices are implied to be summed over.

We use geometric units with  $G = c = 1$ , where  $G$  is the gravitational constant and  $c$  is the speed of light, except in cases where we make the post-Newtonian counting explicit as a formal expansion in  $c^{-2}$ , and for the electric permittivity of the vacuum  $\epsilon_0$  in Gaussian units, where  $4\pi\epsilon_0 = 1$ .

Spatial tensors expressed in the corotating frame of the star are denoted by capital Latin letters  $I, J, K, \dots$ , and we use boldface notation for three-dimensional vectors in this frame. These indices are raised and lowered with the flat Cartesian three-metric  $\delta_{IJ}$ , so their up or down placement has no meaning. We also use round brackets around indices to denote their symmetrization. For instance, for two vectors  $x^I$  and  $v^J$ , we denote  $x^{(I}v^{J)} = (x^I v^J + x^J v^I)/2$ .

Lowercase letters  $i, j, k, \dots$  are used for the inertial frame. Greek letters  $\mu, \nu, \dots$  denote four-dimensional spacetime coordinate indices in the inertial frame, and a calligraphic index  $\mathcal{B}$  indicates the magnetic part of a quantity.”



# Gravitational waves

In this chapter, we give a brief overview of general relativity and gravitational waves [44, 45]. We explain effect of gravitational waves on the matter and generation of gravitational waves due to a binary system in a circular orbit. Then, we review various gravitational waveform models used in later chapters.

## 1.1 Overview of General Relativity

General Relativity is a theory of gravitation based on the geometry of spacetime. The geometry of spacetime is not flat in general but rather curved in the presence of matter. Spacetime geometry is described by a 4-dimensional Lorentzian manifold. A point in this manifold is called an event and is given by

$$x^\mu = (t, x^i), \quad (1.1)$$

where  $t$  is the local time coordinate and  $x^i$  are the local space coordinates.

The manifold is equipped with a metric tensor denoted by  $g_{\mu\nu}$ , which is an important object to calculate path lengths and is defined by

$$ds^2 = g_{\mu\nu} dx^\mu dx^\nu, \quad (1.2)$$

where  $ds$  is infinitesimal path length and  $dx^\mu$  is a basis dual vector. The metric tensor is symmetric and depends on the coordinates. The signature of the metric is chosen to be  $(-, +, +, +)$  for the Lorentzian manifold. The inverse of the metric  $g^{\mu\nu}$  is defined as

$$g^{\mu\nu} g_{\nu\sigma} = \delta_\sigma^\mu, \quad (1.3)$$

where  $\delta_\nu^\mu$  is the Kronecker delta function. The metric tensor Eq. (1.2) is used to raise or lower the indices on the tensor:

$$V^\mu = g^{\mu\nu} V_\nu, \quad (1.4)$$

$$V_\mu = g_{\mu\nu} V^\nu. \quad (1.5)$$

The partial derivative denoted as a comma depends on the coordinate system used, so we define covariant derivative  $\nabla_\mu$

$$\nabla_\mu V^\nu = V^\nu_{,\mu} + \Gamma_{\mu\sigma}^\nu V^\sigma, \quad (1.6)$$

where  $\Gamma_{\mu\sigma}^\nu$  is the Levi-Civita connection and defined as

$$\Gamma_{\mu\nu}^\lambda = \frac{1}{2}g^{\lambda\rho}(g_{\mu\rho,\nu} + g_{\nu\rho,\mu} - g_{\mu\nu,\rho}). \quad (1.7)$$

In flat spacetime, the Levi-Civita connection vanishes, and the covariant derivative coincides with the partial derivative. The Levi-Civita connection is symmetric with respect to the lower indices for torsion-free spacetime. The metric is compatible with the covariant derivative  $\nabla_\lambda g_{\mu\nu} = 0$ .

The principle of equivalence states that the laws of physics in local regions of spacetime should be same as those of special relativity. A freely-falling (unaccelerated) particle with mass in special relativity moves in a straight line, the principle of equivalence implies that it will follow the shortest path in spacetime described by the geodesic equation

$$\frac{d^2x^\mu}{d\tau^2} + \Gamma_{\alpha\beta}^\mu \frac{dx^\alpha}{d\tau} \frac{dx^\beta}{d\tau} = 0, \quad (1.8)$$

where  $\tau$  is proper time given by  $d\tau^2 = -ds^2$ . The proper time is zero for massless particles like photons, so it is replaced by some affine parameter  $\lambda$  in the geodesic equation Eq. (1.8).

The curvature of spacetime is quantified by the Riemann tensor, which is derived from the connection

$$R_{\mu\nu\kappa}^\lambda = \Gamma_{\mu\nu,\kappa}^\lambda - \Gamma_{\mu\kappa,\nu}^\lambda + \Gamma_{\rho\kappa}^\lambda \Gamma_{\mu\nu}^\rho - \Gamma_{\rho\nu}^\lambda \Gamma_{\mu\kappa}^\rho. \quad (1.9)$$

For flat spacetime, the Levi-Civita connection vanishes, which implies  $R_{\mu\nu\kappa}^\lambda = 0$ .

The Ricci tensor is defined even without the metric contraction,

$$R_{\mu\nu} = R_{\mu\nu\kappa}^\kappa. \quad (1.10)$$

The Ricci tensor is symmetric, and the Ricci scalar is defined as,

$$R = g^{\mu\nu} R_{\mu\nu}. \quad (1.11)$$

The tensor with covariant derivative vanishes known as Einstein's tensor given by,

$$G_{\mu\nu} = R_{\mu\nu} - \frac{1}{2}g_{\mu\nu}R. \quad (1.12)$$

We have Einstein's equations for general relativity,

$$R_{\mu\nu} - \frac{1}{2}g_{\mu\nu}R = 8\pi T_{\mu\nu}. \quad (1.13)$$

where  $T_{\mu\nu}$  is the energy-momentum tensor, it should be conserved in curved spacetime,

$$\nabla_\mu T^{\mu\nu} = 0. \quad (1.14)$$

So in Einstein's equation, if we know the energy-momentum tensor  $T_{\mu\nu}$  then we can calculate the metric tensor  $g_{\mu\nu}$ . The physicist, John Wheeler's view on Einstein's general theory of relativity, can be summed up as: "Space-time tells matter how to move; matter tells spacetime how to curve."

## 1.2 Linearised General Relativity

### 1.2.1 Background Lorentz transformations

In order to get some intuition about gravitational waves, we consider the linearised perturbation of the metric as,

$$g_{\mu\nu} = \eta_{\mu\nu} + h_{\mu\nu}, \quad (1.15)$$

where  $\eta_{\mu\nu} = \text{diag}(-1, 1, 1, 1)$  is the Minkowski metric and  $|h_{\mu\nu}| \ll 1$ . This metric is motivated by the fact that spacetime is flat in the absence of gravity, and spacetime will be 'nearly' flat for a weak gravitational field. This metric perturbation is written in a coordinate system called nearly Lorentz coordinates. If one such coordinate system exists, there are many such coordinate systems, and we find a coordinate system in which calculations are easier. We define such a coordinate system as 'background Lorentz transformation'

$$x^{\bar{\alpha}} = \Lambda_{\beta}^{\bar{\alpha}} x^{\beta}, \quad (1.16)$$

where the matrix  $\Lambda_{\beta}^{\bar{\alpha}}$  satisfies,

$$\Lambda_{\beta}^{\bar{\alpha}} \Lambda_{\delta}^{\bar{\gamma}} \eta_{\bar{\alpha}\bar{\gamma}} = \eta_{\beta\delta}. \quad (1.17)$$

Transforming the linearised metric Eq. (1.15) in this coordinate system gives

$$g_{\bar{\alpha}\bar{\beta}} = \Lambda_{\bar{\alpha}}^{\mu} \Lambda_{\bar{\beta}}^{\nu} g_{\mu\nu} = \eta_{\bar{\alpha}\bar{\beta}} + h_{\bar{\alpha}\bar{\beta}}, \quad (1.18)$$

where we have used Eq. (1.17) and  $h_{\bar{\alpha}\bar{\beta}}$  is given by,

$$h_{\bar{\alpha}\bar{\beta}} = \Lambda_{\bar{\alpha}}^{\mu} \Lambda_{\bar{\beta}}^{\nu} h_{\mu\nu}. \quad (1.19)$$

This shows that  $h_{\bar{\alpha}\bar{\beta}}$  transforms like a tensor under background Lorentz transformation.

### 1.2.2 Gauge transformations

There are gauge transformations that leave Eq. (1.18) unchanged, which are given by

$$x^{\alpha'} = x^{\alpha} + \xi^{\alpha}(x^{\beta}), \quad (1.20)$$

where the vector  $\xi^{\alpha}$  is small in the sense that  $|\xi^{\alpha},_{\beta}| \ll 1$ , so that we have a small change in coordinates generated by vector  $\xi^{\alpha}$ , whose components are functions of the position. Then  $g_{\alpha\beta}$  transform

$$g_{\alpha'\beta'} = \frac{\partial x^{\mu}}{\partial x^{\alpha'}} \frac{\partial x^{\nu}}{\partial x^{\beta'}} g_{\mu\nu} = \eta_{\alpha\beta} + h_{\alpha\beta} - \xi_{\beta,\alpha} - \xi_{\alpha,\beta}, \quad (1.21)$$

where we consider only first-order terms in small quantities and  $\xi_{\alpha} = \eta_{\alpha\beta} \xi^{\beta}$ . Under this gauge transformation  $h_{\alpha\beta}$  changes as,

$$h_{\alpha\beta} \rightarrow h_{\alpha\beta} - \xi_{\alpha,\beta} - \xi_{\beta,\alpha}. \quad (1.22)$$



### 1.2.3 Weak-field Einstein equations

We calculate the Riemann tensor Eq. (1.9) to linear order using metric Eq. (1.15),

$$R_{\alpha\beta\mu\nu} = g_{\alpha\lambda} R_{\beta\mu\nu}^{\lambda} = \frac{1}{2} (h_{\alpha\nu,\beta\mu} - h_{\alpha\mu,\beta\nu} + h_{\beta\mu,\alpha\nu} - h_{\beta\nu,\alpha\mu}). \quad (1.23)$$

We notice that this linearized Riemann tensor is invariant under gauge transformations Eq. (1.22). We consider background Lorentz transformation where  $h_{\alpha\beta}$  is a tensor Eq. (1.19) and allowed gauge transformations Eq. (1.22). Based on this point of view, we define trace reverse tensor,

$$\bar{h}_{\alpha\beta} = h_{\alpha\beta} - \frac{1}{2} \eta_{\alpha\beta} h. \quad (1.24)$$

It has this name because  $\bar{h} = h - 2h = -h$ , where  $h = \eta_{\alpha\beta} h^{\alpha\beta}$  and  $h_{\alpha\beta}$  can be inverted as,

$$h_{\alpha\beta} = \bar{h}_{\alpha\beta} - \frac{1}{2} \eta_{\alpha\beta} \bar{h}. \quad (1.25)$$

With these definitions, we calculate Einstein's tensor Eq. (1.12) up to linear order in the trace reverse tensor,

$$G_{\alpha\beta} = -\frac{1}{2} (\bar{h}_{\alpha\beta,\mu}^{\mu} + \eta_{\alpha\beta} \bar{h}_{\mu\nu}^{\mu\nu} - \bar{h}_{\alpha\mu,\beta}^{\mu} - \bar{h}_{\beta\mu,\alpha}^{\mu}). \quad (1.26)$$

To further simplify Einstein's tensor, we impose the following,

$$\bar{h}_{\mu\nu}^{\mu} = 0. \quad (1.27)$$

This condition is known as the Lorentz gauge condition. The Einstein's tensor reduces to,

$$G_{\alpha\beta} = -\frac{1}{2} (\bar{h}_{\alpha\beta,\mu}^{\mu}). \quad (1.28)$$

We need to show this Lorentz gauge condition always exists. Suppose we have some  $\bar{h}_{\alpha\beta}^{OLD,\alpha} \neq 0$ , take new  $\bar{h}_{\alpha\beta}^{NEW}$  and transform it under gauge transformations Eq. (1.20)

$$\bar{h}_{\alpha\beta}^{NEW} = h_{\alpha\beta}^{NEW} - \frac{1}{2} \eta_{\alpha\beta} h^{NEW}, \quad (1.29)$$

$$= \bar{h}_{\alpha\beta}^{OLD} - \xi_{\alpha,\beta} - \xi_{\beta,\alpha} + \eta_{\alpha\beta} \xi_{,\mu}^{\mu}. \quad (1.30)$$

Taking the divergence of Eq. (1.30),

$$\bar{h}_{\alpha\beta}^{NEW,\alpha} = \bar{h}_{\alpha\beta}^{OLD,\alpha} - \xi_{\beta,\alpha}^{\alpha}. \quad (1.31)$$

Since  $\bar{h}_{\alpha\beta}^{OLD} \neq 0$  as assumed, and we want  $\bar{h}_{\alpha\beta}^{NEW,\alpha} = 0$  which implies,

$$\square \xi_{\beta} = \bar{h}_{\alpha\beta}^{OLD,\alpha}, \quad (1.32)$$

where  $\square f = f_{;\alpha}^{\alpha} = \left(-\frac{\partial^2}{\partial t^2} + \nabla^2\right) f$ . This equation always has a solution, because the d'Alembertian  $\square$  operator is invertible:

$$\xi_\beta(x) = \int d^4y G(x-y) \bar{h}_{\alpha\beta}^{OLD,\alpha}(y), \quad (1.33)$$

where  $G(x-y)$  is the Green's function given by  $\square G(x-y) = \delta^4(x-y)$ . This implies that it is always possible to choose the Lorentz gauge condition.

Then the weak-field Einstein's equations in Lorentz gauge condition are,

$$\square \bar{h}^{\alpha\beta} = -16\pi T^{\alpha\beta}. \quad (1.34)$$

These are known as linearised Einstein's equations.

## 1.3 Plane wave solution

We consider the linearised Einstein's equation Eq. (1.34) in vacuum

$$\left(-\frac{\partial^2}{\partial t^2} + \nabla^2\right) \bar{h}^{\alpha\beta} = 0, \quad (1.35)$$

which have plane wave solutions

$$\bar{h}^{\alpha\beta} = A^{\alpha\beta} e^{ik_\mu x^\mu}, \quad (1.36)$$

where,  $A^{\mu\nu}$  are constants and  $k^\mu = (\omega, \vec{k})$ . We insert plane-wave solution Eq. (1.36) in the wave's equation Eq. (1.35) which gives a condition for  $k_\alpha$  as  $\eta^{\mu\nu} k_\mu k_\nu = 0 \Rightarrow \omega^2 = |\vec{k}|^2$ . This gives wave's phase and group velocity equal to 1, which means that gravitational waves travel at the speed of light. We further impose the Lorentz gauge condition Eq. (1.27) for plane wave solution Eq. (1.36)

$$A^{\alpha\beta} k_\beta = 0, \quad (1.37)$$

which is a restriction on  $A^{\alpha\beta}$  that it is orthogonal to  $k^\mu$ .

The plane wave solutions given by Eq. (1.36) with the Lorentz gauge condition specified in Eq. (1.37) still have some gauge freedom which are not physical GWs solutions. In the following subsection, we completely remove this gauge freedom and obtain physical GWs solutions.

### 1.3.1 Transverse-traceless gauge

We have restricted the amplitude  $A^{\alpha\beta}$  in Eq. (1.37), but it can be restricted further using gauge transformations. We change the gauge while remaining within Lorentz gauge using vectors solving Eq. (1.32)

$$\left(-\frac{\partial^2}{\partial t^2} + \nabla^2\right) \chi_\alpha = 0, \quad (1.38)$$

which has a solution

$$\chi_\alpha = B_\alpha e^{ik_\mu x^\mu}, \quad (1.39)$$

where  $k_\mu$  is same null vector and  $B_\alpha$  is a constant. This produces a change in  $h^{\alpha\beta}$

$$h_{\alpha\beta}^{(NEW)} = h_{\alpha\beta}^{(OLD)} - \chi_{\alpha,\beta} - \chi_{\beta,\alpha}, \quad (1.40)$$

that will change the  $\bar{h}^{\alpha\beta}$

$$\bar{h}_{\alpha\beta}^{NEW,\alpha} = \bar{h}_{\alpha\beta}^{OLD,\alpha} - \chi_{\alpha,\beta}^\alpha - \chi_{\beta,\alpha}^\alpha + \eta_{\alpha\beta} \chi_{,\mu}^{\mu,\alpha}, \quad (1.41)$$

$$A_{\alpha\beta}^{(NEW)} = A_{\alpha\beta}^{OLD} - ik_\beta B_\alpha - ik_\alpha B_\beta + i\eta_{\alpha\beta} k_\mu B^\mu. \quad (1.42)$$

The exponential factor has been canceled out from both sides in the above equation. This  $A_{\alpha\beta}^{(NEW)}$  still satisfies the Lorentz gauge condition Eq. (1.37). We can choose  $B_\alpha$  to impose two further restrictions

$$A_\alpha^{\alpha(NEW)} = 0 \quad , \quad A_{\alpha\beta}^{(NEW)} U^\beta = 0, \quad (1.43)$$

where  $U^\beta$  is some fixed four-velocity. The Eq. (1.37) and Eq. (1.43) are known as transverse-traceless (TT) gauge conditions. If we are already in the TT gauge, then the NEW script on  $A$  is irrelevant. In this TT gauge,

$$\bar{h}_{\alpha\beta}^{TT} = h_{\alpha\beta}^{TT}. \quad (1.44)$$

Let us consider the background Lorentz frame in which the vector  $\vec{U}$  upon which we have based the TT gauge is time basis vector  $U^\beta = \delta_0^\beta$ . This implies from Eq. (1.43)  $A_{\alpha 0} U^0 = 0 \Rightarrow A_{\alpha 0} = 0$ . In this frame, let us orient our spatial coordinate axes so that the wave is traveling in the z-direction,  $k^\mu \rightarrow (\omega, 0, 0, \omega)$ . The Eq. (1.37) gives

$$A_{\alpha\beta} k^\beta = 0, \quad A_{\alpha 0} \omega + A_{\alpha z} \omega = 0. \quad (1.45)$$

Since  $A_{\alpha 0} = 0$  which implies that  $A_{\alpha z} = 0$  which means that only  $A_{xx}$ ,  $A_{yy}$  and  $A_{xy} = A_{yx}$  are non-zero and traceless condition implies that  $A_{xx} = -A_{yy}$ . We write the  $h_{\alpha\beta}^{TT}$  in matrix form

$$h_{\alpha\beta}^{TT} = \begin{pmatrix} 0 & 0 & 0 & 0 \\ 0 & h_+ & h_\times & 0 \\ 0 & h_\times & -h_+ & 0 \\ 0 & 0 & 0 & 0 \end{pmatrix}, \quad (1.46)$$

where  $h_+ = h_{xx}$  and  $h_\times = h_{xy}$  are two independent component which give rise to two different polarisations of gravitational waves.

The TT gauge can be considered in terms of the a projection operator, which takes  $h_{ij}$  to  $h_{ij}^{TT}$  as

$$h_{ij}^{TT} = \left( \Lambda_i^k \Lambda_j^l - \frac{1}{2} \Lambda_{ij} \Lambda^{kl} \right) h_{kl}, \quad (1.47)$$

where the projection operator  $\Lambda_{ij}$  is defined as,

$$\Lambda_{ij} = \delta_{ij} - n_i n_j. \quad (1.48)$$

## 1.4 Effect of gravitational waves on matter

We consider a particle in a wave-free region of spacetime to encounter a gravitational wave. Let us choose a background Lorentz frame in which the particle is initially at rest  $U^\mu = (1, 0, 0, 0)$ , and choose the TT gauge in this frame (1.45). The particle obeys the geodesic equation Eq (1.8),

$$\frac{d}{d\tau}U^\mu + \Gamma_{\nu\delta}^\mu U^\nu U^\delta = 0. \quad (1.49)$$

Since the particle is at rest, the above equation reduces to

$$\frac{d}{d\tau}U^\mu = -\Gamma_{00}^\mu = -\frac{1}{2}\eta^{\alpha\beta} (h_{\beta 0,0} + h_{0\beta,0} - h_{00,\beta}), \quad (1.50)$$

but in TT gauge  $h_{\beta 0} = 0$ , which makes  $\frac{d}{d\tau}U^\mu = 0$ . This means the particle will remain at rest forever regardless of the wave. It is not a physical effect but rather TT coordinate effect because  $U^\mu$  is a coordinate-dependent quantity.

We consider the effect of gravitational waves on coordinate-independent quantity proper distance between origin and  $x = \epsilon, y = 0, z = 0$ ,

$$\Delta l = \int |ds^2|^{1/2} = \int |g_{\mu\nu} dx^\mu dx^\nu|^{1/2} \approx \left(1 + \frac{1}{2}h_{xx}^{TT}(x=0)\right) \epsilon. \quad (1.51)$$

Since in the TT gauge,  $h_{xx}^{TT}$  is not generally zero, the proper distance changes with time. The proper distance is proportional to their initial separation  $\epsilon$ , and this is the reason that gravitational wave detectors are bigger. Since the TT coordinate system is not associated with measurement, we choose to work in a coordinate system closely associated with measurements, the local inertial frame. In this frame, coordinate distances are proper distances up to linear order in the coordinates. Consider two freely falling particles connected by  $\xi^\mu$  vector, as gravitational waves pass by the evolution of  $\xi^\mu$  is described by equation of geodesic deviation,

$$\frac{D^2}{d\tau^2}\xi^\mu = R_{\nu\alpha\beta}^\mu U^\nu U^\alpha \xi^\beta, \quad (1.52)$$

where  $\frac{D}{d\tau} = U^\mu \nabla_\mu$ . Initially  $\xi = (0, \epsilon, 0, 0)$  and four velocity  $U = (1, 0, 0, 0)$ , Since Riemann tensor is gauge invariant quantity, we compute it in TT gauge,

$$R_{0j0}^i = -\frac{1}{2}h_{ij,00}^{TT}, \quad (1.53)$$

where all other components are higher-order. We use (1.53) in (1.52)

$$\frac{\partial^2}{\partial t^2}\xi^i = -R_{0x0}^i \xi^j = \frac{1}{2}h_{ij,00}^{TT}\xi^j, \quad (1.54)$$

where we have used  $dt = d\tau$  upto linear order.

To understand Eq. (1.54), we place a ring of test masses in the  $(x, y)$  plane since gravitational waves are transverse. The locations of the test masses are denoted as

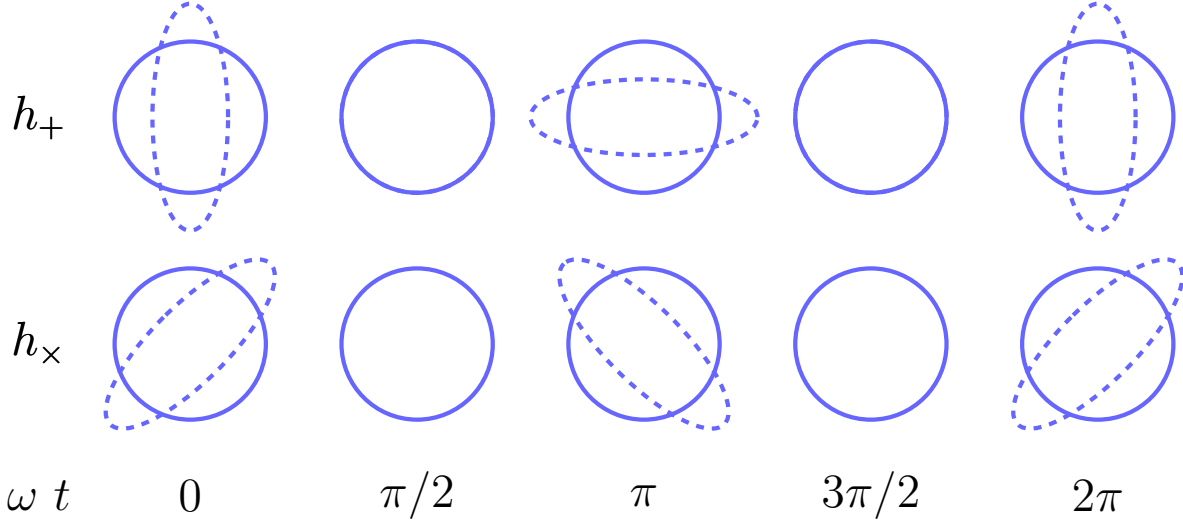


Figure 1.1: Effect of the GW polarizations  $h_+$  and  $h_\times$  on a ring of test masses (blue lines). The wave is always traveling in the  $z$  direction. The solid circles show the original configuration of the test masses before the arrival of oscillatory gravitational wave and the dashed circles and ellipses show the new position of the test masses during the quarter cycles ( $\omega t = 0, \pi/2, \pi, 3\pi/2$ ) of oscillatory gravitational wave.

$(x_0 + \delta x, y_0 + \delta y)$ , where  $(x_0, y_0)$  is the initial position and  $(\delta x, \delta y)$  is the perturbation by the gravitational wave. We can write Eq. (1.54) in the perturbation as

$$\begin{bmatrix} \delta \ddot{x} \\ \delta \ddot{y} \end{bmatrix} = \frac{1}{2} \begin{bmatrix} h_{+,00} & h_{\times,00} \\ h_{\times,00} & -h_{+,00} \end{bmatrix} \begin{bmatrix} x_0 \\ y_0 \end{bmatrix}, \quad (1.55)$$

where leading order terms are considered. We consider  $h_{+,\times} = A_{+,\times} \cos(\omega t)$  and since there are two polarisation, we consider first + polarisation in Eq. (1.55)

$$\begin{bmatrix} \delta \ddot{x} \\ \delta \ddot{y} \end{bmatrix} = \frac{1}{2} A_+ \omega^2 \cos(\omega t) \begin{bmatrix} 1 & 0 \\ 0 & -1 \end{bmatrix} \begin{bmatrix} x_0 \\ y_0 \end{bmatrix}. \quad (1.56)$$

The solution of these linear differential equations is given by,

$$\begin{bmatrix} \delta x \\ \delta y \end{bmatrix} = \frac{1}{2} A_+ \cos(\omega t) \begin{bmatrix} -x_0 \\ y_0 \end{bmatrix}. \quad (1.57)$$

For  $\times$  polarisation in Eq. (1.55),

$$\begin{bmatrix} \delta \ddot{x} \\ \delta \ddot{y} \end{bmatrix} = \frac{1}{2} A_\times \omega^2 \cos(\omega t) \begin{bmatrix} 0 & 1 \\ 1 & 0 \end{bmatrix} \begin{bmatrix} x_0 \\ y_0 \end{bmatrix}. \quad (1.58)$$

The solution of these linear differential equations is given by,

$$\begin{bmatrix} \delta x \\ \delta y \end{bmatrix} = -\frac{1}{2} A_\times \cos(\omega t) \begin{bmatrix} y_0 \\ x_0 \end{bmatrix}. \quad (1.59)$$

The effect of gravitational waves on a ring of test mass is shown in fig. 1.1.

## 1.5 The generation of gravitational waves

After discussing effect of gravitational waves on the matter, we will now consider how GWs are generated by a source. The linearised Einstein's equation Eq. 1.34 in the presence of matter are given by,

$$\left(-\frac{\partial^2}{\partial t^2} + \nabla^2\right) \bar{h}^{\alpha\beta} = -16\pi T^{\alpha\beta}. \quad (1.60)$$

The outgoing-wave solution for arbitrary  $T_{\mu\nu}$  for above equation is given by

$$\bar{h}^{\mu\nu}(t, \mathbf{r}) = 4 \int \frac{T^{\mu\nu}(t - R, \mathbf{r}')}{R} d^3\mathbf{r}', \quad (1.61)$$

where  $R = |\mathbf{r} - \mathbf{r}'|$ ,  $\mathbf{r}$  is the point where we want to calculate the  $\bar{h}^{\mu\nu}$  and  $\mathbf{r}'$  is the point all over the source. If we suppose the field point  $\mathbf{r}$  is far away  $|\mathbf{r}| \gg |\mathbf{r}'|$  which implies  $R \sim |\mathbf{r}|$ . Moreover, we also assume that time derivative of the stress-energy tensor  $T_{\mu\nu}$  is small. Then,

$$\bar{h}^{\mu\nu}(t, \mathbf{r}) = \frac{4}{|\mathbf{r}|} \int T^{\mu\nu}(t - \mathbf{r}, \mathbf{r}') d^3\mathbf{r}'. \quad (1.62)$$

Using Eq. (A.13) into Eq. (1.62) implies that,

$$\bar{h}^{\mu 0}(t, \mathbf{r}) = \frac{\text{constant}}{|\mathbf{r}|}. \quad (1.63)$$

Since  $\bar{h}^{\mu 0}$  and  $\bar{h}^{0\mu} (= \bar{h}^{\mu 0})$  are time independent, they will not contribute to wave. This condition is automatically satisfied when transforming to the TT gauge. The space components  $\bar{h}_{ij}$  are converted in TT gauge using projection operator Eq. (1.47) into Eq. (1.62),

$$\bar{h}_{ij}^{TT}(t, \mathbf{r}) = \left\{ \frac{4}{|\mathbf{r}|} \int T_{ij}(t - \mathbf{r}, \mathbf{r}') d^3\mathbf{r}' \right\}^{TT}. \quad (1.64)$$

We want to show how Eq. (1.64) can be written in term of time-variations in the source that generate GWs similar to the dipole formula in electromagnetism. We use the tensor virial theorem Eq. (A.27)

$$2 \int T^{\mu k} d^3\mathbf{r}' = \frac{\partial^2}{\partial t^2} (I^{\mu k}), \quad (1.65)$$

where the quadrupole moment tensor of the system is

$$I^{\mu k} = \int T^{00} r'^k r'^\mu d^3\mathbf{r}'. \quad (1.66)$$

Furthermore, it is a function of retarded time only since the space part is integrated. Using the result Eq (1.65), we can simplify Eq. (1.64) as

$$\bar{h}_{ij}^{TT}(t, \mathbf{r}) = \left\{ \frac{2}{|\mathbf{r}|} \frac{\partial^2}{\partial t^2} I_{ij}(t - \mathbf{r}) \right\}^{TT} = \left( \Lambda_i^k \Lambda_j^l - \frac{1}{2} \Lambda_{ij} \Lambda^{kl} \right) \frac{2}{|\mathbf{r}|} \frac{\partial^2}{\partial t^2} I_{kl}(t - \mathbf{r}), \quad (1.67)$$

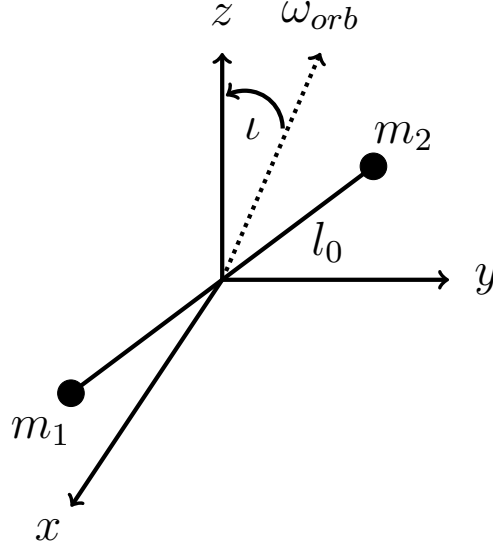


Figure 1.2: A binary system with masses  $m_1$  and  $m_2$ , separated by distance  $l_0$  orbiting around their center of mass with an inclination angle  $\iota$  and orbital frequency  $\omega_{orb}$ . The inclination angle  $\iota$  is defined as the angle between the orbital angular momentum  $\omega_{orb}$  and the line of sight to the observer along  $z$ .

where the projection operator  $\Lambda$  is defined in Eq. (1.48). This is the gravitational wave emitted by a mass-energy system evolving in time. The gravitational wave has a quadrupolar nature, unlike the electromagnetic wave which has a dipole nature. Because if we define the gravitational dipole moment for an isolated system

$$\mathbf{d}_G = \sum_i m_i \mathbf{r}_i, \quad (1.68)$$

which satisfies the conservation law of total momentum for an isolated system

$$\frac{d}{dt} \mathbf{d}_G = 0, \quad (1.69)$$

for this reason, gravitational waves do not have a dipole contribution.

We write  $\bar{h}_{ij}^{TT}(t, \mathbf{r})$  Eq. (1.67) in components as

$$\begin{aligned} h_+ &= \bar{h}_{xx}^{TT} = -\bar{h}_{yy}^{TT} = \frac{1}{|\mathbf{r}|} \frac{\partial^2}{\partial t^2} (I_{xx}(t - \mathbf{r}) - I_{yy}(t - \mathbf{r})), \\ h_\times &= \bar{h}_{xy}^{TT} = \frac{2}{|\mathbf{r}|} \frac{\partial^2}{\partial t^2} (I_{xy}(t - \mathbf{r})). \end{aligned} \quad (1.70)$$

### 1.5.1 Binary system in circular orbit

Having discussed the generation of gravitational waves from generic source, we now focus on gravitational waves from a binary system in circular orbit.

Let us consider a binary system in a circular orbit with two point masses  $m_1$  and  $m_2$  (far from coalescence) having orbital separation  $l_0$ , total mass  $M = m_1 + m_2$  and

coordinate frame with origin coincident with the centre of mass, Fig. 1.2. The position of the masses,  $\mathbf{r}_1$  and  $\mathbf{r}_2$ , are given by

$$\mathbf{r}_1 = \frac{m_2 l_0}{M} \hat{\mathbf{e}}(t), \quad \mathbf{r}_2 = \frac{m_1 l_0}{M} \hat{\mathbf{e}}(t), \quad (1.71)$$

where  $\hat{\mathbf{e}}(t)$  is given by

$$\hat{\mathbf{e}}(t) = (\cos(\omega_{\text{orb}} t), \cos(\iota) \sin(\omega_{\text{orb}} t), -\sin(\iota) \sin(\omega_{\text{orb}} t)). \quad (1.72)$$

Using the component of energy-momentum tensor  $T^{00} = m_1 \delta(\mathbf{r} - \mathbf{r}_1) + m_2 \delta(\mathbf{r} - \mathbf{r}_2)$  in the Eq (1.66) gives quadrupole moment,

$$I_{ij} = \frac{m_1 m_2}{m_1 + m_2} l_0^2 \begin{pmatrix} \cos^2(\omega_{\text{orb}} t) & \cos(\iota) \cos(\omega_{\text{orb}} t) \sin(\omega_{\text{orb}} t) & 0 \\ \cos(\iota) \cos(\omega_{\text{orb}} t) \sin(\omega_{\text{orb}} t) & \cos^2(\iota) \sin^2(\omega_{\text{orb}} t) & 0 \\ 0 & 0 & 0 \end{pmatrix}. \quad (1.73)$$

Using Eq. (1.73) and Eq. (1.70), the gravitational waves polarisations are,

$$\begin{aligned} h_+(t, \mathbf{r}) &= \frac{1}{|\mathbf{r}|} \frac{4m_1 m_2 l_0^2 \omega_{\text{orb}}^2}{m_1 + m_2} \frac{1 + \cos^2(\iota)}{2} \cos(2\omega_{\text{orb}} t_{\text{ret}}), \\ h_\times(t, \mathbf{r}) &= -\frac{1}{|\mathbf{r}|} \frac{4m_1 m_2 l_0^2 \omega_{\text{orb}}^2}{m_1 + m_2} \cos(\iota) \sin(2\omega_{\text{orb}} t_{\text{ret}}), \end{aligned} \quad (1.74)$$

where  $t_{\text{ret}} = t - \mathbf{r}$ . Using the orbital frequency  $\omega_{\text{orb}}$  which can be found from Kepler's law

$$\omega_{\text{orb}} = \sqrt{\frac{M}{l_0^3}}, \quad (1.75)$$

and defining chirp mass  $\mathcal{M}$

$$\mathcal{M} = \frac{(m_1 m_2)^{3/5}}{(m_1 + m_2)^{1/5}}, \quad (1.76)$$

in the Eq. (1.74) gives

$$\begin{aligned} h_+(t, \mathbf{r}) &= \frac{4\mathcal{M}_c^{5/3} \omega_{\text{orb}}^{2/3}}{|\mathbf{r}|} \frac{1 + \cos^2(\iota)}{2} \cos(2\omega_{\text{orb}} t_{\text{ret}}), \\ h_\times(t, \mathbf{r}) &= -\frac{4\mathcal{M}_c^{5/3} \omega_{\text{orb}}^{2/3}}{|\mathbf{r}|} \cos(\iota) \sin(2\omega_{\text{orb}} t_{\text{ret}}). \end{aligned} \quad (1.77)$$

This is gravitational wave radiation emitted by a binary system in terms of  $h_+$  and  $h_\times$  polarisation. The inclination angle  $\iota = 0$  referred to as "face-on" gives the equal and maximum value of  $h_+$  and  $h_\times$ , while  $\iota = \pi/2$  referred to as "edge-on" gives  $h_\times = 0$  and  $h_+$  half of maximum value.

## 1.6 Waveform

Gravitational waves from compact binary systems contain two propagating polarizations  $h_+$  and  $h_\times$ . During the emission of gravitational waves, the two compact objects gradually



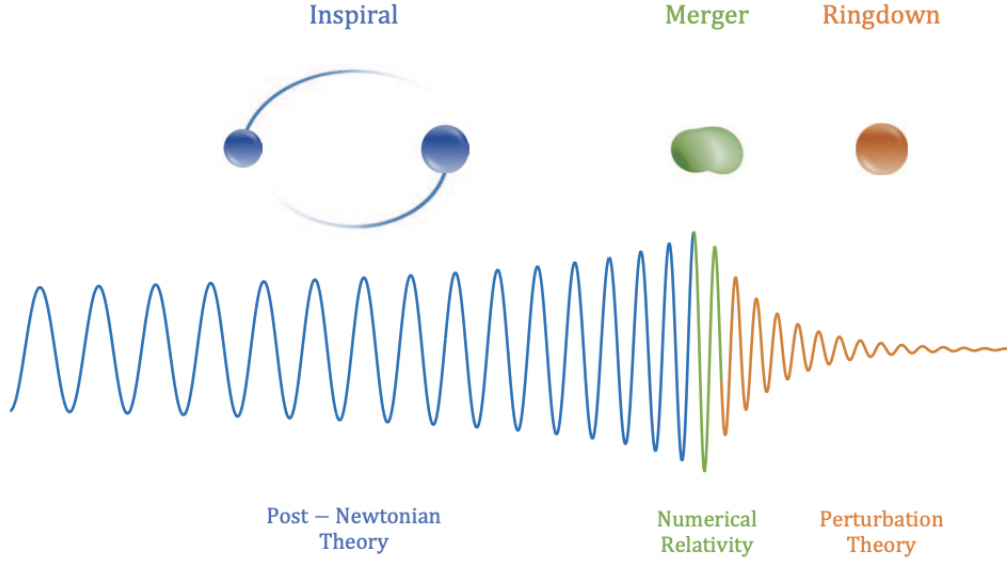


Figure 1.3: The three phases of gravitational waves from a binary system and techniques to model these.[46]

spiral inwards, and this system evolves in three different regimes, inspiral, merger, and ringdown Fig. 1.3.

In the inspiral regime, the two compact objects are orbiting and approaching each other while the orbital frequency increases. During this stage, post-Newtonian approximations are used to analytically model the evolution of the system and calculate the gravitational wave emission. The resulting gravitational wave is a sinusoid with increasing frequency and amplitude up to a limit referred to as a chirp signal.

The merger regime starts when the separation distance between the two objects reaches the innermost stable circular orbit (ISCO), and the two compact objects collide and plunge into one, Eq. (1.94). In this phase, the system evolves through a strong gravity regime which requires solutions of a non-linear Einstein's equation, but there no analytical solution exists. Therefore, numerical relativity is used to compute the gravitational waves during the merger.

Finally, the ringdown regime, when the merged object relaxes to a stationary state. In this phase, perturbation theory is used to solve the Einstein equations analytically, which gives the final compact object's quasi-normal modes. The emitted gravitational wave is modeled by exponentially damped sinusoidal oscillations of these quasi-normal modes.

### 1.6.1 Post-Newtonian approximations

Post-Newtonian (PN) approximations are used to calculate the inspiral phase of a compact binary system. The PN approximation is a series expansion in terms of the binary's gauge-invariant velocity for circular orbits  $v \equiv x^{1/2} = (M\omega)^{1/3}$ . In this formalism, the

orbit is assumed to be quasi-circular and  $v$  small. A  $n$ -PN expansion includes up to  $v^{2n}$  order terms [47].

The orbital phase is computed from the velocity  $v$  expression

$$\begin{aligned}\frac{d\phi}{dt} &= \frac{v^3}{M}, \\ \frac{dv}{dt} &= \frac{dv}{dE} \frac{dE}{dt} = -\frac{dv}{dE} \mathcal{F},\end{aligned}\tag{1.78}$$

where  $\phi$  is the binary's orbital phase,  $\omega = \frac{d\phi}{dt}$ ,  $t$  is time, and the energy balance equation is used

$$\frac{dE}{dt} = -\mathcal{F}.\tag{1.79}$$

Integrating Eqs. (1.78) gives the alternate form

$$\begin{aligned}\phi(v) &= \phi_{\text{ref}} - \frac{1}{M} \int_{v_{\text{ref}}}^v d\hat{v} \hat{v}^3 \frac{E'(\hat{v})}{\mathcal{F}(\hat{v})}, \\ t(v) &= t_{\text{ref}} - \int_{v_{\text{ref}}}^v d\hat{v} \frac{dE/d\hat{v}}{\mathcal{F}(\hat{v})}.\end{aligned}\tag{1.80}$$

where  $\phi_{\text{ref}}$  and  $t_{\text{ref}}$  refer to an arbitrary reference point in the evolution of the binary. Using the solution of orbital phase  $\phi(t)$ , the gravitational waves are given by

$$h(t) = A(t) \cos(2\phi(t)),\tag{1.81}$$

this equation is valid for both polarisations. For parameter estimation, we prefer a frequency domain waveform because the likelihood calculation is performed in the frequency domain, see: 2.2.2. We compute the Fourier-transform of the gravitational waves using

$$\tilde{h}(f) = \int_{-\infty}^{\infty} dt h(t) e^{-2i\pi ft}.\tag{1.82}$$

During the inspiral phase, the amplitude and orbital frequency evolve much more slowly than the orbital phase, i.e.,  $|\dot{A}/A| \ll \Omega$  and  $|\dot{\Omega}| \ll \Omega^2$ . As a result, the integral in Eq. (1.82) is highly oscillatory and can be approximated by expanding the integrand about the time at which the complex phase is stationary, known as the stationary-phase approximation.

Using the stationary-phase approximation (SPA), the Fourier-domain waveform Eq. (1.82) is given by

$$\tilde{h}^{\text{SPA}}(f) = \mathcal{A}(f) e^{-i\psi(f) - i\pi/4}\tag{1.83}$$

$$\psi(f) = 2\pi f t^* - 2\phi(t^*),\tag{1.84}$$

$$\mathcal{A}(f) = A(t^*) \sqrt{\frac{\pi}{\dot{\omega}(t^*)}},\tag{1.85}$$

where  $t^*$  is defined as the time when  $\omega(t^*) = \pi f$ . We define gravitational waves frequency  $f$  as  $v_f \equiv (\pi M f)^{1/3}$  similar as gauge-invariant velocity  $v$  because we find  $v(t^*) = v_f$ . We can rewrite Eq. (1.84) as

$$\psi(f) = 2 \left( \frac{1}{M} v^3 t(v) - \phi(v) \right) \Big|_{v=v_f}.\tag{1.86}$$

Inserting Eq. (1.80) into Eq. (1.86), the Fourier-domain phase is given by

$$\psi(f) = 2\pi f t_{\text{ref}} - \phi_{\text{ref}} + \frac{2}{GM} \int_{v_f}^{v_{\text{ref}}} (v_f^3 - v^3) \frac{E'(v)}{\mathcal{F}(v)} dv. \quad (1.87)$$

### 1.6.2 TaylorF2 waveform

The TaylorF2 waveform model follows by explicitly truncating the energy  $E(v)$  and flux  $\mathcal{F}(v)$  functions to consistent post-Newtonian orders in Eq. (1.87). It is an analytical waveform model which describes the inspiral phase of gravitational wave signals emitted by compact binary systems. It assumes that the binary components are point masses (includes the finite size and spin effects separately), the binary components are slowly rotating, and the binary system's orbit is quasi-circular. It also assumes SPA but it is expected to be quite good approximation [48]. This waveform model is computationally efficient because of analytic in nature but it is also less accurate.

The TaylorF2 waveform model incorporates PN expansion up to the 3.5PN order to model binary inspiral dynamics. The energy  $E(v)$  and the flux  $\mathcal{F}(v)$  are given by [49–60],

$$E(v) = -\frac{1}{2}\eta M v^2 \left[ 1 - \left( \frac{3}{4} + \frac{1}{12}\eta \right) v^2 - \left( \frac{27}{8} - \frac{19}{8}\eta + \frac{1}{24}\eta^2 \right) v^4 - \left( \frac{675}{64} - \left( \frac{34445}{576} - \frac{205}{96}\pi^2 \right) \eta + \frac{155}{96}\eta^2 + \frac{35}{5184}\eta^3 \right) v^6 \right] \quad (1.88)$$

$$\mathcal{F}(v) = \frac{32}{5}\eta^2 v^{10} \left[ 1 - \left( \frac{1247}{336} + \frac{35}{12}\eta \right) v^2 + 4\pi v^3 - \left( \frac{44711}{9072} - \frac{9271}{504}\eta - \frac{65}{18}\eta^2 \right) v^4 - \left( \frac{8191}{672} + \frac{583}{24}\eta \right) \pi v^5 + \left\{ \frac{6643739519}{69854400} + \frac{16}{3}\pi^2 - \frac{1712}{105}\gamma + \left( \frac{41}{48}\pi^2 - \frac{134543}{7776} \right) \eta - \frac{94403}{3024}\eta^2 - \frac{755}{324}\eta^3 - \frac{856}{105} \ln(16v^2) \right\} v^6 - \left( \frac{16285}{504} - \frac{214745}{1728}\eta - \frac{193385}{3024}\eta^2 \right) \pi v^7 \right], \quad (1.89)$$

where  $\eta = m_1 m_2 / M^2$  and  $\gamma = 0.57721\dots$  are the symmetric mass ratio and the Euler-Mascheroni constant, respectively. Inserting Eq. (1.88), (1.89) in to Eq. (1.87), gives the TaylorF2 waveform,

$$\tilde{h}_{+,x}(f) = \mathcal{A}_{+,x} f^{-7/6} e^{-i\psi(f) - i\pi/4}, \quad (1.90)$$

where amplitudes are given by,

$$\begin{aligned} \mathcal{A}_+ &= \frac{1 + \cos^2 \iota}{2r} \sqrt{\frac{5\pi}{96}} \mathcal{M}^{5/6} \pi^{-7/6} \\ \mathcal{A}_\times &= \frac{\cos \iota}{r} \sqrt{\frac{5\pi}{96}} \mathcal{M}^{5/6} \pi^{-7/6} \exp\left(i\frac{\pi}{2}\right), \end{aligned} \quad (1.91)$$

and phase is given by,

$$\psi(f) = 2\pi f t_c - \phi_c - \frac{\pi}{4} + \frac{3}{128\eta v^5} \sum_{k=0}^N \alpha_k v^k, \quad (1.92)$$

where the coefficients  $\alpha_k$ ,  $k = 0, \dots, N$ , (with  $N = 7$  at 3.5PN order) are given by

$$\alpha_0 = 1, \quad (1.93a)$$

$$\alpha_1 = 0, \quad (1.93b)$$

$$\alpha_2 = \frac{20}{9} \left( \frac{743}{336} + \frac{11}{4} \eta \right), \quad (1.93c)$$

$$\alpha_3 = -16\pi, \quad (1.93d)$$

$$\alpha_4 = 10 \left( \frac{3058673}{1016064} + \frac{5429}{1008} \eta + \frac{617}{144} \eta^2 \right), \quad (1.93e)$$

$$\alpha_5 = \pi \left( \frac{38645}{756} + \frac{38645}{252} \log \left( \frac{v}{v_{\text{ISCO}}} \right) - \frac{65}{9} \eta \left[ 1 + 3 \log \left( \frac{v}{v_{\text{ISCO}}} \right) \right] \right), \quad (1.93f)$$

$$\alpha_6 = \left( \frac{11583231236531}{4694215680} - \frac{640}{3} \pi^2 - \frac{6848}{21} \gamma \right) + \eta \left( -\frac{15335597827}{3048192} + \frac{2255}{12} \pi^2 - \frac{1760}{3} \theta + \frac{12320}{9} \lambda \right) + \frac{76055}{1728} \eta^2 - \frac{127825}{1296} \eta^3 - \frac{6848}{21} \log(4v), \quad (1.93g)$$

$$\alpha_7 = \pi \left( \frac{77096675}{254016} + \frac{378515}{1512} \eta - \frac{74045}{756} \eta^2 \right). \quad (1.93h)$$

where  $\lambda = -0.6451$ ,  $\theta = -1.28$  [61] and the gravitational wave frequency corresponding to the innermost stable circular orbit (ISCO) is given by

$$f_{\text{ISCO}} = \frac{1}{6^{3/2} \pi M}. \quad (1.94)$$

This ISCO frequency is computed using a point mass in the Schwarzschild metric and is taken as the fiducial reference frequency. In the case of nearly equal-mass systems, there is no clear ISCO. However, there are several methods available to compute the ISCO [62, 63]. Moreover, there are various methods to calculate ISCO beyond point mass approximation [64, 65]. The TaylorF2 waveform model is suitable for parameter estimation because of the analytical form that makes it fast to evaluate.

The contribution of spins can be calculated similarly, and their phase is given by [66–69],

$$\Psi_{SO} = \frac{3}{128} (\pi \mathcal{M} f)^{-5/3} \left\{ \sum_{k=0}^6 \beta_k x^{k/2} \right\} \quad (1.95)$$

where the coefficients  $\beta_k$ 's, are,

$$\beta_0 = 0, \quad (1.96a)$$

$$\beta_1 = 0, \quad (1.96b)$$

$$\beta_2 = 0, \quad (1.96c)$$

$$\beta_3 = 4 \left( \frac{113}{12} - \frac{19}{3} \eta \right) (\hat{\mathbf{L}} \cdot \boldsymbol{\chi}_s), \quad (1.96d)$$

$$\begin{aligned} \beta_4 = & -10 \left[ \frac{719}{48} \delta_m (\hat{\mathbf{L}} \cdot \boldsymbol{\chi}_s) (\hat{\mathbf{L}} \cdot \boldsymbol{\chi}_a) + \left( \frac{719}{96} + \frac{\eta}{24} \right) (\hat{\mathbf{L}} \cdot \boldsymbol{\chi}_s)^2 + \left( \frac{719}{96} - 30\eta \right) \right. \\ & \left. \times (\hat{\mathbf{L}} \cdot \boldsymbol{\chi}_a)^2 \right], \end{aligned} \quad (1.96e)$$

$$\begin{aligned} \beta_5 = & -(1 + 3 \log v) \left[ \left( \frac{732985}{2268} - \frac{24260}{81} \eta - \frac{340}{9} \eta^2 \right) (\hat{\mathbf{L}} \cdot \boldsymbol{\chi}_s) + \left( \frac{732985}{2268} + \frac{140}{9} \eta \right) \right. \\ & \left. \times \delta_m (\hat{\mathbf{L}} \cdot \boldsymbol{\chi}_a) \right], \end{aligned} \quad (1.96f)$$

$$\beta_6 = + \frac{2270\pi}{3} \left[ \left( 1 - \frac{227}{156} \eta \right) (\hat{\mathbf{L}} \cdot \boldsymbol{\chi}_s) + \delta_m (\hat{\mathbf{L}} \cdot \boldsymbol{\chi}_a) \right]. \quad (1.96g)$$

$\delta_m = (m_1 - m_2)/M$ ,  $\hat{\mathbf{L}}$  is the unit vector along the orbital angular momentum,  $\boldsymbol{\chi}_s = (\boldsymbol{\chi}_1 + \boldsymbol{\chi}_2)/2$  and  $\boldsymbol{\chi}_a = (\boldsymbol{\chi}_1 - \boldsymbol{\chi}_2)/2$  are symmetric and anti-symmetric dimensionless spins respectively. The leading order spin effects come to the 1.5PN order.

The contribution due to the tidal effect for binary neutron star inspiral phase is shown in Eq. (3.22).

The TaylorF2 waveform model can be rapidly evaluated due to its analytical nature, because of this it has a substantial advantage for parameter estimation of binary system which requires generation of waveform for millions of times or more. However, this waveform model has disadvantage of representing the inspiral part of binary evolution, and omitting the merger and ringdown phases. Furthermore, given the higher frequency range sensitivity of current GW detectors, the TaylorF2 waveform model has reduced accuracy for massive systems. This is because of SPA breaks down when the phase variation is slow [50].

### 1.6.3 Phenomenological IMRPhenomPv2 waveform

A phenomenological IMRPhenomPv2 waveform model covers the full inspiral-merger-ringdown regime [70–72]. The inspiral regime is structurally based on improvements to TaylorF2 which incorporates analytical terms calibrated with numerical relativity waveforms. The merger and ringdown regimes also have analytical terms calibrated with numerical relativity waveforms, which are added smoothly with the inspiral regime. A numerical waveform will be extremely costly to generate for parameter estimation; as a result, this phenomenological waveform is used, which is faster to generate.

We will briefly review IMRPhenomD waveform, which describes an aligned-spin binary black holes system whereas IMRPhenomPv2 waveform describes the precessing

binary black holes system. IMRPhenomPv2 waveform model is obtained by using IMRPhenomD waveform model in a comoving frame and then transforming it by Euler rotations  $R$  [73],

$$h_{prec} = R h_{aligned}. \quad (1.97)$$

An aligned-spin binary system requires only the dimensionless spin parameters,

$$\chi_i = \frac{\vec{S}_i \cdot \hat{L}}{m_i^2}, \quad (1.98)$$

where  $\vec{S}_{1,2}$  are black hole spins,  $\hat{L}$  is orbital angular momentum. These dimensional spin parameters lie in the range  $\chi_i \in [-1, 1]$ .

But the spin dependence of the model is parametrised by effective spin parameter [74, 75],

$$\chi_{\text{eff}} = \frac{m_1 \chi_1 + m_2 \chi_2}{M}. \quad (1.99)$$

This is based on the the observation that it is a weighted sum of the spins that constitutes the dominant effect of the spin on the inspiral of the binary. In PN theory, the leading-order spin effect on the binary's phasing is in fact [74, 76, 77],

$$\chi_{\text{PN}} = \chi_{\text{eff}} - \frac{38\eta}{113}(\chi_1 + \chi_2), \quad (1.100)$$

and it has been shown in previous work that this is also a better parameter to use in IMR models [78].

The inspiral phase is defined in the frequency range  $Mf \in [0.0035, 0.018]$  and modelled as,

$$\psi_{\text{Ins}} = \psi_{\text{TaylorF2}} + \frac{1}{\eta} \left( \sigma_0 + \sigma_1 f + \frac{3}{4} \sigma_2 f^{4/3} + \frac{3}{5} \sigma_3 f^{5/3} + \frac{1}{2} \sigma_4 f^2 \right), \quad (1.101)$$

where  $\eta$  is the symmetric mass ratio, and  $\sigma_i$  are the fitting parameters. The  $\psi_{\text{TaylorF2}}$  is the phase from the TaylorF2 waveform model Eq. (1.92), and the additional terms allow the phase to be valid for higher frequency. The intermediate phase connects the inspiral and merger-ringdown phase and lies in frequency range  $Mf \in [0.018, 0.5Mf_{RD}]$  and it is given by,

$$\psi_{\text{Int}} = \frac{1}{\eta} \left( \beta_0 + \beta_1 f + \beta_2 \text{Log}(f) - \frac{\beta_3}{3} f^{-3} \right). \quad (1.102)$$

where  $f_{RD}$  is ringdown quasi-normal mode (QNM) frequency and  $\beta_i$  are the fitting parameters. The last term in Eq. (1.102) has  $-2\text{PN}$  order which helps fit data well across the entire parameter space [72]. The ringdown phase is lies in frequency range  $f \in [0.045, 1.15]f_{RD}$  and is given by,

$$\psi_{\text{MR}} = \frac{1}{\eta} \left\{ \alpha_0 + \alpha_1 f - \alpha_2 f^{-1} + \frac{4}{3} \alpha_3 f^{3/4} + \alpha_4 \tan^{-1} \left( \frac{f - \alpha_5 f_{RD}}{f_{\text{damp}}} \right) \right\}. \quad (1.103)$$

where  $f_{\text{damp}}$  is the ringdown damping frequency and  $\alpha_i$  are the fitting parameters.

The full inspiral-merger-ringdown phase is obtained by joining all these phase terms,

$$\psi_{\text{IMR}}(f) = \psi_{\text{Ins}}(f) \theta_{f_1}^- + \theta_{f_1}^+ \psi_{\text{Int}}(f) \theta_{f_2}^- + \theta_{f_2}^+ \psi_{\text{MR}}(f), \quad (1.104)$$

where  $f_1 = 0.018$  and  $f_2 = 0.5f_{\text{RD}}$ . In order to ensure  $\psi_{\text{IMR}}$  to be  $C(1)$  continuous, a constant and a linear coefficient are added in all 3 phase terms. where,

$$\theta(f - f_0) = \begin{cases} -1, & f < f_0, \\ 1, & f \geq f_0, \end{cases} \quad (1.105)$$

and,

$$\theta_{f_0}^\pm = \frac{1}{2} [1 \pm \theta(f - f_0)]. \quad (1.106)$$

The modeling of amplitude is also divided into these three regimes defined by different frequency ranges. The inspiral amplitude  $A_{\text{Ins}}$  defined up to frequency  $Mf = 0.014$  and given as,

$$A_{\text{Ins}} = A_{\text{PN}} + A_0 \sum_{i=1}^3 \rho_i f^{(6+i)/3}. \quad (1.107)$$

where  $A_{\text{PN}}$  is re-expanded PN amplitude,

$$A_{\text{PN}}(f) = A_0 \sum_{i=0}^6 \mathcal{A}_i (\pi f)^{i/3}, \quad (1.108)$$

where  $A_0$  is the leading order  $f^{-7/6}$ ,  $\mathcal{A}_i$  are re-expanded coefficients and  $\rho_i$  are the fitting parameters. The ringdown amplitude is modeled by a Lorentzian distribution and an exponential decay in the frequency range  $Mf \in [1/1.15, 1.2]f_{\text{RD}}$  and is given by,

$$\frac{A_{\text{MR}}}{A_0} = \gamma_1 \frac{\gamma_3 f_{\text{damp}}}{(f - f_{\text{RD}})^2 + (\gamma_3 f_{\text{damp}})^2} e^{-\frac{\gamma_2(f - f_{\text{RD}})}{\gamma_3 f_{\text{damp}}}} \quad (1.109)$$

where  $\gamma_i$  are the fitting parameters. The amplitude Eq. (1.109) peaks at  $f_{\text{peak}}$ ,

$$f_{\text{peak}} = f_{\text{RD}} + \frac{f_{\text{damp}} \gamma_3 (\sqrt{1 - \gamma_2^2} - 1)}{\gamma_2} \quad (1.110)$$

The intermediate amplitude  $A_{\text{Int}}$  is defined in the frequency range  $Mf \in [0.014, f_{\text{peak}}]$  and given by,

$$\frac{A_{\text{Int}}}{A_0} = \delta_0 + \delta_1 f + \delta_2 f^2 + \delta_3 f^3 + \delta_4 f^4 \quad (1.111)$$

where  $\delta_i$  are determined by solving for the amplitude to be  $C(1)$  continuous at both end of frequency  $Mf = \{0.014, f_{\text{peak}}\}$  and amplitude  $A_{\text{Int}}$  at  $f = (0.014/M + f_{\text{peak}})/2$  is matched with the numerical relativity simulations.

The full inspiral-merger-ringdown amplitude is given by

$$A_{\text{IMR}}(f) = A_{\text{Ins}}(f) \theta_{f_1}^- + \theta_{f_1}^+ A_{\text{Int}}(f) \theta_{f_2}^- + \theta_{f_2}^+ A_{\text{MR}}(f), \quad (1.112)$$

where  $A_{\text{Ins}}$  is given by Eq. (1.107),  $A_{\text{Int}}$  by Eq. (1.111), and  $A_{\text{MR}}$  by Eq. (1.109), and where the transition frequencies are  $f_1 = 0.014$  and  $f_2 = f_{\text{peak}}$ , Eq. (1.110).

Thus the fitting parameters involved  $\{\Lambda_i\}$  in the calibration are

$$\Lambda^i = \underbrace{\{\rho_j\}, \{A_{\text{Int}}\}}_{\text{Amplitude Coefficients}}, \underbrace{\{\gamma_j\}, \{\sigma_j\}, \{\beta_j\}, \{\alpha_j\}}_{\text{Phase Coefficients}}. \quad (1.113)$$

where  $i \in \{1, 2, 3, 4, 5, 6\}$ . These parameters are fit in terms of polynomials up to second order in  $\eta$  and third order in  $\chi_{PN}$  as,

$$\Lambda^j = \sum_{m=0}^3 \sum_{n=0}^2 (\chi_{PN} - 1)^m (\lambda_{nm}^j \eta^n) \quad (1.114)$$

where  $\lambda_{nm}^j$  are the fitting coefficients with numerical relativity simulations [79].

## 1.7 Dark charged binary black holes

### 1.7.1 Binary black holes

The Advanced LIGO [3] and Advanced Virgo [6] gravitational wave (GW) detectors have so far found around 100 candidate signals [80], the majority being from coalescing binary black holes [81–86], in addition to two binary neutron star inspirals [29, 30] and two neutron star-black hole events [87].

In Sec. 1.5, we described the gravitational waves emitted by a binary system with point masses which is the lowest-order approximation for binary black holes, in the next section we modeled the higher-order corrections. In Sec. 1.6.2, we described analytical higher PN order corrections known as the TaylorF2 waveform model which includes 3.5PN point particle phase and spin-orbit contribution. In Sec. 1.6.3, the phenomenological IMRPhenomPv2 waveform model describes the higher order correction which is a more accurate waveform model. For binary black holes, this point mass approximation fails when the separation between two black holes becomes comparable to their sizes.

### 1.7.2 Dark charges on binary black holes

In the analyses of the binary black hole signals, the sources were assumed to be well-modeled as pure vacuum spacetime, although tests of general relativity (GR) were performed which allowed for deviations from the dynamics predicted by Einstein’s theory [7–11].

Dark matter is a form of matter that does not interact with light, making it difficult to directly detect. But, its existence is inferred from the gravitational effects it has on visible matter and the structure of the universe. The first strong evidence comes from the velocities of galaxies in clusters, which was proposed by Zwicky [16]. Additional strong evidence comes from galactic rotation curves [17], the Bullet Cluster [18], and the cosmic microwave background power spectrum [19].

The exact nature of dark matter is not known, but several dark matter candidates have been proposed, such as weakly interacting massive particles (WIMPs), axions, sterile neutrinos, primordial black holes, dark charges, and others [20, 21]. Dark matter



interact extremely weakly with standard model particles and it requires beyond standard model physics. From cosmological observations, dark matter accounts for almost 30% of the matter in the Universe and in astrophysics, the properties of dark matter will determine how structure forms in the Universe. Large Hadron Collider (LHC), XENON and other experiments are actively searching for evidence of dark matter particles [22, 23]. The discovery of dark matter would solve a major problem in physics and will have crucial implications for particle physics, cosmology, and astrophysics.

The WIMPs were favored dark matter candidates because the abundance of dark matter derived from freeze out roughly corresponds to the observed abundance. This nice coincidence is often referred to as the ‘WIMP Miracle’ [88]. But the WIMPs are no longer favored because the null results from direct and indirect searches for dark matter [89]. We consider dark charges as an alternative dark matter candidates. Dark charges are neutral under all standard model gauge interactions [24], but charged under an exact  $U(1)$  gauge symmetry of the hidden sector [25].

There appears to be no known astrophysical processes by which ordinary charges can accumulate on black holes, but there could be an accumulation of dark charges due to their different charge-to-mass ratio etc., which in turn motivates a search for such dark charges. Because, the known astrophysical processes such as kinematic build-up of charge through infall of electrons and dynamical charge accretion by a rotating black hole in a magnetic field is limited by the ratio of electron mass  $m_e$  to charge  $e$ . Also, binary black holes are clean sources, eliminating the need for modelling the surrounding environment. We will explore the existence of dark charges on binary black holes using the GWs signals from these sources.

In Chapter 4, we will look into another possible source for modifications in binary black hole dynamics, namely minicharged dark matter. In models of minicharged dark matter associated with a hidden  $U(1)$  symmetry, astrophysical black holes may acquire a “dark” charge, in such a way that the inspiral dynamics of binary black holes can be formally described by an Einstein-Maxwell theory. Charges enter the gravitational wave signal predominantly through a dipole term, but their effect is known to effectively first post-Newtonian order in the phase, which enables measuring the size of the charge-to-mass ratios,  $|q_i/m_i|$ ,  $i = 1, 2$ , of the individual black holes in a binary.

# Detection and parameter estimation of gravitational waves

In this chapter, we discuss the detection of gravitational waves signal and the characterization of noise. We review the match filtering technique which is used to extract the signal from observed data. Then, we describe the parameter estimation framework that is utilized to analyze the signal and provide a detailed explanation of the sampling algorithms that are used [90].

## 2.1 Detection of gravitational waves



Figure 2.1: Aerial views of three of the existing GW detectors: LIGO Hanford Observatory, Washington USA (left), the LIGO Livingston Observatory, Louisiana USA (centre) and the Virgo detector, Italy (right).

Gravitational waves emitted by astrophysical objects will have strengths of the order of  $h \sim 10^{-22}$ . A highly sensitive instrument is needed to measure these very small strengths. The Laser Interferometer Gravitational-Wave Observatory (LIGO) measures gravitational waves of astrophysical origin. LIGO consists of two L-shape power-recycling

Fabry-Perot Michelson interferometers with arm lengths of 4 Km [91, 92]. There are two LIGO detectors, one located in Hanford, WA (referred to as H1) and the other in Livingston, LA (referred to as L1), and they have separated approximately 3000 Km, which is equivalent to about 10 ms at the speed of light [3]. There are two detectors based on the same principle but with a smaller arm length of 3 km, namely Virgo located in Pisa, Italy [6], and KAGRA located in Gifu Prefecture, Japan [93]. LIGO-India is a collaborative project between the LIGO Scientific Collaboration and the Indian Initiative in Gravitational-wave Observations to build a third advanced LIGO detector in India [94]. Aerial views of the LIGO and Virgo detectors are shown in Fig. 2.1.

Third-generation detectors are being developed to further improve the accuracy of

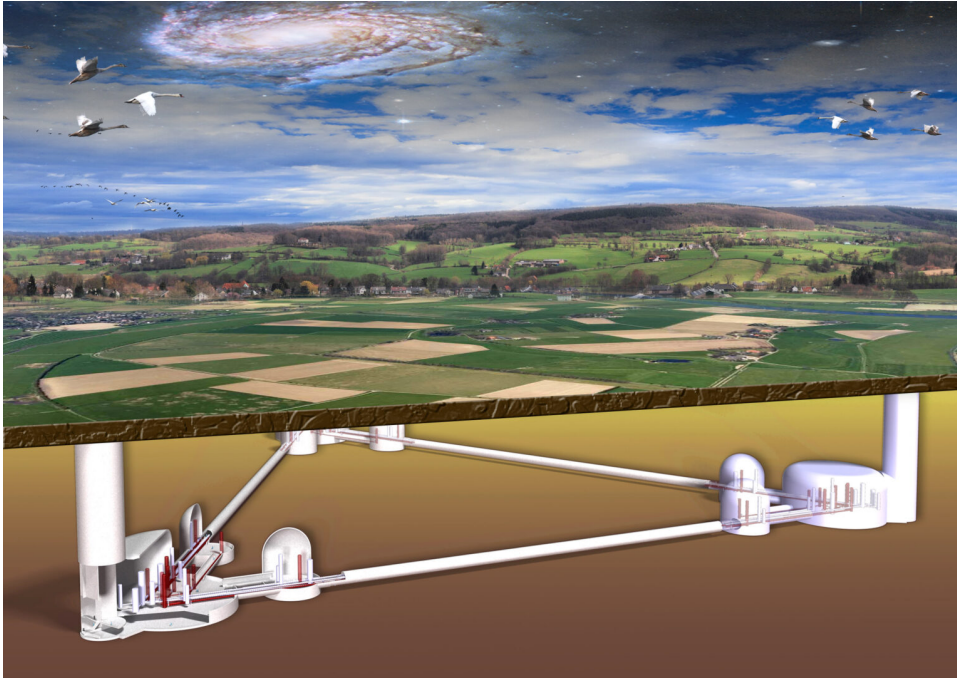


Figure 2.2: Artist's Impression of the future next-generation detector Einstein Telescope by Marco Kraan (Nikhef)

gravitational wave measurements. Einstein Telescope (ET) and Cosmic Explorer (CE) are two proposed third-generation gravitational wave detectors [95–98]. In Fig. 2.2 shows an artist's Impression of ET, which is proposed to be an underground detector featuring a baseline design in the shape of a triangle with 10 km-long arms. CE is proposed to be an above-ground detector with the current layout assumes two interferometers in different locations: one with a 40 km arm length and the other with a 20 km arm length.

Another future detector is the Laser Interferometer Space Antenna (LISA), a space-based gravitational wave detector [99]. LISA will detect gravitational waves in the low-frequency band compared to ground-based detectors, ranging from 0.1 mHz to 1 Hz. It will consist of three spacecraft arranged in an equilateral triangle, each containing a laser interferometer, with a separation distance of 2.5 million kilometers between them.

### 2.1.1 Gravitational waves strain induced in interferometric detectors

Consider an L-shaped detector situated at the origin in the  $(x, y)$  plane, where the end mirrors are positioned at  $(L, 0)$  and  $(0, L)$ . In the presence of gravitational waves propagating along the  $z$ -axis, the displacements of the two mirrors on the  $x$  and  $y$ -axis are given by

$$\delta x = \frac{1}{2}h_+(t)L, \quad \delta y = -\frac{1}{2}h_+(t)L \quad (2.1)$$

and the relative difference in arm lengths is,

$$h(t) \equiv \frac{\delta L}{L} = \frac{\delta x - \delta y}{L} = h_+(t). \quad (2.2)$$

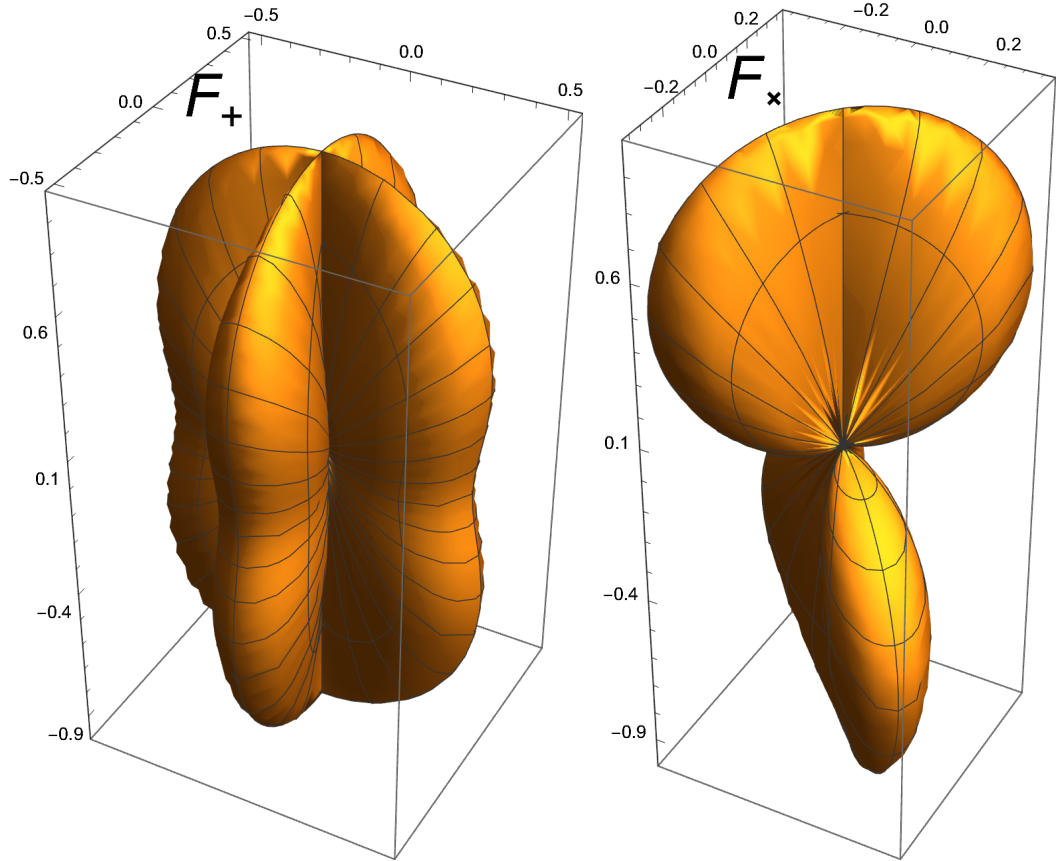


Figure 2.3: The detector's response is characterized by the antenna pattern function for the  $+$  polarization(left) and  $\times$  polarization (right) (here  $\psi = 0$ ).

Generalizing the result for gravitational waves produced by a source located at  $(r, \theta, \phi)$  is straightforward. The relative difference in arm lengths is given by,

$$h(t) = F_+h_+ + F_\times h_\times \quad (2.3)$$

where  $F_+$  and  $F_\times$  are the antenna pattern functions that model the detector's response to the  $+$  and  $\times$  polarizations. For an L-shaped detector, the antenna patterns functions

are given by

$$\begin{aligned} F_+ &= \frac{1}{2} (1 + \cos^2 \theta) \cos 2\phi \cos 2\psi - \cos \theta \sin 2\phi \sin 2\psi \\ F_\times &= \frac{1}{2} (1 + \cos^2 \theta) \cos 2\phi \sin 2\psi + \cos \theta \sin 2\phi \cos 2\psi \end{aligned} \quad (2.4)$$

where  $\psi$  is the polarization angle which fixes an orientation in the plane perpendicular to the propagation direction. The antenna pattern functions are shown in Fig. 2.3 for polarisation angle  $\psi = 0$ .

## 2.2 Signal extraction

Gravitational waves observed by the interferometric detectors are weak; as a result, the effect of noise is significant. The detector's output  $d(t)$  is given by,

$$d(t) = h(t) + n(t) \quad (2.5)$$

where  $h(t)$  is a gravitational wave signal that may be present, and  $n(t)$  is the noise contribution. The latter contribution comes from various sources, e.g., gravitational disruption from nearby mass, seismic activity, etc [100, 101].

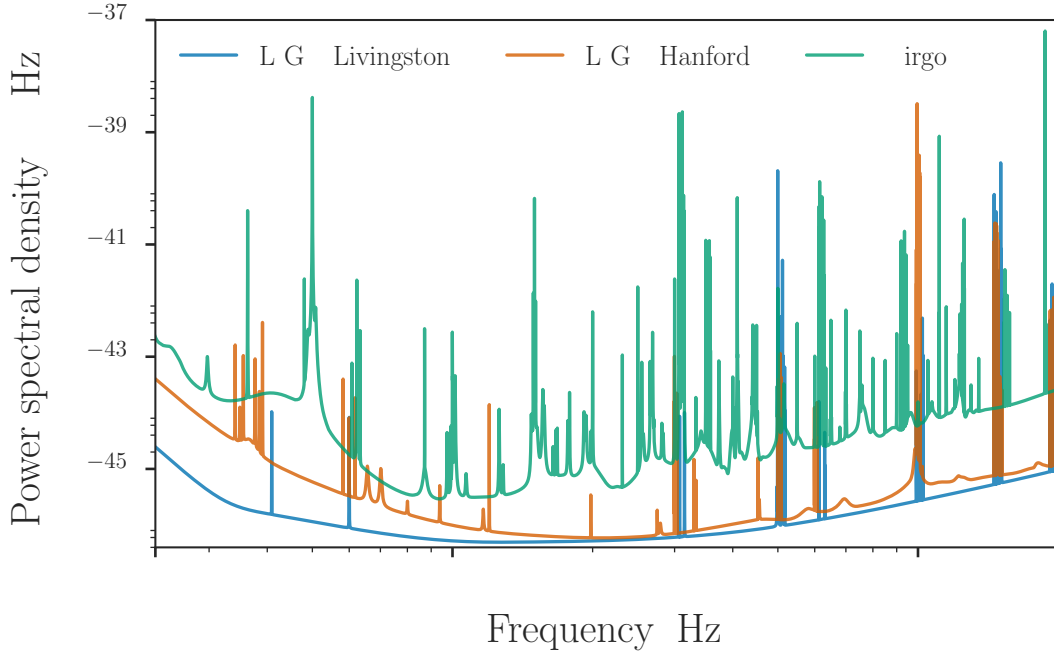


Figure 2.4: PSDs of the Advanced LIGO–Advanced Virgo network. There are high-amplitude narrow-band spectral lines which originate from a variety of sources including the mirror suspensions, the AC electrical supply, or sinusoidal motion imparted on the mirrors for data calibration [102].



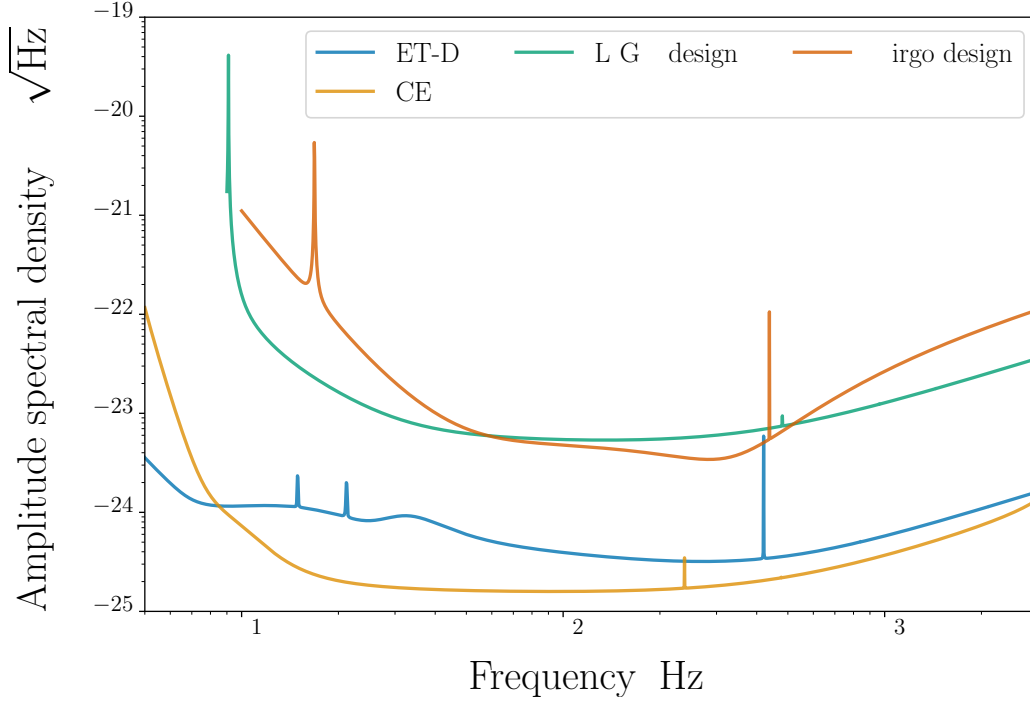


Figure 2.5: ASDs of the ET-D, CE (proposed future facilities), Advanced LIGO and Virgo at design. ET-D is basically a factor  $\sim 10$  more sensitive in a wide frequency range, and has much better sensitivity at low frequencies than Advanced LIGO and Virgo at design. CE is slightly more sensitive in a wide frequency range and less sensitive at lower frequencies compared to ET-D.

### 2.2.1 Characterization of noise

The noise  $n(t)$  is modeled as a stationary Gaussian stochastic process. The mean of the noise is assumed to be zero, which implies that,

$$\langle n(t) \rangle = 0, \quad \Rightarrow \quad \langle \tilde{n}(f) \rangle = 0 \quad (2.6)$$

where  $\langle . \rangle$  is the ensemble average and  $\tilde{n}(f)$  denotes the Fourier transform of  $n(t)$ . Now consider the second moment of the noise defined as autocorrelation function  $K$  to characterize the noise,

$$\langle n(t)n(t') \rangle = K(t, t'). \quad (2.7)$$

From the definition  $K(t, t') = K(t', t)$ . The stationary property of noise means that the noise properties are independent of time which is described by,

$$\langle n(t) \rangle = \langle n(t + \tau) \rangle \quad \langle n(t)n(t') \rangle = \langle n(t + \tau)n(t' + \tau) \rangle \quad (2.8)$$

where  $\tau$  is a time translation. The autocorrelation function satisfies the following relation

$$K(t, t') = K(t + \tau, t' + \tau). \quad (2.9)$$

For  $\tau = -t'$ , the autocorrelation function becomes  $K(t, t') = K(t - t', 0)$ , function of only one variable  $t - t'$ . Using these properties of the autocorrelation function, the second moment in Fourier space is, given by,

$$\begin{aligned}
 \langle \tilde{n}(f) \tilde{n}^*(f') \rangle &= \iint dt dt' \langle n(t) n(t') \rangle e^{-2\pi i f t + 2\pi i f' t'} \\
 &= \iint dt dt' K(t - t') e^{-2\pi i f t + 2\pi i f' t'} \\
 &= \iint dt d\tau K(\tau) e^{-2\pi i f t + 2\pi i f' (t + \tau)} \\
 &= \int d\tau K(\tau) e^{2\pi i f \tau} \times \delta(f - f') \\
 &= S(f) \delta(f - f')
 \end{aligned} \tag{2.10}$$

$\star$  denotes the complex conjugate. Since  $K(\tau) = K(-\tau)$  using Eq. (2.7), implies that it is an even function, so its Fourier transform  $S(f)$  is real. Eq. (2.10) implies that  $S(f) = \langle |\tilde{n}(f)|^2 \rangle \times T$ , where  $T$  is observation time,  $S(f)$  is average of positive quantities that makes it positive definite and even function  $S(f) = S(-f)$ . So,  $S(f)$  can be folded on itself and defined only for  $f \geq 0$ , and  $S_n(f)$  is called the one-sided power spectral density (PSD) shown in Fig. 2.4. For one-sided PSD  $S_n(f)$  Eq. (2.10) becomes,

$$\langle \tilde{n}(f) \tilde{n}^*(f') \rangle = \frac{1}{2} \delta(f - f') S_n(f). \tag{2.11}$$

The amplitude spectral density (ASD) of gravitational waves is defined as the square root of the PSD. Fig. 2.5 shows ASDs of the ET-D, CE, Advanced LIGO and Virgo at design.

## 2.2.2 Matched filtering

The detection of gravitational wave signals is a challenging task, as they are buried within the noise. To overcome this challenge, the matched filtering technique is widely utilized in data analysis. This technique involves comparing a known template waveform, representing the expected signal, to the noisy data in order to efficiently identify any potential signals that may be present.

Suppose we are searching for the gravitational-wave signal  $h(t)$  in the data  $d(t)$  with a matched filter  $W(t)$ . We apply  $W(t)$  as,

$$\hat{d} = \int_{-\infty}^{\infty} dt d(t) W(t) = \int_{-\infty}^{\infty} df \tilde{d}(f) \tilde{W}(f)^*. \tag{2.12}$$

The signal-to-noise ratio is defined by  $\rho = S/N$  where  $S$  is the mean of  $\hat{d}$  in the presence of signal  $h(t)$  and  $N$  is the standard deviation of  $\hat{d}$  in the absence of signal.  $S$  is given

by,

$$\begin{aligned}
 S &\equiv \langle \hat{d} \rangle, \text{ with } d(t) = h(t) + n(t) \\
 &= \left\langle \int_{-\infty}^{\infty} dt d(t) W(t) \right\rangle \\
 &= \int_{-\infty}^{\infty} dt \langle d(t) \rangle W(t) \\
 &= \int_{-\infty}^{\infty} dt h(t) W(t) + \int_{-\infty}^{\infty} dt n(t) W(t) \\
 &= \int_{-\infty}^{\infty} df \tilde{h}(f) \tilde{W}^*(f) \\
 &= 2\Re \int_0^{\infty} df \tilde{h}(f) \tilde{W}^*(f),
 \end{aligned} \tag{2.13}$$

where we have used Eq. (2.6), (2.12).  $N$  is given by,

$$\begin{aligned}
 N^2 &\equiv \langle \hat{d}^2 \rangle - \langle \hat{d} \rangle^2, \text{ with } d(t) = n(t) \\
 &= \int_{-\infty}^{\infty} \int_{-\infty}^{\infty} dt dt' \langle n(t) n(t') \rangle W(t) W(t') \\
 &= \frac{1}{2} \int_{-\infty}^{\infty} df S_n(f) \tilde{W}(f) \tilde{W}^*(f) \\
 &= \int_0^{\infty} df S_n(f) \tilde{W}(f) \tilde{W}^*(f).
 \end{aligned} \tag{2.14}$$

where we have used Eq. (2.11). The signal-to-noise ratio  $\rho = S/N$  is given by,

$$\begin{aligned}
 \rho &= 2\Re \int_0^{\infty} df \tilde{h}(f) \tilde{W}^*(f) / \sqrt{\int_0^{\infty} df S_n(f) \tilde{W}(f) \tilde{W}^*(f)} \\
 &= 4\Re \int_0^{\infty} df \tilde{h}(f) \tilde{W}^*(f) / S_n(f) / \sqrt{4\Re \int_0^{\infty} df \tilde{W}(f) \tilde{W}^*(f) / S_n(f)}
 \end{aligned} \tag{2.15}$$

where  $\tilde{\tilde{W}}(f) = \tilde{W}(f) S_n(f)$ . We can write Eq. (2.15) more compactly by defining inner product,

$$(a|b) = 4\Re \int_0^{\infty} df \frac{\tilde{a}^*(f) \tilde{b}(f)}{S_n(f)} \tag{2.16}$$

The symbol  $\Re$  denotes the operation of taking the real part, the integration limits are the lower and upper frequency range considered,  $S_n$  is the noise spectral density of the detector Eq. (2.11). The signal-to-noise ratio  $\rho$  is written as,

$$\rho = \frac{(h | \hat{W})}{\sqrt{(\hat{W} | \hat{W})}}, \tag{2.17}$$

The signal-to-noise ratio  $\rho$  Eq. (2.15) is maximised for the optimal filter given by,

$$\tilde{W}(f) \sim \frac{\tilde{h}(f)}{S_n(f)} \tag{2.18}$$



and the corresponding signal-to-noise ratio is,

$$\rho = \sqrt{(h|h)} \quad (2.19)$$

This is referred to as the optimal signal-to-noise ratio.

## 2.3 Parameter estimation framework

### 2.3.1 Bayesian framework

A Bayesian data analysis framework is commonly used for gravitational waves signals, as explained e.g. in [103, 104] and briefly reviewed below. In the presence of a signal  $h$  with parameters  $\theta$ , the data  $d$  from the detector output can be decomposed as

$$d = h(\theta) + n, \quad (2.20)$$

for some noise realization  $n$ , Eq. (2.5). Then, for Gaussian noise the likelihood  $p(d|\mathcal{H}, \theta, \mathcal{I})$  for the detector to measure the data  $d$  for a signal with parameters  $\theta$  is given by

$$p(d|\mathcal{H}, \theta, \mathcal{I}) \propto \exp \left[ -\frac{1}{2}(n|n) \right] \propto \exp \left[ -\frac{1}{2}(d - h(\theta)|d - h(\theta)) \right], \quad (2.21)$$

where we have used Eq. (2.20). Here, the meaning of  $(\cdot|\cdot)$  differs on both sides of the equation: on the left hand side,  $p(d|\mathcal{H}, \theta, \mathcal{I})$  denotes the conditional probability of observing the data  $d$  for a collection of signal parameters  $\theta$ , while on the right hand side, the notation  $(\cdot|\cdot)$  indicates an inner product on the vector space of signals which is defined in Eq. (2.16).

This likelihood (2.21) can be further expanded as

$$p(d|\mathcal{H}, \theta, \mathcal{I}) \propto \exp \left[ -\frac{1}{2} [(d|d) + (h(\theta)|h(\theta)) - 2(d|h(\theta))] \right]. \quad (2.22)$$

The second term  $(h(\theta)|h(\theta)) = \rho_{\text{opt}}^2$  is called the optimal matched filter signal-to-noise ratio (SNR) squared.

The posterior probability distribution of the parameters  $\theta$  follows from Bayes' theorem:

$$p(\theta|\mathcal{H}, d, \mathcal{I}) = \frac{p(d|\mathcal{H}, \theta, \mathcal{I})p(\theta|\mathcal{H}, \mathcal{I})}{p(d|\mathcal{H}, \mathcal{I})} \quad (2.23)$$

where  $\mathcal{I}$  is the background information,  $\mathcal{H}$  is the hypothesis, i.e. the waveform model. The quantity  $p(\theta|\mathcal{H}, \mathcal{I})$  is the prior probability, i.e. knowledge about the parameters within the model before analyzing the data,  $p(d|\mathcal{H}, \mathcal{I})$  is the evidence and  $p(d|\mathcal{H}, \theta, \mathcal{I})$  is the likelihood function which is identified with (2.22). The evidence is given by,

$$p(d|\mathcal{H}, \mathcal{I}) = \int d\theta p(d|\mathcal{H}, \theta, \mathcal{I}) p(\theta|\mathcal{H}, \mathcal{I}). \quad (2.24)$$

Computing the posterior probability distribution of the parameters  $\theta$  requires Markov chain Monte Carlo (MCMC) samplers or nested samplers which are described in detail in Sec. 2.4 and Sec. 2.5.

### 2.3.2 Fisher matrix framework

The above framework is general but also computationally intensive, especially for binary neutron star signals from next-generation gravitational waves detectors. These will have a much wider frequency band than current detectors such that signals from neutron star binaries will linger for many hours to days within the sensitive band. The associated tremendous computational costs severely limit the scope of exploratory studies possible with the current MCMC or Nested Sampling code infrastructures. However, 'golden' events similar to GW170817, which would have an SNR of over a thousand in next-generation detectors, will provide rich science yields, especially when combined with the larger number of events with lower SNR. For exploratory studies, we use a simplified data analysis framework based on approximations for large SNR: the Fisher Matrix formalism, which we explain in detail below.

Let  $\boldsymbol{\theta}_0$  be the true value of the parameters and  $\boldsymbol{\theta} = \boldsymbol{\theta}_0 + \Delta\boldsymbol{\theta}$  the best-fit parameters in the presence of Gaussian noise. Then, the likelihood function is given by Eq. (2.22)

$$p(d|\mathcal{H}, \boldsymbol{\theta}, \mathcal{I}) = \mathcal{N}' e^{-\frac{1}{2}[(d|d) + (h(\boldsymbol{\theta})|h(\boldsymbol{\theta})) - 2(d|h(\boldsymbol{\theta}))]} \quad (2.25)$$

At  $\boldsymbol{\theta}_0$  the likelihood function is maximum, we do Taylor expansion of the waveform  $h(\boldsymbol{\theta})$  around  $\boldsymbol{\theta}_0$ ,

$$h(\boldsymbol{\theta}) = h(\boldsymbol{\theta}_0) + \left. \frac{\partial h}{\partial \theta^i} \right|_{\boldsymbol{\theta}_0} \Delta\theta^i + \frac{1}{2} \left. \frac{\partial^2 h}{\partial \theta^i \partial \theta^j} \right|_{\boldsymbol{\theta}_0} \Delta\theta^i \Delta\theta^j \quad (2.26)$$

In the exponent of Eq. (2.25), the first term  $(d|d)$  does not depend upon  $\boldsymbol{\theta}$ , we expand the remaining terms using Eq. (2.26),

$$\begin{aligned} (h(\boldsymbol{\theta})|h(\boldsymbol{\theta})) &= (h(\boldsymbol{\theta}_0)|h(\boldsymbol{\theta}_0)) + 2 \left( h(\boldsymbol{\theta}) \left| \frac{\partial h(\boldsymbol{\theta})}{\partial \theta^i} \right| \right) \Big|_{\boldsymbol{\theta}_0} \Delta\theta^i + \left( \frac{\partial h(\boldsymbol{\theta})}{\partial \theta^i} \left| \frac{\partial h(\boldsymbol{\theta})}{\partial \theta^j} \right| \right) \Big|_{\boldsymbol{\theta}_0} \Delta\theta^i \Delta\theta^j \\ &\quad + \left( h(\boldsymbol{\theta}) \left| \frac{\partial^2 h(\boldsymbol{\theta})}{\partial \theta^i \partial \theta^j} \right| \right) \Big|_{\boldsymbol{\theta}_0} \Delta\theta^i \Delta\theta^j \end{aligned} \quad (2.27)$$

$$(d|h(\boldsymbol{\theta})) = (d|h(\boldsymbol{\theta}_0)) + \left( d \left| \frac{\partial h(\boldsymbol{\theta})}{\partial \theta^i} \right| \right) \Big|_{\boldsymbol{\theta}_0} \Delta\theta^i + \frac{1}{2} \left( d \left| \frac{\partial^2 h(\boldsymbol{\theta})}{\partial \theta^i \partial \theta^j} \right| \right) \Big|_{\boldsymbol{\theta}_0} \Delta\theta^i \Delta\theta^j \quad (2.28)$$

To further simplify these equations, we use the maximum likelihood condition which is given by,

$$\frac{\partial p}{\partial \theta^i} = 0 = -2 \left( d \left| \frac{\partial h(\boldsymbol{\theta})}{\partial \theta^i} \right| \right) \Big|_{\boldsymbol{\theta}_0} + 2 \left( h(\boldsymbol{\theta}) \left| \frac{\partial h(\boldsymbol{\theta})}{\partial \theta^i} \right| \right) \Big|_{\boldsymbol{\theta}_0} \quad (2.29)$$

Inserting Eq. (2.29) in the Eq. (2.28) gives,

$$(d|h(\boldsymbol{\theta})) = (d|h(\boldsymbol{\theta}_0)) + \left( h(\boldsymbol{\theta}) \left| \frac{\partial h(\boldsymbol{\theta})}{\partial \theta^i} \right| \right) \Big|_{\boldsymbol{\theta}_0} \Delta\theta^i + \frac{1}{2} \left( d \left| \frac{\partial^2 h(\boldsymbol{\theta})}{\partial \theta^i \partial \theta^j} \right| \right) \Big|_{\boldsymbol{\theta}_0} \Delta\theta^i \Delta\theta^j \quad (2.30)$$

Putting together Eq. (2.27) and Eq. (2.30), the non constant terms in the exponent are given by

$$-2(d|h(\boldsymbol{\theta})) + (h(\boldsymbol{\theta})|h(\boldsymbol{\theta})) = - \left( n \left| \frac{\partial^2 h(\boldsymbol{\theta})}{\partial \theta^i \partial \theta^j} \right| \right)_{\boldsymbol{\theta}_0} \Delta \theta^i \Delta \theta^j + \left( \frac{\partial h(\boldsymbol{\theta})}{\partial \theta^i} \left| \frac{\partial h(\boldsymbol{\theta})}{\partial \theta^j} \right| \right)_{\boldsymbol{\theta}_0} \Delta \theta^i \Delta \theta^j \quad (2.31)$$

where we have used that  $(h(\boldsymbol{\theta}_0)|h(\boldsymbol{\theta}_0))$  is constant and Eq. (2.20). The first term is proportional to SNR while the second term is square of SNR. For a high SNR, the Likelihood function Eq. (2.25) is given by,

$$p(\boldsymbol{\Delta \theta}) = \mathcal{N} e^{-\frac{1}{2} \Gamma_{ij} \Delta \theta^i \Delta \theta^j} \quad (2.32)$$

where the Fisher matrix  $\Gamma_{ij}$  is defined as,

$$\Gamma_{ij} = \left( \frac{\partial h}{\partial \theta^i} \left| \frac{\partial h}{\partial \theta^j} \right| \right). \quad (2.33)$$

The 1-sigma error  $\sigma^i$  on the parameters  $\theta^i$  is then given by

$$\sigma^i = \sqrt{(\Gamma^{-1})^{ii}} \quad (2.34)$$

These uncertainties on parameters are computed by finding the inverse of the Fisher matrix. If the Fisher matrix is very ill-conditioned then inversion is not possible; in that case we use the Fisher likelihood Eq. (2.32) to find the posterior probability distribution of the parameters using Markov chain Monte Carlo (MCMC) samplers or nested sampler.

## 2.4 Markov Chain Monte Carlo (MCMC)

The Markov chain Monte Carlo (MCMC) method is a combination of two established algorithms: the Monte Carlo algorithm and the Markov chain algorithm. The Monte Carlo algorithm is used to randomly generate samples from any distribution, while the Markov chain algorithm generates samples that depend on the previous sample. By combining these two algorithms, the MCMC method generates samples from the given posterior distribution iteratively.

### Metropolis–Hastings algorithm

Let's look at more details about the MCMC algorithm, particularly the Metropolis–Hastings MCMC algorithm. We want to sample the posterior  $p(\boldsymbol{\theta}|\mathcal{H}, d, \mathcal{I})$  which is given as a product of prior and likelihood Eq. (2.23).

The Metropolis–Hastings algorithm steps are as follows from Fig. 2.6:

- The algorithm first takes the current parameters  $\boldsymbol{\theta}_n$ , and then it proposes new parameters  $\boldsymbol{\theta}_{n+1}$  from proposal distribution  $Q(\boldsymbol{\theta}_{n+1}|\boldsymbol{\theta}_n)$  using the Monte Carlo algorithm.

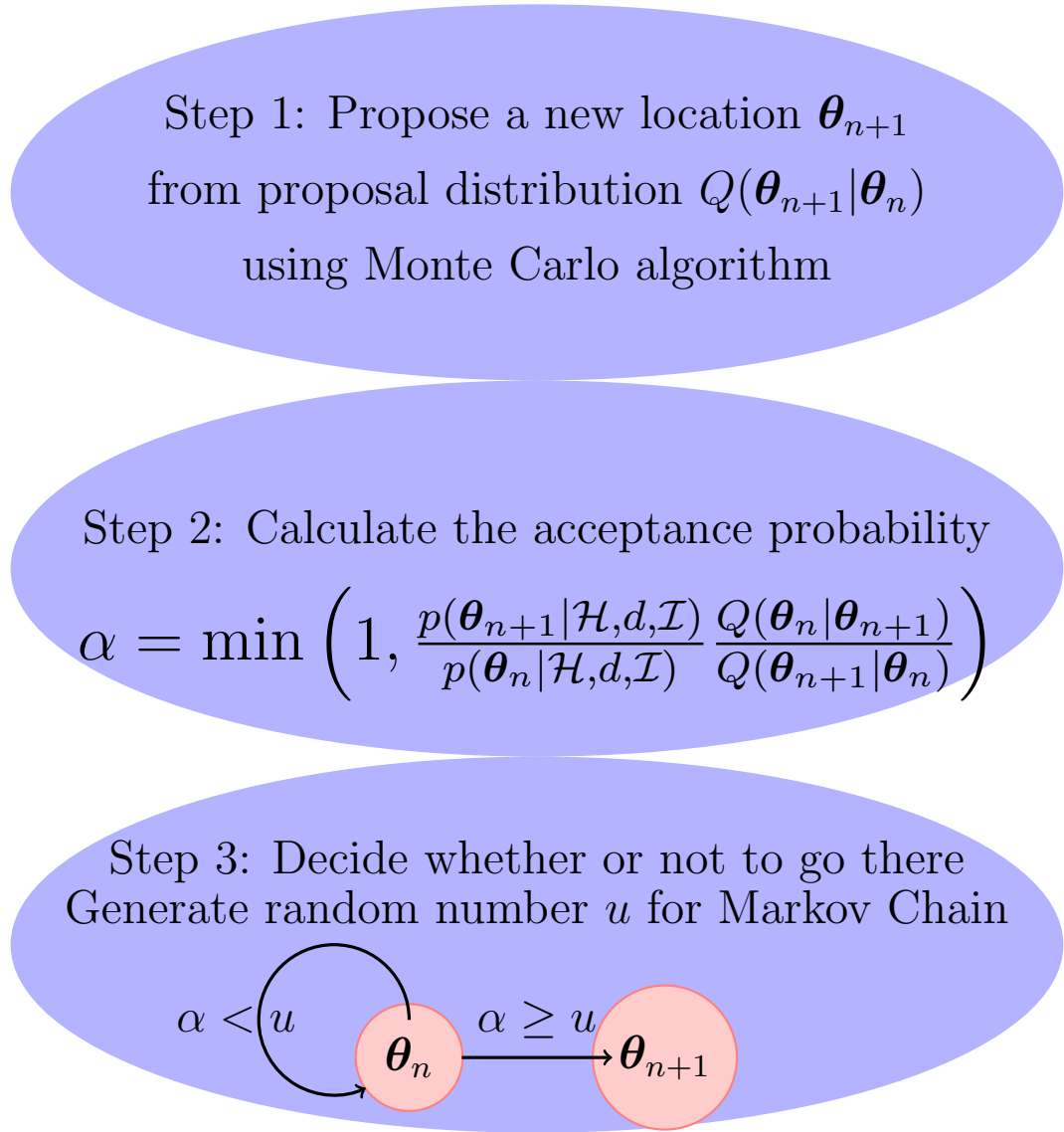


Figure 2.6: Metropolis-Hastings MCMC

- Then, it calculates the acceptance probability  $\alpha$  as,

$$\alpha = \min \left( 1, \frac{p(\boldsymbol{\theta}_{n+1}|\mathcal{H}, d, \mathcal{I})}{p(\boldsymbol{\theta}_n|\mathcal{H}, d, \mathcal{I})} \frac{Q(\boldsymbol{\theta}_n|\boldsymbol{\theta}_{n+1})}{Q(\boldsymbol{\theta}_{n+1}|\boldsymbol{\theta}_n)} \right) \quad (2.35)$$

which involves the ratio of posteriors and proposal distributions for initial parameters  $\boldsymbol{\theta}_n$  and proposed new parameters  $\boldsymbol{\theta}_{n+1}$ . It is defined with function min because probability can't be more than 1.

- In the next step, Markov chain is used to decide whether to accept or reject the new parameters  $\boldsymbol{\theta}_{n+1}$  as follows: Generate a random number  $u \in [0, 1]$ , the new parameters  $\boldsymbol{\theta}_{n+1}$  are accepted if  $\alpha \geq u$  and rejected if  $\alpha < u$ .

The samples from doing these steps for a large number of iterations  $n$  converge to the posterior Eq. (2.23). There are certain disadvantages to this algorithm. The new sample depends on the current sample through the proposal distribution  $Q(\boldsymbol{\theta}_{n+1}|\boldsymbol{\theta}_n)$ , this causes the samples to be correlated as well as dependent upon the initial sample. To remove the initial sample dependence some iterations must be discarded known as burn-in samples. Correlated samples can be removed by keeping the samples every  $N$ -th iteration, where  $N$  must be greater than or equal to the chain's autocorrelation length.

## 2.5 Nested sampling

Nested sampling has a prime target to obtain the evidence, while MCMC has been designed for the posterior. The evidence is important since it allows different model assumptions to be compared. Nested sampling computes the evidence from the representative posterior samples, which are a byproduct. The nested sampling algorithm was first suggested by Skilling in 2006 [105].

We have defined the evidence in Eq. 2.24, the notation can be simplify by defining  $\mathcal{Z} = p(d|\mathcal{H}, \mathcal{I})$ ,  $\mathcal{L}(\boldsymbol{\theta}) = p(d|\mathcal{H}, \boldsymbol{\theta}, \mathcal{I})$  and  $\pi(\boldsymbol{\theta}) = p(\boldsymbol{\theta}|\mathcal{H}, \mathcal{I})$ , so that

$$\mathcal{Z} = \int d\boldsymbol{\theta} \mathcal{L}(\boldsymbol{\theta})\pi(\boldsymbol{\theta}) \quad (2.36)$$

This is a multi-dimensional integral, which is not trivial to calculate. Nested sampling tries to solve this complicated problem by chopping it up into a bunch of simpler problems. We will take our distribution and chop it up into these different contours with some particular volume elements shown in Fig. 2.7, so we go from the distribution shown on the left to this one-dimensional integral as a function of volume shown on the right. Estimating the area under this curve gives the evidence integral. This is accomplished by defining the "prior volume" as,

$$X(\lambda) = \int_{\boldsymbol{\theta}: \mathcal{L}(\boldsymbol{\theta}) > \lambda} \pi(\boldsymbol{\theta}) d\boldsymbol{\theta} \quad (2.37)$$

where the integration is done within parameter space satisfying  $\mathcal{L}(\boldsymbol{\theta}) > \lambda$ . The parameter space corresponds to  $X = 0$  enclosed by the maximum likelihood  $\mathcal{L}_{max}$  and  $X = 1$  enclosed by the minimum likelihood  $\mathcal{L}_{min}$ . Using this, we can write the evidence Eq. (2.36)

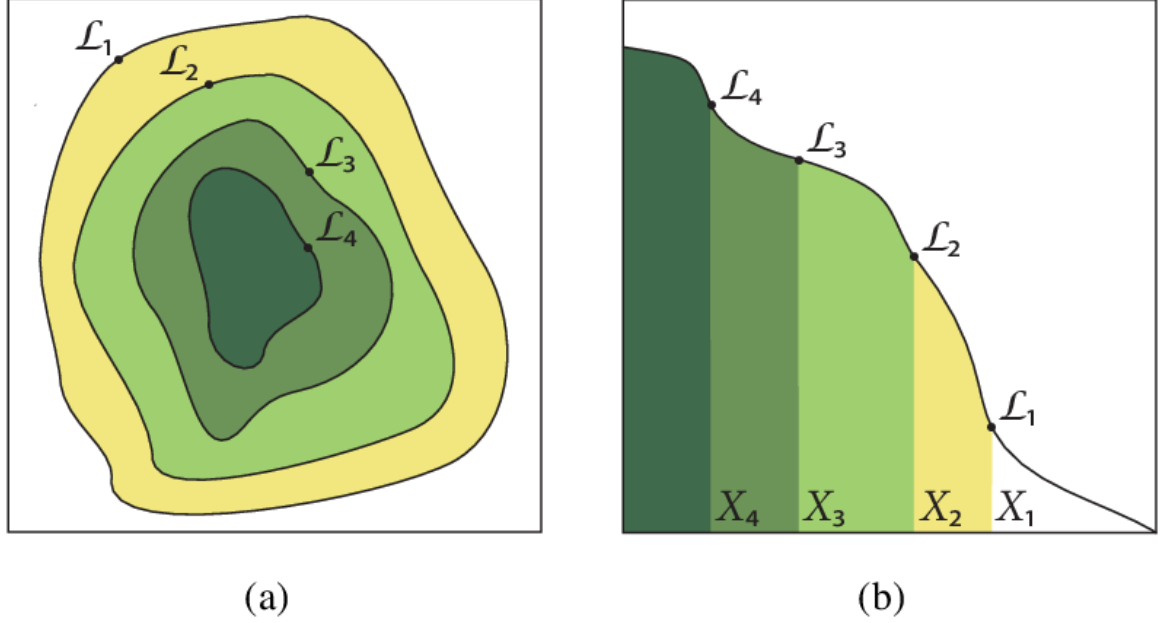


Figure 2.7: Left panel shows the likelihood  $\mathcal{L}(\theta)$  of a two-dimensional problem and right panel shows the transformed the likelihood  $\mathcal{L}(X)$  as function of prior volumes  $X_i$  using Eq. (2.37) [106]. Evidence  $\mathcal{Z}$  is easier to evaluate with the likelihood  $\mathcal{L}(X)$  as it is one dimensional integral shown in Eq. (2.39).

as,

$$\mathcal{Z} = \int d\lambda X(\lambda) \quad (2.38)$$

From Eq. (2.37)  $X(\lambda)$  is inverted in terms of likelihood  $\mathcal{L}(X)$  as a function of  $X$  as  $\mathcal{L}(X)$ , then the evidence integral is written as,

$$\mathcal{Z} = \int_0^1 dX \mathcal{L}(X) \quad (2.39)$$

This is a trick used by nested sampling to convert multidimensional integral to one-dimensional. This integral limit is from 0 to 1 because these prior volume elements Eq. (2.37) are normalized relative to the prior. By evaluating likelihood  $\mathcal{L}(X)$  at deterministic sequence of  $X$  values shown in Fig. 2.7, the evidence Eq. (2.39) is approximated as,

$$\mathcal{Z} \approx \sum_{i=1}^n \mathcal{L}_i \times w_i \quad (2.40)$$

where  $\mathcal{L}_i$  are evaluated at  $X_i$ , and the weights  $w_i = \frac{1}{2}(X_{i-1} - X_{i+1})$  following trapezium rule.

In the nested sampling algorithm, the summation in Eq. (2.40) is performed as follows.

- First  $N_{\text{live}}$  ‘live’ points are drawn from the prior,  $\pi(\theta)$ , and the initial prior volume,  $X_0$ , is set to unity.

- At each subsequent iteration,  $i$ , the point with the lowest likelihood value,  $\mathcal{L}_i$ , is removed from the live point set and replaced by another point drawn from the prior under the constraint that its likelihood is higher than  $\mathcal{L}_i$ .
- The prior volume is probabilistically estimated instead of numerically calculating it. The prior volume contained within this region at the  $i^{\text{th}}$  iteration, is a random variable distributed as  $X_i = t_i X_{i-1}$ , where  $t_i$  is largest of  $N_{\text{live}}$  samples drawn uniformly from the interval  $[0, 1]$  and follows the distribution  $\text{Pr}(t) = N_{\text{live}} t^{N_{\text{live}}-1}$ .
- This sampling process continues until the entire prior volume has been traversed, with the live points moving through *nested* shells of constrained likelihood as the prior volume is steadily reduced.

The termination condition is given by,

$$\epsilon > \Delta \mathcal{Z}_i = \mathcal{L}_{\text{max}} X_i \quad (2.41)$$

where  $\epsilon$  is the user-specified tolerance and  $\Delta \mathcal{Z}_i$  is estimate of the evidence still to be accumulated, and  $\mathcal{L}_{\text{max}}$  is the maximum likelihood value amongst the current set of live points.

The posterior probability is obtained by using the final set of live points and the complete sequence of discarded points with the importance weight,

$$p_i \approx \frac{\mathcal{L}_i \times w_i}{\mathcal{Z}}. \quad (2.42)$$

## Neutron stars

In 1934 Baade and Zwicky proposed the idea of neutron stars, pointing out that they would be at very high density and small radius. They also suggested that neutron stars would be formed in supernova explosions. The first serious attempts to discover neutron stars were made when the era of practical X-ray astronomy began in the 1960s. Pulsars were discovered in late 1967 by Jocelyn Bell, a graduate student supervised by Hewish and Ryle. A pulsar is a highly magnetized, rotating star that emits a beam of electromagnetic radiation. This radiation can be observed only when the beam of emission is pointing toward Earth and is responsible for the pulsed appearance of emission. So naturally, In 1968, Gold proposed that pulsars are rotating neutron stars, and now it is accepted by astronomical society. The typical mass of a neutron star is 1.4 solar masses and its radius is approximately 10 km, as a result, the matter inside of neutron stars exists at very high density and low temperature. This state of matter greatly differs from those found in the early Universe or achieved in terrestrial experiments [107].

This chapter provides a review of neutron stars in the framework of general relativity. We derive the Tolman-Oppenheimer-Volkoff (TOV) equations, which are fundamental equations governing the structure and stability of neutron stars [44]. Then, we discuss the electric tidal effects and oscillation modes for neutron stars [39]. Also, we mention approximate-universal relations that have been found for neutron stars.

### 3.1 TOV equations

Neutron stars require a framework of general relativity to understand their interior structure. We consider a non-rotating spherical neutron star which is described by the static and spherically symmetric metric,

$$ds^2 = -e^{2\Phi(r)} dt^2 + e^{2\lambda(r)} dr^2 + r^2 d\theta^2 + r^2 \sin^2 \theta d\phi^2. \quad (3.1)$$

The matter inside the neutron star is given by perfect fluid,

$$T_{\mu\nu} = pg_{\mu\nu} + (p + \rho)U_\mu U_\nu, \quad (3.2)$$

where  $U^\nu$  is four-velocity of perfect fluid. It is also considered that fluid has no motion  $U^i = 0$  which gives  $U^0 = e^{\Phi(r)}$  from normalization condition  $U^\mu U_\mu = -1$ .



We calculate components of energy-momentum tensor  $T^{\mu\nu}$  using metric Eq. (3.1),

$$T_{tt} = -pe^{2\Phi(r)} + (p + \rho)e^{2\Phi(r)} = \rho e^{2\Phi(r)}, \quad (3.3a)$$

$$T_{rr} = pe^{2\lambda(r)}, \quad (3.3b)$$

$$T_{\theta\theta} = pr^2, \quad (3.3c)$$

$$T_{\phi\phi} = pr^2 \sin^2 \theta = \sin^2 \theta T_{\theta\theta}. \quad (3.3d)$$

To use the Einstein's equation Eq. (1.13), we calculate the components of the Einstein tensor Eq. (1.12) using the metric Eq. (3.1),

$$G_{tt} = \frac{1}{r^2} e^{2\Phi(r)} \frac{d}{dr} [r (1 - e^{2\lambda(r)})], \quad (3.4a)$$

$$G_{rr} = -\frac{1}{r^2} e^{2\lambda(r)} (1 - e^{-2\lambda(r)}) + \frac{2}{r} \frac{d}{dr} \Phi, \quad (3.4b)$$

$$G_{\theta\theta} = r^2 e^{2\lambda(r)} \left[ \frac{d^2 \Phi}{dr^2} + \left( \frac{d\Phi}{dr} \right)^2 + \frac{1}{r} \frac{d\Phi}{dr} - \frac{d\Phi}{dr} \frac{d\lambda}{dr} - \frac{1}{r} \frac{d\lambda}{dr} \right], \quad (3.4c)$$

$$G_{\phi\phi} = \sin^2 \theta G_{\theta\theta}. \quad (3.4d)$$

There will be ten components of the Einstein's tensor  $G_{\mu\nu}$ , but we are left with only four because of the symmetries of the metric Eq. (3.1). We use the Einstein's equation component-wise, the  $tt$  component gives,

$$G_{tt} = 8\pi T_{tt}, \quad (3.5a)$$

$$\frac{d}{dr} [r (1 - e^{2\lambda(r)})] = 8\pi \rho r^2. \quad (3.5b)$$

We define mass  $M(r) \equiv \frac{1}{2}r (1 - e^{2\lambda(r)}) \Rightarrow e^{2\lambda(r)} = 1 - \frac{2M}{r}$ , then Eq. (3.5b) simplifies to,

$$\frac{dM(r)}{dr} = 4\pi \rho r^2. \quad (3.6)$$

Let's take the  $rr$  component

$$G_{rr} = 8\pi T_{rr} \quad (3.7a)$$

$$\frac{d\Phi}{dr} = \frac{M(r) + 4\pi r^3 p}{r(r - 2M(r))} \quad (3.7b)$$

$\theta\theta$  and  $\phi\phi$  components give the same equation and using Bianchi identities, this equation can be reduced to  $rr$  and  $tt$  component equation.

We use the energy momentum conservation Eq. (1.14), and take its  $r$  component, which gives,

$$(p + \rho) \frac{d\Phi}{dr} = -\frac{dp}{dr}. \quad (3.8)$$

This equation relates  $p$  with  $\Phi$  which we use to eliminate the  $\frac{d\Phi}{dr}$  in Eq. (3.7b)

$$-\frac{dp}{dr} = (p + \rho) \frac{M(r) + 4\pi r^3 p}{r(r - 2M(r))}, \quad (3.9a)$$

$$\frac{dp}{dr} = -\frac{M(r)\rho}{r^2} \left( 1 + \frac{p}{\rho} \right) \left( 1 + \frac{4\pi r^3 p}{M(r)} \right) \left( 1 - \frac{2M}{r} \right)^{-1}. \quad (3.9b)$$

These two equations are known as Tolman–Oppenheimer–Volkoff (TOV) equations,

$$\frac{dp}{dr} = -\frac{G\epsilon(r)M(r)}{c^2 r^2} \left(1 + \frac{p(r)}{\epsilon(r)}\right) \left(1 + \frac{4\pi r^3 p(r)}{M(r)c^2}\right) \left(1 - \frac{2GM(r)}{c^2 r}\right)^{-1}, \quad (3.10a)$$

$$\frac{dM(r)}{dr} = \frac{4\pi r^2 \epsilon(r)}{c^2}. \quad (3.10b)$$

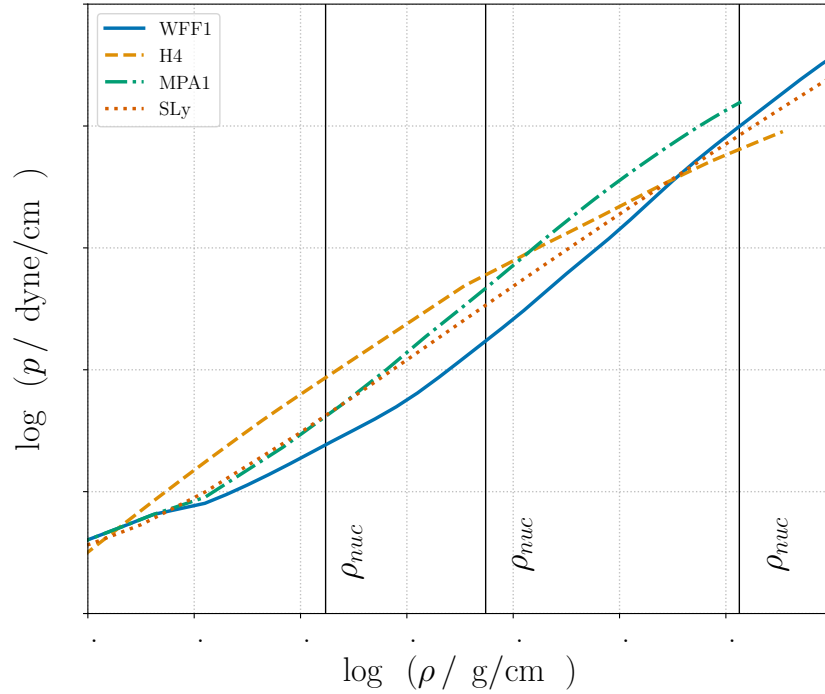


Figure 3.1: Examples of proposed nuclear equations of state: WFF1, H4, AP4 and SLy. The saturation density of nuclei is  $\rho_{nuc} = 2.8 \times 10^{14} \text{g/cm}^3$ . The termination of EOS at high density is an artefact of the tabulated data set for given EOS.

The TOV equations Eq. (3.10) have three variables,  $p(r)$ ,  $\epsilon(r)$  and  $M(r)$  and two equations, so we need another equation which relates  $p(r)$  and  $\epsilon(r)$ , known as the equation of state (EOS) of neutron stars. These EOS are calculated using microscopic properties of matter inside the neutron stars. The modeling of these neutron stars is built by using nuclear properties of matter like saturation density, incompressibility, and slope of nuclear parameters. In fig. 3.1, we show four nuclear equation of state WFF1, H4, AP4, and SLy, which have been calculated using nuclear physics. We need boundary conditions to solve TOV equations Eq. (3.10) which are,

$$r = 0, \quad M(0) = 0 \quad ; \quad p(0) = p_c, \quad (3.11a)$$

$$r = R, \quad M(R) = M_{ns} \quad ; \quad p(R) = 0, \quad (3.11b)$$

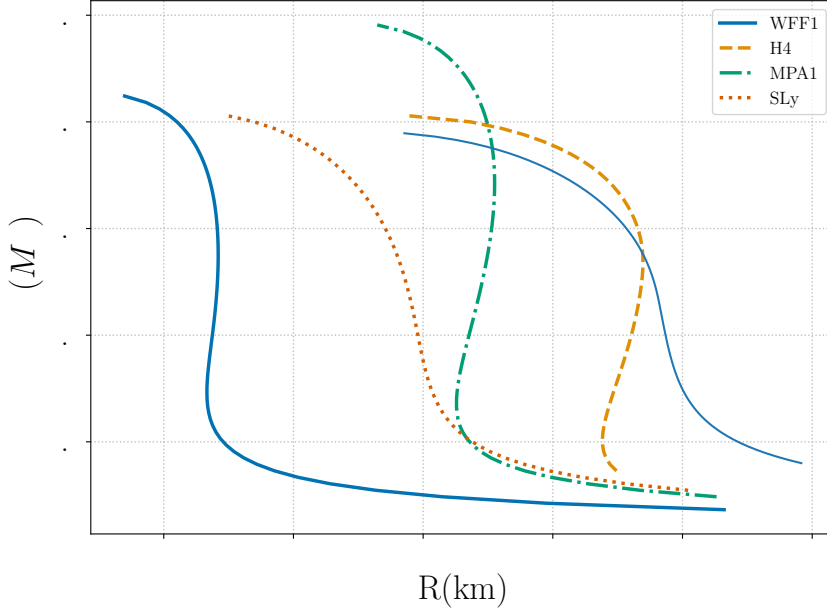


Figure 3.2: Mass radius after solving the TOV equations for WFF1, H4, AP4 and SLy. Each point along a curve is obtained by solving TOV equations with a different central pressure configuration and the central density increases from right to left. TOV equations also describes relativistic hydrostatic equilibrium of a star, as a result, when there is no hydrostatic relativistic equilibrium for a given high central density, the curves terminate, while termination of low central density is due to numerical reason of TOV solver in LALSuite [108].

where  $R$  is radius and  $M_{ns}$  is mass of neutron star, and  $p_c$  is central pressure. We solve the TOV equations numerically for WFF1, H4, AP4, and SLy equation of state and obtain mass-radius relations for neutron stars shown in Fig. 3.2.

### 3.1.1 Uncertainties in the neutron star equation of state

There are numerous uncertainties in modelling neutron star equation of state because of the complexity of the nuclear matter inside the star. Additionally, there are uncertainties due to the presence of exotic particles in the cores, such as hyperons or quark matter. Because of these uncertainties, there are many possible EOSs that could describe the observed mass and radius of neutron stars. In Fig. 3.1, we show four examples of neutron star equations of state: WFF1, H4, AP4, and SLy. All of them, except H4, consider only normal nuclear matter, while H4 also includes hyperons. These EOSs differ due to large uncertainties in nuclear many-body interactions and assumptions about nuclear matter properties, such as symmetry energy, etc. Additionally, there are different approximations and computational methods that are used to model these EOSs. As a result, these EOSs predict different properties of neutron stars, such as their maximum mass, radius, and tidal deformability. One of the main motivation of this thesis is to measure the equation

of state which gives insight about nuclear matter inside neutron stars. In Sec. 3.5, we have provided an overview of the chapters that cover various aspects of the equation of state from modelling tidal effects to measuring it with next-generation detectors.

## 3.2 Tidal effects for neutron stars

In the previous section, we discussed how mass and radius of a neutron star are dependent on the equation of state. However, GWs from a binary neutron star are not directly sensitive to mass and radius of individual neutron star but to their tidal effects. In the following section, we will discuss the tidal effects of neutron stars.

The tidal forces of a gravitational field can be understood from the equation of geodesic deviation Eq. (1.52). This equation shows how the tidal forces can be represented by the curvature of spacetime. The Riemann curvature tensor in 4-dimensions can be written in terms of the Weyl tensor given by,

$$C_{\mu\nu\rho\sigma} = R_{\mu\nu\rho\sigma} - (g_{\mu[\rho}R_{\sigma]\nu} - g_{\nu[\rho}R_{\sigma]\mu}) + \frac{1}{3}Rg_{\mu[\rho}g_{\sigma]\nu}. \quad (3.12)$$

where  $R_{\mu\nu\rho\sigma} = g_{\mu\lambda}R^\lambda_{\nu\rho\sigma}$  and the symbol  $[\rho, \sigma]$  stands for antisymmetrization in the corresponding indices e.g.  $g_{\mu[\rho}R_{\sigma]\nu} = \frac{1}{2}(g_{\mu\rho}R_{\sigma\nu} - g_{\mu\sigma}R_{\rho\nu})$ . The tidal effects for neutron stars are complicated due to this Weyl tensor having two decompositions: electric and magnetic types (5.47). This also gives rise to two different type of responses: gravitoelectric and gravitomagnetic. For simplicity, we will refer to the gravitoelectric response as the electric response and the gravitomagnetic response as the magnetic response. The electric-type tidal effects have a Newtonian analogue, which allows for a more intuitive understanding, whereas the magnetic-type tidal effects have no Newtonian analogs. In this section, we focus on a detailed discussion of the electric type tidal effects [109], while, the magnetic type tidal effects are the main component of this thesis and will be discussed in greater detail in chapter 5. Together, these analyses aim to provide a comprehensive understanding of the intricate tidal effects that play a critical role in shaping the structure and behavior of neutron stars.

We consider a non-rotating spherical neutron star that is placed in a static external quadrupolar tidal field  $\mathcal{E}_{ij}$ , and the star will develop quadrupole moment  $Q_{ij}$ . The induced quadrupole moment  $Q_{ij}$  in linear order of external quadrupolar tidal field  $\mathcal{E}_{ij}$  is

$$Q_{ij} = -\lambda\mathcal{E}_{ij}, \quad (3.13)$$

where  $\lambda$  is a constant and related to the tidal Love number  $k_2$  which is given by

$$k_2 = \frac{3}{2}\lambda R^{-5}. \quad (3.14)$$

We consider the static and spherically symmetric metric as the equilibrium configuration and linearized perturbations due to an external quadrupolar tidal field. The metric of spacetime is given by

$$g_{\mu\nu} = g_{\mu\nu}^0 + h_{\mu\nu}, \quad (3.15)$$

where  $g_{\mu\nu}^0$  metric is given by Eq. (3.1) and  $h_{\mu\nu}$  is linear metric perturbation. This perturbed metric  $h_{\mu\nu}$  in the Regge-Wheeler gauge can be written as

$$h_{\mu\nu} = \text{diag}[-e^{2\Phi(r)}H_0(r), e^{2\lambda(r)}H_1(r), r^2K(r), r^2\sin(\theta)^2K(r)]Y_{lm}(\theta, \phi), \quad (3.16)$$

where  $\Phi(r)$  and  $\lambda(r)$  are same as Eq. (3.1). The perturbation on the energy-momentum tensor Eq. (3.2) is given by

$$\delta T_0^0 = -\delta\rho_l Y_{lm}(\theta, \phi) = -\frac{d\rho}{dp}\delta p_l Y_{lm}(\theta, \phi), \quad (3.17a)$$

$$\delta T_i^i = \delta p_l Y_{lm}(\theta, \phi). \quad (3.17b)$$

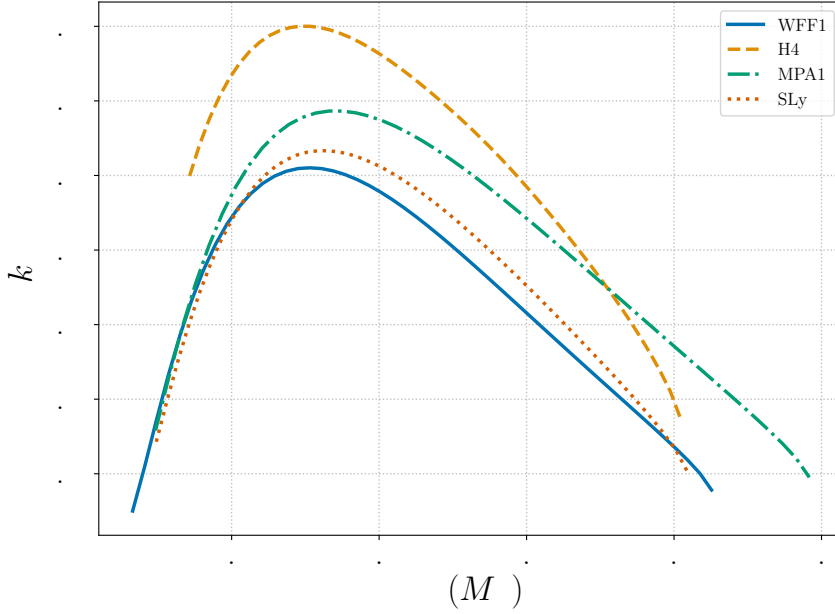


Figure 3.3: Tidal Love number  $k_2$  for WFF1, H4, AP4 and SLy EOS. Each point along a curve is obtained by solving Eq. (3.19) with TOV equations Eq. (3.10) for a different central pressure configuration and the central density increases from left to right.

We insert the perturbation of energy-momentum tensor Eq. (3.17) and the metric perturbation Eq. (3.16) into the linearly perturbed Einstein equation,

$$\delta G_\nu^\mu = 8\pi\delta T_\nu^\mu. \quad (3.18)$$

We finally get the following equations,

$$\begin{aligned} H_2 = H_0 = H, \\ H'' + H' \left\{ \frac{2}{r} + e^\lambda \left[ \frac{2m}{r^2} + 4\pi r(p - \rho) \right] \right\} + H \left\{ e^\lambda \left[ -\frac{6}{r^2} + 4\pi(\rho + p)\frac{d\rho}{dp} + 4\pi(5\rho + 9p) \right] \right. \\ \left. - \left( \frac{d\Phi}{dr} \right)^2 \right\} = 0, \end{aligned} \quad (3.19)$$

where we have considered only the  $l = 2$  component. The boundary conditions are as follows: regularity of  $H(r)$  at  $r = 0$ , which implies  $H(r) \propto r^2$  and continuity of  $H(r)$  and its first derivatives at the boundary of the star. We integrate Eq. (3.19) from  $r = 0$  to  $r = R$  and use Eq. (3.14) to calculate tidal Love number  $k_2$ ,

$$k_2 = \frac{8C^5}{5}(1-2C)^2[2+2C(y-1)-y] \times \left\{ 2C[6-3y+3C(5y-8)] + 4C^3[13-11y+C(3y-2)+2C^2(1+y)] + 3(1-2C)^2[2-y+2C(y-1)]\ln(1-2C) \right\}^{-1}, \quad (3.20)$$

where  $C = M/R$  is star's compactness and the quantity  $y = RH'(R)/H(R)$ . In fig. 3.3, tidal love number  $k_2$  has been computed for WFF1, H4, AP4, and SLy EOS as a function of mass  $M_{ns}$ .

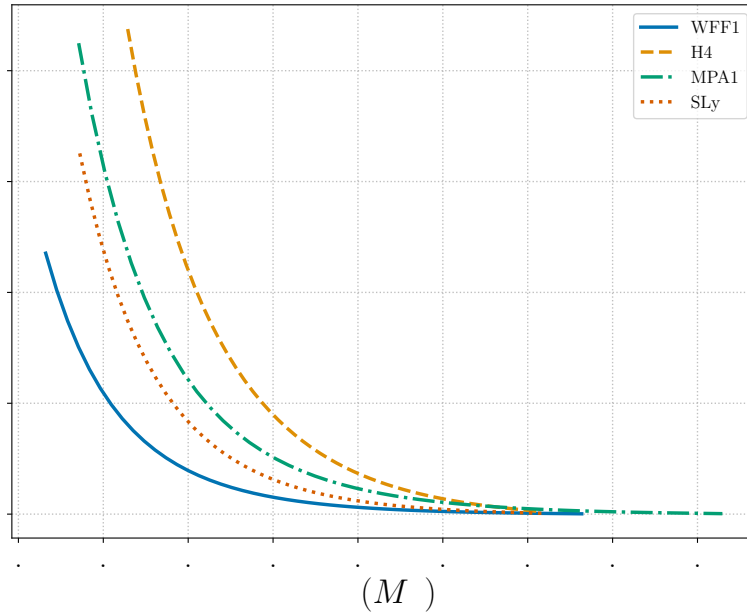


Figure 3.4: Dimensionless tidal Love number  $\Lambda$  for WFF1, H4, AP4 and SLy EOS which is directly constrained by GW measurements.

The relevant physical quantity is the response  $\lambda$  but it is not dimensionless (3.13), so we define dimensionless tidal Love number  $\Lambda$ ,

$$\Lambda = \frac{2}{3} \frac{k_2 R^5}{M^5}, \quad (3.21)$$

where  $R$  is radius,  $M$  is mass of neutron star and  $\Lambda$  only depends on  $y$  and compactness  $C$ . In fig. 3.4, dimensionless tidal love number  $k_2$  has been computed for WFF1, H4, AP4, and SLy EOS as a function of mass  $M$ .

The effects of tidal Love number on the orbital motion can be calculated for the TaylorF2 phase in the post-Newtonian formalism as described in Sec. 1.6.2. The phase due to tidal effects for a binary neutron star system is given by [109–111]

$$\Psi_{\Lambda_{(1)}} = -\frac{3}{16\eta}x^{5/2}(12 - 11\Xi)\Lambda_{(1)}\Xi^4 \left\{ \sum_{k=0}^5 \gamma_k x^{k/2} \right\} \quad (3.22)$$

$$\Psi_{\Lambda_{(2)}} = (1 \rightarrow 2 \quad \text{and} \quad \Xi \rightarrow 1 - \Xi),$$

$$\gamma_0 = 1, \quad (3.23a)$$

$$\gamma_1 = 0, \quad (3.23b)$$

$$\gamma_2 = \frac{5(3179 - 919\Xi - 2286\Xi^2 + 260\Xi^3)}{672(12 - 11\Xi)}, \quad (3.23c)$$

$$\gamma_3 = -\pi, \quad (3.23d)$$

$$\gamma_4 = \frac{1}{12 - 11\Xi} \left[ \frac{39927845}{508032} - \frac{480043345}{9144576}\Xi + \frac{9860575}{127008}\Xi^2 - \frac{421821905}{2286144}\Xi^3 + \frac{4359700}{35721}\Xi^4 - \frac{10578445}{285768}\Xi^5 \right], \quad (3.23e)$$

$$\gamma_5 = -\frac{\pi(27719 - 22127\Xi + 7022\Xi^2 - 10232\Xi^3)}{672(12 - 11\Xi)}, \quad (3.23f)$$

where  $\Xi = m_1/M$  and dimensionless tidal Love numbers  $\Lambda_{(1,2)}$  are defined in Eq. (3.21). The leading order tidal effects come to the 5PN order.

The external quadrupolar tidal field, represented by the magnetic type tensor  $\mathcal{B}_{ij}$ , gives rise to the magnetic Love number  $\Sigma$ . The detailed explanation of the magnetic tidal Love number will be discussed in chapter 5.

### 3.3 Oscillation modes

Oscillation modes of neutron stars, also known as QNMs are periodic variations in the density and velocity of the neutron star. These oscillation modes can be excited by the external tidal effect which gives rise to a rich set of modes. The frequencies of the oscillation modes are determined by the properties of the star, such as its mass, radius, equation of state, buoyancy and composition gradients. So, the study of these oscillation modes can provide valuable information about the properties of neutron star matter. In this section, we describe the rich set of electric type modes associated with neutron stars [39], and discuss magnetic type modes in chapter 5.

QNMs of neutron stars also includes spacetime modes which does not have Newtonian analogue [40, 41]. In the following, we will discuss mainly Newtonian limit of QNMs to keep the discussion tractable.

Consider a rotating neutron star in the presence of an external tidal field, the matter inside this neutron star is described by energy-momentum conservation  $T_{;\nu}^{\mu\nu} = 0$  which gives

$$\ddot{\xi} + 2\Omega \times \dot{\xi} = -\mathcal{D}\xi + \mathbf{a}_{\text{ext}}, \quad (3.24)$$

where  $\boldsymbol{\xi} = \delta \mathbf{U}$ ,  $\boldsymbol{\Omega}$  is angular frequency of the neutron star,  $\mathbf{a}^{\text{ext}}$  is external tidal force, and the linear operator  $\mathcal{D}$  is defined by

$$\mathcal{D}\boldsymbol{\xi} = -\nabla \left\{ \left[ \frac{c_s^2}{\rho_0} + 4\pi G \Delta^{-1} \right] \nabla \cdot (\rho_0 \boldsymbol{\xi}) \right\}, \quad (3.25)$$

where  $c_s = \sqrt{(\partial p_0 / \partial \rho_0)}$  is the speed of sound, and we have considered the density perturbation  $\delta \rho = \nabla \cdot (\rho_0 \boldsymbol{\xi})$ . Note that  $\mathcal{D}$  is the differential operator describing perturbations of a nonrotating Newtonian star, and effects of rotation are included explicitly as the Coriolis term on the left-hand side of Eq. (5.13). The operator  $\mathcal{D}$  is Hermitian under the product  $\langle \boldsymbol{\xi}, \boldsymbol{\xi}' \rangle = \int d^3x \rho_0 \boldsymbol{\xi}^* \cdot \boldsymbol{\xi}'$  [112]. Hence, its eigenvectors  $\boldsymbol{\xi}_{n\ell m}$ —the normal modes—form an orthonormal basis with

$$\langle \boldsymbol{\xi}_{n\ell m}, \boldsymbol{\xi}_{n'\ell'm'} \rangle = \delta_{nn'} \delta_{\ell\ell'} \delta_{mm'}. \quad (3.26)$$

where type of mode or number of radial nodes is denoted by  $n$ , the multipolar order  $\ell$ , and an angular-momentum number  $m$  associated with a decomposition into (vector) spherical harmonics. Their eigenvalues  $\bar{\omega}_{n\ell}^2$  are real

$$\mathcal{D}\boldsymbol{\xi}_{n\ell m} = \bar{\omega}_{n\ell}^2 \boldsymbol{\xi}_{n\ell m}. \quad (3.27)$$

We can decompose a generic fluid displacement  $\boldsymbol{\xi}$  into this basis as

$$\boldsymbol{\xi} = \sum_{n\ell m} q_{n\ell m}(t) \boldsymbol{\xi}_{n\ell m}(\mathbf{x}), \quad q_{n\ell m} = \langle \boldsymbol{\xi}_{n\ell m}, \boldsymbol{\xi} \rangle, \quad (3.28)$$

with time-dependent amplitudes  $q_{n\ell m}(t)$ . The fact that the fluid displacement is real,  $\boldsymbol{\xi} = \boldsymbol{\xi}^*$ , implies that  $q_{n\ell m}^* = (-1)^m q_{n\ell -m}$  due to the analogous relation for the spherical harmonics, which arise because in the corotating frame and to linear order in the rotation, the modes are the same as for a nonrotating star and can be decomposed into vector spherical harmonics. In general, three types of vector harmonics contribute to the modes, each with different parity: the parity-even electric and radial harmonics, and the parity-odd magnetic-type ones [113].

## Electric-type

For the gravitoelectric tidal effects only electric type contributions to  $\boldsymbol{\xi}_{n\ell m}$  are relevant, which is given by

$$\boldsymbol{\xi}_{n\ell m} = \xi_{n\ell}^E(r) \mathbf{Y}^{E,\ell m}(\theta, \phi), \quad (3.29)$$

where  $\xi_{n\ell}^E(r)$  is the radial dependence and  $\mathbf{Y}^{E,\ell m}(\theta, \phi)$  is the electric vector spherical harmonic. The classification of electric type modes is shown in Fig. 3.5.

In this case, the linear operator  $\mathcal{D}(\boldsymbol{\xi}) \neq 0$ , gives rise to non-zero mode frequencies for the non-rotating star. We get three types of mode frequencies for an electric type known as  $f$ -modes,  $g$ -modes, and  $p$ -modes. The  $f$ -modes frequency is given by,

$$\omega_\ell^f = \frac{4\pi G \rho_0 \ell}{3}. \quad (3.30)$$



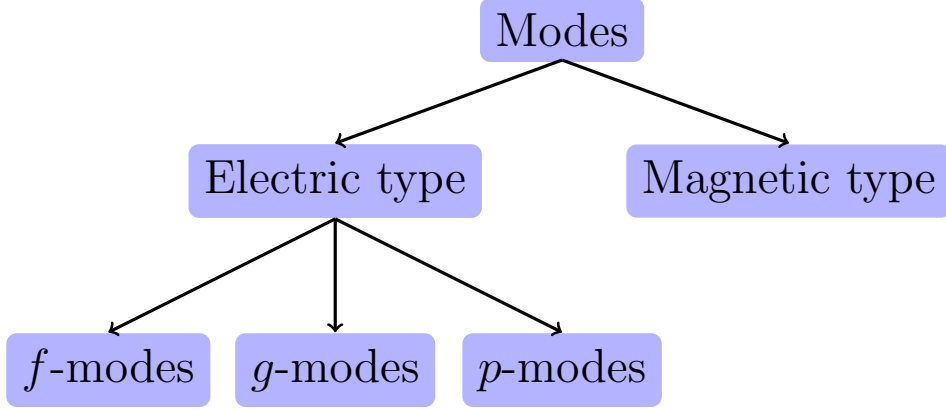


Figure 3.5: Classification of electric type oscillation modes of Newtonian stars. For  $f$ -modes and  $p$ -modes pressure is the restoring force while for  $g$ -modes buoyancy is restoring force.

The  $p$ -modes and  $g$ -modes follow following dispersion relation

$$k^2 = \frac{1}{c_s^2 \omega^2} (N^2 - \omega^2)(L_\ell^2 - \omega^2), \quad (3.31)$$

where  $L_\ell^2$  and  $N^2$  are given by

$$L_\ell^2 = \frac{\ell(\ell+1)}{r^2} c_s^2, \quad (3.32)$$

$$N^2 = g \left( \frac{1}{\Gamma_1 p} \frac{dp}{dr} - \frac{1}{\rho_0} \frac{d\rho}{dr} \right), \quad (3.33)$$

where  $\Gamma_1$  is the adiabatic index. The first thing to notice is that the left side of the Eq. (3.31) is always positive, which means that either

- $N^2 < \omega^2$ ,  $L_\ell^2 < \omega^2$ ,
- $N^2 > \omega^2$ ,  $L_\ell^2 > \omega^2$ .

For simplicity, we will assume that  $\ell \gg kr$  holds. Under this assumption, the first condition gives rise to  $p$ -modes and typically we have  $\omega \gg N$ , so that the frequencies can be approximated as  $\omega_p^2 \approx L_\ell^2$ . The second condition corresponds to  $g$ -modes and typically we have  $L_\ell \gg \omega$ , so that the frequencies can be approximated as  $\omega_g^2 \approx N^2$ .

### 3.4 Approximate-universal relations

When a set of properties of a physical system does not depend upon the internal details of the system, this is known as universal behavior. General Relativity involves the universality of black holes: Black holes can be entirely described in terms of only three global parameters: the mass, the electric charge, and the spin angular momentum; this is known as the no-hair theorem [114]. However, the same kind of universality can not be expected in neutron stars, as their interior structure can exceed the nuclear saturation

$y_i$	$x_i$	$a_i$	$b_i$	$c_i$	$d_i$	$e_i$
$\bar{I}$	$\bar{\Lambda}$	1.47	0.0817	0.0149	$2.87 \times 10^{-4}$	$-3.64 \times 10^{-5}$
$\bar{I}$	$\bar{Q}$	1.35	0.697	-0.143	$9.94 \times 10^{-2}$	$-1.24 \times 10^{-2}$
$\bar{Q}$	$\bar{\Lambda}$	0.194	0.0936	0.0474	$-4.21 \times 10^{-3}$	$1.23 \times 10^{-4}$

Table 3.1: Numerical coefficients for the fitting formula of the I-Love, I-Q, and Q-Love relations given in Eq. (3.34) [115].

limit and may contain hyperons, kaon-condensates, and quark-gluon plasma. Despite this, there are approximate-universal relations, known as the I-Love-Q relations, that are approximately independent of a neutron star’s internal composition to the percent level [115, 116].

The I-Love-Q relations are inter-relations between the neutron stars’ moment of inertia  $I$ , the quadrupolar electric tidal deformability  $\Lambda$ , and the (spin-induced) quadrupole moment  $Q$ , given by

$$\ln y_i = a_i + b_i \ln x_i + c_i (\ln x_i)^2 + d_i (\ln x_i)^3 + e_i (\ln x_i)^4, \quad (3.34)$$

where the coefficients are given in Table 3.1,  $\bar{I} = I/M^3$  is the dimensionless moment of inertia, and  $\bar{Q} = -Q/(M^3 \chi^2)$  is the dimensionless quadrupole moment.

For the magnetic tidal deformability discussed in chapter 5, there are approximate-universal relations that relate magnetic tidal deformability to electric tidal deformability Eq. (6.35). We also found a universal relation for the r-mode frequencies in Eq. (6.38).

## 3.5 Binary neutron stars

The detection with Advanced LIGO and Advanced Virgo of a gravitational waves from the binary neutron star (NS) inspiral GW170817 [5] provided, for the first time, a unique opportunity to measure dimensionless tidal love numbers. The effect of tidal Love numbers Eq. (3.21) on gravitational waves from a binary neutron star is encoded in the phase as Eq. (3.22), and the measurement of tidal Love numbers from GW170817 event are shown in Fig. 3.6. The neutron star equation of state (EOS) is translated from tidal Love numbers, which gives insight into the interior of neutron stars [118].

GW170817 [5] and GW190425 [30], together with electromagnetic observations [119–121] has already had a significant impact on our insight into the structure of neutron stars; for a recent review, see e.g. [122]. Even so, the neutron star equation of state (EOS) remains poorly constrained. This is expected to change as existing detectors (such as LIGO, Virgo, KAGRA) improve in sensitivity in the coming years [123] and next-decade’s envisioned third generation facilities such as Einstein Telescope (ET) and Cosmic Explorer (CE), become operational. These next-generation detectors will have a much higher sensitivity and wider bandwidth, which will open opportunities for transformative insights into the dense matter under extreme gravity [124–126], because they are likely to see hundreds of thousands of binary neutron star coalescences, of which hundreds may have signal-to-noise ratios (SNRs) in excess of 100; see [127] for recent estimates.

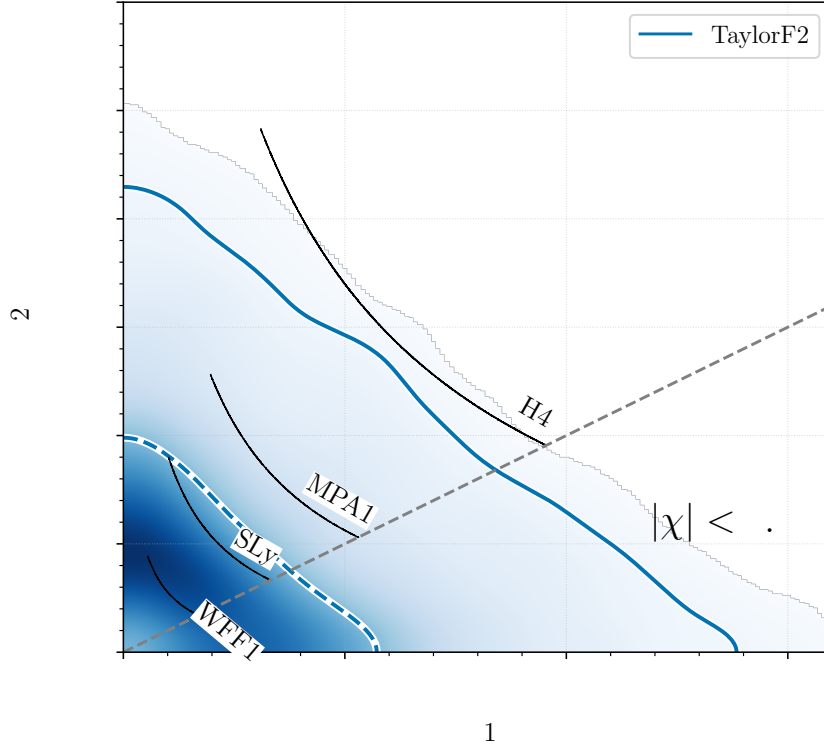


Figure 3.6: PDFs for the tidal deformability parameters  $\Lambda_1$  and  $\Lambda_2$  for low-spin priors. The dashed and solid lines are 50% and 90% credible regions respectively. The black curves are the tidal parameters for the EOS models using the masses estimated with TaylorF2 model [117]. This is data for the first binary neutron star inspiral event GW170817 and that  $\Lambda_1$  and  $\Lambda_2$  correspond to the two bodies in the binary.

Whereas with current detectors we only have access to the inspiral signal, ET and CE will also probe the post-merger [124, 128].

Realizing this science potential critically relies on advancing theoretical models of the GWs from binary systems with matter effects, which are needed to extract information about the source properties from the data, as reviewed in [103]. To date, GW measurements have only been sensitive to the dominant effects of NS matter on the signals and had relatively large statistical errors, causing systematic errors due to shortcomings in the modeling to be subdominant [84]. However, similar measurements at a higher sensitivity or with future detectors will require models that are significantly more accurate and include more realistic physics to enable more stringent constraints on NS matter and avoid biases in the interpretation.

In Chapter 5, we take an important step towards incorporating tidal effects in waveform models by developing a relativistic effective action for the gravitomagnetic dynamics that clarifies a number of subtleties. Working in the slow-rotation limit, we first consider the post-Newtonian approximation and explicitly derive the effective action from the equations of motion. We demonstrate that this formulation opens a way to compute mode frequencies, yields insights into the relevant matter variables, and elucidates

the role of a shift symmetry of the fluid properties under a displacement of the gravitomagnetic mode amplitudes. We then construct a fully relativistic action based on the symmetries and a power counting scheme. This action involves four coupling coefficients that depend on the internal structure of the neutron star and characterize the key matter parameters imprinted in the gravitational waves. We show that, after fixing one of the coefficients by normalization, the other three directly involve the two kinds of gravitomagnetic Love numbers (static and irrotational), and the mode frequencies. We discuss several interesting features and dynamical consequences of this action, and analyze the frequency-domain response function (the frequency-dependent ratio between the induced flux quadrupole and the external gravitomagnetic field), and a corresponding Love operator representing the time-domain response.

In Chapter 6, we advance the GW models for tidal effects that are needed for data analysis by first developing a description for the adiabatic signatures from gravitomagnetic modes in slowly rotating NSs. We show that they can be encapsulated in an effective Love number which differs before and after a mode resonance. Combining this with a known generic model for abrupt changes in the GWs at the mode resonance and a point-mass baseline leads to an efficient description which we use to perform case studies of the impacts of gravitomagnetic effects for measurements with Cosmic Explorer, an envisioned next-generation GW detector. We quantify the extent to which neglecting (including) the effect of gravitomagnetic modes induces biases (significantly reduces statistical errors) in the measured tidal deformability parameters, which depend on the equation of state.

In Chapter 7, we make predictions about how well ET in particular will enable us to reconstruct the neutron star equation of state through observations of tens of binary neutron star coalescences with signal-to-noise ratios in the hundreds. We restrict ourselves to information that can be extracted from the inspiral, which includes tidal effects and possibly r-mode resonances. In treating the latter we go beyond the Newtonian approximation, introducing and utilizing new universal relations.



# Bounding dark charges on binary black holes using gravitational waves

## 4.1 Introduction

As is well-known, astrophysical black holes are unlikely to be able to accrue large amounts of electric charge, at least in the context of the Standard Model of particle physics (see e.g. [129] for an overview). Kinematic build-up of charge through infall of electrons is limited by the ratio of electron mass  $m_e$  to charge  $e$ , to  $Q/M \leq m_e/e \simeq 5 \times 10^{-22}$ , with  $Q$  and  $M$  respectively the charge and mass of the black hole. Also dynamical processes such as charge accretion by a rotating black hole in a magnetic field  $B$  can only produce charge-to-mass ratios of  $Q/M \lesssim 1.7 \times 10^{-20} (M/M_\odot) (B/\text{Gauss})$  [130]. Moreover, surrounding plasma in the form of interstellar matter will discharge even an extremal black hole with  $Q = M$  on a timescale of  $\tau \sim 10^{-6}$  s [131].

The situation is different if one considers so-called minicharged dark matter models [25, 132], which involve new fermions that are charged under a hidden  $U(1)$  symmetry and whose “dark” charges are much smaller than that of the electron. Such minicharged particles are viable cold dark matter candidates, and have been searched for in a variety of observations and experiments [133–145]. For a dark fermion with mass  $m$  and charge  $q$ , it is possible to have  $m/q > 1$ , in which case values of  $Q/M \simeq 1$  can be attained, and discharge timescales by the surrounding (dark matter) plasma can be in the order of billions of years [129].

Assuming a single dark fermion and dark photon, the interaction of the hidden sector with gravity can be described by an Einstein-Maxwell action

$$S = \int d^4x \sqrt{-g} \left[ \frac{R}{16\pi} - \frac{1}{4} F_{\mu\nu} F^{\mu\nu} + 4\pi A_\mu j^\mu \right], \quad (4.1)$$

with  $g$  the determinant of the metric  $g_{\mu\nu}$ ,  $A_\mu$  the vector potential of the hidden  $U(1)$  interaction,  $F_{\mu\nu} = \nabla_\mu A_\nu - \nabla_\nu A_\mu$  the associated field tensor, and  $j^\mu$  the hidden current. Here we want to look at the inspiral of binary black holes in the presence of a dark sector, and search for, or put bounds on, dark charges which may be carried by them, using some of the GW signals that have been detected. The leading post-Newtonian modification

to the phase is at -1PN in the usual notation, corresponding to dipole radiation. This is mostly determined by the combination

$$\xi = \left| \frac{q_1}{m_1} - \frac{q_2}{m_2} \right|, \quad (4.2)$$

where  $(q_1, q_2)$  and  $(m_1, m_2)$  are respectively the charges and masses of the individual black holes [129, 146]. However, Khalil et al. [147] also computed higher-order effects, at 0PN and 1PN orders in phase, in the context of Einstein-Maxwell-dilaton theory, which reduces to Einstein-Maxwell theory when scalar charges are set to zero. Since these beyond-leading order contributions also depend on different combinations of  $q_1/m_1$  and  $q_2/m_2$  from the one in Eq. (4.2), including them will allow us to make statements on these two quantities separately. Thus, our gravitational waveform model will include these modifications to the point particle inspiral phase, in addition to effects of (precessing) spins, which start from 1.5PN order. Finally, though leading-order modifications of the ringdown spectrum of the remnant black hole resulting from the merger have been computed [148–152], here we will focus only on the post-Newtonian inspiral, since to our knowledge the behavior at plunge and merger, which connects the early inspiral to the ringdown, has yet to be analytically investigated in the presence of charge. We will be particularly interested in relatively low-mass binary black hole signals, for which inspiral dominates the signal-to-noise ratio.

This chapter is structured as follows. In Sec. 4.2 we explain our waveform approximant and the data analysis set-up. In Sec. 4.3 we describe simulations that were done to provide a basic validation of the analysis framework. Sec. 4.4 applies our methodology to a selection of detected signals. A summary and conclusions are provided in Sec. 4.5.

## 4.2 Waveform model and analysis framework

Our baseline waveform model will be the frequency domain inspiral-merger-ringdown approximant IMRPhenomPv2 described in Sec. 1.6.3, which we modify to reflect the presence of charges. This waveform stitches together in  $C^1$  fashion (a) an *inspiral* regime which mostly follows the post-Newtonian description; (b) a phenomenological *intermediate* regime describing the late inspiral and plunge; and (c) a phenomenological *merger-ringdown* regime. Spin precession is captured by “twisting up” an underlying aligned-spin model [73, 153]. Since with current detectors most of our information tends to come from the phase rather than the amplitude (though also see [31, 154]), we will focus on the former, and in particular on the inspiral phase. When electric charges are small and the inspiral is mainly driven by the tensor quadrupole flux, a good approximation to the inspiral phase is given by

$$\phi_{\text{Ins}}(v) = 2\pi f t_c - \varphi_c - \pi/4 + \frac{1}{v^5} \left[ \frac{\rho_{-2}^{\text{QD}}}{v^2} + \rho_0^{\text{QD}} + \rho_2^{\text{QD}} v^2 + \phi_{\text{Ins}}^{\text{higher-order}}(v) \right]. \quad (4.3)$$

Here  $t_c$  and  $\varphi_c$  are respectively a reference time and reference phase. One has  $v = (\pi M f)^{1/3}$ , with  $f$  the GW frequency, and where  $M$  is a “dressed” total mass; specifically  $M = G_{12} \bar{M}$ , with  $G_{12} = 1 - q_1 q_2 / (m_1 m_2)$ , where  $\bar{M}$  is the observed total mass in the

absence of charges. The first three terms in the square brackets include the charge-induced modifications to the phase computed by Khalil et al. [147] up to 1PN order. The leading-order (-1PN) contribution is set by

$$\rho_{-2}^{\text{QD}} = -\frac{5G_{12}}{3584\nu} \left( \frac{q_1}{m_1} - \frac{q_2}{m_2} \right)^2, \quad (4.4)$$

with  $\nu = m_1 m_2 / M^2$  the symmetric mass ratio. The expressions for  $\rho_0^{\text{QD}}$  and  $\rho_2^{\text{QD}}$  are shown explicitly in Appendix A.3, they are obtained straightforwardly from the ones in [147] (see their Eqs. (3.34a)-(3.34c) and Appendix B) by setting scalar charges to zero but retaining electric charges. These coefficients further reduce to the usual 0PN and 1PN coefficients for the vacuum case when electric charges are also set to zero. Finally,  $\phi_{\text{Ins}}^{\text{higher-order}}$  collects all higher-order contributions in  $\nu$ , including PN contributions as well as phenomenological corrections to the late inspiral, as detailed in [71].

In the IMRPhenomPv2 approximant, the inspiral regime is stitched onto the intermediate regime at a frequency  $f$  such that  $Mf = 0.018$ . Since we do not know how charges affect the latter regime, one option would be to smoothly let the waveform go to zero around that frequency, e.g. by applying a Planck tapering window [155]. However, especially when performing parameter estimation on high-mass systems for which the merger is well inside the detectors' sensitive band, we found a tendency for the tapered template waveform to try and match part of the post-inspiral signal, leading to a significant underestimation of the masses. As a pragmatic solution, we opt to not taper the waveform; instead we will only analyze signals for which less than 5% of the matched-filtering signal-to-noise ratio is contained in the regime  $Mf > 0.018$ . Note that this transition always precedes the nominal last stable orbit (given by  $Mf_{\text{LSO}} = 1/(6^{3/2}\pi) \simeq 0.022$ ), so that in this way we select signals for which only the inspiral has significant power in band.

Next we turn to our data analysis framework. Given a detected binary black hole coalescence signal, a waveform approximant  $\tilde{h}_C(f)$  with modified phasing as in Eq. (4.3) can be viewed as corresponding to a Bayesian hypothesis  $\mathcal{H}_C$ , which states that one or both of the black holes carried a Maxwell charge. If on the other hand charges are restricted to zero, the associated waveform model  $\tilde{h}_{\text{NC}}$  defines a hypothesis  $\mathcal{H}_{\text{NC}}$ , stating that no charges were present. Given a hypothesis  $\mathcal{H}$ , data  $d$ , and whatever background information  $\mathcal{I}$  we use a Bayesian analysis framework described in Sec. 2.3.1.

In this chapter we will set  $f_{\text{low}} = 20$  Hz, and  $f_{\text{high}}$  is determined by the parameters entering the IMRPhenomPv2 waveform. Given our hypotheses  $\mathcal{H}_C$  and  $\mathcal{H}_{\text{NC}}$ , the general expression for the evidence (2.24) enables computation of a Bayes factor which can be used to rank the hypotheses:

$$B_{\text{NC}}^C \equiv \frac{p(d|\mathcal{H}_C, \mathcal{I})}{p(d|\mathcal{H}_{\text{NC}}, \mathcal{I})}. \quad (4.5)$$

In our studies, the `lal inference nest` algorithm in the LALInference library [156] is used to sample the likelihood function of Eq. (2.22), while the waveform model described in the previous section was implemented as an extension of the IMRPhenomPv2 approximant in the LALSsimulation library of LALSuite [108].

Together with spin-related parameters, the intrinsic parameters being sampled over directly are the (dressed) total mass  $M$ , the mass ratio  $q = m_2/m_1$  (with the convention



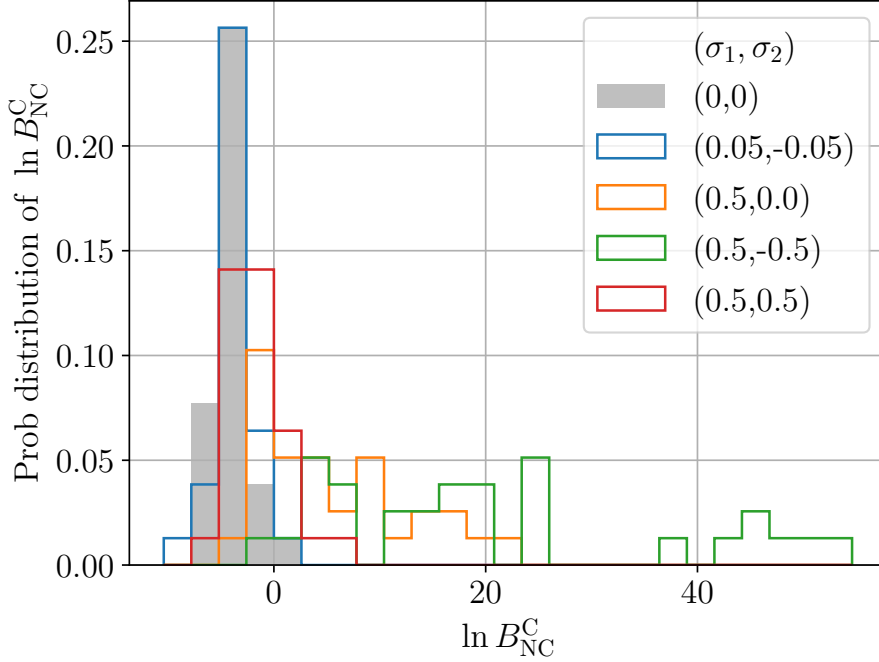


Figure 4.1: Histograms for  $\ln B_{\text{NC}}^{\text{C}}$  for 67 choices of masses and spins with ranges as detailed in the main text, and the five different choices of  $(\sigma_1, \sigma_2)$  indicated in the legend.

$m_2 \leq m_1$ ), and the charge-to-mass ratios  $\sigma_1 \equiv q_1/m_1$ ,  $\sigma_2 \equiv q_2/m_2$ . For  $M$  and  $q$  we use uniform priors chosen wide enough so as to accommodate the supports of the PDFs (with an upper bound of 1 for  $q$ ). Regarding the  $\sigma_i$ , for the examples in this chapter a uniform prior spanning  $\sigma_i \in [-2, 2]$  amply sufficed; here the sampling was done with the additional constraint  $\sigma_1\sigma_2 < 1$ , corresponding to the requirement of inspiraling orbits. Priors on the spin magnitudes  $a_1, a_2$  are taken to be uniform in the range  $[0, 0.99]$ , and priors on spin directions are uniform on the sphere. Both for simulated signals and for template waveforms we impose the Kerr-Newman condition for the presence of black hole horizons, i.e.  $a_i^2 + \sigma_i^2 \leq 1$ ,  $i = 1, 2$  [157]. For the extrinsic parameters, the priors on sky position and the orientation of the orbital plane at some reference frequency are also uniform on the sphere. We use a uniform-in-volume prior on distance, up to a maximum distance needed to accommodate the PDF.

### 4.3 Simulations

We now turn to the simulations we performed to gain insight into the measurability of black hole charges for signals typical of the long-duration binary black hole signals seen in the second Gravitational Wave Transient Catalog (GWTC-2) [85]. Signals were injected into a network consisting of the two Advanced LIGO interferometers and Advanced Virgo, assuming stationary, Gaussian noise following the projected design sensitivities of these observatories [3, 6]. As explained in Sec. 4.2, we will focus on signals that are relatively low-mass, such that no more than 5% of signal-to-noise ratio (SNR) is present beyond  $Mf = 0.018$ ; we require this of our injections as well. Also, we pick injected

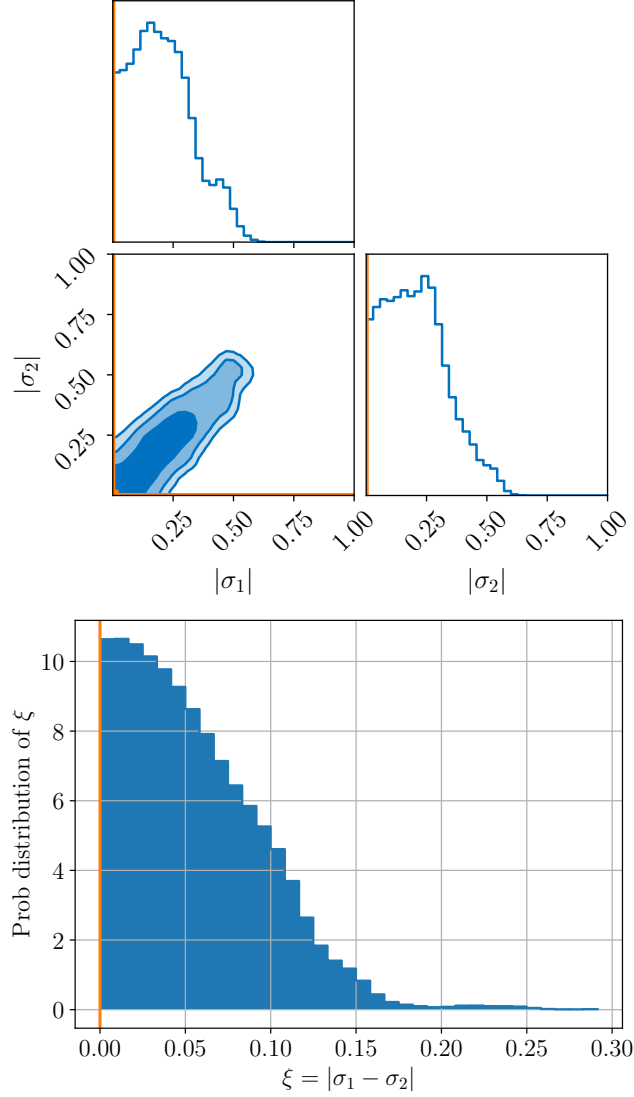


Figure 4.2: Posterior distributions for an injection with  $(m_1, m_2) = (13.87, 6.36) M_\odot$  at an SNR of 12.52, and  $(\sigma_1, \sigma_2) = (0, 0)$ . The left panel shows a corner plot for the posterior distributions of  $|\sigma_1|$  and  $|\sigma_2|$  (with the contours enclosing respectively 68%, 95%, and 99.7% of probability), while the right one is the posterior for  $\xi = |\sigma_1 - \sigma_2|$ . Here and in the analogous figures below, orange lines indicate the injected parameters.

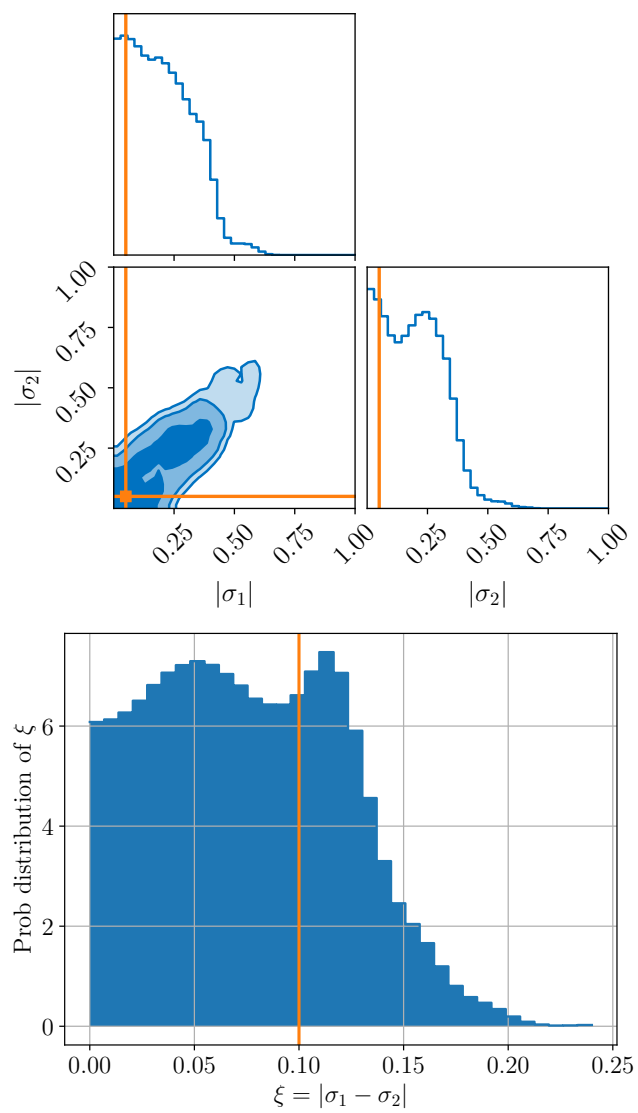


Figure 4.3: Same as in Fig. 4.2 but for  $(\sigma_1, \sigma_2) = (0.05, -0.05)$ .

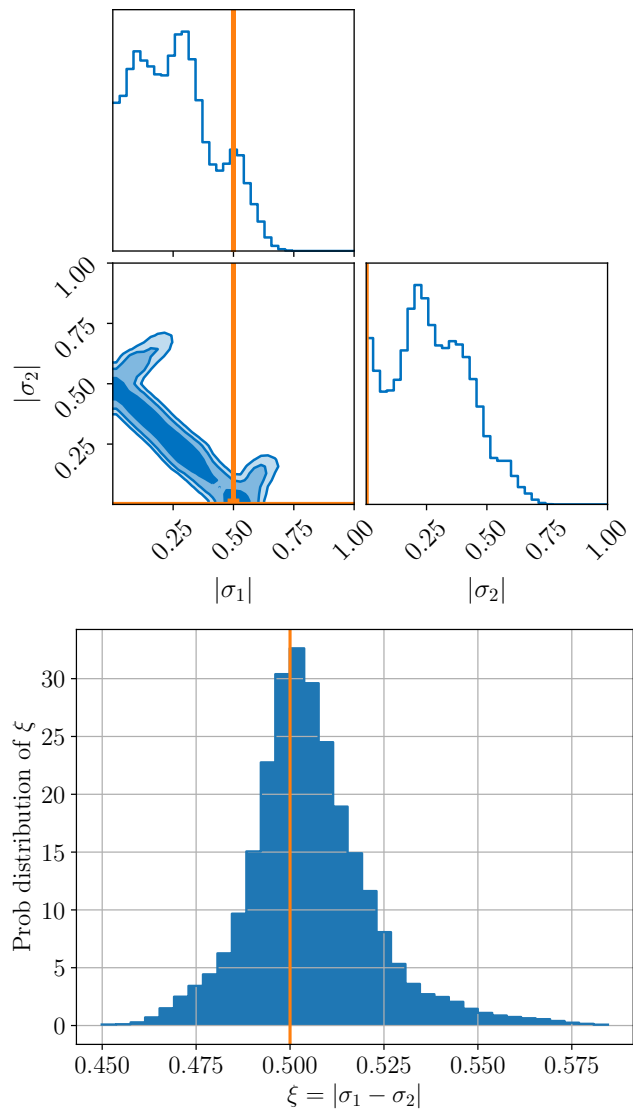


Figure 4.4: Same as in Fig. 4.2 but for  $(\sigma_1, \sigma_2) = (0.5, 0)$ .

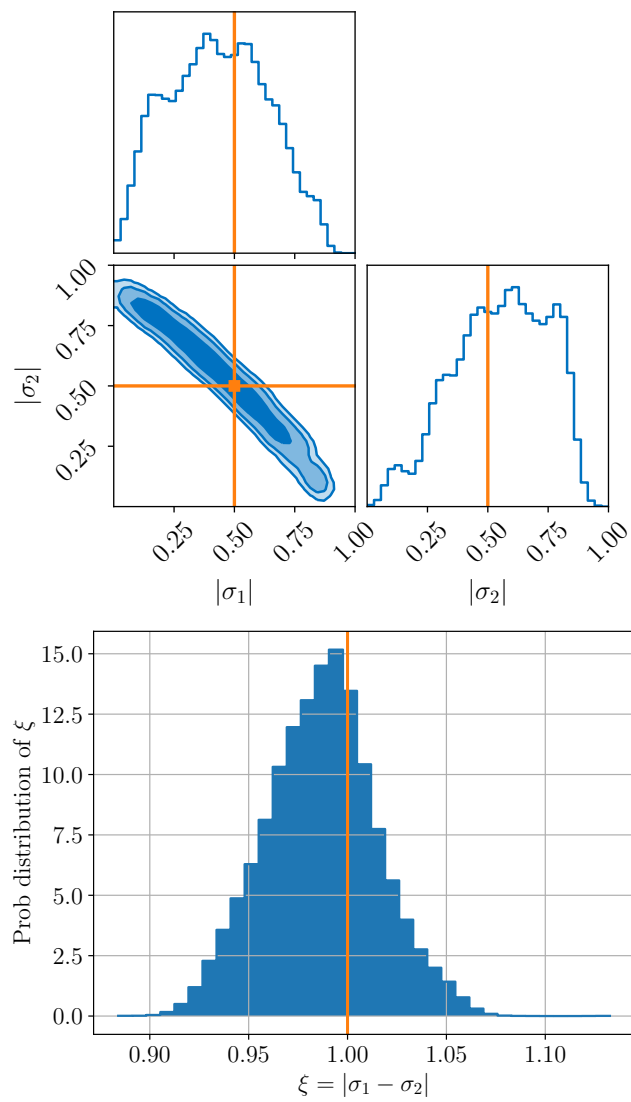


Figure 4.5: Same as in Fig. 4.2 but for  $(\sigma_1, \sigma_2) = (0.5, -0.5)$ .

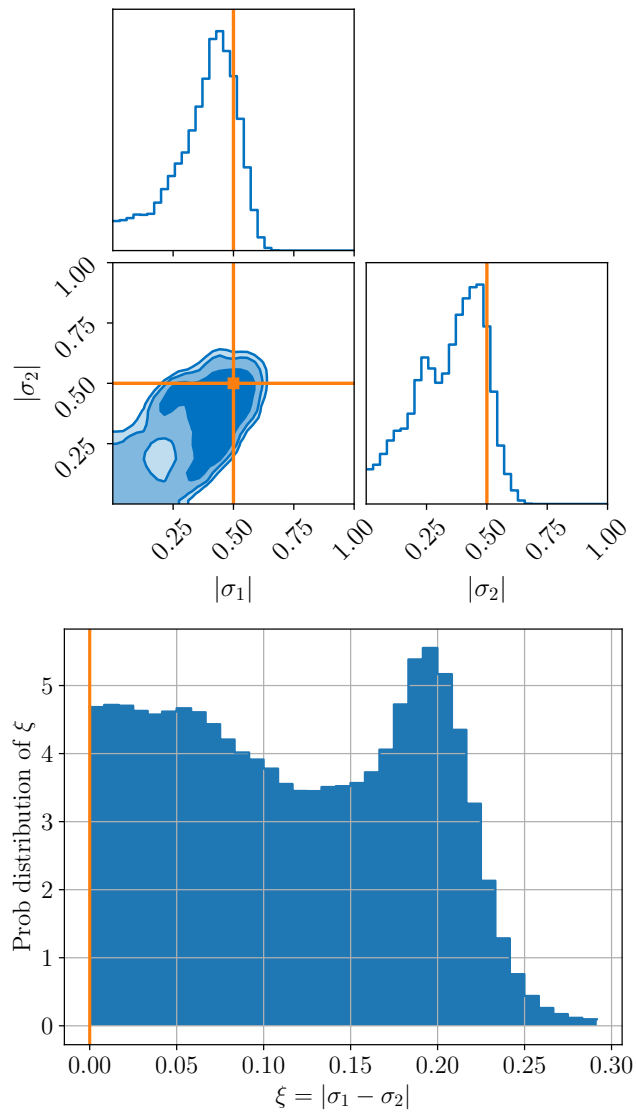


Figure 4.6: Same as in Fig. 4.2 but for  $(\sigma_1, \sigma_2) = (0.5, 0.5)$ .

$(\sigma_1, \sigma_2)$	$(0, 0)$	$(0.05, -0.05)$	$(0.5, 0)$	$(0.5, -0.5)$	$(0.5, 0.5)$
$\ln B_{\text{NC}}^{\text{C}}$	-4.19	-3.11	10.25	43.82	-1.01

Table 4.1: Values of  $\ln B_{\text{NC}}^{\text{C}}$  for different injected values of  $(\sigma_1, \sigma_2)$ , in the case of an injection with  $(m_1, m_2) = (13.87, 6.36) M_{\odot}$  and an SNR of 12.52, for which PDFs are shown in Figs. 4.2-4.6.

chirp masses  $\mathcal{M} = M\nu^{3/5}$  in the range  $[7, 9] M_{\odot}$ , and mass ratios  $q \in [0.4, 1]$ , choices that are representative of those signals in GWTC-2 that satisfy our post-inspiral SNR requirement. For the purpose of studying the behavior of  $\ln B_{\text{NC}}^{\text{C}}$ , SNRs are chosen to be in the range 10 – 15, again representative of the signals in GWTC-2 that we will analyze later on. For  $(\sigma_1, \sigma_2)$ , we pick the following values:

- $(\sigma_1, \sigma_2) = (0, 0)$ ,
- $(\sigma_1, \sigma_2) = (0.05, -0.05)$ ,
- $(\sigma_1, \sigma_2) = (0.5, 0)$ ,
- $(\sigma_1, \sigma_2) = (0.5, -0.5)$ ,
- $(\sigma_1, \sigma_2) = (0.5, 0.5)$ ,

where the larger numbers are inspired by Fisher matrix estimates on the measurability with Advanced LIGO and Virgo of the strength of a dipole contribution to the phase [129, 146].

First we look at  $\ln B_{\text{NC}}^{\text{C}}$  for 67 injections in stationary, Gaussian noise for an Advanced LIGO-Virgo network, with (dressed) masses and spins in the ranges specified above, SNRs in the range 10 – 15, and our five different choices for  $(\sigma_1, \sigma_2)$ . Histograms for the log Bayes factor are given in Fig. 4.1. The following trends are seen:

- For  $(\sigma_1, \sigma_2) = (0, 0)$ , all of the  $\ln B_{\text{NC}}^{\text{C}}$  are negative except for one at  $\ln B_{\text{NC}}^{\text{C}} = 0.50$ , consistent with the absence of charges in the injected signals.
- Also for  $(\sigma_1, \sigma_2) = (0.05, -0.05)$ , the great majority of  $\ln B_{\text{NC}}^{\text{C}}$  are negative, indicating that charge-to-mass ratios of this size are not discernable at the given SNRs.
- For  $(\sigma_1, \sigma_2) = (0.5, 0)$ , most signals show a positive  $\ln B_{\text{NC}}^{\text{C}}$ .
- The choice  $(\sigma_1, \sigma_2) = (0.5, -0.5)$  leads to the highest log Bayes factors, consistent with the fact that this yields the strongest leading-order (-1PN) contribution to the phasing; see Eqs. (4.3) and (4.4).
- However, for  $(\sigma_1, \sigma_2) = (0.5, 0.5)$ , though the individual charge-to-mass ratios are large, the -1PN contribution vanishes identically, leading to small (in fact, mostly negative) values of  $\ln B_{\text{NC}}^{\text{C}}$ .

Next we turn to parameter estimation. As a representative example, we focus on an injected signal with  $(m_1, m_2) = (13.87, 6.36) M_\odot$  and an SNR of 12.52. Bearing in mind the invariance of our waveform model under  $(\sigma_1, \sigma_2) \rightarrow (-\sigma_1, -\sigma_2)$ , we find it convenient to show posteriors for  $|\sigma_1|$ ,  $|\sigma_2|$ , and  $\xi = |\sigma_1 - \sigma_2|$ . Log Bayes factors for the different injected  $(\sigma_1, \sigma_2)$  are shown in Table 4.1; they are consistent with the trends observed in Fig. 4.1.

Fig. 4.2 shows the results for the above mass pair and  $(\sigma_1, \sigma_2) = (0, 0)$ . We see that the posterior densities for the  $|\sigma_i|$  are consistent with zero charges. They do show a peak away from zero; this is because random noise fluctuations cause the peaks of the distributions for the  $\sigma_i$  themselves (before taking the absolute value) to be away from zero. Bounds of  $|\sigma_i| \lesssim 0.26$  are obtained at 68% confidence. A somewhat more stringent bound is obtained for  $\xi$ , namely  $\xi \lesssim 0.07$  at the same confidence level; this is again as expected because it sets the leading-order term in the phase.

Next, Fig. 4.3 shows results for the same mass pair, but now  $(\sigma_1, \sigma_2) = (0.05, -0.05)$ . As already indicated by the log Bayes factor in Table 4.1, such values of  $\sigma_i$  are not detectable, and indeed the posteriors are consistent with zero charges. However, we note that the posterior for  $\xi$  does show a slight peak near  $|\sigma_1 - \sigma_2| = 0.1$ .

In Fig. 4.4 we consider the case  $(\sigma_1, \sigma_2) = (0.5, 0)$ , for which the log Bayes factor clearly indicated the presence of charge. Here the posteriors show clear support for both  $(|\sigma_1|, |\sigma_2|) = (0.5, 0)$  and  $(|\sigma_1|, |\sigma_2|) = (0, 0.5)$ , consistent with another symmetry of the waveform, namely  $(\sigma_1, \sigma_2) \rightarrow (\sigma_2, \sigma_1)$ . Meanwhile the posterior for  $\xi$  correctly has a strong peak near 0.5.

Fig. 4.5 shows results for  $(\sigma_1, \sigma_2) = (0.5, -0.5)$ . Though the individual posteriors for the  $|\sigma_i|$  are wide, there is clear support for the values  $(|\sigma_1|, |\sigma_2|) = (0.5, 0.5)$ . The posterior for  $\xi$  is tightly peaked near  $\xi = 1$ .

Finally we consider the case  $(\sigma_1, \sigma_2) = (0.5, 0.5)$ , in Fig. 4.6. This is a case where the log Bayes factor was negative (see again Table 4.1), presumably because of the absence of the dipole contribution together with the moderate SNR. And indeed, the posterior for  $\xi$  is not very informative, although the ones for the  $|\sigma_i|$  are consistent with the injected values.

## 4.4 Analysis of selected binary black hole signals

Let us now turn to actual signals from GWTC-2 [85], and in particular those that satisfy our criterion that at most 5% of the SNR resides in the post-inspiral phase, defined as  $Mf > 0.018$ . To assess which signals are in accordance with this benchmark, we take the median estimated parameter values reported in [84, 85], and substitute them into an IMRPhenomPv2 waveform. The events we end up with are listed in Table 4.2, which also gives the values for  $\ln B_{\text{NC}}^C$ . Since all log Bayes factors are negative, we find no evidence for charges in any of these.

For completeness, we also show posteriors for  $|\sigma_1|$  and  $|\sigma_2|$  (Fig. 4.7), and  $\xi = |\sigma_1 - \sigma_2|$  (Fig. 4.8). Here too, all the signals show consistency with  $(\sigma_1, \sigma_2) = (0, 0)$ . Events like GW190707, GW190728, and GW190924 have posteriors for the individual  $|\sigma_1|$  and  $|\sigma_2|$



Events	GW151226	GW170608	GW190707	GW190720	GW190728
$\ln B_{\text{NC}}^{\text{C}}$	-7.52	-7.63	-2.94	-3.71	-3.11
Events	GW190924	GW190930			
$\ln B_{\text{NC}}^{\text{C}}$	-3.67	-3.04			

Table 4.2: The GWTC-2 events analyzed, with their log Bayes factors for charges versus no charges.

that seem to have a peak away from zero, but as in the case of our simulated signal with  $(\sigma_1, \sigma_2) = (0, 0)$  (see Fig. 4.2), this can be attributed to noise fluctuations causing the peaks of the  $\sigma_i$  themselves (before taking the absolute value) to be away from zero. However, these three events also have a peak in  $\xi$  that is away from zero; in the case of GW190728 there is even a relatively strong peak at  $\xi \sim 0.3$ . That said, the log Bayes factor for GW190728 ( $\ln B_{\text{NC}}^{\text{C}} = -3.11$ ) is below the largest log Bayes factor for injections with  $(\sigma_1, \sigma_2) = (0, 0)$  shown in Fig. 4.1, which is  $\ln B_{\text{NC}}^{\text{C}} = 0.50$ ; the same is true of all the other real events in Table 4.2. Although the injection set of Fig. 4.1 pertained to stationary, Gaussian noise, we expect a more complete “background distribution” for  $\ln B_{\text{NC}}^{\text{C}}$  in real noise to extend to even larger values. Therefore, we are not induced to conclude that charges were present on any of the binary black holes that generated the real signals we analyzed.

For all our real events, the  $1\text{-}\sigma$  bounds on the  $|\sigma_i|$  tend to be at the level of  $0.2 - 0.3$ , consistent with the zero-charge injection which we studied PDFs for in the previous section. Similarly, bounds on  $\xi$  tend to be somewhat more stringent, varying from  $0.08$  (for GW170608) to  $0.3$  (for GW190728).

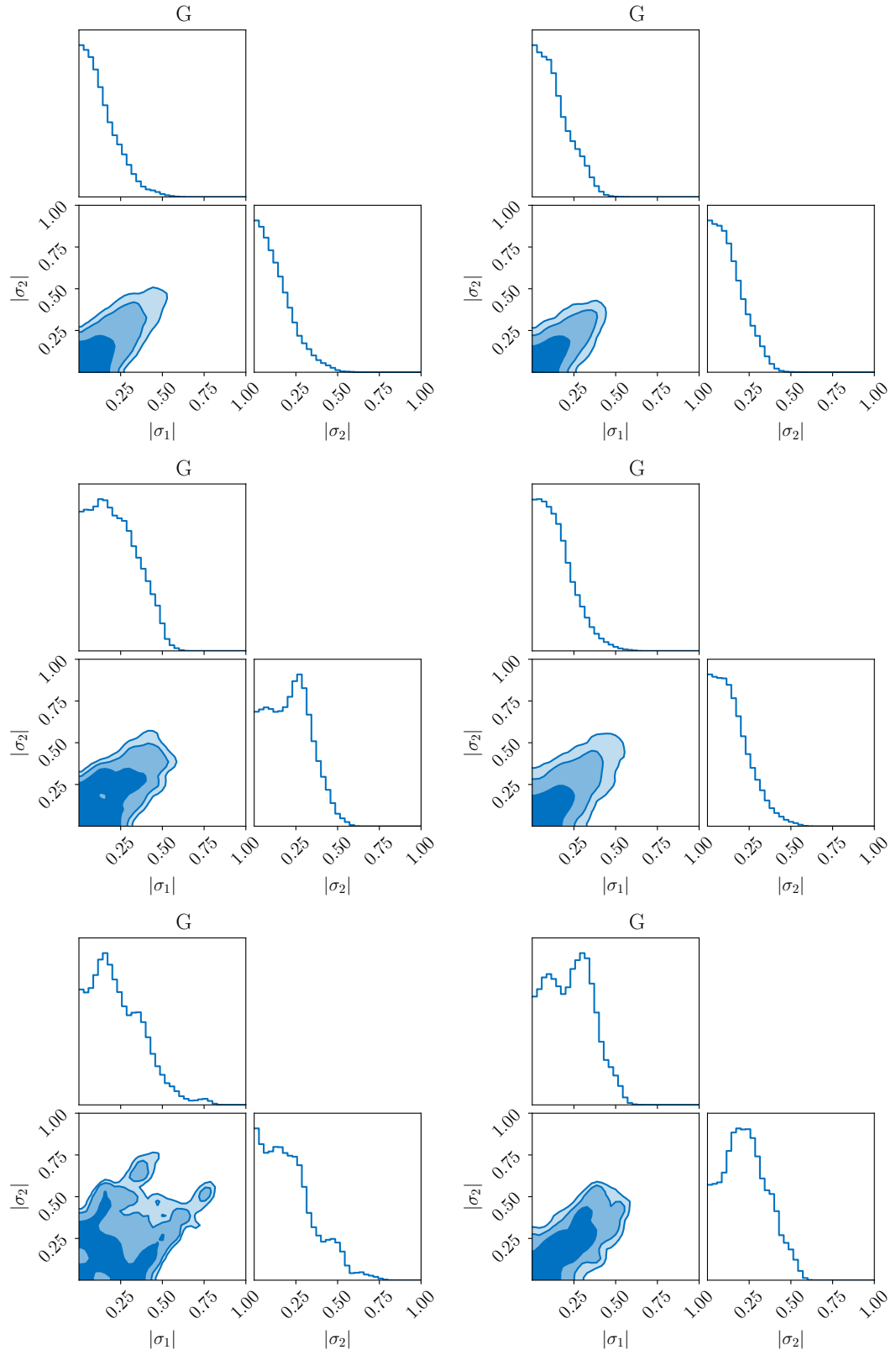
## 4.5 Summary and conclusions

We have set up a Bayesian analysis framework to search for, or constrain, (dark) electric charges on binary black holes using gravitational waves. In particular, the inspiral part of the phasing of the precessing-spin IMRPhenomPv2 inspiral-merger-ringdown waveform was modified to include the effect of such charges up to 1PN order. This was then used for both injections and template waveforms, focusing on signals with less than 5% of their SNR in the post-inspiral regime, in view of the currently unknown effect of charges during plunge and merger.

To test the analysis set-up, we looked at the log Bayes factor,  $\ln B_{\text{NC}}^{\text{C}}$ , comparing the hypothesis that charges are present with the one that assumes zero charges, for signals with SNRs between 10 and 15. Choosing different injected values for the charge-to-mass ratios  $(\sigma_1, \sigma_2)$ , expected trends were seen in the distributions of  $\ln B_{\text{NC}}^{\text{C}}$ : (a) when the  $\sigma_i$  were zero or small, the great majority of our simulated signals yielded  $\ln B_{\text{NC}}^{\text{C}} < 0$ , and (b) for larger  $\sigma_i$ , the typical magnitude of  $\ln B_{\text{NC}}^{\text{C}}$  was set by the strength of the leading-order contribution of charges to the phase, which is determined by  $\xi = |\sigma_1 - \sigma_2|$ .

As a case study for parameter estimation we used an injection with an SNR of 12.52. PDFs were indicative of the injected  $(\sigma_1, \sigma_2)$ , and for  $(\sigma_1, \sigma_2) = (0, 0)$ ,  $1\text{-}\sigma$  upper bounds came out to be  $|\sigma_i| \lesssim 0.26$  and  $\xi \lesssim 0.07$ .

Finally, we turned to real signals from GWTC-2, again selected to have a long inspiral



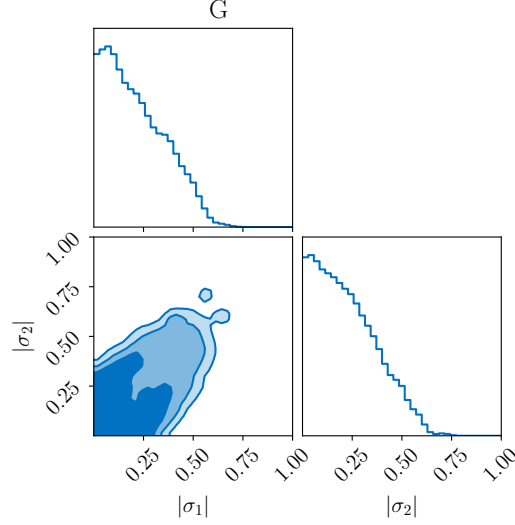


Figure 4.7: Corner plots for the posteriors of  $|\sigma_1|$ ,  $|\sigma_2|$ , for the events of Table 4.2.

in band. All of the  $\ln B_{\text{NC}}^{\text{C}}$  came out to be negative, consistent with the absence of charges, and also the PDFs for the  $|\sigma_i|$  and  $\xi$  were consistent with zero charge. Typical bounds on charge-related parameters were  $|\sigma_i| \lesssim 0.2 - 0.3$  and  $\xi \lesssim 0.08 - 0.3$ .

In this work we focused on the inspiral regime, but charge-induced modifications of the ringdown spectrum have also been computed [148–152]. It would be of interest to search for the signature of charges in the ringdown signal of high-mass events, whose ringdown modes are starting to be probed even with Advanced LIGO and Virgo at O3 sensitivity [11]. Finally, should appropriate waveform models become available in the future, it will be interesting to see how charge measurements will sharpen when the entire inspiral-merger-ringdown process can be used.

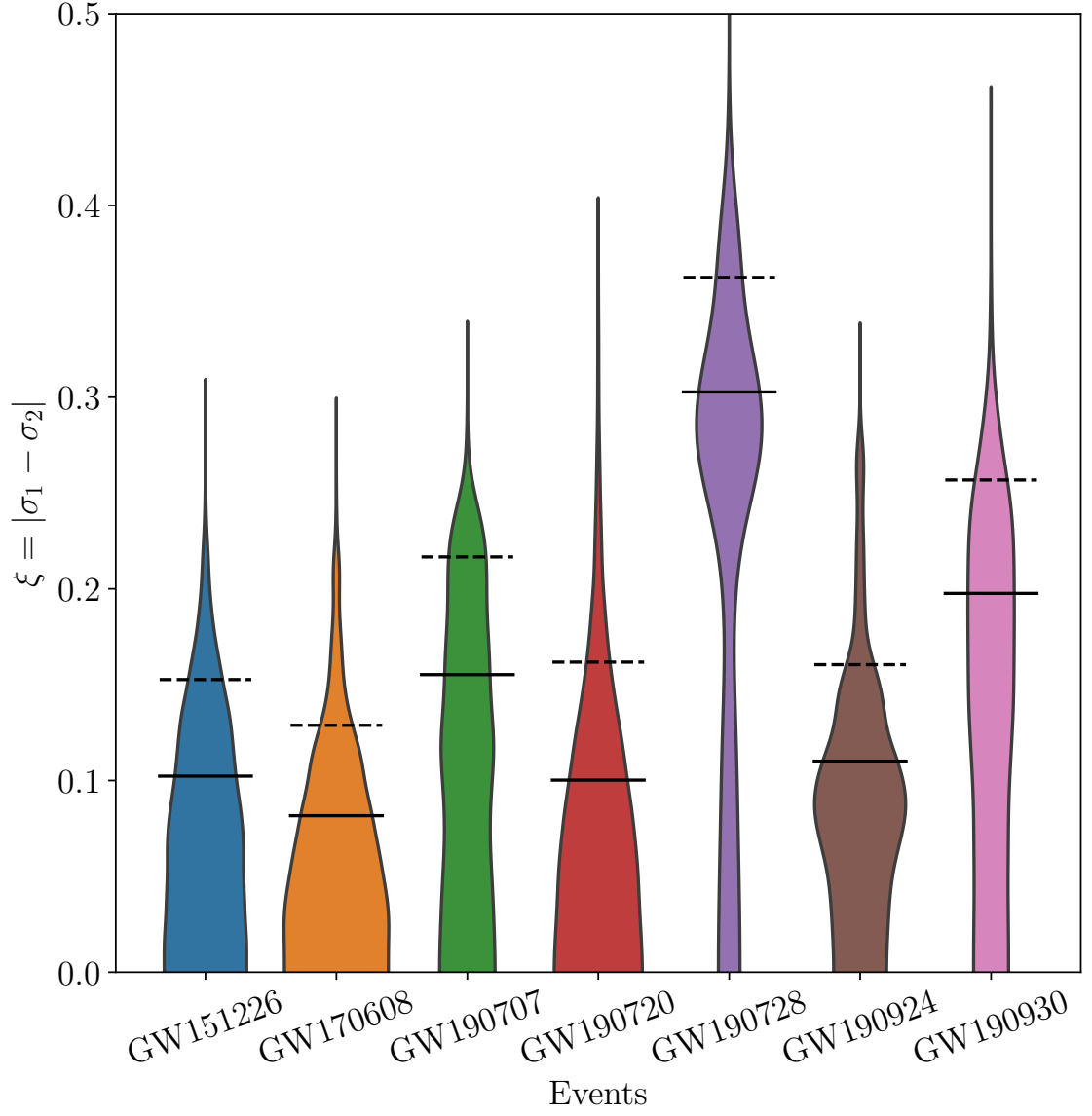


Figure 4.8: Posterior densities for  $\xi = |\sigma_1 - \sigma_2|$ , for the events of Table 4.2. The solid lines indicate 68% confidence levels, the dashed lines 90% confidence levels.



# Relativistic effective action of dynamical gravitomagnetic tides for slowly rotating neutron stars

## 5.1 Introduction

An intriguing feature of general relativity is the emergence of new types of gravitomagnetic tides, which have no Newtonian analogs. Gravitomagnetic tides most strongly excite the magnetic (odd-parity) sector of inertial modes of a rotating star. Inertial modes are associated with the Coriolis effect and include the  $r$ -modes [158–161], which are inertial modes with purely magnetic parity. The  $r$ -modes have received significant attention due to their unusual properties and the fact that they can become unstable to gravitational radiation (see, e.g., Refs. [38, 160, 162–168]). The remaining inertial modes have no specific name and are of mixed parity. In the slow-rotation limit, only their magnetic parts are directly relevant for gravitomagnetic tides. The inertial mode frequencies are approximately proportional to the rotation frequency of the star. Consequently, the gravitomagnetic inertial-mode resonances in a binary generally lie well within the sensitive frequency band of ground-based gravitational-wave detectors [3, 6, 93, 169]. This opens interesting prospects for probing properties of neutron-star matter beyond the information encoded in gravitoelectric tidal deformability or radius. However, it is currently not possible to measure this new physics because a relativistic modeling framework of gravitomagnetic dynamical tides is not developed.

The tidal excitation of a quasi-normal mode in quasi-circular binaries is analogous to a harmonic oscillator with a quasi-periodic force. The effect of quadrupolar gravitomagnetic tidal mode excitation was estimated in Refs. [38, 165, 166, 168]; see Refs. [37, 159, 170] for studies based on the weaker coupling to gravitoelectric fields. These results indicate that the impact on the gravitational-wave phasing is large enough to be potentially measurable with the planned future upgrades to current detectors and third-generation facilities. The gravitational-wave signatures from mode excitations directly depend on key matter parameters: the Love numbers characterizing how strongly the mode couples to the tidal field, and the mode frequency. These parameters are computed from linearized perturbations to a relativistic star in equilibrium. The gravitomagnetic mode

frequencies were obtained, e.g., in Refs. [41, 164, 171–173]. The Love numbers, however, require taking the limit that the perturbing frequency goes to zero, which has proved subtle, and leads to two distinct Love numbers. They are associated with the different assumptions of a static or irrotational perturbed fluid. These unusual features of the response of a neutron star to a gravitomagnetic tidal perturbation have prompted several discussions in the literature [174–179], and were recently re-examined in the context of a post-Newtonian star in Refs. [165–167].

The promising prospects for measuring the gravitomagnetic modes motivate the need for modern gravitational-wave models to include these phenomena. A crucial foundation for developing state-of-the-art waveform models of matter effects in binary inspirals is a relativistic effective action for the dynamics. The Love numbers and mode frequencies immediately appear in the coupling coefficients in this effective action. In this chapter, we derive a relativistic effective action for gravitomagnetic tidal effects in the slow-rotation limit. We develop the theory by first considering a post-Newtonian approximation of the neutron-star interior. This enables us to identify a new way to compute the mode frequencies from the perspective of a rotation-induced shift away from its vanishing value for nonrotating stars. It also yields important insights into the relevant matter variables for the dynamics, and their connection to the mode functions. Further, these studies reveal the important role of a shift symmetry, whereby a displacement of the gravitomagnetic mode amplitudes leaves the global properties of the fluid unchanged. Ensuring that the action respect this symmetry has direct consequences for its formulations in the corotating and inertial frames.

Next, we develop the fully relativistic theory based on the symmetries and a power counting scheme. We find that within our approximations, the dominant effects are described by four nontrivial couplings that come with coefficients that encode the microphysics of neutron-star interiors. We discuss the matching of these coefficients to the relativistic magnetic tidal deformabilities (Love numbers) and mode frequencies. Notably, we show that both kinds of magnetic Love numbers, the static and irrotational ones, appear in the action and are thus relevant for gravitational waves. The static Love number corresponds to the coefficient of a nonlinear field contribution, as discussed in the post-Newtonian context in Ref. [167]. The difference between static and irrotational Love numbers characterizes the direct contribution from the magnetic modes. To identify and match the mode frequency we calculate the relativistic response function and discuss its features. We also derive its limiting form in several regimes after clarifying various subtleties, and obtain a corresponding Love operator representing the time-domain response. Our action provides a key foundation for accurately modeling gravitomagnetic effects in gravitational waves and interpreting the information on subatomic physics they encode.

The chapter is organized as follows. In Sec. 5.2 we review the treatment of dynamical gravitomagnetic tides in a first post-Newtonian (1PN) approximation from Ref. [38]. We work to linear order in the rotation of the star and derive an action that encodes the excitation of magnetic modes by an external gravitomagnetic field. We discuss the relevant degrees of freedom and their relation to contributions from individual modes. We also highlight the shift symmetry that occurs in the gravitomagnetic sector and its importance for the Lagrangians in the corotating and inertial frames. In Sec. 5.3 we construct a fully relativistic action in the framework of effective field theory. We briefly

discuss the power counting scheme, and further specialize to the four interaction terms that are most important based on the post-Newtonian limit. In Sec. 5.4 we perform the matching of the coefficients in the effective action to the relativistic mode frequencies and tidal deformabilities. Section 5.5 discusses the frequency- and time-domain tidal response and their limiting forms in different regimes. In Sec. 5.6 we provide a brief summary of the relativistic Lagrangian and the coupling coefficients involved. We also discuss the physical insights and dynamical consequences of this action. Section 5.7 summarizes our conclusions, and Appendix A.1 contains a short compilation of useful formulas.

## 5.2 Dynamical magnetic tides of rotating stars

In this section, we briefly review the description of gravitomagnetic modes of a neutron star in the presence of an external gravitomagnetic field from Ref. [38]. We work within a double perturbative expansion in the post-Newtonian and slow-rotation approximations. From the equations of motion we develop an effective action in the corotating frame of the neutron star. The Lagrangian formulation provides a clean, elegantly concise description of the unusual features of the gravitomagnetic dynamics compared to the more familiar gravitoelectric tides. We formulate the action in terms of symmetric-tracefree tensors of magnetic parity, which conveniently isolates the relevant contributions from associated modes into effective degrees of freedom and elucidates the underlying physics of gravitomagnetic tides. We give an explicit example demonstrating the utility of the Lagrangian by exhibiting a way to calculate the gravitomagnetic mode frequency. We also discuss the important role of a shift symmetry, whereby a displacement in the mode amplitudes leaves the fluid properties unchanged. Requiring that the Lagrangian respect this symmetry has an impact on its form in the inertial frame. The insights on the matter variables and symmetries developed in this section will be important for constructing the relativistic theory in Sec. 5.3.

### 5.2.1 Metric of a slowly rotating neutron star

We consider a (approximately) spherical neutron star of mass  $M$  that is slowly rotating with angular velocity  $\Omega$  and immersed in an external gravitomagnetic tidal potential of 1PN order. The post-Newtonian approximation can be understood as a formal expansion in the squared inverse of the speed of light  $c$ . To highlight similarities with electromagnetism, it is convenient to write the metric for the neutron star in the inertial<sup>1</sup> frame, denoted by indices  $i, j, k, \dots$ , in the form [180–182]

$$ds^2 = -\exp\left[\frac{2\phi}{c^2}\right] \left[ c dt - \frac{1}{c^3} A_i dx^i \right]^2 + \exp\left[-\frac{2\phi}{c^2}\right] \gamma_{ij} dx^i dx^j, \quad (5.1)$$

where  $\phi$  is the gravitoelectric (Newtonian) potential,  $A^i$  is the gravitomagnetic potential, and to 1PN order  $\gamma_{ij} = \delta_{ij} + \mathcal{O}(c^{-4})$ . We next make a spatial coordinate change that

---

<sup>1</sup>We understand here an inertial frame in the global Newtonian sense. The metric asymptotically approaches the Minkowski one in the inertial frame.



keeps  $t$  unchanged from the inertial frame  $x^i$  to the corotating frame  $x^I$  (denoted by capitalized indices  $I, J, K, \dots$ ). This transformation is given by

$$x^j = R_I^j x^I, \quad R_I^j = C_J^j \exp(*\Omega t)_I^J, \quad (5.2)$$

where  $\Omega$  is the angular velocity vector,  $*\Omega_{IJ} \equiv \Omega_{IJ} = \epsilon_{IJK}\Omega^K$  is its antisymmetric dual tensor,  $\epsilon_{IJK}$  the Levi-Civita symbol,  $R_I^j$  is a rotation matrix ( $R_I^k R_{Jk} = \delta_{IJ}$ ) expressed here using a matrix exponential of  $*\Omega t$ , and  $C_I^j$  a constant rotation matrix identical to  $R_I^j$  at  $t = 0$ . We adopt the convention that boldface notation for spatial vectors refers to components in the corotating frame, e.g.,  $\Omega = (\Omega^I)$ , and that spatial indices are raised and lowered using the Kronecker delta. The angular velocity can be expressed as

$$\Omega^I = \frac{1}{2}\epsilon^{IJK}\Omega_{JK}, \quad \Omega_{JK} = -\Omega_{KJ} = \dot{R}_J^i R_{Ki}. \quad (5.3)$$

Applying this coordinate change to the line element (5.1) is straightforward. The differentials of the coordinates are related by

$$dx^j = R_I^j [dx^I - (\mathbf{x} \times \Omega)^I dt], \quad (5.4)$$

which leads to the corotating-frame 1PN line element

$$\begin{aligned} ds^2 = & - \left[ c^2 + 2\phi + \frac{2\phi^2}{c^2} - \frac{2}{c^2} \Omega \cdot (\mathbf{x} \times \mathbf{A}) \right] dt^2 + 2 \left[ -\mathbf{x} \times \Omega \left( 1 - \frac{2\phi}{c^2} \right) + \frac{\mathbf{A}}{c^2} \right] \cdot d\mathbf{x} dt \\ & + \left[ 1 - \frac{2\phi}{c^2} \right] d\mathbf{x} \cdot d\mathbf{x} + \mathcal{O}(c^{-4}, \Omega^2). \end{aligned} \quad (5.5)$$

We have only kept terms linear in the angular velocity, since we are interested in slowly rotating stars. In the next section, we use the metric in Eq. (5.5) to obtain the Euler equation for the matter inside the slowly rotating neutron star.

### 5.2.2 Fluid perturbation in the corotating frame

We describe the matter inside the neutron star as a perfect fluid with energy-momentum tensor

$$T^{\mu\nu} = \left( \rho + \frac{p}{c^2} \right) u^\mu u^\nu + p g^{\mu\nu}, \quad (5.6)$$

where  $\rho$  is the mass density,  $p$  is the pressure, and  $u^\mu$  is the 4-velocity of the fluid normalized as  $u_\mu u^\mu = -c^2$ . The neutron-star matter is subject to energy-momentum conservation  $T^{\mu\nu}_{;\nu} = 0$ , where the semicolon denotes the covariant derivative. Evaluating the energy-momentum conservation using the metric in Eq. (5.5) leads to the corotating-frame Euler equation in Lagrangian form given by

$$\dot{\mathbf{u}} + 2\Omega \times \mathbf{u} + \mathbf{u} \cdot \nabla \mathbf{u} = -\frac{\nabla p}{\rho} - \nabla \phi + \frac{\boldsymbol{\zeta}}{c^2} + \dots \quad (5.7)$$

Here, at 1PN order ( $c^{-2}$ ) we show only the terms involving the gravitomagnetic potential defined by

$$\boldsymbol{\zeta} = -\dot{\mathbf{A}} - \Omega \times \mathbf{A} + (\Omega \times \mathbf{x}) \cdot \nabla \mathbf{A} + (\mathbf{u} + \Omega \times \mathbf{x}) \times (\nabla \times \mathbf{A}), \quad (5.8)$$

where the overdot denotes a time derivative  $\dot{\phantom{x}} = \partial/\partial t$ . Recall that we also work to linear order in the angular velocity. This is the reason for the absence of the centripetal force, which is quadratic in  $\Omega$ , from Eq. (5.7).

Next, we consider Eq. (5.7) for small linearized perturbations about an equilibrium background configuration. We denote the background quantities by a subscript '0' and use a  $\delta$  in front of the perturbed quantities, as in  $\mathbf{u} = \mathbf{u}_0 + \delta\mathbf{u}$ . Let us recapitulate the arguments in Ref. [38] that lead to the finding that the magnetic part of the perturbation equation for the fluid at the leading 1PN order simply reduces to the *Newtonian* one augmented by a 1PN driving force from  $\zeta$ . We assume that the fluid perturbation is only generated by an external gravitomagnetic field  $\mathbf{A}_{\text{ext}}$ , which is of 1PN order. This implies that all perturbed quantities must also be of 1PN order, e.g.,  $\delta\mathbf{u} = \mathcal{O}(c^{-2})$ . The perturbed magnetic Euler equation at 1PN order is then given by a perturbation of the Newtonian terms and  $\zeta$ , that is, it derives solely from the terms shown in Eq. (5.7). The matter inside the perturbed neutron star is not static, and thus there is a gravitomagnetic field emanating from the neutron star. However, the perturbations sourcing this field are of 1PN order and the gravitomagnetic field equation is 1PN order, so the gravitomagnetic “response” field of the neutron-star perturbation is of 2PN order, which we can ignore for our purposes here. On the other hand, the fluid perturbations source a 1PN gravitoelectric field  $\delta\phi$ . Altogether, the 1PN harmonic-gauge perturbed field equations are given by

$$\Delta\delta\mathbf{A} = 0, \quad \Delta\delta\phi = 4\pi G \delta\rho. \quad (5.9)$$

This implies that the perturbed gravitomagnetic potential only has contributions from sources external to the star  $\delta\mathbf{A} = \mathbf{A}_{\text{ext}}$ . As mentioned above, we assume that there is no external gravitoelectric potential,  $\phi_{\text{ext}} = 0$ ; we further comment on the 1PN gravitoelectric driving of magnetic modes in Sec. 5.3.5, finding that it is subleading at quadrupolar level.

Having identified the relevant field contributions, and terms at 1PN order, we now consider the perturbed fluid and no longer exhibit powers of  $c$  explicitly. The background fluid is at rest in the corotating frame,  $\mathbf{u}_0 = 0$ . The external gravitomagnetic perturbation induces a Lagrangian fluid displacement  $\xi(\mathbf{x}, t)$  in the star, such that  $\delta\mathbf{u} = \dot{\xi}$ . Calculating the perturbations to the Euler equation (5.7) and keeping only 1PN terms up to linear order in the perturbations and in the angular velocity leads to

$$\ddot{\xi} + 2\Omega \times \dot{\xi} = -\frac{\nabla\delta p}{\rho_0} + \frac{\nabla p_0}{\rho_0^2}\delta\rho - \nabla\delta\phi + \mathbf{a}_{\text{ext}}. \quad (5.10)$$

The fluid acceleration induced by the external field  $\mathbf{a}_{\text{ext}} = \delta\zeta$  is given by

$$\mathbf{a}_{\text{ext}} = -\dot{\mathbf{A}}_{\text{ext}} + \nabla[(\Omega \times \mathbf{x}) \cdot \mathbf{A}_{\text{ext}}]. \quad (5.11)$$

We emphasize that the above results are in the corotating frame; the analogous fluid perturbation equation in the inertial frame can be found in Eq. (5.16) of Ref. [38].

Note that the background quantities in Eq. (5.10) refer to the zeroth order in the double expansion of post-Newtonian and rotational corrections: it is the equilibrium configuration computed for a Newtonian, nonrotating star. The feature that the background is identical to a nonrotating star at linear order in angular velocity is due to

the fact that the Coriolis force on the background vanishes and the centripetal force is quadratic in  $\Omega$ . Hence the background quantities  $\rho_0, p_0$  are spherically symmetric in our approximations. In the following section, we obtain the Lagrangian for the perturbed Euler equation (5.10).

Before proceeding, we highlight the following. To define the tidal deformability or Love number one studies the response of the star to the external field  $\mathbf{A}_{\text{ext}}$  that is encoded in the induced gravitomagnetic field  $\mathbf{A}$ . In our approximation, this response is sourced by the fluid perturbation  $\boldsymbol{\xi}$  and is hence of 2PN order. At that order, the nonlinear terms in the field equations lead to another source for the response field [166, 176]. Likewise, in our relativistic theory developed in Sec. 5.3, we recover two contributions to the response, which can be attributed to the fluid displacement and field nonlinearities, respectively. In the present section, however, we only consider the effect of the external field on the 1PN fluid displacement and focus instead on understanding the matter variables.

### 5.2.3 Magnetic tidal Lagrangian for slow rotation

We assume that the fluid is characterized by a simple temperature- and composition-independent equation of state of the form  $p = p(\rho)$ . Then the pressure perturbation is  $\delta p = \delta \rho dp/d\rho$  and the forcing terms on the right hand side of Eq. (5.10) can be written as

$$-\frac{\nabla \delta p}{\rho_0} + \frac{\nabla p_0}{\rho_0^2} \delta \rho - \nabla \delta \phi = -\nabla \left( c_s^2 \frac{\delta \rho}{\rho_0} + \delta \phi \right), \quad (5.12)$$

where  $c_s^2 = dp/d\rho$  is the speed of sound. We also use that  $\delta \rho = -\nabla \cdot (\rho_0 \boldsymbol{\xi})$ , which follows from perturbing the Newtonian continuity equation  $\dot{\rho} = -\nabla \cdot (\rho \mathbf{u})$ , and a solution for  $\delta \phi$  from its field equation (5.9). Inserting the relation (5.12) into the equations of motion (5.10) yields

$$\ddot{\boldsymbol{\xi}} + 2\Omega \times \dot{\boldsymbol{\xi}} = -\mathcal{D}\boldsymbol{\xi} + \mathbf{a}_{\text{ext}}, \quad (5.13)$$

where the linear operator  $\mathcal{D}$  is defined as

$$\mathcal{D}\boldsymbol{\xi} = -\nabla \left\{ \left[ \frac{c_s^2}{\rho_0} + 4\pi G \Delta^{-1} \right] \nabla \cdot (\rho_0 \boldsymbol{\xi}) \right\}. \quad (5.14)$$

For the gravitomagnetic tidal dynamics considered here, only the magnetic-type ( $\mathcal{B}$ ) contributions  $\boldsymbol{\xi}^{\mathcal{B}} = \sum q_{n\ell m}^{\mathcal{B}} \boldsymbol{\xi}_{n\ell m}^{\mathcal{B}}$  are relevant, and we henceforth drop the other contributions. The magnetic modes  $\boldsymbol{\xi}_{n\ell m}^{\mathcal{B}}$  have the general decomposition into a radial dependence  $\xi_{n\ell}^{\mathcal{B}}(r)$  and the magnetic vector spherical harmonic  $\mathbf{Y}_{\ell m}^{\mathcal{B}}(\theta, \varphi)$  depending on the polar and azimuthal angles  $(\theta, \varphi)$ , see Appendix A.1,

$$\boldsymbol{\xi}_{n\ell m}^{\mathcal{B}} = \xi_{n\ell}^{\mathcal{B}}(r) \mathbf{Y}_{\ell m}^{\mathcal{B}}(\theta, \varphi). \quad (5.15)$$

The normalization of the real radial mode function  $\xi_{n\ell}^{\mathcal{B}}$  follows from Eq. (3.26) and (A.9),

$$\int dr \rho_0 r^2 \xi_{n\ell}^{\mathcal{B}}(r) \xi_{n'\ell}^{\mathcal{B}}(r) = \delta_{nn'}, \quad (5.16)$$

and is accompanied by a completeness relation,

$$\sum_n \xi_{n\ell}^{\mathcal{B}}(r) \xi_{n\ell}^{\mathcal{B}}(r') = \frac{\delta(r - r')}{\rho_0 r^2}. \quad (5.17)$$

Note that at linear order in spin (and for the perfect fluid used here), the radial functions  $\xi_{n\ell}^{\mathcal{B}}(r)$  are rather degenerate [158] and we can pick them to be any complete basis of functions labeled by  $n$ .

An important property of the magnetic modes that directly follows from the definition of the vector spherical harmonic (A.7) is that  $\nabla \cdot (\rho_0 \xi^{\mathcal{B}}) = 0$  and  $\mathcal{D}\xi_{n\ell m}^{\mathcal{B}} = 0$ . Eq. (3.27) then tells us that the magnetic modes of the nonrotating star all have zero frequency,

$$\bar{\omega}_{n\ell}^{\mathcal{B}} = 0. \quad (5.18)$$

As a result, the equations of motion (5.13) simplify to

$$\ddot{\xi}^{\mathcal{B}} + 2\Omega \times \dot{\xi}^{\mathcal{B}} = \mathbf{a}_{\text{ext}}. \quad (5.19)$$

The Lagrangian for these equations of motion (5.19) is

$$L_{\text{DT}}^{\mathcal{B}} = \frac{1}{2} \langle \dot{\xi}^{\mathcal{B}}, \dot{\xi}^{\mathcal{B}} \rangle - \langle \xi^{\mathcal{B}}, \Omega \times \dot{\xi}^{\mathcal{B}} \rangle + \langle \mathbf{a}_{\text{ext}}, \xi^{\mathcal{B}} \rangle. \quad (5.20)$$

Note that, if  $\phi_{\text{ext}}$  was nonzero, the magnetic modes do not couple to the gravitoelectric potential at Newtonian order,  $\langle \nabla \phi_{\text{ext}}, \xi^{\mathcal{B}} \rangle = 0$ . Indeed, using the definition of the inner product, the coefficient  $\langle \nabla \phi_{\text{ext}}, \xi^{\mathcal{B}} \rangle$  is given by

$$\int d^3x \rho_0 \nabla \phi_{\text{ext}} \cdot \xi^{\mathcal{B}} = - \int d^3x \phi_{\text{ext}} \nabla \cdot (\rho_0 \xi^{\mathcal{B}}) = 0, \quad (5.21)$$

where we dropped a surface term since  $\xi^{\mathcal{B}} = 0$  on the surface of the star and used that  $\nabla \cdot (\rho_0 \xi^{\mathcal{B}}) = 0$ . We further discuss the coupling to the gravitoelectric potential beyond Newtonian order in Sec. 5.3.5.

In the next section, we discuss an interesting application of this Lagrangian that illustrates the utility of our formalism to calculate the gravitomagnetic mode frequency for the slowly rotating neutron star. However, it is important to review the classification of inertial modes, which is based on parity, as shown in Fig. 5.1. Specifically, the gravitomagnetic mode frequency will correspond to the inertial mode frequencies with purely magnetic parity.

## 5.2.4 Gravitomagnetic mode frequency

The operator  $\mathcal{D}$  associated with the nonrotating star has eigenvalues  $(\bar{\omega}_{n\ell}^{\mathcal{B}})^2 = 0$ . However, the Coriolis term will give rise to nonzero eigenvalues which correspond to the gravitomagnetic mode frequency. The calculation of the mode frequency does not require the external gravitomagnetic force term; it is sufficient to consider the free oscillations described by the Lagrangian from Eq. (5.20)

$$L_{\text{DT,free}}^{\mathcal{B}} = \frac{1}{2} \langle \dot{\xi}^{\mathcal{B}}, \dot{\xi}^{\mathcal{B}} \rangle - \langle \xi^{\mathcal{B}}, \Omega \times \dot{\xi}^{\mathcal{B}} \rangle. \quad (5.22)$$

Using the decomposition into mode amplitudes (3.28) and aligning the angular momentum as  $\Omega = (0, 0, \Omega)$ , the terms in the Lagrangian simplify as follows:

$$\frac{1}{2} \langle \dot{\xi}^{\mathcal{B}}, \dot{\xi}^{\mathcal{B}} \rangle = \sum_{n\ell m} \frac{1}{2} \dot{q}_{n\ell m}^{\mathcal{B}*}(t) \dot{q}_{n\ell m}^{\mathcal{B}}(t), \quad (5.23a)$$

$$- \langle \xi^{\mathcal{B}}, \Omega \times \dot{\xi}^{\mathcal{B}} \rangle = \sum_{n\ell m} q_{n\ell m}^{\mathcal{B}*}(t) \dot{q}_{n\ell m}^{\mathcal{B}}(t) \frac{im\Omega}{\ell(\ell+1)}. \quad (5.23b)$$

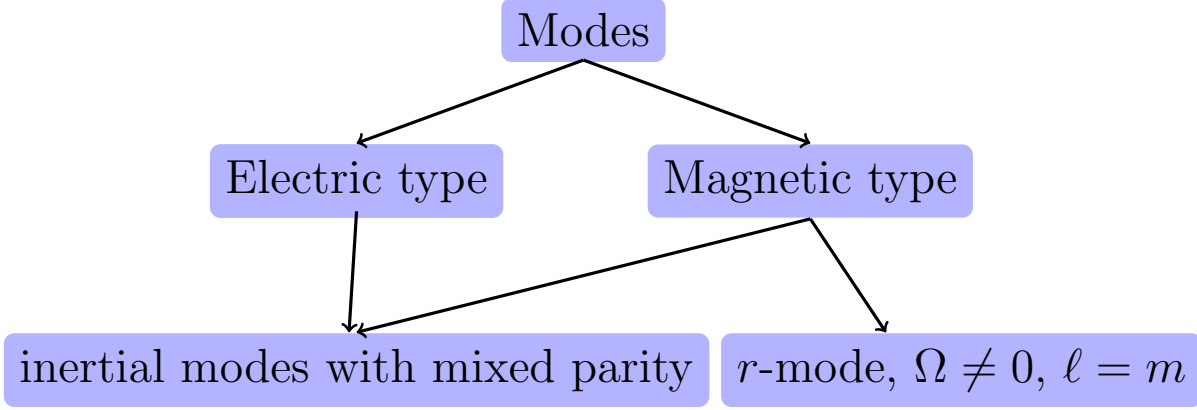


Figure 5.1: Classification of magnetic type oscillation modes of Newtonian stars. For r-modes Coriolis force is the restoring force.

To arrive at these expressions, we made use of Eqs. (5.16), (A.9), (A.10), and (A.3). We insert the results (5.23) into the free Lagrangian (5.22) and obtain the free equations of motion for the mode amplitudes  $q_{n\ell m}^{\mathcal{B}}(t)$

$$\ddot{q}_{n\ell m}^{\mathcal{B}} = \frac{2im\Omega}{\ell(\ell+1)} \dot{q}_{n\ell m}^{\mathcal{B}}. \quad (5.24)$$

To determine the mode frequency, we make the ansatz  $q_{n\ell m}(t) = Ce^{-i\omega_{\ell m}^{\mathcal{B}}t}$ . We choose the minus sign in the exponent so that the modes with positive  $m$  have negative frequencies (see below), which matches the usual conventions for mode expansions in the presence of an external tidal driving  $\sim e^{-im\phi}$ . Eq. (5.24) and find that it is a solution for frequencies  $\omega_{\ell m}^{\mathcal{B}}$ —the mode frequencies—given by

$$\omega_{\ell m}^{\mathcal{B}} = -\frac{2m\Omega}{\ell(\ell+1)}. \quad (5.25)$$

Our calculation makes explicit that the effect of rotation is to shift the mode frequency away from its nonspinning value of  $\bar{\omega}_{n\ell}^{\mathcal{B}} = 0$  to the finite value given in Eq. (5.25). We recall that these gravitomagnetic mode frequencies are expressed in the corotating frame.

An important point to note is that the force-free equations (5.24) have an additional solution with  $\omega_{\ell m}^{\mathcal{B}} = 0$ , which describes a constant mode amplitude. This zero-mode is associated with the trivial displacements analyzed in Ref. [183] (see also Ref. [38]). That is, constant displacements in the gravitomagnetic modes corresponding to the transformation

$$q_{n\ell m}^{\mathcal{B}} \rightarrow q_{n\ell m}^{\mathcal{B}} + \text{const}_{n\ell m}, \quad (5.26)$$

leave the macroscopic properties of the fluid (density, pressure, velocity) unchanged and hence must be physically inconsequential.

### 5.2.5 Lagrangian in the symmetric tracefree basis

Next, we transform from the description in terms of  $(\ell, m)$  modes to an equivalent one in terms of symmetric-tracefree tensors. This is advantageous for making the connection to the relativistic effective action in the next section.

We start by decomposing the Lagrangian (5.20) into the normal modes, using that

$$\langle \dot{\xi}^{\mathcal{B}}, \dot{\xi}^{\mathcal{B}} \rangle = \sum_{n\ell m' m} \dot{q}_{n\ell m'}^{\mathcal{B}*} \dot{q}_{n\ell m}^{\mathcal{B}} N_{\ell}^2 \mathcal{Y}_{S_1 \dots S_{\ell}}^{*\ell m'} \mathcal{Y}_{S_1 \dots S_{\ell}}^{\ell m}, \quad (5.27a)$$

$$\langle \xi^{\mathcal{B}}, \Omega \times \dot{\xi}^{\mathcal{B}} \rangle = \sum_{n\ell m' m} \frac{1}{\ell + 1} q_{n\ell m'}^{\mathcal{B}*} \dot{q}_{n\ell m}^{\mathcal{B}} \Omega^{AB} \times N_{\ell}^2 \mathcal{Y}_{AS_1 \dots S_{\ell-1}}^{*\ell m'} \mathcal{Y}_{BS_1 \dots S_{\ell-1}}^{\ell m}, \quad (5.27b)$$

where  $N_{\ell} = \sqrt{4\pi\ell!/(2\ell+1)!!}$ , and we have used the identities in Eqs. (A.9) and (A.10) together with the normalization in Eq. (5.16). The symmetric-tracefree tensors  $\mathcal{Y}_{s_1 s_2 \dots s_{\ell}}^{\ell m}$  are explained in Appendix A.1.

We next evaluate the coupling to the external field from  $\langle \mathbf{a}_{\text{ext}}, \xi^{\mathcal{B}} \rangle$  and Eq. (5.11). For this purpose, it is useful to expand the external fields in a Taylor series in  $\mathbf{x}$  around the center at  $\mathbf{x} = \mathbf{0}$ . The first ( $\ell = 0$ ) and second ( $\ell = 1$ ) term in this expansion can be ignored, since they can not have a physical effect in a local free-falling frame due to the equivalence principle. Hence from now on we specialize to the quadrupole case ( $\ell = 2$ ) giving the leading-order driving force, i.e., it contributes the largest effect in a binary. Recalling that  $\nabla \cdot (\rho_0 \xi^{\mathcal{B}}) = 0$ , we see that the second term in Eq. (5.11) does not contribute, since one can partially integrate the gradient under the integral, as in Eq. (5.21). The only contribution then comes from the magnetic-spherical-harmonic ( $\mathbf{Y}_{2m}^{\mathcal{B}}$ ) part of  $\mathbf{A}^{\text{ext}}$ , so we write its Taylor expansion in  $\mathbf{x}$  as (different by a conventional sign from Ref. [38])

$$A_I^{\text{ext}} = - \sum_m \sqrt{\frac{2}{3}} N_2 \mathcal{B}_m(t) r^2 Y_{2m}^{\mathcal{B}I}(\theta, \varphi) + \dots \quad (5.28)$$

$$= -\frac{2}{3} \epsilon_{IJK} \mathcal{B}_{KL}(t) x^J x^K + \dots, \quad (5.29)$$

where we used the definition of the magnetic vector spherical harmonic in the form of Eq. (A.8) and we encoded the external quadrupolar gravitomagnetic field in a symmetric-tracefree tensor  $\mathcal{B}_{KL}(t) = N_2 \sum_m \mathcal{Y}_{KL}^{2m} \mathcal{B}_m(t)$ . Note that the vacuum field equations  $\Delta \mathbf{A}^{\text{ext}} = 0$  are satisfied. Now we straightforwardly obtain (for  $\ell = 2$ )

$$\langle \mathbf{a}_{\text{ext}}, \xi^{\mathcal{B}} \rangle = \sum_{nm} \sqrt{\frac{2}{3}} N_2^2 I_n q_{n2m}^{\mathcal{B}} \mathcal{Y}_{IJ}^{2m} \dot{\mathcal{B}}_{IJ}, \quad (5.30)$$

using  $B_m = N_2 \mathcal{Y}_{IJ}^{*2m} \mathcal{B}_{IJ}$  and Eqs. (A.9), (A.2), and where we defined the gravitomagnetic overlap integral as [38]

$$I_n = \int dr \rho_0 r^4 \xi_{n2}^{\mathcal{B}}. \quad (5.31)$$

The quadrupolar mode amplitudes can be written in terms of symmetric-tracefree tensors as

$$Q_{\mathcal{B}n}^{IJ}(t) = \sum_m \sqrt{\frac{2}{3}} 2N_2^2 I_n \mathcal{Y}_{IJ}^{2m} q_{n2m}^{\mathcal{B}}(t), \quad (5.32)$$

where the prefactor is chosen to simplify the coupling term with the external field. With this definition, and after dropping total time derivatives, the Lagrangian becomes

$$L_{\text{DT}}^{\mathcal{B}} = \sum_n \frac{3}{16N_2^2 I_n^2} \left( \dot{Q}_{\mathcal{B}n}^{IJ} \dot{Q}_{\mathcal{B}n}^{IJ} - \frac{2}{3} \Omega^{JK} \dot{Q}_{\mathcal{B}n}^{IJ} Q_{\mathcal{B}n}^{KI} \right) - \frac{1}{2} \mathcal{B}_{IJ} \sum_n \dot{Q}_{\mathcal{B}n}^{IJ}. \quad (5.33)$$

### 5.2.6 Effective Lagrangian

As we are mainly interested in the bulk interaction of the star with the gravitomagnetic field rather than the dynamics of individual modes  $Q_{Bn}^{IJ}$  with different radial profiles (but identical mode frequencies), it is convenient to define an effective internal degree of freedom as

$$Q_B^{IJ} = \sum_n Q_{Bn}^{IJ}. \quad (5.34)$$

Its equation of motion follows from those for the individual modes  $Q_{Bn}^{IJ}$  and is given by

$$\ddot{Q}_B^{IJ} + \frac{2}{3}\Omega^{K(I}\dot{Q}_B^{J)K} = \frac{4}{3}N_2^2 I_B^2 \dot{\mathcal{B}}_{IJ}, \quad (5.35)$$

where

$$I_B^2 \equiv \sum_n I_n^2 = \int dr \rho_0 r^6. \quad (5.36)$$

In the last step we used the completeness relation of the modes (5.17) together with the definition of the  $I_n$ . This new overlap integral  $I_B$  only depends on the background density  $\rho_0$ ; compare also to Eq. (6.13) in Ref. [176]. It is directly related to the post-Newtonian magnetic tidal deformabilities, c.f., Eq. (6.20) in Ref. [176]. We elucidate the concrete connection to the Love numbers in the relativistic case in Sec. 5.4 below.

We can write the Lagrangian for the effective gravitomagnetic degrees of freedom as

$$L_{\text{DT}}^{\mathcal{B}} = C_{\dot{Q}^2}^{\mathcal{B}} \dot{Q}_B^{IJ} \dot{Q}_B^{IJ} + C_{\Omega Q \dot{Q}}^{\mathcal{B}} \Omega^{JK} \dot{Q}_B^{IJ} Q_B^{KI} - \frac{1}{2} \mathcal{B}_{IJ} \dot{Q}_B^{IJ}. \quad (5.37)$$

Note that this action is not identical to Eq. (5.33) yet describes a physically equivalent interaction of the star with the gravitomagnetic field. Here, we have kept the coefficients of the interaction terms as general constants, as will become important for the relativistic extension discussed in the next section. For a neutron star approximated to 1PN order they take the values ( $N_2^2 = 8\pi/15$ )

$$C_{\dot{Q}^2}^{\mathcal{B}} = \frac{3}{16N_2^2 I_B^2} = \frac{45}{128\pi I_B^2}, \quad C_{\Omega Q \dot{Q}}^{\mathcal{B}} = -\frac{2}{3} C_{\dot{Q}^2}^{\mathcal{B}}. \quad (5.38)$$

Furthermore, since  $\Omega^{IJ} = \text{const}$  for an isolated star, the action (5.37) exhibits a shift symmetry

$$Q_B^{IJ} \rightarrow Q_B^{IJ} + \text{const}^{IJ}, \quad (5.39)$$

as expected from the symmetry of the fluid under trivial displacements (5.26) of the gravitomagnetic mode amplitudes [183].

The Lagrangian in Eq. (5.37) is expressed in the corotating frame. The transformation to the inertial frame is accomplished similarly as discussed for the metric in the beginning of Sec. 5.2, e.g.,  $Q_B^{IJ} = R_I^i R_J^j Q_B^{ij}$ . This implies that the time derivatives transform as

$$\begin{aligned} \dot{Q}_B^{IJ} &= R_I^i R_J^j \left( \dot{Q}_B^{ij} - 2\Omega^{k(i} Q_B^{j)k} \right), \\ &\equiv \underbrace{\dot{Q}_B^{ij}}_{\equiv Q_B^{\prime ij}} \end{aligned} \quad (5.40)$$



where  $\Omega^{ij} = R_I^i \dot{R}^{Ij}$ . In order to maintain the shift symmetry (5.39), we express the inertial-frame action using the quantity  $Q_B^{ij}$  which is invariant under the symmetry. The action then becomes

$$L_{\text{DT}}^{\mathcal{B}} = C_{\dot{Q}^2}^{\mathcal{B}} Q_B^{ij} Q_B^{ij} + C_{\Omega Q \dot{Q}}^{\mathcal{B}} \Omega^{jk} Q_B^{ij} Q_B^{ki} - \frac{1}{2} \mathcal{B}_{ij} Q_B^{ij}. \quad (5.41)$$

The insights about the relevant effective degrees of freedom and the role of the shift symmetry will be important inputs for constructing the relativistic effective action, as we discuss in the next section.

## 5.3 Relativistic effective action

In this section, we go beyond the 1PN corotating-frame Lagrangian for the magnetic modes by developing a fully relativistic action along a worldline. We follow an effective-field-theory approach [184–189], and construct an ansatz for such an action from symmetries, keeping interaction terms only up to a certain order (accuracy) in some power counting, e.g, the multipole counting. The coefficients of the resulting terms in this action depend on the internal structure of the star and are fixed through a matching calculation that we will discuss in Sec. 5.4 below. Similar effective-field-theory treatments of dynamical tides and tidal absorption can be found in Refs. [190, 191], of spin can be found in Refs. [192–194], and of spin-tides can be found in Refs. [195, 196]. Recently, effective-field-theory calculations of tidal effects in scattering events have also come into focus [197, 198], see also Ref. [199], and Refs. [200–203] for analogous work based on massive quantum fields or scattering amplitudes.

We consider here a worldline  $z^\mu(\tau)$  as a macroscopic, coarse-grained, effective description for a compact star. We write the action as an integral of a Lagrangian  $L$  over the proper time  $\tau$  here,

$$\mathcal{S} = \int d\tau L. \quad (5.42)$$

The simplest example of the Lagrangian is  $L = m_0 = \text{const}$  which describes a point mass and neglects tides and spin. The oscillation modes of the star are represented by dynamical variables that evolve along the worldline. We start with an analysis of the symmetries of the problem, and demand that the building blocks of the action transform irreducibly under the symmetries.

Equipped with such a relativistic effective action, it is straightforward to calculate the orbital dynamics and gravitational radiation [184–189], see Ref. [204] for a publicly available code and Refs. [111, 205–208] for applications to tidal effects. The development of a relativistic effective action for gravitomagnetic tides is hence a crucial step towards more realistic waveform models for neutron stars.

### 5.3.1 Spherical symmetry and dynamical variables

The most important symmetry assumption is the spherical symmetry of the nonrotating star in equilibrium. This symmetry means that tidal degrees of freedom, or any other quantity from which we build the action, can be arranged into 3-dimensional symmetric-tracefree tensors, which transform irreducibly under rotations [the  $\text{SO}(3)$  group]. For



generic spinning stars, the spherical symmetry is broken and only an axial symmetry remains. However, since we treat the spin perturbatively we can still base our description on the rotation symmetry and the symmetric-tracefree tensor representation of the nonrotating case, as in the previous section. Following the effective action approach for electric tides [191], we consider a dynamical variable  $Q^{\mu\nu}(\tau)$  along the worldline representing quadrupolar ( $\ell = 2$ ) oscillation modes. This quantity should be symmetric  $Q^{[\mu\nu]} = 0$ , tracefree  $Q^\mu{}_\mu = 0$ , and should have physical components in the rest-frame only,  $Q^{\mu\nu}U_\nu = 0$ . The rest-frame is aligned with the tangent to the worldline, i.e., the normalized 4-velocity  $U^\mu = \dot{z}^\mu$  with  $U_\mu U^\mu = -1$  and in this section, an overdot denotes a derivative with respect to proper time  $\dot{\phantom{x}} = d/d\tau$ . We thus have a description of the mode in the coordinate frame with indices  $\mu, \nu \dots$  running through 0, 1, 2, 3.

It is convenient to express the action manifestly in terms of only the physical components of all quantities. To achieve this, we introduce a corotating (body-fixed) frame  $\Lambda_I{}^\mu$  with labels  $I, J, \dots = 1, 2, 3$  and assume orthonormality,  $\Lambda_I{}^\mu \Lambda_{J\mu} = \delta_{IJ}$ . The temporal part  $\Lambda_0{}^\mu$  is aligned with the rest-frame,

$$\Lambda_0{}^\mu = U^\mu, \quad \text{or } \Lambda_I{}^\mu U_\mu = 0. \quad (5.43)$$

Hence  $\Lambda_I{}^\mu$  contains three independent angular degrees of freedom, as expected. The three independent components of the angular velocity are

$$\Omega_I = \frac{1}{2} \epsilon_{IJK} \Omega^{JK} \quad (5.44)$$

with

$$\Omega^{JK} = -\Omega^{KJ} = \frac{D\Lambda^J{}_\mu}{d\tau} \Lambda^{K\mu}, \quad (5.45)$$

and  $D$  is the covariant differential, see also Refs. [196, 209]. This is a covariant generalization of the Newtonian angular velocity (5.3). Now, the independent components of the dynamical quadrupole are given by a symmetric tracefree 3-tensor in the corotating frame

$$Q^{IJ} = \Lambda^I{}_\mu \Lambda^J{}_\nu Q^{\mu\nu}, \quad Q^{[IJ]} = 0 = Q^I{}_I. \quad (5.46)$$

Other internal or tidal degrees of freedom can likewise be expressed as symmetric-tracefree tensors in the corotating frame, such as an ( $\ell = 3$ ) octupole  $Q^{IJK}$  and higher multipoles  $Q^{IJK\dots}$ . In this section we omit the label  $n$  for enumerating different (families of) modes for simplicity.

### 5.3.2 Coordinate invariance and external fields

Another important symmetry of the action is general coordinate invariance, which requires that external fields coupling to the worldline must be tensors on spacetime. However, in our setup, the external fields such as the curvature tensor entering the action must also be expressed in the corotating frame, followed by a decomposition into symmetric-tracefree parts. The curvature tensor  $R_{\mu\nu\alpha\beta}$  can be decomposed into the Weyl tensor  $C_{\mu\nu\alpha\beta}$  and the Ricci tensor  $R_{\mu\nu}$ . The latter can be removed from the worldline action through redefinitions of the metric [184, 190], which essentially corresponds to using the

vacuum field equations  $R_{\mu\nu} = 0$ . Furthermore, the Weyl tensor can be decomposed into symmetric-tracefree electric  $E_{IJ}$  and magnetic  $B_{IJ}$  parts as

$$E_{IJ} = C_{I0J0} = \Lambda_I^\mu \Lambda_0^\alpha \Lambda_J^\nu \Lambda_0^\beta C_{\mu\alpha\nu\beta}, \quad (5.47)$$

$$B_{IJ} = *C_{I0J0} = \Lambda_I^\mu \Lambda_0^\alpha \Lambda_J^\nu \Lambda_0^\beta *C_{\mu\alpha\nu\beta}, \quad (5.48)$$

with the dual  $*C_{\mu\nu\alpha\beta} = 1/2 \eta_{\mu\nu\rho\sigma} C^{\rho\sigma}{}_{\alpha\beta}$  and the volume form  $\eta_{\mu\nu\rho\sigma}$ . Notice that  $\epsilon_{IJK} = \eta_{0IJK} = \Lambda_0^\mu \Lambda_I^\nu \Lambda_J^\rho \Lambda_K^\sigma \eta_{\mu\nu\rho\sigma}$ . Derivatives of the Weyl curvature can be decomposed into the tensors (for  $s \geq 2$ )

$$E_{K_1 \dots K_s} = \Lambda_0^\alpha \Lambda_0^\beta \Lambda_{(K_1}^{\mu_1} \dots \Lambda_{K_s)}^{\mu_s} \nabla_{\mu_3 \dots \mu_s} C_{\mu_1 \alpha \mu_2 \beta}, \quad (5.49)$$

$$B_{K_1 \dots K_s} = \Lambda_0^\alpha \Lambda_0^\beta \Lambda_{(K_1}^{\mu_1} \dots \Lambda_{K_s)}^{\mu_s} \nabla_{\mu_3 \dots \mu_s} *C_{\mu_1 \alpha \mu_2 \beta}. \quad (5.50)$$

Other components can be written as time derivatives via  $\Lambda_0^\mu \nabla_\mu \equiv D/d\tau$ , see Ref. [194] for more details. We indicate the parity of the modes by a subscript:  $Q_\mathcal{E}^{IJK\dots}$  are even parity (electric) and  $Q_\mathcal{B}^{IJK\dots}$  are odd parity (magnetic) modes.

### 5.3.3 Final set of building blocks for the action

Based on the considerations above, the tensors entering the effective action are

$$\epsilon_{IJK}, \quad \Omega^I, \quad Q_\mathcal{E}^{IJ\dots}, \quad Q_\mathcal{B}^{IJ\dots}, \quad E_{IJ\dots}, \quad B_{IJ\dots}, \quad (5.51)$$

together with their  $\tau$ -derivatives, and the tensors  $\delta_{IJ}$ ,  $\delta^{IJ}$ . Recall that  $U^I = \Lambda^{I\mu} U_\mu = 0$ , which implies that the four-velocity cannot appear explicitly in the action. All of these building blocks for the action are conveniently written in the corotating frame.

### 5.3.4 Symmetry restrictions on the possible couplings

Overall, we require the following symmetries from the effective worldline action, see also Ref. [194]:

1. First, we require general coordinate invariance, required by general relativity.
2. Second, we require  $\text{SO}(3)$  symmetry of internal degrees of freedom due to the spherical symmetry of the body in the nonrotating limit. We already discussed one of the implications of this symmetry in the context of the building blocks of the action above.
3. Third, we require an “external”  $\text{SO}(3)$  symmetry of the corotating frame describing the orientation of the body.<sup>2</sup> In the case considered here, this  $\text{SO}(3)$  symmetry appears together with the internal  $\text{SO}(3)$  symmetry of 2. as one, which is very economic.

---

<sup>2</sup>A point-particle is characterized by an irreducible representation of the Poincaré group. The “external”  $\text{SO}(3)$  symmetry is the so called little group of that representation and is associated to the spin, see also [196].

4. Fourth, we require spacetime parity invariance. In principle, weak interactions could violate this symmetry, however, they play a subdominant role for the structure of a neutron star.
5. Fifth, we require time reversal invariance. This would be broken by dissipative effects such as tidal heating or fluid viscosity, which we neglect here.<sup>3</sup>
6. Sixth, we require shift symmetry of the gravitomagnetic dynamical tidal variables

$$Q_B^{IJ\cdots} \rightarrow Q_B^{IJ\cdots} + \text{const}^{IJ\cdots}, \quad (5.52)$$

which is related to macroscopically unobservable fluid displacements [183], as explained in the previous section around Eq. (5.26). This realization (5.52) of the symmetry was only demonstrated for  $\Omega^{IJ} = \text{const}$  and might need to be amended in a more general setting.

The consequences of the above symmetries on the terms in the action are the following. The first three symmetries imply that interactions must be composed of scalar contractions between the tensors in Eq. (5.51) and their  $\tau$ -derivatives. Symmetry 4 requires interactions to contain an even number of odd-parity variables  $\{\epsilon_{IJK}, \Omega^I, Q_B^{IJ\cdots}, B_{IJ\cdots}\}$ . Symmetry 5 requires an even number of variables that are odd under time reversal, which comprises  $\Omega^I$  and  $B_{IJ\cdots}$ , plus a number of extra  $\tau$ -derivatives. Finally, symmetry 6 requires that terms in the action either depend on  $Q_B^{IJ\cdots}$  only via  $\dot{Q}_B^{IJ\cdots}$ , or are of the form  $Q_B^{IJ\cdots}$  times a total  $\tau$ -derivative. It is interesting to note that the terms that are not allowed by these symmetry requirements exactly match to what one would call selection rules, in analogy to atomic physics, for the overlap integrals appearing in Sec. 5.2.

We note that in contrast to Ref. [194], here, we assume time-reversal invariance and spell out parity invariance explicitly. Furthermore, we find it more convenient here to not include worldline reparametrization and spin-gauge invariance from the beginning. Those symmetries are important for calculating the post-Newtonian binary dynamics and can readily be introduced at a later stage by changing the evolution parameter from proper time  $\tau$  to a generic affine parameter and performing a boost of the corotating frame, as explained in Sec. 3.2 of Ref. [194]. For the purpose of post-Newtonian calculations, it is also convenient to promote the spin (conjugate to  $\Omega^I$ ) to an additional dynamical variable via a Legendre transformation. The spin variable then absorbs the derivative coupling to the metric contained in  $\Omega^I$ . This leads to considerable simplifications but will not be needed here.

### 5.3.5 Power counting

The next step in constructing an effective action is to include all interaction terms allowed by the symmetries listed above and up to a certain order in some power counting in a ratio of scales. Here, two distinct types of scale-ratios are relevant: (i) for spatial scales we use the multipole counting in the ratio of the object's size and the radius of curvature of the external fields and (ii) for the time scales, we consider powers of the ratio of the

---

<sup>3</sup>An action-based treatment of dissipative tidal effects requires a more general approach, see Refs. [195, 196, 209–213]. In this chapter, we consider only conservative effects at the body scale.

various internal relaxation times and variations of the external tidal field. In the case where the external field is sourced by the companion in a binary system, (i) involves the orbital separation and (ii) involves multiples of the orbital period. These power countings must in general be treated as independent, e.g., for eccentric orbits. We do not introduce an *a priori* cutoff in a ratio of time scales, i.e., we allow for an arbitrary number of time derivatives. However, we are interested here in the leading (quadrupolar) gravitomagnetic interaction, so we work to quadratic order in the odd-parity quadrupolar variables  $Q_B^{IJ}$ ,  $B_{IJ}$ .

We note that a driving of magnetic modes by a quadrupolar gravitoelectric field is possible via couplings such as  $E_{IJ}\Omega_K\dot{Q}_B^{IJK}$  and  $E_{IJ}\Omega^I\dot{Q}_B^J$ , and similar couplings between electric and magnetic modes. At 1PN order, these derive from a term of the form  $\mathbf{\Omega} \times \mathbf{x} \cdot \dot{\phi}$  in the Euler equation (5.7). However, these couplings are suppressed by the angular velocity (flux dipole), making them effectively higher than quadrupolar order. Likewise, the octupolar electric driving for the quadrupolar magnetic modes from the coupling  $E_{IJK}\Omega_K\dot{Q}_B^{IJ}$  is of higher order in the multipole counting.

Furthermore, we consider the angular velocity (spin) and its associated time (length) scale as an independent parameter and work to linear order in the angular velocity in the tidal interactions. Finally, variable redefinitions can in general be used to remove some interaction terms from the action. In particular higher-order time derivatives of the dynamical degrees of freedom on the worldline can be removed in this way [214]. In the present case, this means that we can disregard  $\ddot{Q}_B^{IJ}$  or  $\dot{\Omega}^{IJ}$  or even higher time derivatives from the ansatz.

### 5.3.6 Relativistic action in the corotating frame

We now have all the inputs for deriving the relativistic tidal Lagrangian following the procedure outlined above. The complete Lagrangian consists of a nontidal and a magnetic tidal part,

$$L = L_{\text{NT}} + L_{\text{DT}}^{\mathcal{B}}. \quad (5.53)$$

The nontidal part contains terms such as

$$L_{\text{NT}} = -m_0 + C_{\Omega^2}\Omega^I\Omega^I + C_{E\Omega^2}E_{IJ}\Omega^I\Omega^J + \dots, \quad (5.54)$$

where  $C_{\Omega^2}$  is related to the moment of inertia and  $C_{E\Omega^2}$  is related to the spin-induced quadrupole moment of the star [215–217].

Following the symmetries listed above and assuming a single type of quadrupolar gravitomagnetic modes  $Q_B^{IJ}$ , we obtain the following relativistic effective action in the corotating frame for dynamical magnetic tides to quadratic order in the tidal variables and linear order in the angular velocity of the star,

$$\begin{aligned} L_{\text{DT}}^{\mathcal{B}} \approx & C_{\dot{Q}^2}^{\mathcal{B}}\dot{Q}_B^{IJ}\dot{Q}_B^{IJ} + C_{\Omega Q \dot{Q}}^{\mathcal{B}}\Omega^{JK}\dot{Q}_B^{IJ}Q_B^{KI} - \frac{1}{2}B_{IJ}\dot{Q}_B^{IJ} \\ & + B_{IJ}\sum_{k=0}^{\infty}\left[C_{BB^{(2k)}}\partial_{\tau}^{2k}B_{IJ} + C_{BB^{(2k+1)}}\Omega^{KI}\partial_{\tau}^{2k+1}B_{JK}\right], \end{aligned} \quad (5.55)$$

where  $\partial_{\tau} = d/d\tau$ . We choose the convention for the normalization of  $Q_B^{IJ}$  such that the coefficient in front of the third term is  $-\frac{1}{2}$ , as in the 1PN case. Higher  $\tau$ -derivatives on

$\Omega^{IJ}$  and  $Q_B^{IJ}$  can be removed by variable redefinitions in the action. The second term here is invariant under the shift symmetry (5.52) since  $\dot{\Omega}^{IJ} \approx 0 + \mathcal{O}(E, B)$ .<sup>4</sup> We note that  $B_{IJ} \approx A_{K,L(I}^{\text{ext}} \epsilon_{J)LK}/2 \approx \mathcal{B}_{IJ}$  to 1PN order for a star at rest. This can be checked by calculating the curvature tensor from the inertial-frame metric (5.1) and using its transformation property under coordinate changes to arrive at the corotating frame via Eq. (5.2).

The equations of motion for the mode amplitudes read

$$C_{\dot{Q}^2}^{\mathcal{B}} \ddot{Q}_B^{IJ} - C_{\Omega Q \dot{Q}}^{\mathcal{B}} \Omega^{K(I} \dot{Q}_B^{J)K} = \frac{1}{4} \dot{B}_{IJ}. \quad (5.56)$$

The source of the gravitational field equations, the energy momentum tensor, follows from a variation with respect to the metric. This source can be decomposed into mass and flux multipoles, with the order corresponding to the number of spatial derivatives acting on the metric in the action. Indeed, the star's current or flux quadrupole  $\mathcal{J}^{IJ}$  in the corotating frame can be identified directly from the action [206]: it is the quantity that couples to  $B_{IJ}$  as  $2/3 B_{IJ} \mathcal{J}^{IJ}$ , and is given by

$$\mathcal{J}^{IJ} \equiv \frac{3}{2} \frac{\delta L}{\delta B_{IJ}} \approx -\frac{3}{4} \dot{Q}_B^{IJ} + 3 \sum_{k=0}^{\infty} \left[ C_{BB(2k)} \partial_{\tau}^{2k} B_{IJ} + C_{BB(2k+1)\Omega} \Omega_{K(I} \partial_{\tau}^{2k+1} B_{J)K} \right]. \quad (5.57)$$

The flux quadrupole is the source term for the gravitomagnetic response field of the star. The first contribution in Eq. (5.57) is due to the odd-parity fluid perturbation described by  $Q_B^{IJ}$ . In the absence of any additional fluid modes besides  $Q_B^{IJ}$ , as we assume here, the remaining terms in Eq. (5.57) may be interpreted as a nonlinear field contribution. This interpretation is in agreement with the post-Newtonian analysis in Ref. [176] and in the last section.

In the post-Newtonian approximation, e.g., for a bound binary system, each time derivative on  $B_{IJ}$  leads to a further suppression of the term. At leading order, we may therefore neglect all but the term without  $\tau$ -derivatives in the second line of Eq. (5.55). By contrast, terms with time derivatives on  $Q_B^{IJ}$  must be kept, since the fluid modes can be resonantly excited. This yields the simplified action

$$L_{\text{DT}}^{\mathcal{B}} \approx C_{\dot{Q}^2}^{\mathcal{B}} \dot{Q}_B^{IJ} \dot{Q}_B^{IJ} + C_{\Omega Q \dot{Q}}^{\mathcal{B}} \Omega^{JK} \dot{Q}_B^{IJ} Q_B^{KI} - \frac{1}{2} B_{IJ} \dot{Q}_B^{IJ} + C_{B^2} B_{IJ} B_{IJ}, \quad (5.58)$$

with  $C_{B^2} \equiv C_{BB(0)}$ . The equations of motion (5.56) are not affected by this additional approximation.

### 5.3.7 Relativistic action in the coordinate frame

It is straightforward to rewrite the action in the coordinate frame using the transformation matrices  $\Lambda_I^{\mu}$ ,

$$L_{\text{DT}}^{\mathcal{B}} \approx C_{\dot{Q}^2}^{\mathcal{B}} Q_B'^{\mu\nu} Q_B'^{\mu\nu} + C_{\Omega Q \dot{Q}}^{\mathcal{B}} \Omega_{\nu\rho} Q_B'^{\mu\nu} Q_{B\mu}^{\rho} - \frac{1}{2} B_{\mu\nu} Q_B'^{\mu\nu} + C_{B^2} B_{\mu\nu} B^{\mu\nu}, \quad (5.59)$$

<sup>4</sup>Strictly speaking, the shift symmetry has to hold without using equations of motion. However, since one can shift the dynamical variables to remove time derivatives like  $\dot{\Omega}$ , one way to fix this is to amend the transformation rule (5.52). We leave such a more rigorous treatment for the case  $\dot{\Omega} \neq 0$  for future work.

where  $\Omega^{\mu\nu} = \Lambda_I^\mu D\Lambda^{I\nu}/d\tau$ . We have defined the quantity

$$Q_{\mathcal{B}}'^{\mu\nu} = \frac{DQ_{\mathcal{B}}^{\mu\nu}}{d\tau} + 2\Omega^{(\mu}{}_\rho Q_{\mathcal{B}}^{\nu)\rho}, \quad (5.60)$$

which is invariant under the shift symmetry (5.52). We note that even though we work to  $\mathcal{O}(\Omega)$ , the dependence on the angular velocity in Eq. (5.60) should not be expanded out, to ensure that the zero-mode is preserved. Also, since  $\Lambda_I^\mu U_\mu = 0$ , the variables in the coordinate-frame action are subject to constraints (or supplementary conditions),

$$\Omega^{\mu\nu}U_\nu = 0, \quad Q_{\mathcal{B}}^{\mu\nu}U_\nu = 0. \quad (5.61)$$

From this effective action (5.59), one can follow Refs. [191, 194, 204] to work out the post-Newtonian description of a binary system by performing a Legendre transform in  $\Omega^{\mu\nu}$  and  $\dot{Q}_{\mathcal{B}}^{\mu\nu}$ , introducing worldline reparametrization- and spin-gauge invariance, implementing a gauge fixing, deriving the Feynman rules, and calculating observables. It is important that the post-Newtonian approximation is applied only at the scale of the binary. That is, the neutron-star interior is treated in full general relativity and its internal structure is encoded in the coefficients of the effective action.

The post-Newtonian predictions for observables depend on the coefficients in the action (5.59). The next important step is thus to match them for a given fully relativistic neutron-star model. Before doing so, it is illustrative to compare Eq. (5.59) to the corresponding Lagrangian for dynamical, electric fundamental (f-)modes for a nonrotating star given by [191]

$$L_{\text{DT}}^{\mathcal{E}} \approx \frac{1}{4\lambda\omega_f^2} \left[ \frac{DQ_{\mathcal{E}}^{\mu\nu}}{d\tau} \frac{DQ_{\mu\nu}^{\mathcal{E}}}{d\tau} - \omega_f^2 Q_{\mathcal{E}}^{\mu\nu} Q_{\mu\nu}^{\mathcal{E}} \right] - \frac{1}{2} E_{\mu\nu} Q_{\mathcal{E}}^{\mu\nu}, \quad (5.62)$$

where  $\omega_f$  is the f-mode frequency and  $\lambda$  the electric quadrupolar Love number (tidal deformability). The differences to the magnetic action (5.59) are due to the different parity and time-reversal properties of the magnetic variables and the shift symmetry (5.52). In particular, the latter implies the absence of a  $Q_{\mathcal{B}}^2$ -term, meaning that the magnetic modes have zero frequency in the nonrotating case. As a consequence, the adiabatic limit of the magnetic action is not immediately obvious, in particular when the nonrotating limit is taken at the same time (see also Ref. [166]). In fact, as we show below, in the nonrotating adiabatic case the coefficients in the action are connected to both the irrotational and static versions of the Love numbers. Another difference to the gravitomagnetic case is that possible  $E_{\mu\nu}E^{\mu\nu}$ -terms in Eq. (5.62) are approximately negligible for the description of dynamical f-modes [191, 218].

## 5.4 Matching the coefficients

The relativistic effective action (5.58) for dynamical gravitomagnetic tides has an immediate connection to gravitational-wave observables. The action can be directly used in a post-Newtonian approximate calculation of the binary dynamics as in Refs. [111, 205–208] or included in the effective one body model [191, 219] to predict the effect of

these tidal interactions on the gravitational waves from a binary inspiral. This prediction generally depends on the coefficients in the effective action. Hence the constants  $C_{\dots}$  can be measured or constrained with gravitational-wave observations.

In order to link measurements to the nuclear physics of neutron stars, it is essential to theoretically calculate the coefficients in the action for relativistic neutron-star models. In this section, we use matching arguments to relate the constants  $C_{\dots}$  in Eq. (5.58) to the quadrupolar relativistic magnetic mode frequencies  $\omega_{2m}^B$  and the tidal deformabilities (Love numbers)  $\sigma_{\text{irr}}$  and  $\sigma_{\text{stat}}$ . Two distinct magnetic Love numbers have been defined in the literature for nonrotating neutron stars: negative irrotational ones  $\sigma_{\text{irr}} < 0$  [174] and positive static ones  $\sigma_{\text{static}} > 0$  [175], which differ by the boundary conditions imposed in the fluid. These can be computed numerically from linear perturbations of neutron stars, for  $\omega_{2m}^B$  see Refs. [164, 171–173, 220] and for  $\sigma_{\dots}$  see Refs. [174–177, 179].

Note that the matching of tidal coefficients is inherently difficult and the definition of Love numbers may even be considered ambiguous [221]. However, those ambiguities are expected to be comparable to rather small effects at 6PN order for magnetic tides (5PN order for electric tides). For the black-hole case, it is crucial to understand these subtleties since tidal effects, if nonzero, would be very small. Here, for neutron stars described by a perfect fluid equation of state, we can take a more heuristic approach to the matching as explained below. But when accounting for more realistic physics such as different classes of magnetic modes, more terms in the effective action become relevant and it is important to work out a more general and rigorous approach to the matching. This can be accomplished by matching the tidal parameters defined by coefficients in the effective action based on observables such as the binding energy, redshift, or scattering angle. We leave this for future work.

Finally, we note that quasi-universal relations, i.e., relations that are approximately independent of the nuclear equation of state, were studied for the magnetic Love numbers for neutron stars in Ref. [222]. The result was that these relations hold only to approximately 5% (10%) for irrotational (static) Love numbers; for irrotational Love numbers this was also found in recent follow-up work in Refs. [223–225]. This should be compared to the nearly sub-percent-level universality for the electric-type Love numbers [226], and opens interesting prospects for learning new information about the equation of state.

### 5.4.1 Matching the static Love number

We start by considering the case of no rotation  $\Omega^I = 0$  and a static fluid  $\dot{Q}_B^{IJ} = 0$ , and identify which coefficients can be fixed. The condition  $\dot{Q}_B^{IJ} = 0$  corresponds to a vanishing fluid velocity perturbation, which is the boundary condition leading to the static Love number  $\sigma_{\text{stat}}$  [176]. Furthermore, the Love numbers are defined in the adiabatic limit, meaning that one also neglects time derivatives of  $B_{IJ}$ . In this case, the flux quadrupole (5.57) and the action (5.55) reduce to

$$\mathcal{J}_{\text{stat}}^{IJ} \approx 3C_{B^2} B_{IJ}, \quad L_{\text{stat}}^B \approx C_{B^2} B_{IJ} B_{IJ}. \quad (5.63)$$

In general, the magnetic quadrupolar Love numbers  $\sigma \equiv \sigma_2$  can be defined either as the proportionality constant between the magnetic tidal field  $B_{IJ}$  and the flux quadrupole



moment  $S^{IJ}$ , or as a coefficient in the adiabatic tidal action,

$$\mathcal{J}^{IJ} = 2\sigma B^{IJ}, \quad \text{or} \quad L_{\text{ad}}^{\mathcal{B}} = \frac{2\sigma}{3} B_{\mu\nu} B^{\mu\nu}. \quad (5.64)$$

This definition holds for both the irrotational  $\sigma_{\text{irr}}$  and static  $\sigma_{\text{stat}}$  Love numbers. Since we consider a static fluid in this subsection, we identify  $\sigma$  with the static Love number  $\sigma_{\text{stat}}$  here. Comparing either definition in Eq. (5.64) with the above relations, we can match  $C_{B^2}$  as

$$C_{B^2} = \frac{2}{3} \sigma_{\text{stat}}. \quad (5.65)$$

### 5.4.2 Matching the irrotational Love number

The irrotational Love number  $\sigma_{\text{irr}}$  for a nonrotating fluid  $\Omega^I = 0$  can be obtained by keeping the time/frequency dependence general, here in particular of  $Q_B^{IJ}$ , and taking the adiabatic limit after arriving at a master equation for the perturbations [174, 179].

The equation of motion (5.56) for  $Q_B^{IJ}$  simply reads  $\ddot{Q}_B^{IJ} = \dot{B}_{IJ}/(4C_{\dot{Q}^2}^{\mathcal{B}})$  in the nonrotating case. Integrating this equation with respect to  $\tau$  and dropping the integration constant, which would lead to a permanent flux quadrupole, we obtain

$$\dot{Q}_B^{IJ} \approx \frac{B_{IJ}}{4C_{\dot{Q}^2}^{\mathcal{B}}}. \quad (5.66)$$

Inserting this into Eq. (5.57) or Eq. (5.55), taking the adiabatic limit by dropping time derivatives of  $B_{IJ}$ , and comparing to the definition of the Love number (5.64) leads to

$$\sigma_{\text{irr}} = \frac{3C_{B^2}}{2} - \frac{3}{32C_{\dot{Q}^2}^{\mathcal{B}}}. \quad (5.67)$$

To make the matching of the coefficients in the action more transparent, we split the Love number into its matter  $\sigma_M$  and field  $\sigma_F$  contributions (analogous to the post-Newtonian case in Ref. [166]),

$$\sigma_M \equiv \sigma_{\text{irr}} - \sigma_{\text{stat}} < 0, \quad \sigma_F \equiv \sigma_{\text{stat}} > 0. \quad (5.68)$$

These quantities are related to coefficients in the nonrotating action by

$$C_{\dot{Q}^2}^{\mathcal{B}} = -\frac{3}{32\sigma_M} > 0, \quad C_{B^2} = \frac{2\sigma_F}{3} > 0. \quad (5.69)$$

Indeed, we must have  $C_{\dot{Q}^2}^{\mathcal{B}} > 0$  for consistency since the energy of the modes must be bounded from below. To the leading post-Newtonian order, the static and irrotational Love numbers are approximately related by  $\sigma_{\text{stat}} \approx -3\sigma_{\text{irr}}$  [176], which implies that  $\sigma_F \approx -3\sigma_M/4$ . However, both Love numbers can be obtained numerically from full relativistic perturbations of neutron stars and there is no immediate need to resort to these approximations. Note that calculations based on the post-Newtonian theory for the mode amplitudes can be upgraded to a fully relativistic treatment of the interior by replacing



the coefficients in the action (5.38) by the relativistic values just identified. Comparing to Eq. (5.38), we hence find for the overlap integral  $I_B$  the relativistic expression

$$I_B^2 = -\frac{15}{4\pi}\sigma_M = \frac{15}{4\pi}(\sigma_{\text{stat}} - \sigma_{\text{irr}}). \quad (5.70)$$

Similarly, for the mode frequencies one should use relativistic results, which we discuss now.

### 5.4.3 Matching the mode frequency

To identify the mode frequencies we follow the method discussed in Sec. 5.2.4. For this purpose, we first express the corotating-frame equations of motion (5.56) of the mode amplitudes for an isolated neutron star at rest in the spherical-harmonic basis, using  $Q_B^{IJ} = N_2 \sum_m \mathcal{Y}_{IJ}^{2m} Q_m^B$ , where  $N_2 = \sqrt{8\pi/15}$ , and similarly for  $B_{IJ}$ . Assuming that the (constant) angular velocity is aligned with the z-axis  $\boldsymbol{\Omega} = (0, 0, \Omega)$ , the equations of motion (5.56) read

$$2C_{\dot{Q}^2}^B \ddot{Q}_m^B + im\Omega C_{\Omega Q \dot{Q}}^B \dot{Q}_m^B = \frac{1}{2}\dot{B}_m, \quad (5.71)$$

which follows from contracting the equations of motion with  $2N_2 \mathcal{Y}_{IJ}^{*2m}$  and using (A.2), (A.3). The reality conditions  $Q_B^{IJ} = Q_B^{*IJ}$  imply that  $Q_m^{B*} = (-1)^m Q_{-m}^B$  and similarly for  $B_m$ . We can determine the corotating-frame mode frequencies  $\omega_{2m}^B$  by making the ansatz  $Q_m = C e^{-i\omega_{2m}^B \tau}$  in the free ( $B_m = 0$ ) equations of motion, which leads to

$$\hat{\omega}_B \equiv \frac{\omega_{2m}^B}{m\Omega} = \frac{C_{\Omega Q \dot{Q}}^B}{2C_{\dot{Q}^2}^B} < 0, \quad (5.72)$$

and to the zero-mode  $\omega_{2m}^B = 0$ . We can thus match the coefficient  $C_{\Omega Q \dot{Q}}^B$  as

$$C_{\Omega Q \dot{Q}}^B = 2C_{\dot{Q}^2}^B \hat{\omega}_B = -\frac{3\hat{\omega}_B}{16\sigma_M} < 0. \quad (5.73)$$

This completes the matching of all coefficients in the simplified effective Lagrangian (5.58). We discuss in the next section how the matching of all coefficients in the Lagrangian in Eq. (5.55) could be achieved based on the tidal response function, as a foundation for future work on the matching in more complicated scenarios.

The relativistic frequencies  $\omega_{2m}^B$  were computed in Ref. [171] for polytropes and in Ref. [172] for nuclear physics-based equations of state. In the slow-rotation limit and for typical neutron-star compactnesses  $GM/(Rc^2) \lesssim 0.2$ , they may differ by up to 15% from the Newtonian estimate  $\hat{\omega}_B \approx -1/3$ , c.f., Eq. (5.25). The relativistic corrections introduce a dependence of the mode frequency on the equation of state. See Ref. [164] for a review of the magnitude and equation-of-state dependence of relativistic and higher-order rotational corrections. For superfluid stars, a second family of r-modes emerges, which has interesting consequences [173, 220]. Such a scenario can be described in our effective theory framework by introducing effective dynamical tidal variables  $Q_{B_n}^{IJ}$  and corresponding coefficients for each family of modes, where  $n$  labels the family of modes. We briefly elaborate on the matching in this scenario based on the response function below.

## 5.5 Tidal response and Love operator

The quadrupolar tidal response function, or quadrupole propagator on the worldline, was introduced for the description of dissipative tides in the effective-field-theory context in Refs. [190, 195]. For conservative electric dynamical tides, it was further explored numerically in Refs. [218, 227]. An extension of this work to magnetic tides and slow rotation would be valuable.

In this section, we derive the frequency-domain linear tidal response function from the relativistic effective action (5.55). We also discuss the response in three different limiting regimes: when the external frequency is smaller than the rotation frequency (pre-resonance), when they are comparable (near-resonance), and when the external frequency is larger than the rotation frequency (post-resonance). In the time domain, the response is encoded in a tensorial linear integral operator, which may be dubbed the Love operator.

### 5.5.1 The response function

It is most transparent to study the tidal response in spherical-harmonic basis and frequency domain. We hence further transform to the Fourier domain by using

$$Q_m^{\mathcal{B}}(\tau) = \int \frac{d\omega}{2\pi} \tilde{Q}_m^{\mathcal{B}}(\omega) e^{-i\omega\tau}, \quad (5.74)$$

and similarly for other tensors like  $B_m$ . Based on the transformed flux quadrupole  $\tilde{\mathcal{J}}_m$ , we define the linear tidal response function  $\tilde{F}_m^{\mathcal{B}}(\omega)$  of the neutron star in the corotating frame as a generalization of the Love number (5.64),

$$\tilde{\mathcal{J}}_m = 2\tilde{F}_m^{\mathcal{B}}\tilde{B}_m. \quad (5.75)$$

This response is the relativistic analog of the Love tensor from Ref. [167], see also Ref. [228] for the black-hole case. The flux quadrupole in the spherical-harmonic decomposition in the frequency domain  $\tilde{\mathcal{J}}_m$  can be obtained from Eq. (5.57),

$$\tilde{\mathcal{J}}_m = \frac{3}{4}i\omega\tilde{Q}_m^{\mathcal{B}} + 3\tilde{B}_m \sum_{k=0}^{\infty} (i\omega)^{2k} \left[ C_{BB(2k)} - \frac{m\omega\Omega}{2} C_{BB(2k+1)\Omega} \right]. \quad (5.76)$$

To obtain its explicit expression requires a solution for  $\tilde{Q}_m^{\mathcal{B}}$ , which we obtain by writing its equations of motion (5.71) in the frequency domain,

$$\frac{3}{16\sigma_M}\omega(\omega - m\Omega\hat{\omega}_{\mathcal{B}})\tilde{Q}_m^{\mathcal{B}} = -\frac{i\omega}{2}\tilde{B}_m. \quad (5.77)$$

Solving for  $\tilde{Q}_m^{\mathcal{B}}$  and using the above expression for  $\tilde{\mathcal{J}}_m$ , we arrive at the response function

$$\begin{aligned} \tilde{F}_m^{\mathcal{B}} &= \sigma_M \frac{\omega}{\omega - m\Omega\hat{\omega}_{\mathcal{B}}} + \frac{3}{2} \sum_{k=0}^{\infty} (i\omega)^{2k} \left( C_{BB(2k)} - \frac{m\omega\Omega}{2} C_{BB(2k+1)\Omega} \right) \\ &\approx \sigma_M \frac{\omega}{\omega - m\Omega\hat{\omega}_{\mathcal{B}}} + \sigma_F, \end{aligned}$$

where the last line refers to the simplified action (5.58). With this, the action can be written as

$$S_{\text{DT}}^{\mathcal{B}} \approx \int \frac{d\omega}{2\pi} \sum_{m=-2}^2 \frac{2}{3} \tilde{F}_m^{\mathcal{B}} \tilde{B}_m \tilde{B}_m^*. \quad (5.78)$$

Note that although we are working only to linear order in the spin, we do not expand the denominator in the response (5.78). The reason is similar to the textbook example of an anharmonic oscillator [229], where one perturbatively expands all terms at the level of the equations of motion yet leaves any denominators of the solution unexpanded. This is crucial in order to preserve essential features of the dynamics, i.e., poles at resonances. For the same reason, it is important to keep the shift symmetry (5.52) without expanding in spin, so that the zero-frequency mode is preserved.

The corotating-frame response function (5.78) can be extended to the case of several mode families by summing over the contributions from several  $Q_{\mathcal{B}n}^{IJ}$ ,

$$\tilde{F}_m^{\mathcal{B}} = \sum_n \sigma_{Mn} \frac{\omega}{\omega - m\Omega\hat{\omega}_{\mathcal{B}n}} + \frac{3}{2} \sum_{n=0}^{\infty} (i\omega)^{2n} \left( C_{BB^{(2n)}} - \frac{m\omega\Omega}{2} C_{BB^{(2n+1)}\Omega} \right), \quad (5.79)$$

where  $32\sigma_{Mn}C_{n\dot{Q}^2}^{\mathcal{B}} = -3$  and  $16\sigma_{Mn}C_{n\Omega Q\dot{Q}}^{\mathcal{B}} = -3\hat{\omega}_{\mathcal{B}n}$ . In the presence of more than one family of modes, and in order to fix all coefficients in Eq. (5.55), a more general matching procedure than outlined above is necessary. This could be accomplished through a numerical investigation of the magnetic tidal response  $\tilde{F}_m^{\mathcal{B}}$  based on relativistic linear perturbation theory, similar to the nonrotating electric case in Ref. [218]. A fit of such a numerical result for  $\tilde{F}_m^{\mathcal{B}}$  to Eq. (5.79) should in principle fix all the (linear, conservative) tidal coefficients: The behavior of the response around its poles fixes the number of mode families and their coefficients  $C_{n\dot{Q}^2}^{\mathcal{B}}$ ,  $C_{n\Omega Q\dot{Q}}^{\mathcal{B}}$ , while the global frequency dependence fixes the  $C_{BB^{(2k)}}$ ,  $C_{BB^{(2k+1)}\Omega}$ . Such a matching of the response could be further improved and made rigorous by basing it on gauge-invariant observables, as mentioned above.

### 5.5.2 Time-domain response and Love operator

Returning to the case of a single family of modes, we next show how to transform the response (5.78) back to the time-domain and bypass the problems encountered in Ref. [166]. For this purpose, we work in the symmetric tracefree basis and choose retarded boundary conditions by setting  $\omega \rightarrow \omega + i\epsilon$  with the limit  $\epsilon \rightarrow 0^+$  implied.<sup>5</sup> It is useful then to further shift the frequency by  $\omega \rightarrow \omega + m\Omega\hat{\omega}_{\mathcal{B}}$ , which introduces a phase  $e^{-im\Omega\hat{\omega}_{\mathcal{B}}\tau}$  from the Fourier transform. Now, in the spherical harmonic basis, that phase can be absorbed by a shift of the azimuthal angle  $\varphi$ , i.e., a rotation around the spin axis. After this chain of transformations, it is straightforward to perform the Fourier integral. However, one can follow a more direct approach, also based on using rotations to conveniently simplify expressions, which we delineate in more detail below.

<sup>5</sup>We note that the denominator describing the propagator is linear in  $\omega$  instead of quadratic, the latter being the more familiar case in field theory. This inhibits one to directly pick the Feynman prescription  $\omega^2 \rightarrow \omega^2 + i\epsilon$  for the propagator/boundary conditions here. Advanced boundary conditions correspond to  $\omega \rightarrow \omega - i\epsilon$ .

We start from the equations of motion (5.56) for  $Q_B^{IJ}$  and write them in terms of the matter contribution to the flux quadrupole  $\mathcal{J}_M^{IJ} \equiv -3Q_B^{IJ}/4$  as

$$\frac{1}{4\sigma_M} C_{Q^2}^B \left( \dot{\mathcal{J}}_M^{IJ} - 2\hat{\omega}_B \Omega^{K(I} \mathcal{J}_M^{J)K} \right) = \frac{1}{2} \dot{B}_{IJ}. \quad (5.80)$$

This can be simplified by performing a rotation around the spin axis with

$$\mathcal{J}_M^{IJ} = \bar{R}^I{}_K \bar{R}^J{}_L \bar{\mathcal{J}}_M^{KL}, \quad \bar{R} = \exp(-\hat{\omega}_B * \boldsymbol{\Omega} \tau). \quad (5.81)$$

We note the identity  $\bar{R}(\tau) = \exp(-\hat{\omega}_B * \boldsymbol{\Omega}^\top \tau)^\top = \bar{R}^\top(-\tau)$  since  $*\boldsymbol{\Omega}^\top = -*\boldsymbol{\Omega}$ , where  $^\top$  denotes the matrix transpose. Hence  $\bar{R}$  is indeed a rotation matrix,  $\bar{R}^{-1} = \bar{R}^\top$ . This rotation turns Eq. (5.80) into the simpler relation

$$\bar{R}^I{}_K \bar{R}^J{}_L \dot{\bar{\mathcal{J}}}_M^{KL} = 2\sigma_M \dot{B}_{IJ}, \quad (5.82)$$

where we recall our assumption that  $\boldsymbol{\Omega} = \text{const.}$  The retarded solution for  $\mathcal{J}_M^{IJ}$  is then given by

$$\mathcal{J}_M^{IJ}(\tau) = 2\sigma_M \bar{R}^I{}_K(\tau) \bar{R}^J{}_L(\tau) \times \int_{-\infty}^{\tau} d\tau' \bar{R}^A{}_K(\tau') \bar{R}^B{}_L(\tau') \frac{dB_{AB}(\tau')}{d\tau'}. \quad (5.83)$$

With this solution at hand, assuming that  $B_{AB}(-\infty) = 0$ , and noting that  $\bar{R}(\tau) \bar{R}^\top(\tau') = \bar{R}(\tau - \tau')$ , we can define a tensorial magnetic Love operator  $\hat{\sigma}_{\text{ret}}^{IJKL}$  such that

$$\mathcal{J}^{IJ} = 2\hat{\sigma}_{\text{ret}}^{IJKL} B_{KL} \equiv 2 \int_{-\infty}^{\infty} d\tau' F_{\text{B,ret}}^{IJKL}(\tau - \tau') B_{KL}(\tau'), \quad (5.84)$$

with the time-domain response given by

$$F_{\text{B,ret}}^{IJKL}(\tau) \approx \sigma_M \hat{\sigma}^{IJAB} \frac{d(\Theta(\tau) \bar{R}^A{}_K(\tau) \bar{R}^B{}_L(\tau))}{d\tau} + \sigma_F \hat{\sigma}^{IJKL} \delta(\tau). \quad (5.85)$$

Here,  $\Theta(\tau)$  is the Heaviside step function which implements the retarded boundary conditions, and the symmetric-tracefree projector is given by

$$\hat{\sigma}^{IJKL} = \delta^{I(K} \delta^{L)J} - \frac{1}{3} \delta^{IJ} \delta^{KL}. \quad (5.86)$$

This result (5.85) is specialized to the simplified action (5.58). For the more general action in (5.55), the retarded solution (5.83) continues to apply but with the response

$$\begin{aligned} F_{\text{B,ret}}^{IJKL}(\tau) &= \sigma_M \hat{\sigma}^{IJAB} \frac{d(\Theta(\tau) \bar{R}^A{}_K(\tau) \bar{R}^B{}_L(\tau))}{d\tau} + \frac{3}{2} \sum_{k=0}^{\infty} \left[ C_{BB(2k)} \hat{\sigma}^{IJKL} \partial_\tau^{2k} \delta(\tau) \right. \\ &\quad \left. + C_{BB(2k+1)\Omega} \hat{\sigma}^{IJA(K} \Omega^{L)A} \partial_\tau^{2k+1} \delta(\tau) \right]. \end{aligned} \quad (5.87)$$

Finally, we note that the action can be written as

$$S_{\text{DT}}^B = \int d\tau \frac{2}{3} B_{IJ} \hat{\sigma}^{IJKL} B_{KL} \quad (5.88)$$

$$= \int d\tau d\tau' \frac{2}{3} B_{IJ}(\tau) F_{\text{B}}^{IJKL}(\tau - \tau') B_{KL}(\tau'), \quad (5.89)$$

which is nonlocal in time. However, this action only encodes the time-symmetric part of the dynamics (the integrand can be symmetrized under  $\tau \leftrightarrow \tau'$ ) and does not correspond to retarded boundary conditions [213].

### 5.5.3 Asymptotic limits of the response function in the inertial frame

We next discuss the frequency-domain response for the simplified effective Lagrangian in Eq. (5.58) involving a single mode family in the inertial frame. The frequency in the inertial frame follows from that in the corotating frame via the relation

$$\tilde{\omega} = \omega + m\Omega. \quad (5.90)$$

Likewise, the inertial-frame mode frequency is  $\tilde{\omega}_{2m}^{\mathcal{B}} = \omega_{2m}^{\mathcal{B}} + m\Omega$ . The gravitomagnetic response can then be expressed as

$$\tilde{F}_m^{\mathcal{B}} \approx \sigma_M \frac{\tilde{\omega} - m\Omega}{\underbrace{\tilde{\omega} - (1 + \hat{\omega}_{\mathcal{B}})m\Omega}_{\tilde{\omega}_{2m}^{\mathcal{B}}}} + \sigma_F, \quad (5.91)$$

where  $\hat{\omega}_{\mathcal{B}}$  is defined in (5.72) and  $\sigma_{M,F}$  is defined in (5.68). We note that the adiabatic limit  $\tilde{\omega} \rightarrow 0$  and the nonrotating limit  $\Omega \rightarrow 0$  of the response do not commute [166]. Physically, this is not a problem since neither the neutron-star rotation frequency  $\Omega$  nor the frequency of the external tidal field  $\tilde{\omega}$  in a binary system is ever exactly zero. What matters is the relation between  $\tilde{\omega}$  and  $\Omega$ . Away from the mode resonances, the response behaves as

$$\tilde{F}_m^{\mathcal{B}} \approx \begin{cases} \frac{\sigma_M}{1 + \hat{\omega}_{\mathcal{B}}} + \sigma_F & \text{for } |\tilde{\omega}| \ll |\Omega|, m \neq 0, \\ \sigma_M + \sigma_F = \sigma_{\text{irr}} & \text{for } |\tilde{\omega}| \gg |\Omega| \text{ or } m = 0. \end{cases} \quad (5.92)$$

However, we note that a proper treatment of the post-resonance regime  $|\tilde{\omega}| \gg |\Omega|$  requires more care, in particular an analysis of the mode damping after resonant excitation.

## 5.6 Summary and discussion

Summarizing our findings, quadrupolar magnetic dynamical tides are approximately described by an effective action in the corotating frame given by

$$L_{\text{DT}}^{\mathcal{B}} \approx -\frac{3}{32\sigma_M} \left( \dot{Q}_{\mathcal{B}}^{IJ} \dot{Q}_{\mathcal{B}}^{IJ} + 2\hat{\omega}_{\mathcal{B}}\Omega^{JK} \dot{Q}_{\mathcal{B}}^{IJ} Q_{\mathcal{B}}^{KI} \right) - \frac{1}{2} B_{IJ} \dot{Q}_{\mathcal{B}}^{IJ} + \frac{2\sigma_F}{3} B_{IJ} B_{IJ}, \quad (5.93)$$

where

$$\sigma_M \equiv \sigma_{\text{irr}} - \sigma_{\text{stat}}, \quad \sigma_F \equiv \sigma_{\text{stat}}, \quad \hat{\omega}_{\mathcal{B}} \equiv \frac{\omega_{2m}^{\mathcal{B}}}{m\Omega}, \quad (5.94)$$

$\sigma_{\text{irr,stat}}$  are the irrotational and static relativistic magnetic tidal deformabilities and  $\omega_{2m}^{\mathcal{B}}$  are the relativistic mode frequencies. These frequencies  $\omega_{2m}^{\mathcal{B}}$  are linear in the magnetic spherical-harmonic number  $m$  and angular velocity  $\Omega$ . Hence  $\hat{\omega}_{\mathcal{B}}$  is indeed independent of  $m$  and  $\Omega$ . We stress that for this action, the matching of the coefficients does not assume a post-Newtonian or low-compactness approximation of the neutron-star interior. (In the low-compactness limit,  $\hat{\omega}_{\mathcal{B}} \approx -1/3$  and  $\sigma_F \approx -3\sigma_M/4$ .)

However, the above model may become insufficient for a realistic inclusion of the microphysics of the neutron star. For instance, the presence of superfluidity implies

several families of magnetic modes [173, 220, 230] and hence a more involved matching of the tidal parameters, as explained above. Yet these complications also open new prospects for extracting precious information on neutron-star structure from gravitational waves.

The response function in the corotating frame is

$$\tilde{F}_m^{\mathcal{B}} \approx \sigma_M \frac{\omega}{\omega - m\Omega\hat{\omega}_{\mathcal{B}}} + \sigma_F. \quad (5.95)$$

In the inertial frame, where the frequency is  $\omega + m\Omega$ , the limiting forms of the response for  $|\omega + m\Omega|/|\omega| \rightarrow 0, \infty$  (away from resonance) are

$$\tilde{F}_m^{\mathcal{B}} \approx \begin{cases} \frac{\sigma_{\text{irr}} + \hat{\omega}_{\mathcal{B}}\sigma_{\text{stat}}}{1 + \hat{\omega}_{\mathcal{B}}}, & |\tilde{\omega}| \ll |\Omega|, m \neq 0, \\ \sigma_{\text{irr}}, & |\tilde{\omega}| \gg |\Omega| \text{ or } m = 0. \end{cases} \quad (5.96)$$

The main effect of a resonance is a phase shift in the gravitational waves, see the seminal work of Ref. [38] for detailed calculations and Ref. [168] for data-analysis implications. This phase shift crucially depends on the overlap integral  $I_{\mathcal{B}}$ , which we are able to determine relativistically (for generic compactness) here,

$$I_{\mathcal{B}}^2 = -\frac{15}{4\pi}\sigma_M = \frac{15}{4\pi}(\sigma_{\text{stat}} - \sigma_{\text{irr}}). \quad (5.97)$$

In addition, using a convenient set of rotations to simplify the equations leads to a tensorial magnetic Love operator characterizing the time-domain response as defined by the relation between flux quadrupole and gravitomagnetic field

$$\mathcal{J}^{IJ} = 2\hat{\sigma}_{\text{ret}}^{IJKL} B_{KL} \equiv 2 \int_{-\infty}^{\infty} d\tau' F_{\mathcal{B},\text{ret}}^{IJKL}(\tau - \tau') B_{KL}(\tau'), \quad (5.98)$$

with the response given by

$$F_{\mathcal{B},\text{ret}}^{IJKL}(\tau) \approx \sigma_M \hat{\sigma}^{IJAB} \frac{d(\Theta(\tau) \bar{R}^A{}_K(\tau) \bar{R}^B{}_L(\tau))}{d\tau} + \sigma_F \hat{\sigma}^{IJKL} \delta(\tau). \quad (5.99)$$

It is interesting to consider the importance of the effects derived here for waveforms. The impact of the dynamical gravitomagnetic effects on the gravitational-wave phasing can be approximated as a sudden jump in the gravitational-wave phase  $\psi$  at the resonance as [38]

$$\psi^{\text{dyn. res.}} = \Theta(f - f_{\text{res}}) \left(1 - \frac{f}{f_{\text{res}}}\right) \Delta\Phi_{\text{res}}, \quad (5.100)$$

where  $f$  is the gravitational-wave frequency. The coefficient  $\Delta\Phi_{\text{res}}$ , which sets the size of the jump and depends on  $I_{\mathcal{B}}^2$  and  $\hat{\omega}_{\mathcal{B}}$  among other binary parameters, is given explicitly in Eqs. (5.37) in Ref. [38] (the derivation being based on a post-Newtonian star). The instantaneous effect of the resonance on the phase is small. However, it occurs early in the inspiral, at frequencies  $f_{\text{res}} \sim \tilde{\omega}_{2m}^{\mathcal{B}}/(m\pi)$  proportional to the spin frequencies  $\Omega$ . This implies that resonances can occur over a wide range of gravitational-wave frequencies from below 10 Hz to a few hundred hertz. The information about these effects thus accumulates over numerous gravitational-wave cycles. As an order-of-magnitude estimate,

the net change in the gravitational-wave phase scales as  $\Delta\psi \sim 0.05R^4\Omega^{2/3}$  for equal masses [38]. Measuring these signatures from gravitomagnetic mode resonances is thus an important scientific opportunity with third-generation detectors such as the Einstein Telescope and Cosmic Explorer, and must be taken into account to avoid biases in the measured parameters [168]. For loud signals, these modes could also have an impact for measurements with current detectors as they further improve in their sensitivity to binary inspirals.

The general form of the resonance effects on gravitational waves (5.100) applies for any kind of tidal resonance that occurs early during the inspiral, both gravitoelectric and gravitomagnetic. The kinds of tides are encoded in the coefficient  $\Delta\Phi$ . These dynamical resonance effects on the phase (5.100) are approximated by a step function in frequency and are hence very different from smooth-in- $f$  post-Newtonian contributions. In general, matter effects in binary systems are described by distinct perturbative expansions from the post-Newtonian one (e.g., the multipole expansion), with dimensionless parameters characterizing finite size effects as outlined in our discussion on the effective action and power counting in Sec. 5.3.5. For simplicity, assigning fiducial post-Newtonian orders to all physical effects is nevertheless often used to describe terms in the phasing with different powers of  $f$ , though formally this applies only to black holes. For instance, when considering tidal effects specialized to the adiabatic limit, the Fourier-domain phasing has the expansion

$$\psi^{\text{adiabatic}} = \frac{3}{128\eta x^{5/2}} \left[ 1 + a_{\text{1PN}}x + O(x^{3/2}) - \frac{39}{2}\tilde{\Lambda}x^5 + (\delta\Lambda + \tilde{\Sigma})x^6 + \dots \right], \quad (5.101)$$

where  $x = [\pi f(m_1 + m_2)]^{2/3}$  is a dimensionless frequency parameter,  $\tilde{\Lambda}$  and  $\delta\Lambda$  are dimensionless combinations of the individual gravitoelectric Love numbers  $\lambda_{1,2}$  and the masses  $m_{1,2}$  of the binary (characterizing adiabatic gravitoelectric tidal effects), and  $\tilde{\Sigma}$  is a similar weighted average of the gravitomagnetic Love numbers  $\sigma_{1,2}$ . Effective post-Newtonian orders are attributed to each contribution according to the powers of  $x$  involved, e.g., the leading-order gravitoelectric effects scale effectively as 5PN terms would, and magnetic effects start at effectively 6PN in this scheme. The coefficients  $\Lambda$  and  $\Sigma$  differ by nearly two orders of magnitude, i.e., the adiabatic magnetic effect is much smaller than even the subleading gravitoelectric effect.

However, the dynamical resonance effects induce nearly sudden changes at a particular frequency, as in Eq. (5.100), and do not fit even the fiducial post-Newtonian counting scheme of the adiabatic effects. They are a distinct phenomenon that can lead to a significantly larger imprint on the gravitational waves than suggested by the adiabatic limit. Thus, even though the contributions from *adiabatic* gravitomagnetic effects (5.101) are very small, the *dynamical* effects (5.100) can be much more significant: Reference [168] demonstrates that including such dynamical effects in waveform models (and using quasi-universal relations) could improve constraints on certain tidal parameters by about two orders of magnitude for third-generation detectors. Furthermore, these gravitomagnetic resonances are not resolvable in numerical-relativity simulations of binary systems due to the length and timescales involved. This makes accurate *analytical* modeling of these effects critically important. The analytical results depend on strong-field effects and the microphysics of the neutron stars in parametrized form through the overlap integral and



the resonance frequency. This makes them broadly applicable to any type of compact object, and useful for tests of exotic objects, black holes, and gravity.

## 5.7 Conclusions

The observation of gravitational waves from binary neutron stars opens up exciting opportunities for exploring matter at supra-nuclear density in their interiors. This requires understanding how the nuclear physics of neutron-star matter translates into tidal effects during the long inspiral phase of the binary, which constitutes a substantial part of the observed gravitational-wave signal. In this chapter, we made important progress on this topic by investigating how relativistic gravitomagnetic tides of neutron stars can be modeled with an effective action, both in the highly dynamical regime close to oscillation-mode resonances and away from resonance.

To gain intuition, we started from the 1PN description of a slowly rotating isolated neutron star, composed of an idealized fluid, in the presence of a gravitomagnetic tidal field. We derived a Lagrangian formulation of the linearized perturbations to the Euler equations for the fluid displacement. We used this Lagrangian to calculate the gravitomagnetic mode frequencies and to develop an effective action for composite degrees of freedom characterizing the gravitomagnetic interactions of the star. A crucial finding was a symmetry of the action under shifts of the dynamical mode degrees of freedom.

The major result of this chapter is the fully relativistic effective action for gravitomagnetic tidal effects for slowly rotating neutron stars that we developed. We started from symmetry principles to construct the terms in the action, where the shift symmetry played an essential role. Each of these interaction terms comes with undetermined coefficients that encode the neutron-star structure. We demonstrated how the most important coefficients in the action match to the magnetic Love numbers and mode frequencies of the neutron star, showing that both kinds of magnetic Love numbers have physical relevance. We provide a relativistic expression for the overlap integral in terms of the Love numbers that may be used to improve estimates for the gravitational-wave phase shift when a neutron-star binary inspirals through magnetic-mode resonances. We also discussed several interesting dynamical consequences and unusual features compared to the gravitoelectric case, including the frequency-domain response function and time-domain Love operator.

An important goal for future work is to construct waveform models for gravitational waves from binary inspirals based on our effective action. The tidal coefficients in the action directly characterize the potentially measurable parameters in gravitational waves. These coefficients are related to the magnetic Love numbers and mode frequencies, which contain valuable information to better understand the extreme states of matter inside neutron stars. Another target for future work is to formulate the matching in terms of the tidal response function, which would allow a generalization to more realistic microphysics, e.g., the inclusion of several mode families in the presence of a superfluid.





# Effect of dynamical gravitomagnetic tides on measurability of tidal parameters for binary neutron stars using gravitational waves

## 6.1 Introduction

During a binary inspiral, the GW signatures of the properties of matter in NSs are due to spin and tidal effects. Tidal effects encompass various phenomena associated with the resonant or non-resonant excitation of characteristic oscillation modes of the NS, whose properties in turn depend on the properties of dense subatomic matter. The modes are driven by the tidal fields of the companion, which vary in time due to the orbital motion and can be decomposed into gravitoelectric and *-magnetic* fields depending on their parity properties. The former are involved in the dominant tidal effects due to the fundamental modes of the NS, which have the strongest tidal couplings and relatively high resonance frequencies that leave their excitation non-resonant for most of a quasi-circular inspiral [34, 191, 231]. By contrast, gravitomagnetic tidal fields associated with relativistic frame-dragging effects lead to the excitation of inertial modes of NSs whose frequencies are proportional to the spin [41, 164, 171–173] and will thus invariably pass through resonances in binary inspirals. The resonant energy and angular momentum transfer between the modes, orbit, and GWs leads to comparatively sudden changes in the GW frequency evolution, thus contributing a small but distinctive feature to the signals.

There has been much previous work on gravitomagnetic modes of NSs, which are associated with the Coriolis effect and include inertial modes such as the ‘r-modes’ [158–161]. Racine and Flanagan [38] computed the direct effects of the resonance on the dynamics and developed an effective waveform model for the resulting GW imprints. This model was recently revisited to assess the impact for measuring tidal deformabilities with next-generation detectors [165, 166, 168]; see [232] for use of the model for other classes of modes and [233] for studies of inertial modes in postmerger GWs. Studies have also modeled and examined the effect of nonresonant gravitomagnetic tides on the inferred tidal deformability [234], and included them in an effective one body model [235]. However, the conclusions were limited due to an interesting feature of the response of a

NS's matter and spacetime to a gravitomagnetic tidal perturbation, which leads to two possible kinds gravitomagnetic tidal deformabilities depending on the assumptions on the state of the perturbed fluid [174–179]. As we saw in the previous chapter, It turns out that the significance of these two tidal deformabilities is that both are relevant but in different ways for the asymptotic limits of the response before and after a gravitomagnetic mode resonance.

In this chapter, we first derive an explicit expression for the effective gravitomagnetic response function characterizing the ratio of the induced current quadrupole moment to the gravitoelectric tidal field in the context of a binary system at large separation with arbitrary spin orientations and low spin magnitudes. The asymptotic limits of this response before and after resonance yield the relevant combinations of the gravitomagnetic tidal deformabilities in the different regimes. A new aspect in this chapter is that we include these effects together with the direct resonance-induced changes in the GWs from [38, 168]. A further difference compared to this previous work is that we map all EoS-dependent parameters that appear in the resonance expressions and were thus far only considered for Newtonian descriptions of NSs to their fully relativistic counterparts, which we employ for further studies of the impact of gravitomagnetic tides on parameter estimation. In general, multiple quadrupolar gravitomagnetic modes with azimuthal number  $|m| = 1, 2$  are resonantly excited in an inspiral, however, certain spin orientations mainly favor the excitation of only one of them, which can be exploited to simplify an initial exploratory study [38]. We also make use of previous findings that for NSs, the equation of state information contained in gravitomagnetic Love numbers can be approximately related to the main tidal deformability  $\Lambda$ , which reduces the number of signal parameters [234, 236]. Furthermore, as the full parameter estimation in the entire parameter space for binary NS signals in third-generation detectors is prohibitive and the largest constraints will come from events with a high signal-to-noise ratio, we use restricted Fisher matrix computations as a proxy for the statistical errors. While all of these assumptions are restrictive, the aim of our work is to scope out the importance of gravitomagnetic modes on GW measurements with third-generation detectors using a more realistic model of these effects than in previous such studies. We first estimate the plausible changes in the width of the posterior distributions when using full Markov Chain Monte Carlo (MCMC) pipelines versus the Fisher matrix, perform a number of sanity checks on the results, and compare with previous work. We then study the impact of different mode resonances as well as the asymptotic adiabatic contributions on the accuracy with which tidal deformability can be measured in a few different case studies, and the biases incurred when neglecting the gravitomagnetic effects.

The chapter is organized as follows. In Sec. 6.2 we obtain the effective Love number, discuss its features, and the description of gravitomagnetic tidal effects far from resonance. In Sec. 6.3 we incorporate these results into a frequency-domain waveform model. We discuss the results in Sec. 6.4 obtained using data analysis framework Sec. 2.3, Sec. 6.6 contains our conclusions and outlook.

## 6.2 Effective Gravitomagnetic Love number

In this section, we review the identification of an effective magnetic Love number based on a fully relativistic formalism for slowly rotating bodies that we worked out in the previous chapter and calculate an explicit expression for the case of the leading-order gravitomagnetic tidal fields in a binary system. We also derive the adiabatic limits of these results for arbitrary spin orientations using an orbit-averaging procedure. Our results are based on considerations to linear order in the spins and focus on the quadrupole which is expected to give the largest effect. As in chapter 5, the entire framework we use is adapted to approximations based on the hierarchy of length- and timescales during the early part of a binary inspiral.

### 6.2.1 Definition of gravitomagnetic Love numbers

A NS immersed in an external gravitomagnetic tidal field  $B_{IJ}$  will develop an induced flux quadrupole moment  $\mathcal{J}_{IJ}$ . The gravitomagnetic quadrupolar Love number, which we denote by  $\sigma$ , is defined as the ratio

$$\sigma = \frac{1}{2} \frac{\mathcal{J}^{IJ}}{B^{IJ}}. \quad (6.1a)$$

Alternatively,  $\sigma$  can be identified as the coupling coefficient in the Lagrangian (5.64) describing gravitomagnetic tides in the adiabatic limit according to the conventions

$$L_{\text{ad}}^{\mathcal{B}} = \frac{2\sigma}{3} B_{IJ} B^{IJ}. \quad (6.1b)$$

Calculations of magnetic Love numbers based on relativistic perturbations of a NS revealed that magnetic quadrupolar Love numbers  $\sigma$  can be of two types, depending on assumptions on the perturbed fluid inside the non-rotating neutron star [174–179]. Restricting the fluid to remain static under perturbations leads to the static Love number  $\sigma_{\text{stat}}$ , while allowing it to be irrotational yields a different result  $\sigma_{\text{irrot}}$ . As discussed in chapter 5 and detailed below, both Love numbers are relevant for characterizing the gravitomagnetic tidal response of a NS asymptotically far from a mode resonance.

### Effective frequency-dependent Love number

When going beyond the restriction to adiabatic limits, the tidal deformability generalizes to an effective frequency-dependent response function. Its particular form is given by considering the dynamics of the matter contributions to the flux quadrupole moment  $Q_B^{IJ}$  described by the Lagrangian given in Eq. (5.58) as

$$L^{\mathcal{B}} \approx -\frac{3}{32(\sigma_{\text{irrot}} - \sigma_{\text{stat}})} \left[ \dot{Q}_B^{IJ} \dot{Q}_B^{IJ} - 2\hat{\omega}^{\mathcal{B}} \Omega^{JK} \dot{Q}_B^{IJ} Q_B^{KI} \right] - \frac{1}{2} B_{IJ} \dot{Q}_B^{IJ} + \frac{2\sigma_{\text{stat}}}{3} B_{IJ} B_{IJ}. \quad (6.2)$$

Here, overdots denote proper time derivatives and the tensor  $\Omega_{IJ}$  is related to the NS's spin frequency  $\Omega$  by

$$\Omega_{IJ} = \epsilon_{IJK} \Omega^K, \quad (6.3)$$

where  $\epsilon_{IJK}$  is the Levi-Civita permutation tensor. The dimensionless frequency quantity  $\hat{\omega}_B$  is given in terms of the quadrupolar gravitomagnetic mode frequencies in the co-rotating frame  $\omega_{2m}^B$ , where  $l = 2$  denotes the quadrupolar modes and  $m$  the azimuthal mode number, by

$$\hat{\omega}^B = \frac{\omega_{2m}^B}{m\Omega}. \quad (6.4)$$

In the Newtonian limit, the mode frequencies  $\omega_{2m}^B$  reduce to  $\omega_{2m}^{\text{Newt}} = -m\Omega/3$  in this frame, making (6.4) independent of  $m$ .

To obtain an effective adiabatic Lagrangian in the form of (6.1) we integrate the first term in (6.2) by parts and neglect the total time derivative. We then eliminate the acceleration  $\ddot{Q}_B^{IJ}$  by using the oscillator equations of motion

$$\ddot{Q}_B^{IJ} - 2\hat{\omega}^B \Omega^{K(I} \dot{Q}_B^{J)K} = \frac{8}{3}(\sigma_{\text{irrot}} - \sigma_{\text{stat}})\dot{B}_{IJ}. \quad (6.5)$$

Substituting these equations of motion (6.5) for  $\ddot{Q}_B^{IJ}$  into the Lagrangian and omitting total derivatives leads to

$$\bar{L}^B \approx -\frac{1}{4}B_{IJ}\dot{Q}_B^{IJ} + \frac{2\sigma_{\text{stat}}}{3}B_{IJ}B_{IJ}, \quad (6.6)$$

which is only valid for configurations of the system that satisfy the equations of motion (6.5).

We identify the effective response function by requiring that the Lagrangian (6.6) take the form of the adiabatic Lagrangian (6.1) with  $\sigma$  replaced by an effective Love number

$$\bar{L}^B \stackrel{!}{=} \frac{2\sigma_{\text{eff}}}{3}B_{IJ}B_{IJ}. \quad (6.7)$$

Omitting total derivatives, this leads to the identification of an instantaneous (inst) effective Love number

$$\sigma_{\text{eff}}^{\text{inst}} = \frac{-\frac{3}{8}B_{IJ}\dot{Q}_B^{IJ} + \sigma_{\text{stat}}B_{IJ}B_{IJ}}{B_{KL}B_{KL}}. \quad (6.8)$$

This result for an effective Love number still has undesirable features, for instance, it varies over an orbit and the definition is not unique due to the different ways of assigning the time derivatives up to total derivative terms. For example, the first term in the numerator of (6.8) could equivalently be written as  $3\dot{B}_{IJ}Q_B^{IJ}/8$ . These subtleties disappear when we impose that the above definitions hold only at the level of the orbit-averaged Lagrangians. Denoting the orbit-average by angular brackets, we define the effective Love number by

$$\sigma_{\text{eff}} = \sigma_{\text{stat}} - \frac{3}{8} \frac{\langle B_{IJ}\dot{Q}_B^{IJ} \rangle}{\langle B_{IJ}B_{IJ} \rangle}, \quad (6.9)$$

with  $\dot{Q}_B^{IJ}$  a solution to the equations of motion (6.5). The above definition of the effective Love number (6.9) becomes more transparent when expressed in terms of the flux quadrupole defined in (6.1) which, as discussed in [237], is given by  $\mathcal{J}^{IJ} = 2\sigma_{\text{stat}}B_{IJ} - 3\dot{Q}_B^{IJ}/4$ . With this,

$$\sigma_{\text{eff}} = \frac{1}{2} \frac{\langle B_{IJ}\mathcal{J}^{IJ} \rangle}{\langle B_{IJ}B_{IJ} \rangle}, \quad (6.10)$$

which is directly analogous to the definition in the gravitoelectric case.

### 6.2.2 Application to a binary system

To obtain an explicit expression for the effective Love number requires specifying the relevant tidal field  $B_{IJ}$ . Here, we consider a binary system composed of the NS with mass  $m_1$  and a point-mass companion  $m_2$  at large orbital separation. We work in the center of mass frame of the NS and introduce a coordinate system in which the position of the center of mass of the companion is  $\mathbf{z}(t)$  and its velocity is  $\dot{\mathbf{z}}(t)$ . The gravitomagnetic tidal field  $B_{ij}$  due to the companion is then given to the leading post-Newtonian order by [38]

$$B_{ij} = \frac{6m_2}{r^5} z_{(i} \epsilon_{j)kl} z_k \dot{z}_l \quad (6.11)$$

where  $r$  is the relative separation and we use lower-case Latin indices for the spatial components of tensors in this frame.

We further specialize to quasi-circular orbits of constant radius  $\dot{r} = \ddot{r} = 0$  and parameterize the orbit using two angles: the azimuthal orbital phase  $\phi$  and the inclination angle  $\psi$  of the spin axis of the NS relative to the orbital angular momentum such that the position vector becomes

$$\mathbf{z}(t) = r(\cos \psi \cos \phi(t), \sin \phi(t), \sin \psi \cos \phi(t)). \quad (6.12)$$

The spin inclination angle  $\psi$  is often approximated as constant because its change is very small [168, 238]. The transformation of (6.11) from the NS's center of mass frame to the co-rotating frame is given by

$$B_{IJ} = R_I^i R_J^j B_{ij}, \quad (6.13)$$

where  $R_I^i$  are rotation matrices. We assume that the NS's spin is along the  $z$ -axis in the co-rotating frame such that  $\boldsymbol{\Omega} = (0, 0, \Omega)$  and  $R_1^1 = R_2^2 = \cos(\Omega t)$ ,  $R_1^2 = \sin(\Omega t) = -R_2^1$ ,  $R_3^3 = 1$  with all other components vanishing. The body label 1 on  $\Omega$  is implied here. To reduce (6.9) to a function of the orbital parameters also requires the steady-state solution of the oscillator equations of motion (6.5). This is most conveniently calculated in a spherical-harmonic basis, using that

$$Q_B^{IJ} = N_2 \sum_m \mathcal{Y}_{IJ}^{2m} Q_m^B, \quad (6.14)$$

where  $N_2 = \sqrt{8\pi/15}$  and  $\mathcal{Y}_{IJ}^{2m}$  are symmetric-trace-free tensors whose components are complex numbers [239]. We use a similar decomposition as (6.14) for  $B_{IJ}$ . The equations of motion (6.5) can then be expressed as

$$\ddot{Q}_m^B + im\Omega \hat{\omega}^B \dot{Q}_m^B = -\frac{8}{3}(\sigma_{\text{irrot}} - \sigma_{\text{stat}}) \dot{B}_m, \quad (6.15)$$

In order to solve (6.15) for the case of interest here, we extract from (6.11), (6.13) and (6.12) the spherical harmonic components

$$B_m = N_2 \mathcal{Y}_{IJ}^{*2m} B_{IJ}, \quad (6.16)$$

where the asterisk denotes complex conjugation. For circular orbits, these coefficients are given by

$$2B_2 e^{-2i\Omega t} = \bar{B}(2i \sin \psi \sin \phi - \sin 2\psi \cos \phi) \quad (6.17a)$$

$$B_1 e^{-i\Omega t} = \bar{B}(i \cos \psi \sin \phi - \cos 2\psi \cos \phi) \quad (6.17b)$$

$$B_0 = \bar{B} \sqrt{3/2} \cos \phi \sin 2\psi, \quad (6.17c)$$

with

$$\bar{\mathcal{B}} = \frac{3m_2\omega}{r^2}, \quad \omega = \dot{\phi}. \quad (6.17d)$$

The results for negative  $m$  are obtained from the relation

$$B_{-m} = (-1)^m B_m^*. \quad (6.18)$$

Using these forcing terms in the equations of motion (6.15) and solving for steady state solutions for  $Q_m^{\mathcal{B}}$  leads to

$$Q_2 e^{-2i\Omega t} = \frac{8\bar{\mathcal{B}}(\sigma_{\text{irrot}} - \sigma_{\text{stat}})}{3D_2} [i\mathcal{A}_{2,s}c_\phi + C_{2,s}s_\phi], \quad (6.19a)$$

$$Q_1 e^{-i\Omega t} = \frac{8\bar{\mathcal{B}}(\sigma_{\text{irrot}} - \sigma_{\text{stat}})}{3D_1} [i\mathcal{A}_{1,c}c_\phi + C_{1,c}s_\phi] \quad (6.19b)$$

$$Q_0 = -4\sqrt{6}\frac{m_2(\sigma_{\text{irrot}} - \sigma_{\text{stat}})}{r^2} \sin 2\psi \sin \phi, \quad (6.19c)$$

where  $c_\phi = \cos(\phi)$ ,  $s_\phi = \sin(\phi)$  and

$$\mathcal{A}_{m,s} = \omega \sin \psi + (1 + \hat{\omega}^{\mathcal{B}})\Omega \sin 2\psi \quad (6.19d)$$

$$C_{m,s} = m\Omega(1 + \hat{\omega}^{\mathcal{B}}) \sin \psi + \frac{\omega}{m} \sin 2\psi, \quad (6.19e)$$

with the corresponding quantities with subscripts  $c$  obtained by replacing 'sin' by 'cos' in the above expressions. The denominators in (6.19) are given by

$$D_m = [\omega - m\Omega(1 + \hat{\omega}^{\mathcal{B}})] [\omega + m\Omega(1 + \hat{\omega}^{\mathcal{B}})]. \quad (6.19f)$$

The final step is to use these results to obtain the effective Love number. The relevant tensor contractions entering (6.9) are given by

$$B_{IJ}B^{IJ} = 2\bar{\mathcal{B}}^2, \quad \dot{Q}_{IJ}B^{IJ} = \sum_{m=-2}^2 \dot{Q}_m B_{-m}. \quad (6.20)$$

Using (6.20) in (6.9) leads to the instantaneous effective Love number. Performing an orbit-average for the case considered here amounts to

$$\sigma_{\text{eff}} = \sigma_{\text{stat}} - \frac{3}{16\bar{\mathcal{B}}^2} \frac{\omega}{2\pi} \int_0^{2\pi/\omega} \sum_{m=-2}^2 \dot{Q}_m B_{-m} dt. \quad (6.21)$$

Substituting (6.19) and (6.17a) into (6.21) leads to the final result for the effective Love number for one of the bodies

$$\begin{aligned} \sigma_{\text{eff}} = \sigma_{\text{stat}} &+ \frac{3(\sigma_{\text{irrot}} - \sigma_{\text{stat}})}{8} (\sin 2\psi)^2 + \frac{(\sigma_{\text{irrot}} - \sigma_{\text{stat}})}{2D_1} \left\{ \omega\Omega\hat{\omega}^{\mathcal{B}} (\cos \psi + \cos 3\psi) \right. \\ &+ \left. [\omega^2 - \Omega^2(1 + \hat{\omega}^{\mathcal{B}})] (1 + \cos \psi \cos 3\psi) \right\} \\ &+ \frac{(\sigma_{\text{irrot}} - \sigma_{\text{stat}})(\sin \psi)^2}{4D_2} [8\omega\Omega\hat{\omega}^{\mathcal{B}} \cos \psi + (\omega^2 - 4\Omega^2(1 + \hat{\omega}^{\mathcal{B}})) (3 + \cos 2\psi)]. \end{aligned} \quad (6.22)$$

In a binary system of two NSs, one must add the same contribution but with the parameters of the companion body.

### 6.2.3 Features of the effective response

#### Effects of the spin orientation

The poles of the response (6.22), i.e. where one of the factors in the denominators given in (6.19f) vanishes, correspond to the four different mode resonances for the  $m \neq 0$  modes. For special cases of the spin inclination angle only a subset of the modes contributes to  $\sigma_{\text{eff}}$ , as also evident from (6.19). For example, for aligned spin corresponding to  $\psi = 0$  the response (6.22) reduces to

$$\sigma_{\text{eff}}|_{\psi=0} = \sigma_{\text{stat}} + \frac{(\sigma_{\text{irrot}} - \sigma_{\text{stat}})(\omega - \Omega)}{\omega - \Omega(1 + \hat{\omega}^{\mathcal{B}})} \quad (6.23)$$

This shows that for aligned spins, and within our approximations, the only pole in the response is  $\omega \rightarrow \Omega(1 + \hat{\omega}^{\mathcal{B}})$  which corresponds to the  $m = 1$  resonance frequency.

Another special case is a spin inclination of  $\psi = \pi/3$ , where the contribution from the  $|m| = 1$  modes is non-resonant. This can be seen either from (6.19), by noticing that the numerator in  $Q_1$  for this special value of  $\psi$  will involve factors of  $\omega - \Omega(1 + \hat{\omega}^{\mathcal{B}})$  which cancel the divergent term in the denominator, or by considering the third term in (6.22) showing the same effect.

#### Adiabatic limits

Above, we have computed the response assuming a fixed orbit, obtaining divergences in the response at the resonances. However, in a binary inspiral, the continued GW dissipation causes the system to evolve through the resonance, exciting the mode amplitudes only to a finite maximum value. This effect was already examined in detail in [38], who also developed an effective waveform model for these resonance-induced effects. A missing phenomenon from these and subsequent studies were the additional adiabatic effects due to the behavior of the modes far from the resonances. To compute the relevant NS parameters characterizing the adiabatic response, we consider the asymptotic limits of  $\sigma_{\text{eff}}$  long before or after a resonance. The subtleties with extracting the relevant limits were discussed in detail in [237], as the appropriate ordering of limits between  $\omega, \Omega \rightarrow 0$  is delicate and depends on the situation. In particular, the relevant adiabatic limit before the mode resonance is obtained by considering  $\omega \rightarrow 0$  in (6.22), while the post-resonance adiabatic limit is given by taking the limit  $\Omega \rightarrow 0$  first. This leads to the asymptotic expressions pre- and post-resonance respectively

$$\sigma^{\text{asym}} = \begin{cases} \sigma_{\text{stat}} + \frac{(\sigma_{\text{irrot}} - \sigma_{\text{stat}})[8 + 3\hat{\omega}_{\mathcal{B}} \sin(2\psi)^2]}{8(1 + \hat{\omega}_{\mathcal{B}})} \\ \sigma_{\text{irrot}} \end{cases}. \quad (6.24)$$

We will use the above insights into the features of the response to assemble an approximate waveform model that properly accounts for both resonance and adiabatic effects.



## 6.3 Effective waveform model with adiabatic and resonance effects

### Approximate waveform model

Computing the impact of gravitomagnetic tidal effects on the GW signals from inspiraling NS binary systems is a complicated task. Here, we bypass these challenges by assembling a simple effective model for the gravitomagnetic imprints in frequency-domain descriptions of the GW signals based on adapting existing results using the insights developed in the previous section. Such a model is very useful for scoping out the features, magnitude, and consequences of the various gravitomagnetic effects in future GW measurements, and for identifying focus areas for more detailed modeling. In addition to the gravitomagnetic effects, we also include the dominant adiabatic gravitoelectric tidal effects to understand the impacts on the overall information on NS matter.

Specifically, we write the GW phasing in the frequency domain as

$$\Psi = 2\pi f t_c - \phi_c + \Psi_{\text{pm}} + \Psi_{\text{ad}}^{\text{tidal}} + \Psi_{\text{res}}^{\text{tidal}}, \quad (6.25a)$$

where  $t_c$ , and  $\phi_c$  are the reference time and phase and  $f$  is the GW frequency. The term  $\Psi_{\text{pm}}$  is the point-mass contribution, for which we use the post-Newtonian TaylorF2 results given in Eq. (1.92) of Sec. 1.6.2. For the adiabatic tidal contributions  $\Psi_{\text{ad}}^{\text{tidal}}$  we use Eq. (3.22) and the results of [110, 111, 206, 234, 236] given by

$$\begin{aligned} \Psi_{\text{ad}}^{\text{tidal}} = & -b_0 \tilde{\Lambda} f^{5/3} + \left( -b_1 \tilde{\Lambda} + b_2 \delta \tilde{\Lambda} + b_3 \tilde{\Sigma} \right) f^{7/3} \\ & -b_5 \hat{\Sigma}(\chi_1, \chi_2) f^{8/3} + f_2 f^{8/3} + f_3 f^3 + f_4 f^{10/3}, \end{aligned} \quad (6.25b)$$

and take the resonance-induced effects from [38, 168] in the form

$$\Psi_{\text{res}}^{\text{tidal}} = - \sum_{i=1,2} \left( 1 - \frac{f}{f_i^{\text{res}}} \right) |\Delta \Phi_i| \Theta(f - f_i^{\text{res}}). \quad (6.25c)$$

We note that the signs of all the contributions made explicit here correspond to those relevant for the parameter choices for the case studies discussed in Sec. 6.4 below, with all the tidal parameters  $\tilde{\Lambda}, \delta \tilde{\Lambda}, \tilde{\Sigma}, \hat{\Sigma}$  defined below being positive. We also see that the resonance contribution is a distinct sudden change in the phase and time of the GW signal at the resonance, whose scaling with the frequency is degenerate with that of the gauge parameters  $\phi_c$  and  $t_c$  in the phasing (6.25a). The various coefficients in (6.25b) are given by

$$b_0 = \frac{117(\pi M)^{5/3}}{256\nu}, \quad b_1 = \frac{9345(\pi M)^{7/3}}{8192\nu} \quad (6.26)$$

$$b_2 = \frac{19785(\pi M)^{7/3}}{46592\nu} \sqrt{1 - 4\nu} \quad (6.27)$$

$$b_3 = \frac{3(\pi M)^{7/3}}{128\nu} = b_4/(\pi M)^{1/3}, \quad (6.28)$$

with  $M = m_1 + m_2$  the total mass and  $\nu = m_1 m_2 / M^2$ . The functions  $f_j$  depend on  $\tilde{\Lambda}, \delta \tilde{\Lambda}$ , and for  $f_2$  additionally on the spins  $\chi_{1,2}$ . In particular, the expression for the function  $f_2$

in (6.25b) is obtained from Eqs. (7) and (9) of [225] and those for  $f_3, f_4$  from Eq. (6.6b) of [111]. The parameters  $\tilde{\Lambda}$  and  $\delta\tilde{\Lambda}$  characterizing the gravitoelectric effects are given by

$$\tilde{\Lambda} = \frac{16}{13} \left( \frac{12}{X_1} - 11 \right) X_1^5 \Lambda_1 + (1 \leftrightarrow 2), \quad (6.29)$$

$$\begin{aligned} 2\delta\tilde{\Lambda} = & \sqrt{1-4\nu} \left( 1 - \frac{13272}{1319}\nu + \frac{8944}{1319}\nu^2 \right) (\Lambda_1 + \Lambda_2) \\ & + \left( 1 - \frac{15910}{1319}\nu + \frac{32850}{1319}\nu^2 + \frac{3380}{1319}\nu^3 \right) (\Lambda_1 - \Lambda_2) \end{aligned} \quad (6.30)$$

with  $\Lambda_i$  the dimensionless quadrupolar gravitoelectric tidal deformability parameters of each body indexed here by  $i$ . We also denote  $X_i = m_i/M$  and  $(1 \leftrightarrow 2)$  indicates the operation of adding the same terms but with the body labels interchanged. The gravitomagnetic parameters in (6.25b) are defined by [225]

$$\tilde{\Sigma} = \left( \frac{6920}{7} - \frac{20740}{21X_1} \right) X_1^5 \Sigma_1 + (1 \leftrightarrow 2) \quad (6.31a)$$

$$\begin{aligned} \hat{\Sigma} = & \left[ \chi_1 - \left( \frac{4933}{3X_1} - \frac{9865}{3} + 1644X_1 \right) \chi_2 \right] X_1^5 \Sigma_1 \\ & + (1 \leftrightarrow 2), \end{aligned} \quad (6.31b)$$

with  $\chi_i = S_i/m_i^2$  the dimensionless spin parameter of each body. We use for the dimensionless gravitomagnetic deformability parameters  $\Sigma_i$  the asymptotic results of Sec. 6.2.3 to replace

$$\Sigma_i = \frac{\sigma_i^{\text{asym}}}{m_i^5} \quad (6.31c)$$

using the appropriate pre- or post-resonance expressions from (6.24).

In the resonance contributions (6.25c), the quantity  $\Theta$  denotes the Heaviside step function,  $f_i^{\text{res}}$  are the GW frequencies at which the mode resonances occur. They are related to the gravitomagnetic mode frequencies  $\omega_{2m}^{\mathcal{B}}$  by

$$f^{\text{res}} = \frac{\omega_{2m}^{\text{inertial}}}{\pi}, \quad (6.32)$$

where the mode frequencies in the inertial frame can be obtained by shifting

$$\omega_{2m}^{\text{inertial}} = \omega_{2m}^{\mathcal{B}} - m\Omega. \quad (6.33)$$

The quantities  $\Delta\Phi_{1,2}$  are the corresponding resonance-induced phase shifts, which, for the  $l=2$  modes with  $m=2$  and  $m=1$ , are given by [38]

$$\Delta\Phi_{2m} = -\frac{10\pi^2}{192} \left( \frac{2m}{3} \right)^{2/3} (m_i \Omega_i)^{2/3} \left( \frac{m_i}{\mathcal{M}} \right)^{10/3} \mathcal{I}_i^{2m}, \quad (6.34a)$$

where  $\mathcal{M} = (m_1 m_2)^{3/5} / M^{1/5}$  is the chirp mass and

$$\mathcal{I}_i^{22} = (\bar{I}_i^r)^2 \sin^2(\psi_i) \cos^4\left(\frac{\psi_i}{2}\right) (1 - X_i) \quad (6.34b)$$

$$(6.34c)$$

$$\mathcal{I}_i^{21} = (\bar{I}_i^r)^2 \cos^2\left(\frac{3\psi_i}{2}\right) \cos^2\left(\frac{\psi_i}{2}\right) (1 - X_i), \quad (6.34d)$$

with  $\bar{I}_i^r$  related to the dimensionless relativistic tidal deformabilities by [237]

$$(\bar{I}^r)^2 = \frac{15}{4\pi}(\Sigma_{\text{stat}} - \Sigma_{\text{irrot}}). \quad (6.34\text{e})$$

### Reducing the number of matter parameters using quasi-universal relations

Even within the restricted context considered here, the effective GW model for the tidal signatures (6.25b) and (6.25c) contains ten matter parameters, namely the deformabilities  $\Lambda_i, \sigma_i^{\text{stat}}, \sigma_i^{\text{irrot}}$  and resonance frequencies for the  $m = 1$  and  $m = 2$  modes for each body. Such a large number of extra parameters prevents the data analysis from yielding meaningful results. We reduce the number of parameters by using empirical quasi-universal relations that are approximately independent of the equation of state and enable an approximate reduction of the matter parameters to one deformability  $\Lambda$  for each body. The quasi-universal relations are of the form [234, 236]

$$\ln(\mp\Sigma) = \sum_{n=0}^5 a_n Y^n, \quad (6.35)$$

with the irrotational case corresponding to the minus sign and coefficients  $a_n^{\text{irrot}} = \{-2.03, 0.487, 0.00969, 0.00103, 9.37 \times 10^{-5}, 2.24 \times 10^{-6}\}$ , while the plus sign applies for the static case with  $a_n^{\text{stat}} = \{-2.66, 0.786, -0.01, 0.00128, -6.37 \times 10^{-5}, 1.18 \times 10^{-6}\}$  and where

$$Y = \ln(\Lambda). \quad (6.36)$$

The GW frequencies appearing in the resonant mode contributions (6.25c) are given by (6.32), which can be written explicitly as

$$f^{\text{res}} = \frac{1}{\pi}(\kappa_m - m)\Omega, \quad (6.37)$$

where the parameter  $\kappa_m$  reduces to  $\kappa_m \rightarrow 2m/3$  in the Newtonian limit, while for relativistic stars, it is approximately related to  $\Lambda$  by Eq. (7.7)

$$\kappa_2 = 0.3668 + 0.0498Y - 0.0025Y^2, \quad (6.38)$$

We note that these results from [172] are specialized to the  $m = 2$  mode. Within the effective action model (6.2) we are using, the modes with different  $m$  all have the same scaled frequency  $\hat{\omega}_{\mathcal{B}}$  and hence the same  $\kappa$ . Thus, we use (6.38) also for the  $m = 1$  modes.

With the GW phasing model for the gravitomagnetic effects in hand, we next apply it in a data analysis framework to study the impact on GW measurements.

## 6.4 Results

We use the analysis frameworks described in Sec. 2.3 to analyze the impact of gravitomagnetic tides on the measurability of the tidal Love number  $\Lambda$ . For simplicity, we focus on the Cosmic Explorer (CE) detector [97], however, we expect similar results for the Einstein Telescope [95].

### 6.4.1 Setup and parameter choices for case studies

We consider a few illustrative cases for our analysis. These examples represent only a small subset of the expected range of diverse events but nevertheless yield useful insights. Specifically, we consider binary neutron stars with masses  $(m_1, m_2) = (1.5, 1.3) M_\odot$  and explore two values of the dimensionless spin parameters  $\chi = 0.005$  and  $\chi = 0.01$  for each NS, where  $\chi$  refers to the spin magnitudes. For the tidal deformability parameters we choose  $(\tilde{\Lambda}, \delta\tilde{\Lambda}) = (519, 48)$  [118], corresponding to the MPA1 equation of state. We use quasi-universal relations [226] between the moment of inertia and  $\Lambda$  to convert from  $\chi$  to the spin frequency  $\Omega$ . In general, both the  $m = 1$  and  $m = 2$  resonances will contribute to the signals. To isolate each of these resonance effects and analyze its contributions, we choose spin inclination angles of  $\psi = 0$  (aligned spins) and  $\psi = \pi/3$  such that only the  $m = 1$  or  $m = 2$  modes respectively undergo a resonant excitation within our approximations. We assume the same spin magnitudes and orientations for both NSs.

We analyze the signals in the CE detector sensitivity [97] between  $f_{\text{low}} = 5\text{Hz}$  and  $f_{\text{high}} \sim 1720\text{Hz}$ , which is a proxy for the merger frequency based on the estimates for nonspinning NSs from [240]. Unless otherwise specified, the SNR for the signals from these systems is 1800 for the CE detector, which corresponds to an event similar to GW170817.

For the above choices of binary parameters, the mode resonance frequencies for the larger and smaller mass NSs are given by  $f_1^{\text{res}} = 12$  (24)Hz and  $f_2^{\text{res}} = 13$  (26)Hz for the  $m = 1$  ( $m = 2$ ) modes respectively and taking the spin magnitudes to be  $\chi = 0.005$ ; they increase to twice these numbers when doubling the spin magnitudes to  $\chi = 0.01$ . Figure 6.1 illustrates the location of these resonance together with the power spectral density of the CE detector [97].

To study the consequences of different effects, we consider different tidal waveform models. We refer to the 'PNTidal' model as the piece of (6.25b) involving only the adiabatic gravitoelectric tidal effects characterized by  $\tilde{\Lambda}, \delta\tilde{\Lambda}$ , and denote models that also include gravitomagnetic effects by  $\text{PNTidal}^{\text{modes}}$  for the resonant contributions (6.25c),  $\text{PNTidal}_{\text{asym}}$  for the asymptotic adiabatic contributions, and  $\text{PNTidal}_{\text{asym}}^{\text{modes}}$  for the model which includes all gravitomagnetic effects. Because we work only to linear order in the spins, we neglect the effects of spin-induced multipole moments on the GWs.

### 6.4.2 Consistency checks

#### Fisher matrix versus Bayesian parameter estimation and effect of the dimensionality of the parameter space

The Fisher matrix approximation is valid for high SNR, which we expect to hold for most of the case studies considered here. To assess the validity of this expectation we compare with Bayesian parameter estimation results for the case of the PNTidal matter model. In principle, the waveforms are characterized by 17 parameters, after reducing the matter parameters to just  $\Lambda$  for each body. Exploring the full parameter space is thus very computationally expensive. For efficiency, we focus the comparative analysis here only on the following restricted subset the intrinsic parameters

$$\theta = (t_c, \phi_c, \tilde{\Lambda}, \delta\tilde{\Lambda}) \quad (6.39)$$

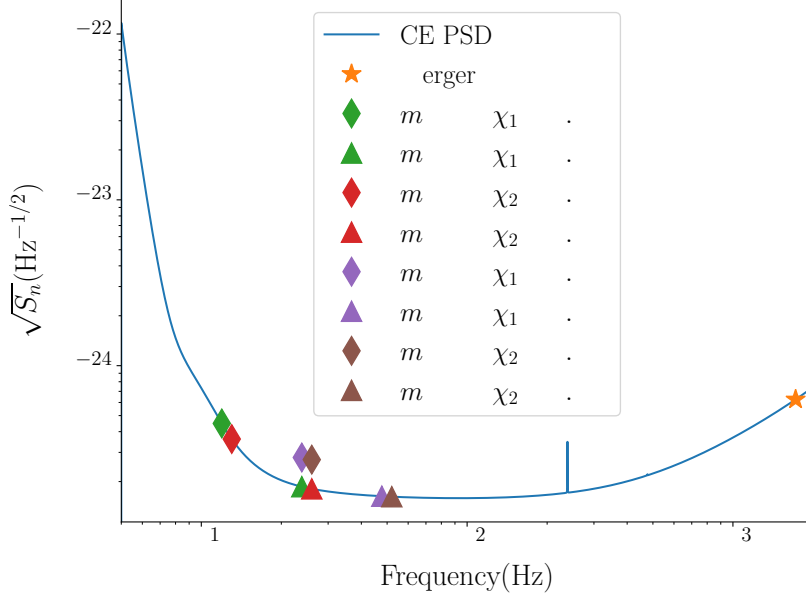


Figure 6.1: *CE noise spectral density and various mode resonances* for the two bodies and varying spins  $\chi$ . Green and purple symbols refer to the NS with mass  $m_1 = 1.5M_\odot$  with lower and higher spin respectively, while red and brown symbols are the corresponding values for the companion of mass  $m_2 = 1.3M_\odot$ . Diamond shapes denote the modes with azimuthal number  $m = 1$ , triangles those with  $m = 2$ .

and fix the other parameters to be  $\psi_1 = 0$ ,  $\psi_2 = 0$ ,  $\chi_1 = 0.01$ ,  $\chi_2 = 0.01$ . This subset was chosen to contain the matter-related parameters  $\tilde{\Lambda}$  and  $\delta\tilde{\Lambda}$  as well as  $t_c$  and  $\phi_c$  which are degenerate with mode resonance effects. We sample the Fisher likelihood with the prior constraints  $\Lambda_1 \geq 0$ ,  $\Lambda_2 \geq 0$ . We also perform a Bayesian analysis for the same setup using the `emcee` sampler to obtain the posterior probability distribution of the parameters. Figure 6.2 shows the results of both analyses. We see that in this case, the results from the Fisher (blue curve) and Bayesian (orange curve) frameworks agree well and are centered on the injected value (vertical line). To obtain an estimate of the changes in the width of the posterior distributions when including more parameters, in particular the masses and spin magnitudes for each body, we also perform a Fisher analysis for eight free parameters  $\theta = (t_c, \phi_c, m_1, m_2, \tilde{\Lambda}, \delta\tilde{\Lambda}, \chi_1, \chi_2)$ . More specifically, we obtain a mean and 90 percentile results of  $\tilde{\Lambda} = 519^{+5.1}_{-4.7}$  from the MCMC and  $\tilde{\Lambda} = 518.9^{+4.8}_{-4.9}$  from the Fisher analyses with four free parameters respectively, which shows that they are in good agreement. For an eight-dimensional parameter space we find  $\tilde{\Lambda} = 518.9^{+11.3}_{-11.2}$ , which indicates that when doubling the dimensionality of the parameter space the posterior distributions increase in width by about a factor of two. The good agreement between the Fisher and Bayesian results also provides a useful check of the 4D MCMC sampling, which is the method we will continue to use in what follows.

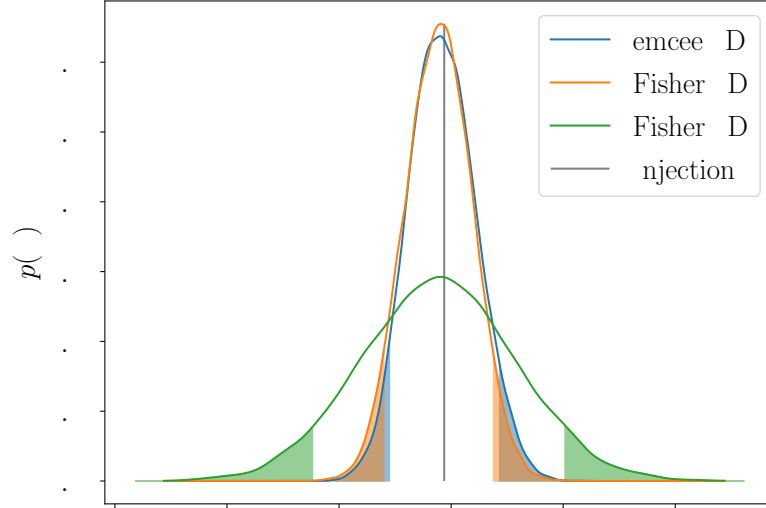


Figure 6.2: *Posterior probability distribution of  $\tilde{\Lambda}$  for SNR 1800 with the PNTidal waveform model (without gravitomagnetic effects) used for injection and recovery.* The label 4D refers to a reduced parameter space of the tidal deformabilities  $\tilde{\Lambda}, \delta\tilde{\Lambda}$  and the time and phase of coalescence  $t_c, \phi_c$  with all other parameters fixed, while 8D also includes the sampling of the mass and spin parameters for each body. The results from the Fisher matrix (orange curve) agree well with the corresponding Bayesian analysis (blue curve), with both centered on the injected value (vertical line). The green curve shows the broadening of the distribution when doubling the dimensionality of the parameter space sampled. The shaded tails of the curves indicate regions outside the 90% credible interval. For the parameter  $\delta\tilde{\Lambda}$ , both the 4D and 8D posteriors are essentially flat in this case.

### Comparison to the adiabatic effects studied in [225]

The final consistency check we perform here is to compare with the results of [225] for the impact of adiabatic gravitomagnetic effects on measurements of  $\tilde{\Lambda}$ . Following [225] we restrict our analysis to only three free parameters  $\theta = (t_c, \phi_c, \tilde{\Lambda})$ , with all the other parameters fixed. Figure 6.3 shows the results for aligned spins of magnitude  $\chi = 0.005$ . Comparing the orange curve (no mode resonances) and blue curve (no adiabatic effects) to the green curve shows that in this case the largest impact of gravitomagnetic effects is due to the adiabatic limits, while mode resonances play a subdominant role. Specifically, we obtain  $\tilde{\Lambda} = 519.3^{4.5}_{-4.5}$  with the full model (green curve) that was also used for the injection and thus quantifies the statistical errors. Using only the adiabatic effects (orange curve) leads to  $\tilde{\Lambda} = 520.9^{4.4}_{-4.4}$ , which is close to the injected value. On the other hand, when including only the mode resonances for the recovery while neglecting the adiabatic effects (blue curve) leads to a distribution that is significantly shifted away from the injected value with  $\tilde{\Lambda} = 515.1^{4.6}_{-4.5}$ . The smallness of the effect of the mode resonances on measurements of  $\tilde{\Lambda}$  is in part due to the fact that the resonance-induced phase

corrections (6.25c) have a scaling in frequency degenerate with the gauge parameters  $t_c$  and  $\phi_c$  in the phase (6.25a), which absorbs some of the resonance effects into shifts of  $t_c$  and  $\phi_c$ . The adiabatic effects show a similar magnitude as found in [225] based on only the irrotational or static Love numbers, which lead to shifts in the posterior distributions to lower and higher values respectively, c.f. Fig. 6 therein. While the specific choices for the case study here differ from [225] the setup is similar enough to interpret qualitative trends by comparing their findings to the adiabatic results represented by the orange curve in Fig. 6.3, which uses the more realistic asymptotic Love numbers from (6.24) as opposed to only  $\sigma_{\text{irrot}}$  for the entire waveform.

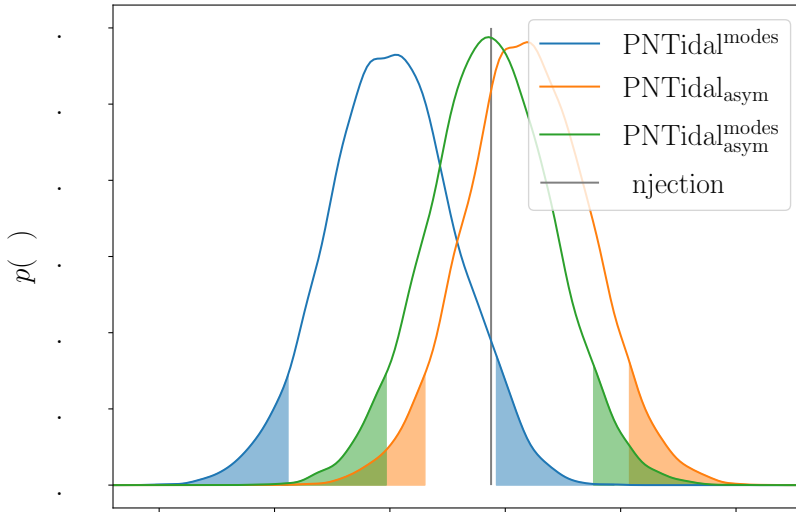


Figure 6.3: *Shifts in the posterior distribution for  $\tilde{\Lambda}$  due to adiabatic and resonant gravitomagnetic effects.* This case study is for SNR 1800, aligned spins  $\chi = 0.005$  and sampling only on  $(\tilde{\Lambda}, t_c, \phi_c)$  with all other parameters fixed. We inject with a waveform that includes all effects  $\text{PNTidal}^{\text{modes}}_{\text{asym}}$  and recover with the same waveform (green curve) and those that include only the resonance jumps (blue curve) and only the adiabatic effects (orange curve). In this case the contribution from the adiabatic effects is dominant; omitting them (as for the results shown by the blue curve) leads to the largest shifts in the distribution.

### 6.4.3 Physical effects

Having performed the consistency checks discussed above, we next analyze the impact of various physical effects and parameter dependencies by sampling on the four-dimensional parameter space (6.39). We first consider nonspinning systems, where there is no effect from the mode resonances, then aligned spins with only the  $m = 1$  modes resonant, and finally spin orientations that maximize the effects of the  $m = 2$  modes.

### Gravitomagnetic effects for nonspinning systems

For this study we use the PNTidal model without the gravitomagnetic effects as the reference baseline for the injection and set  $\chi = 0$ . Figure 6.4 shows the results for the posterior distributions in the tidal parameters  $\tilde{\Lambda}$  and  $\delta\tilde{\Lambda}$ , with the two-dimensional representations given in the lower left panel, and the one-dimensional projections for each parameter in the upper and right panels. The one-dimensional representations are the full distributions, while the contours in the  $\tilde{\Lambda} - \delta\tilde{\Lambda}$  plane correspond to the credible intervals at the one (68%) and two (95%) sigma confidence level. The blue curves in Fig. 6.4 represent a consistency check that when injecting and recovering with the same model the mean is centered on the injected value indicated by the gray lines and quantify the statistical uncertainties. The orange curve in Fig. 6.4 corresponds to the results obtained when including all gravitomagnetic effects, where, however, for nonspinning systems there is only an adiabatic gravitomagnetic effect, no resonances. As expected, we see that they induce a small shift in the posterior for  $\tilde{\Lambda}$ . We note that the difference to the study in Sec. 6.4.2 is the model used for the injection, the value of the spins, which also impacts the adiabatic gravitomagnetic parameters (6.31), and the dimensionality of the parameter space sampled. We also observe that the adiabatic effects have no significant impact on the measurability of  $\delta\tilde{\Lambda}$  in this case, as the shape of the error ellipses and the flat distribution in  $\delta\tilde{\Lambda}$  remain largely unaffected.

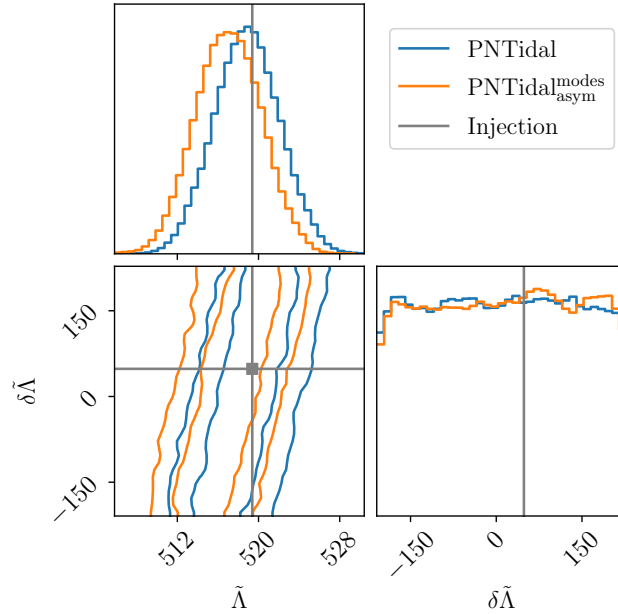


Figure 6.4: *Posterior distributions of the tidal parameters for nonspinning NSs at SNR 1800. The injection neglected gravitomagnetic tides, and the blue curve illustrates the recovery with the same waveform. The effect of gravitomagnetic tides, which are purely adiabatic in this case, is indicated by the orange curve. In the two-dimensional representation in the lower-left panel, the contours correspond to the one and two sigma confidence levels.*



### Effect of gravitomagnetic tides for aligned spins

A more realistic scenario is to include finite spins of the NSs. We first consider the case of aligned spins, where the  $m = 1$  mode resonances contribute in addition to the adiabatic effects. As in Sec. 6.4.3, we use the model without gravitomagnetic tides as the reference baseline for the injection and recover with the the same model (blue curve) as well as the model including all gravitomagnetic effects (orange curve). For small spins  $\chi = 0.005$ ,

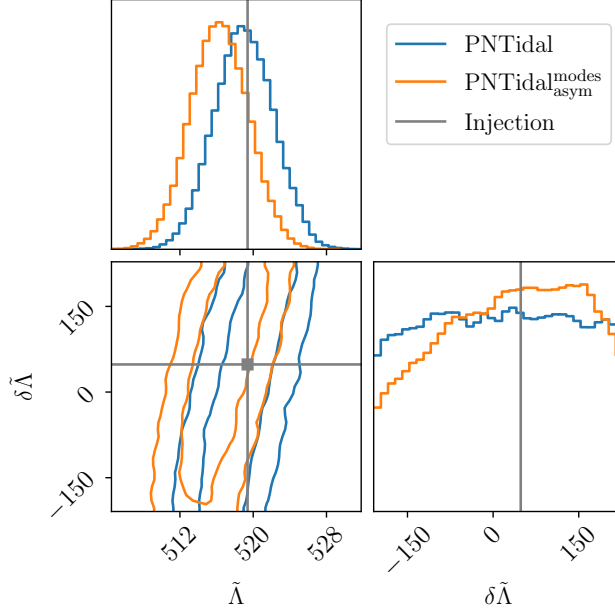


Figure 6.5: *Gravitomagnetic effects for aligned spins of  $\chi_{1,2} = 0.005$  and SNR 1800.* The blue curve corresponds to using the same waveform for injection and recovery. Comparing this with the orange curve indicates the changes due to gravitomagnetic tides from both the  $m = 1$  mode resonances and the adiabatic effects, which lead to a shift in the distribution of  $\tilde{\Lambda}$  and a slight change in the shape of the  $\delta\tilde{\Lambda}$  posterior.

we see from Fig. 6.5 that the gravitomagnetic effects lead to a slightly larger shift in the posterior probability distributions than in the nonspinning case shown in Fig. 6.4. These trends become more discernible for higher spins of  $\chi = 0.01$  shown in Fig. 6.6. For higher spins, the recovered distributions for  $\tilde{\Lambda}$  with and without gravitomagnetic effects have essentially no overlap. We also notice that compared to the low-spin case in Fig. 6.5 the shift in the distribution for  $\tilde{\Lambda}$  is in the opposite direction. We will investigate the causes of this below in Sec. 6.5. Roughly, it can be attributed to the fact that for higher spins the resonances occur at higher frequency, as seen in Fig. 6.1. Furthermore, as also found in [168], which included only the mode resonance effects with Newtonian parameters, the presence of gravitomagnetic tides significantly improves the measurability of  $\delta\tilde{\Lambda}$ . This is indicated by a peak in the one-dimensional projection or the size of the ellipse in the  $\tilde{\Lambda} - \delta\tilde{\Lambda}$  plane, which is in contrast to the distribution being essentially uninformative when neglecting the gravitomagnetic effects (c.f. the blue curves in Fig 6.6).

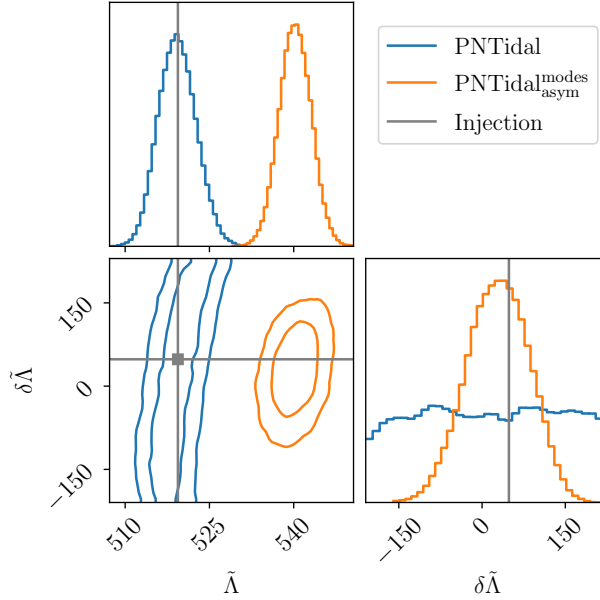


Figure 6.6: *Gravitomagnetic effects for aligned spins* of  $\chi_{1,2} = 0.01$  and SNR 1800. The blue curve corresponds to using the same waveform for injection and recovery, the orange curve indicates the effect of gravitomagnetic tides from both the  $m = 1$  mode resonances and the adiabatic effects. Significant shifts in  $\tilde{\Lambda}$  and a peaked shape of the distribution of  $\delta\tilde{\Lambda}$  are clearly visible in this case. This is also illustrated by the two-dimensional representation of the error ellipses in the lower left panel.

### Effects of different gravitomagnetic contributions for aligned spins

Having quantified the impact of gravitomagnetic effects, we next investigate the relative importance of adiabatic and resonant contributions to these results. For this purpose, we switch to using the full tidal model  $\text{PNTidal}_{\text{modes}}^{\text{asym}}$  for the injections. The results when recovering with different models that are missing various effects for the case with spins of  $\chi = 0.005$  are shown in the upper panels of Fig. 6.7. The green curve illustrates the recovery with the same model as the injection, the blue curve corresponds to omitting the adiabatic effects, while the orange curve illustrates the omission of resonance effects from the model. From the large (small) shift away from the injected value in the distribution for  $\tilde{\Lambda}$  when omitting (including) adiabatic effects it follows that the conclusions of Sec. 6.4.2 about the signatures from adiabatic tides dominating over the resonance effects in this case continue to hold for the larger parameter space considered here. Furthermore, we also see by comparing the orange and blue curves in the upper panels of Fig. 6.7 that the more peaked distribution in  $\delta\tilde{\Lambda}$  can be primarily attributed to the mode resonances in this case.

The lower panel of Fig. 6.7 shows the same study with higher spins of  $\chi = 0.01$ . We see the opposite behavior compared to the case with lower spins: now the mode resonances (blue curves) dominate over adiabatic effects (orange curve) for measuring  $\tilde{\Lambda}$  without bias; in fact the inferred  $\tilde{\Lambda}$  with the adiabatic model has no overlap with the injected

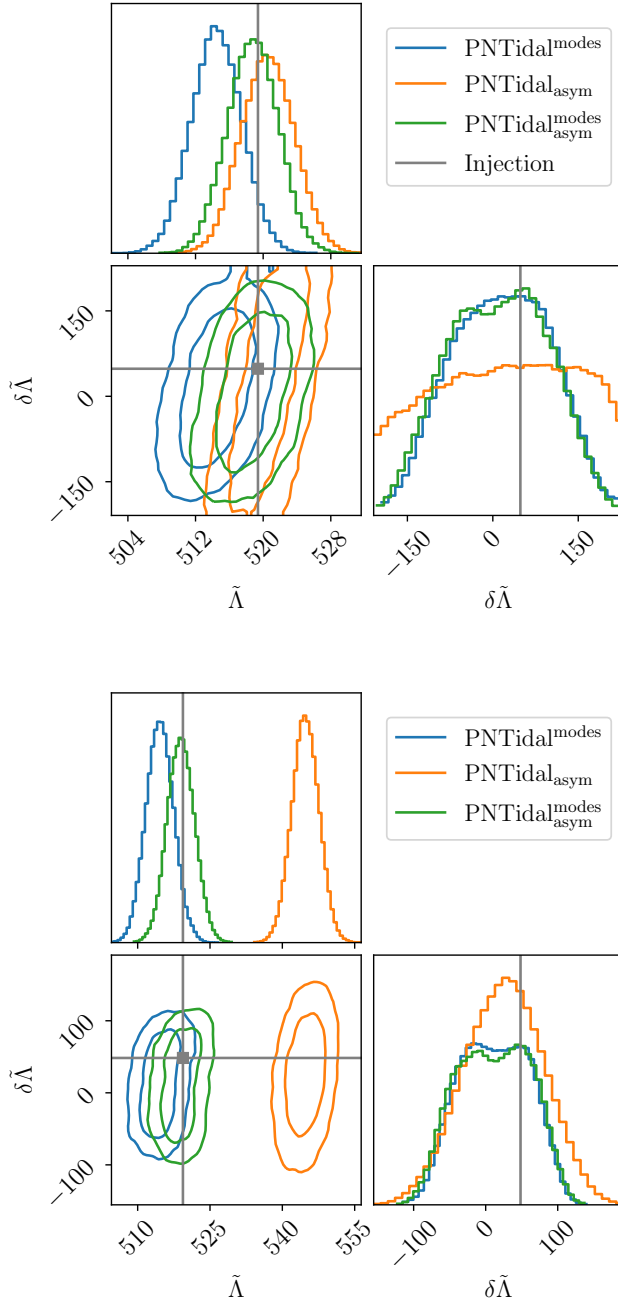


Figure 6.7: *Effects of various gravitomagnetic contributions on the parameter recovery for aligned spins.* The results are for the systems with SNR 1800 and spins of  $\chi = 0.005$  (upper panels) and  $\chi = 0.01$  (lower panels). Green curves correspond to recovering with the same full model as used for the injection, blue curves include only the mode resonances, while orange curves indicate the adiabatic effects. We see that the conclusions about the impact of the resonance and adiabatic effect is opposite for the lower and higher spins: for low spins, adiabatic effects are most important for reducing the bias in  $\tilde{\Lambda}$ , while resonances give the dominant contribution to the measurability of  $\delta\tilde{\Lambda}$ . For high spins, the largest reduction in the bias in  $\tilde{\Lambda}$  is due to the resonances, while the impact on  $\delta\tilde{\Lambda}$  is comparable between resonance and adiabatic effects.

value in this case. In all cases, a peaked distribution in  $\delta\tilde{\Lambda}$  emerges, indicating that it is measurable, though with significantly larger errors than  $\tilde{\Lambda}$ . The resonance effects yield a double-peaked distribution in this parameter for  $\chi = 0.01$ , which we attribute to the larger spacing of the two resonances in this case. Interestingly, for  $\chi = 0.01$  the adiabatic effects contribute about equally to measuring  $\delta\tilde{\Lambda}$  as the mode resonances, which is in contrast with the case of lower spins.

### Effect of the $m = 2$ modes (r-modes)

The analysis thus far focused on aligned-spin systems where only the  $m = 1$  modes are resonant. In this subsection we quantify the impact of the  $m = 2$  mode resonances by choosing spin orientations  $\psi = \pi/3$  following a similar line of analysis as for the aligned-spin case.

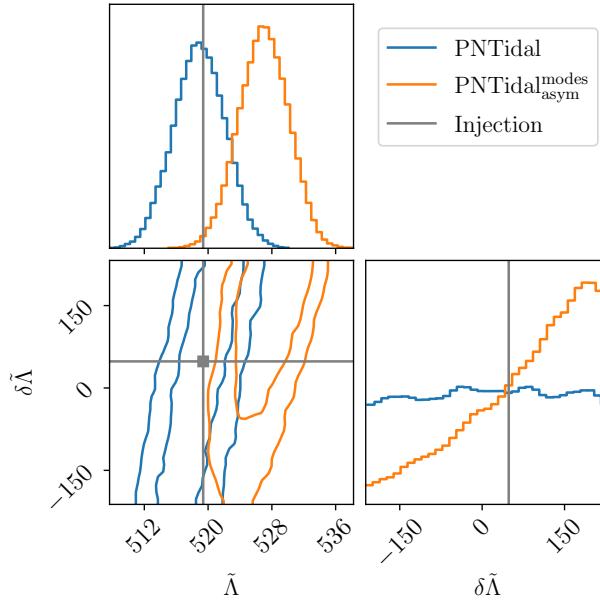


Figure 6.8: *Gravitomagnetic effects for spin orientations  $\psi = \pi/3$  and magnitudes  $\chi = 0.005$  at SNR 1800. The blue curve corresponds to using the same waveform for injection and recovery. Comparing this with the orange curve indicates the changes due to gravitomagnetic tides from both the  $m = 2$  mode resonances and the adiabatic effects, which lead to a shift in the distribution of  $\tilde{\Lambda}$  and a more peaked shape of the  $\delta\tilde{\Lambda}$  posterior.*

First, we consider the impact of including all gravitomagnetic effects. From Fig. 6.8 we see that even for small spins of  $\chi = 0.005$ , the gravitomagnetic effects lead to larger shifts in the posterior probability distribution for  $\tilde{\Lambda}$  and in the opposite direction compared to the aligned spin case in Fig. 6.5. An approximate reasoning for this behavior is that the  $m = 2$  resonances occur later in the inspiral than the  $m = 1$  resonances, as we will discuss in more depth in Sec. 6.5. Figure 6.8 also shows a peak in the distribution for  $\delta\Lambda$  when including gravitomagnetic tides (orange curves), however, because the injection neglected gravitomagnetic effects, it is not centered on the injected value.

For higher spins of  $\chi = 0.01$ , the above trends are more pronounced, as seen in Fig. 6.9. We observe that the two-dimensional confidence intervals have no overlaps at all in this case, and that the distribution in  $\delta\tilde{\Lambda}$  becomes more distinctly peaked.

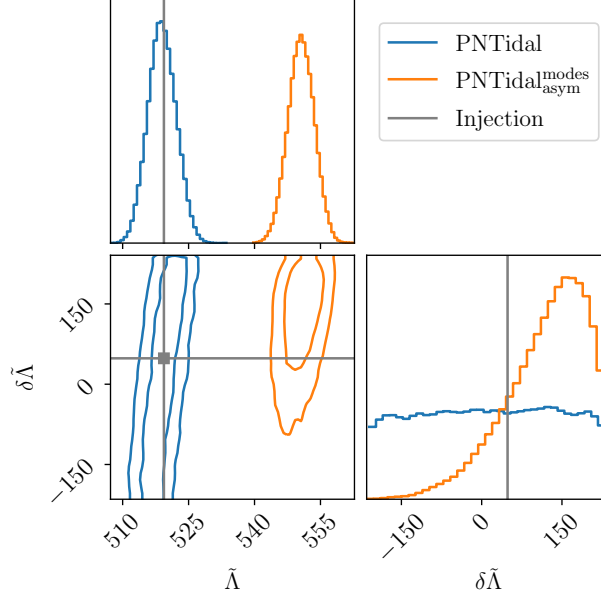


Figure 6.9: *Gravitomagnetic effects for spin orientations  $\psi = \pi/3$  and magnitudes  $\chi_{1,2} = 0.01$  at SNR 1800.* The blue curve corresponds to using the same waveform for injection and recovery. Comparing this with the orange curve indicates the changes due to gravitomagnetic tides from both the  $m = 2$  mode resonances and the adiabatic effects, which lead to a substantial shift in the distribution of  $\tilde{\Lambda}$  and clear peak in the  $\delta\tilde{\Lambda}$  posterior.

To gain deeper insights into the reasons for these results, we next characterize the impact of the resonant and adiabatic contributions to gravitomagnetic effects separately. The results of injecting with the full  $\text{PNTidal}_{\text{modes}}^{\text{asym}}$  and recovering with different models for cases with smaller and larger spins are shown in the upper and lower panels of Fig. 6.10 respectively. We see that the contributions of the  $m = 2$  mode resonances (blue curves) are more significant for reducing biases than the adiabatic effects (orange curves) for both the smaller and larger spin magnitudes in this case, though both effects are important to accurately recover the parameters.

#### 6.4.4 Measurement accuracy for different spins

Having characterized the importance of the various contributions and gravitomagnetic tides overall, we next compare the net effects on the measurement accuracy for different spin magnitudes. In this study, the injected and recovered waveform is the full  $\text{PNTidal}_{\text{asym}}^{\text{modes}}$  model with increasing spin  $\chi = 0, 0.005, 0.01$ . The results for aligned spins are shown in Fig. 6.11 for increasing spin magnitudes  $\chi = 0, 0.005, 0.01$  corresponding to the blue, orange, and green curves respectively. We see that changing the spins has very

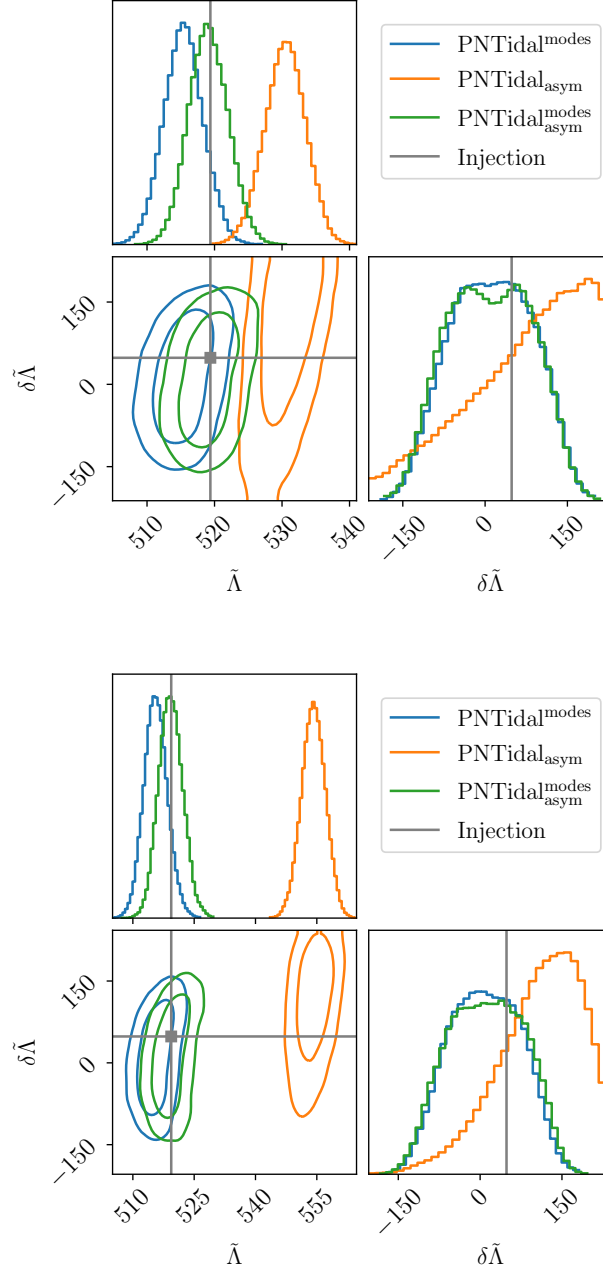


Figure 6.10: *Effects of various gravitomagnetic contributions on the parameter recovery for misaligned spins.* The results are for the systems with SNR 1800 and spin orientations of  $\psi = \pi/3$  with  $\chi = 0.005$  (upper panels) and  $\chi = 0.01$  (lower panels). Green curves correspond to recovering with the same full model as the injection, blue curves include only the mode resonances, while orange curves indicate the adiabatic effects. We see that in both cases the mode resonances play a larger role for reducing biases than the adiabatic effects.

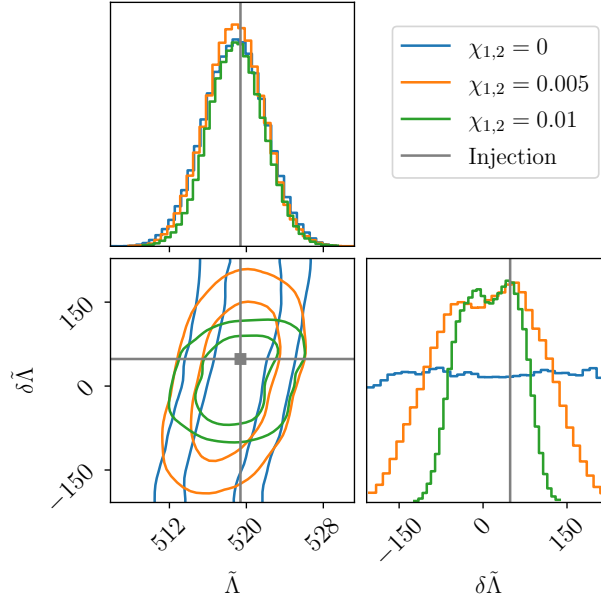


Figure 6.11: *Effect of the spin magnitude on inferred tidal parameters for aligned spins and SNR of 1800. The injection and recovery both use the same model  $\text{PNTidal}_{\text{modes}}^{\text{asym}}$  with corresponding spin magnitudes, as indicated in the legend. Increasing the spin magnitude has very little impact on the width of the posterior in  $\tilde{\Lambda}$  but significantly affects that of  $\delta\tilde{\Lambda}$ , where a higher spin leads to tighter bounds.*

little impact on the posterior distributions for  $\tilde{\Lambda}$  in this case. By contrast, a decreasing spin results in a broader distribution in  $\delta\tilde{\Lambda}$ . As our analysis keeps the spins fixed, the impact of spins is through their coupling with adiabatic tidal parameters through (6.31), the resonance phase shift  $\sim \Omega^{2/3}$ , and the mode resonance frequency, as we will further discuss in Sec. 6.5. From the above results, we also infer that the double-peak in the distribution of  $\delta\tilde{\Lambda}$  for  $\chi = 0.005$  arises from the combination of adiabatic and resonant effects, which act in opposite directions, while for  $\chi = 0.01$  it is largely due to the presence of two resonances spaced widely enough to be noticeable in the data analysis.

A different perspective on the behavior can be gained by considering where in frequency the information about tidal parameters accumulates. This is not immediately visible from the phasing (6.25a) due to the implicit and nontrivial dependencies of the gravitomagnetic parameters on  $\tilde{\Lambda}$  and  $\delta\tilde{\Lambda}$  upon using the quasi-universal relations. Figure 6.12 shows the normalized integrands entering the Fisher matrix error computations. For  $\tilde{\Lambda}$ , the abrupt changes due to the resonances are too small to be visible on the scale of this plot, which is in contrast to the information on  $\delta\tilde{\Lambda}$ , where the resonance features are clearly visible.

The corresponding results with varying spin magnitudes for the case with misaligned spins of  $\psi = \pi/3$  are shown in Fig. 6.13. We find similar trends as for the aligned spin case. However, a notable difference is that while the presence of spin has the expected impacts on the distributions, the consequences of any change in its magnitude are very small. This is in contrast with the trends in Fig. 6.11 for the  $m = 1$  modes. An explanation

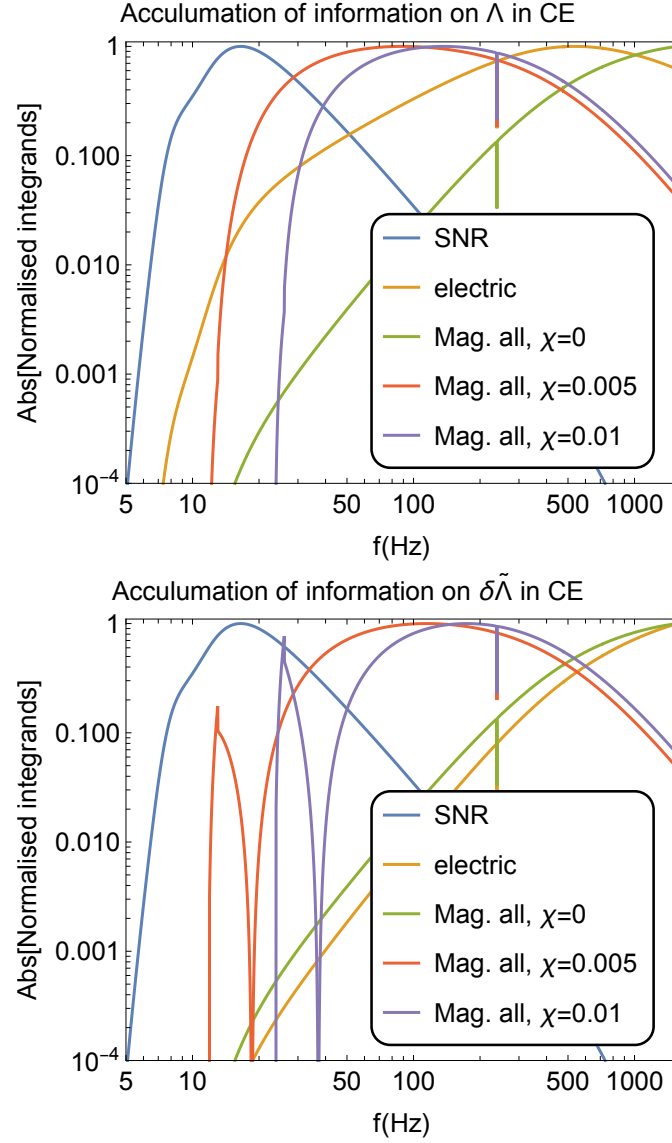


Figure 6.12: Accumulation of information encoded in integrands  $\text{Abs}\left(\frac{\partial \tilde{h}^*}{\partial \theta_i} \frac{\partial \tilde{h}}{\partial \theta_i} * \frac{1}{S_n(f)}\right)$  (normalized to its maximum value) for  $\theta_i = \tilde{\Lambda}$  (left panel) and  $\theta_i = \delta\tilde{\Lambda}$  (right panel) as a function of frequency for the injected value of aligned spins  $\{0.0, 0.005, 0.01\}$ ,  $\tilde{\Lambda} = 519.38$  and  $\delta\tilde{\Lambda} = 48.37$ . “SNR” denotes the integrands  $\text{Abs}\left(\frac{\tilde{h}^* \tilde{h}}{S_n(f)}\right)$ , “electric” denotes only adiabatic gravitoelectric tidal contribution in (6.25a) and “Mag. all” denotes adiabatic and resonant gravitomagnetic tidal contribution in (6.25a).



of this behavior could potentially come from considering the location of the resonances studied here with respect to the noise curve shown in Fig. 6.1, where changing the spin has a more drastic impact on the relative location of the  $m = 1$  resonances (diamonds) in the detector sensitivity.

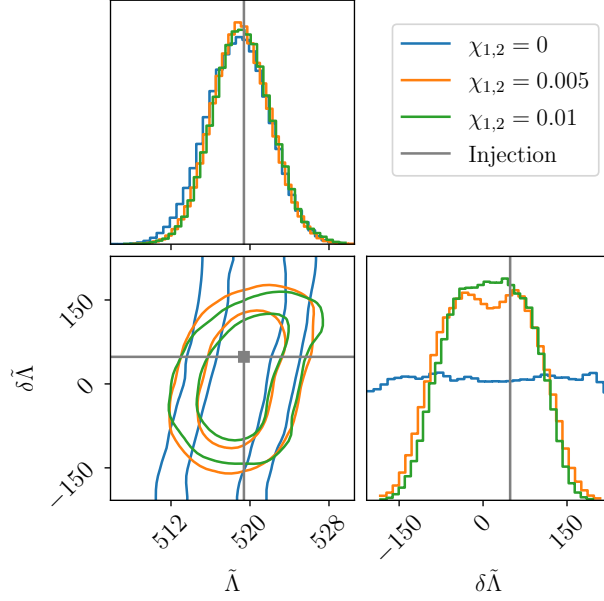


Figure 6.13: *Effect of the spin magnitude on inferred tidal parameters for inclined spins at  $60^\circ$  and SNR of 1800.* The injection and recovery both use the full model  $\text{PNTidal}_{\text{asym}}^{\text{modes}}$  with varying spin magnitudes as indicated in the legend. Increasing the spin magnitude from a finite value to a higher one has very little impact on the width of the posteriors in this case.

### Extrapolating to lower SNR of 400

Thus far, we have assumed a SNR of 1800 in the CE detector, which is plausible for an event similar to GW170817. However, many more events will be observed at a lower SNR. To estimate the changes in our conclusions for such more numerous events, we perform the same analysis as above but for a SNR of 400 instead of 1800. From Fig. 6.14 we see that for lower SNR the qualitative trends of the effects of increasing the spins remain: there is little impact on the posterior distribution for  $\tilde{\Lambda}$ , while that for  $\delta\tilde{\Lambda}$  becomes tighter. Comparing the left and right panels of Fig. 6.14, which correspond respectively to the spin orientations where only the  $m = 1$  and  $m = 2$  modes are present, we also notice that for the higher spins considered here, the  $m = 1$  modes have a larger effect on the measurability of  $\delta\tilde{\Lambda}$  than the  $m = 2$  modes. Comparing the results of Fig. 6.14 with the cases with higher SNR in Figs. 6.11 and 6.13 also quantifies the expected trends of a higher SNR resulting in tighter posterior distributions in the parameters. Table 6.1 lists the specific values obtained for the mean and 90% credible intervals of the inferred  $\tilde{\Lambda}$  and  $\delta\tilde{\Lambda}$  distributions. From these results we see that for  $\tilde{\Lambda}$ , the change in the 90%

$\chi$	$\psi = 0$	$\psi = \pi/3$
	SNR 1800	SNR 1800
0.0	$518.8^{+5.0}_{-5.3} (10.5^{+193.2}_{-194.2})$	$518.8^{+5.0}_{-5.3} (10.5^{+193.2}_{-194.2})$
0.005	$518.8^{+4.7}_{-4.9} (12.1^{+135.5}_{-143.5})$	$519.1^{+4.8}_{-4.6} (9.2^{+118.5}_{-118.4})$
0.01	$519.0^{+4.7}_{-4.5} (12.1^{+75.6}_{-79.4})$	$519.2^{+4.9}_{-4.6} (12.5^{+106.8}_{-109.7})$
	SNR 400	SNR 400
0.0	$518.9^{+20.6}_{-20.3} (14.6^{+190.1}_{-198.8})$	$518.9^{+20.6}_{-20.3} (14.6^{+190.1}_{-198.8})$
0.005	$519.1^{+20.5}_{-20.5} (10.9^{+191.9}_{-191.6})$	$520.1^{+20.1}_{-20.5} (12.2^{+187.0}_{-191.8})$
0.01	$520.4^{+20.1}_{-20.0} (12.0^{+158.5}_{-162.0})$	$521.1^{+20.0}_{-19.4} (8.4^{+188.3}_{-189.1})$

Table 6.1: Recovered mean and 90% credible intervals of  $\tilde{\Lambda}(\delta\tilde{\Lambda})$  for SNR 1800 and 400. The injected values are  $\tilde{\Lambda} = 519$  and  $\delta\tilde{\Lambda} = 48$ . The spin magnitude  $\chi$  on each NS increases from top to bottom, and we recall that in the aligned spin case  $\psi = 0$  only the  $m = 1$  modes pass through resonance, for  $\psi = \pi/3$  it is only the  $m = 2$  modes, and in the nonspinning case the resonances are absent.

interval for SNR 400 compared to 1800 is largely consistent with an approximate scaling of the errors as  $(\text{SNR})^{-1}$ , i.e. the width increases by roughly a factor of  $\sim 4.5$ . By contrast, the broadening of the 90% interval in  $\delta\tilde{\Lambda}$  with lower SNR is significantly less than expected from such a scaling, which is a promising indication for measurements, however, corroborating this for more realistic data analysis implications will require further work.

## 6.5 Discussion

In this section, we discuss interesting aspects of the above findings and their interpretation. The high-level outcome of the case studies in Sec. 6.4 is that they corroborate previously disconnected findings [168, 225] that gravitomagnetic tidal signatures in the GWs from both adiabatic and resonance-induced effects can have important impacts on the GW phasing for measurements with third-generation detectors. In addition, our analysis provided insights into the quantitative dependencies of these results on different features associated to the resonance-induced and adiabatic contributions and showed that their relative importance strongly depends on the system parameters. We discuss these findings below.

### Features and parameter dependencies of gravitomagnetic effects in GWs

*Asymptotic adiabatic effects.* The leading-order contribution in the phase is parameterized by the quantity  $\tilde{\Sigma}$  in (6.25b), which increases slowly with  $\tilde{\Lambda}$  and is positive both before and after a resonance. However, its magnitude significantly drops to much lower values across a resonance. In the GW phase,  $\tilde{\Sigma}$  first enters together with  $\delta\tilde{\Lambda}$  at the same scaling with frequency, and both with the opposite sign as the  $\tilde{\Lambda}$  contribution, c.f. (6.25b). These effects thus lead to a reduction of the net size of tidal GW signatures. Spin effects coupled with the adiabatic gravitomagnetic effects enter at a higher order in frequency through the parameter  $\hat{\Sigma}$ , thus contributing new information that breaks the degeneracy

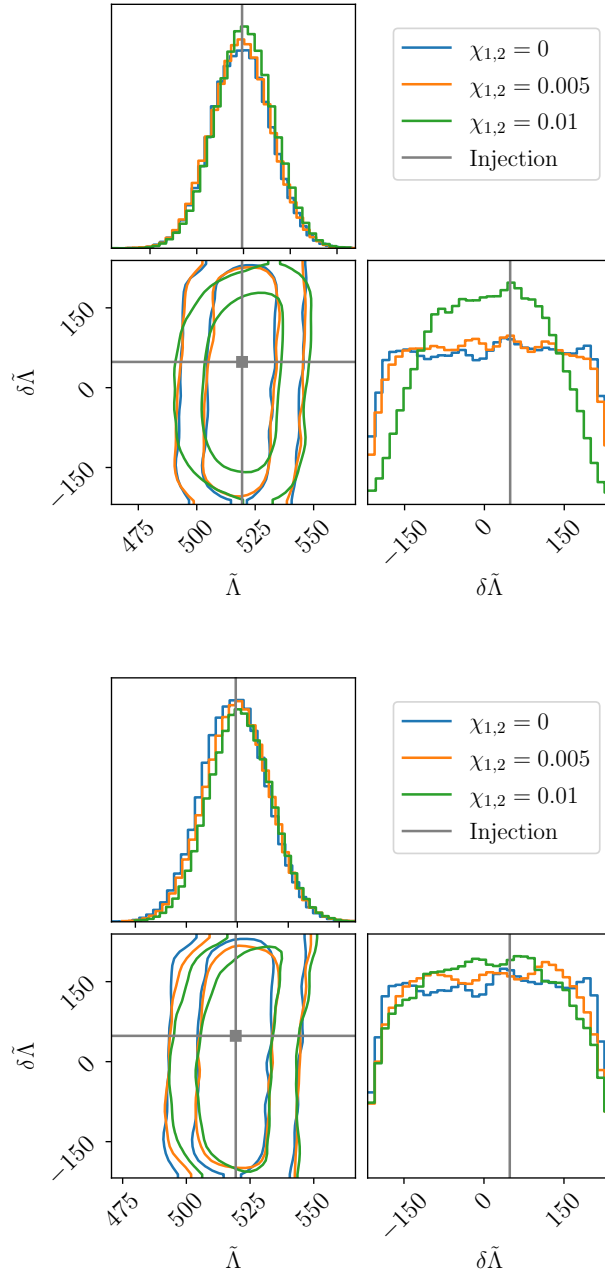


Figure 6.14: *Fisher matrix results for systems with SNR 400 for different spins.* The injection and recovery both use the model  $\text{PNTidal}_{\text{asym}}^{\text{modes}}$  with the corresponding spin magnitude indicated in the legend. *Left panel:* aligned spins, *right panel:* spin inclinations of  $60^\circ$ . Same as Figs. 6.11 and 6.13 except for lower SNR.

with  $\delta\tilde{\Lambda}$ . For the specific cases considered here,  $\hat{\Sigma}$  is positive. The spin orientation impacts the size of the pre-resonance values of the adiabatic parameters  $\tilde{\Sigma}$  and  $\hat{\Sigma}$ , which can be larger for misaligned spins than for aligned spins.

*Resonance-induced effects.* The resonance effects in the GW phase introduce a behavior that is very different from other contributions to the phasing because of its abruptness. Once present, the scaling with frequency is the same as for the gauge parameters  $t_c, \phi_c$ . The size of the resonance-induced phase shifts depend on the spin magnitude and orientation, as well as the static and irrotational gravitomagnetic Love numbers characterizing how strongly the modes couple to the tidal field. The resonance jumps induce a negative GW phase correction, accelerating the inspiral and increasing the difference to a non-tidal signal. This is the opposite behavior as the leading-order adiabatic effects from gravitomagnetic tides discussed above. The resonance effects increase with larger  $\tilde{\Lambda}$  and decrease for larger  $\delta\tilde{\Lambda}$ . Furthermore, larger spins lead to larger resonance jumps, as also seen from the spin dependence of (6.34), where  $\Delta\Phi_{2m} \sim \chi^{2/3}$ , and where we also note that the dependence on the spin orientation is such that  $\Delta\Phi_{2m}$  is largest for aligned spins. In addition, the resonance frequencies are approximately proportional to the spin frequency as well as the mode number  $m$ . Larger spins and  $m$  shift the resonances to higher frequencies, which can have several consequences depending on the resonance location. For example, for the case studies considered here, a shift of the resonances to higher frequencies leads to an enhanced accumulation of information from the pre-resonance adiabatic effects, the resonance jumps being within regimes of greater detector sensitivity, and a reduction in the number of cycles over which information from the resonances accumulates. As expected, when resonances occur within the most sensitive band of the detector, which in Sec. 6.4 were the cases with  $\chi = 0.01$  and the scenario with  $\chi = 0.005$  with spins misaligned by  $60^\circ$ , the relative importance of the resonance effects is larger.

### Case studies of aligned-spin systems

For systems with aligned spins, we found different trends depending on the spin magnitudes. In the nonspinning case, only the adiabatic post-resonance effects contribute to the GW phase. As explained above, the leading-order adiabatic gravitomagnetic parameter  $\tilde{\Sigma}$  contributes to the phasing (6.25b) in the same way as  $\delta\tilde{\Lambda}$ , while the contribution from  $\hat{\Sigma}$  vanishes for zero spins. Consequently, gravitomagnetic effects have a rather small impact on the measurability of  $\delta\tilde{\Lambda}$ , as also seen in Fig. 6.4. Furthermore, the  $\tilde{\Sigma}$ -dependent contribution effectively reduces the size of the tidal effects in the phasing, which in this Fisher matrix study leads to the shift of the recovered  $\tilde{\Lambda}$  to lower values, as also seen in Fig. 6.4.

For finite but low spins of  $\chi = 0.005$ , the gravitomagnetic mode resonances occur at the lower end of CE's sensitive band, c.f. Fig. 6.1, where the sensitivity is deteriorating. As seen in the upper panel of Fig. 6.7, we find that in this case that the dominant contribution for recovering the correct mean for  $\tilde{\Lambda}$  is the post-resonance asymptotic values. Consequently, the results for  $\tilde{\Lambda}$  shown in Fig. 6.5, are similar to the nonspinning case in Fig. 6.4. When compared to the full baseline model with all gravitomagnetic effects, the mode resonances tend to lead to lower  $\tilde{\Lambda}$  mean values, while adiabatic effects shift the distribution more towards higher ones in this case. A new feature with spins is that the  $\delta\tilde{\Lambda}$  distribution becomes less flat, implying that this parameter becomes measurable,

albeit with much larger statistical errors than  $\tilde{\Lambda}$ . As seen from Fig. 6.7, a non-flat distribution arises from both adiabatic effects and resonance jumps, however, the contribution from the latter is larger in this case.

For the higher spin system with  $\chi = 0.01$ , where the resonances occur at higher frequencies, the posterior in  $\tilde{\Lambda}$  with all gravitomagnetic effects is shifted in the opposite direction relative to the gravitoelectric baseline than the case with lower spins  $\chi = 0.005$ , as seen by comparing Figs. 6.5 and 6.6. This is due to the resonance effects becoming the dominant contribution to the results for  $\tilde{\Lambda}$ , as seen in the lower panel of Fig. 6.7. Interestingly, the measurement of  $\delta\tilde{\Lambda}$  in this higher-spin case is impacted nearly equally by both adiabatic and resonance effects, which both give similarly tight posteriors. We attribute the enhanced contribution from adiabatic effects for higher spins primarily to the larger contribution from  $\hat{\Sigma}$ , which breaks the degeneracies, with a potential further enhancement due to the resonance occurring at higher frequency, which increases the importance of the larger pre-resonance contribution to  $\tilde{\Sigma}(\tilde{\Lambda}, \delta\tilde{\Lambda})$ , making the effects larger overall.

### Spins inclined at $60^\circ$

The system with misaligned spins of  $\chi = 0.005$  we considered has the same resonance frequencies as the case study of aligned spins with  $\chi = 0.01$ . However, the other parameters of these systems differ, which enables us to study their dependencies for a fixed resonance location. Specifically, the value of the phase jumps  $\Delta\Phi_{2m}$  from (6.34) are about four times larger for the high-spin  $m = 1$  case than for  $m = 2$  with low spin. Conversely, in the same comparison,  $\tilde{\Sigma}$  is smaller by a factor of four and  $|\hat{\Sigma}|$  is smaller by a factor of about two for the pre-resonance regime. The post-resonance values of  $\tilde{\Sigma}$  are the same in the two cases. The outcomes of our analysis for the  $m = 2$  case with low spins are indeed qualitatively similar to that with the same resonance location but aligned spins. Notably, we find that the gravitomagnetic effects lead to a significant shift in  $\tilde{\Lambda}$  compared to the gravitoelectric baseline and to a non-flat distribution of  $\delta\tilde{\Lambda}$ . Overall, the effects are larger for aligned high spins than for the misaligned low spin case, as can be seen by comparing, for example, Figs. 6.6 and 6.8.

For the case of misaligned spins with  $\chi = 0.01$ , the results are similar to those with the lower spin magnitudes, as seen in Fig. 6.13. This is in contrast with the aligned-spin case, where an increasing spin magnitude changes the importance of different gravitomagnetic contributions and noticeably improves the measurability as seen in Fig. 6.11, for reasons explained above.

## 6.6 Conclusion

In this work, we developed an approximate but efficient adaptation of known results to incorporate more realistic descriptions of resonant and adiabatic gravitomagnetic tidal effects in the Fourier-domain GW phasing for slowly rotating neutron stars and focusing on the quadrupole effects. We discussed the subtleties with adiabatic effects in this case, where calculations based on relativistic perturbation theory identified two different characteristic tidal deformability parameters. We derived the combinations of these

parameters that appear together with a dependence on the spin orientation and the normalized mode frequencies in the GW signals and emphasized that they are different before and after a mode resonance. We also showed how to adapt an existing model for the resonance-induced GW phase shift to incorporate the fully relativistic properties of the neutron stars. In general, each neutron star passes through two quadrupolar gravitomagnetic resonances corresponding to the  $m = 1$  and  $m = 2$  modes, which for spins of  $\chi \gtrsim 0.005$  lie within the sensitive band of third-generation GW detectors.

We used the above model to perform a data analysis study of the impact of gravitomagnetic effects on the measurements of tidal parameters with third-generation GW detectors, which relied on several simplifying assumptions. In particular, we used quasi-universal relations to reduce all matter parameters to the two tidal deformabilities, considered neutron stars with slightly unequal masses but equal spins and -orientations such that only one set of modes is resonantly excited during the inspiral, and mainly adopted a MCMC approach restricted to a four-dimensional subspace of parameters for GW170817-like events. These case studies enabled us to gain several quantitative insights and demonstrated that gravitomagnetic tides can be important to avoid biases in the inferred  $\tilde{\Lambda}$  and lead to a peaked distribution in  $\delta\tilde{\Lambda}$ , which is flat and thus uninformative when neglecting gravitomagnetic effects.

To gain further insights into the underlying reasons for these results, we analyzed the different contributions to the gravitomagnetic tides, adiabatic versus resonance-induced, and compared the impacts from the  $m = 1$  modes (relevant for the aligned-spin configuration) to those of the  $m = 2$  modes (relevant for the case with misaligned spins). We found that for the  $m = 1$  modes, increasing the spin leads to increasingly better measurements of the tidal parameters. Furthermore, for aligned spins of magnitude  $\chi = 0.005$ , the adiabatic effects are most important to avoid biases in the parameter  $\tilde{\Lambda}$ , while for larger spins of  $\chi = 0.01$  it is the mode resonances. In all cases, the mode resonances have a significant impact on the measurability of  $\delta\tilde{\Lambda}$ . On the other hand, for spin orientations where only the  $m = 2$  modes are resonant, we found no significant changes in the results with increasing spins. We also considered a case with a lower SNR of 400, as is expected for a larger number of events, and found that similar qualitative trends persist. Interestingly, we noticed that while the broadening of the inferred posterior probability distribution seems to scale inversely with the SNR, the broadening of the posterior in  $\delta\tilde{\Lambda}$  is much less than this scaling. This is a promising indication for future measurements but will need to be confirmed with more realistic data analysis studies.

In conclusion, our work represents an exploratory study based on more realistic modeling of gravitomagnetic tides than in previous work. We made several simplifying assumptions and approximations, and neglected a number of additional matter effects that impact the GWs. Our results about the importance of the gravitomagnetic effects for measurements motivate more detailed data analysis studies as well as further advances in the modeling, which we leave to future work.



# Determining the equation of state of neutron stars with Einstein Telescope using tidal effects and r-mode excitations from a population of binary inspirals

## 7.1 Introduction

In this chapter we will quantify to what extent the equation of state – essentially pressure versus density,  $p(\rho)$  – of neutron stars can be probed with third-generation GW observatories, based on inspiral physics alone, but using a population of inspirals. The main EOS-related effect that enters the inspiral signal is that of tides on the neutron stars [34, 109]. These can already be investigated with second-generation detectors [241–243], as has indeed been done with GW170817 [5, 118, 244]. Tidal effects are the most noticeable at high frequencies. However, given sufficiently high SNR, it may also be possible to see resonant r-modes [38], gravitomagnetic excitations of Rossby modes that are induced when the monotonically increasing GW frequency reaches an associated resonance frequency of one of the neutron stars. Assuming slowly rotating neutron stars, these will mainly manifest themselves at lower frequencies, i.e. tens of Hz. Though the imprints of resonant r-modes on GW signals will generally be weak, they can be within reach of third-generation observatories [165]. Moreover, as recently indicated by Ma et al. [168], EOS measurements may gain from the ability to access r-mode information in addition to tidal effects. In this study we will focus on ET, in part because it is predicted to have excellent low frequency sensitivity.

In [168], Fisher matrix estimates were made to assess the measurability of tidal deformabilities and other parameters related to neutron stars in binary inspiral, with or without resonant r-modes. For the purpose of initial estimates, in the latter chapter the r-modes were largely treated in the Newtonian approximation, but it is known that relativistic corrections on both the resonance frequency and the size of the induced GW phase shift can be sizeable; see e.g. [172, 234, 237]. Here we do take such corrections into account, and we introduce and use new universal relations for both. Moreover, we want



to know what is the impact of having a sizeable number of high-SNR BNS signals at one's disposal. Ideally we would want to perform Bayesian parameter estimation simulations, but limited computational resources prevent us from doing so. As a compromise, we will still use the Fisher matrix to obtain multivariate Gaussian approximations for the likelihoods of individual sources, but we sample from those to obtain estimates for EOS measurements with input from multiple detected sources. Recently, catalogs of binary black hole and binary neutron star detections by ET and CE were simulated [127] based on predictions for merger rate as a function of redshift; we will draw from this work to obtain a representative sample for the 20 loudest BNS signals that ET is likely to detect based on its predicted sensitivity curve. Based on these we will arrive at estimates for how accurately one will be able to reconstruct  $p(\rho)$  with observations by ET, with or without r-modes.

The rest of this chapter is structured as follows. In Sec. 7.2 we describe our treatment of resonant r-modes in terms of universal relations. In Sec. 7.3 we explain the setup of our analyses. Results are given in Sec. 7.4. Finally, an overview and conclusions are presented in Sec. 7.5.

## 7.2 Resonant r-modes: Frequencies, phase shifts, and universal relations

As two neutron stars spiral towards each other, the GW frequency increases monotonically, and at one or more points in time it can become equal to an internal resonance frequency of one of the neutron stars. The resulting excitation takes away part of the orbital energy, which speeds up the orbital motion; this in turn gets imprinted upon the phasing of the GW signal. Assuming the two neutron star each undergo near-instantaneous resonances at respective frequencies  $f_0^{(1,2)}$ , the resulting change in the frequency-domain GW phase with respect to the point particle case can be modeled as [34, 38]

$$\Psi_r = \left(1 - \frac{f}{f_0^{(1)}}\right) \Delta\Phi_1 \Theta(f - f_0^{(1)}) + \left(1 - \frac{f}{f_0^{(2)}}\right) \Delta\Phi_2 \Theta(f - f_0^{(2)}), \quad (7.1)$$

where  $\Theta(x)$  denotes the usual step function. Specializing to r-mode excitations, the shifts  $\Delta\Phi_i$ ,  $i = 1, 2$  take the form [168]

$$\Delta\Phi_i = -2 \frac{5\pi^2}{192} \left(\frac{4}{3}\right)^{2/3} \frac{\Omega_i^{2/3}}{\mathcal{M}^{10/3}} \mathcal{I}_i. \quad (7.2)$$

Here  $\Omega_i$ ,  $i = 1, 2$  are the angular rotation frequencies of the neutron stars, and  $\mathcal{M} = (m_1 m_2)^{3/5} / (m_1 + m_2)^{1/5}$  is the chirp mass associated with the component masses  $m_1, m_2$ . The r-mode couplings  $\mathcal{I}_i$  take the form

$$\mathcal{I}_i = (\bar{I}_i^r)^2 m_i^4 \sin^2(\psi_i) \cos^4(\psi_i/2) \left(1 - \frac{m_i}{M}\right), \quad (7.3)$$

where  $M = m_1 + m_2$  is the total mass, and  $\psi_i$  are the angles between the neutron stars' spin vectors  $\mathbf{S}_i$  and the orbital angular momentum. The r-mode *overlaps*  $\bar{I}_i^r$  depend on the neutron stars' internal structure.

Let us now discuss in turn our treatment of r-mode frequencies and overlaps.

### 7.2.1 Universal relation for the r-mode frequencies

For a slowly rotating neutron stars and in the Newtonian limit, the r-mode frequencies in the co-rotating frame are proportional to the angular rotation frequency  $\Omega$ , and given by [38]

$$\omega_{\ell m} = -\frac{2m}{\ell(\ell+1)}\Omega. \quad (7.4)$$

For given values of the spherical harmonic indices  $(\ell, m)$ , the corresponding resonance frequency in the inertial frame is

$$\omega_0 = m\Omega + \omega_{\ell m} = m\Omega - \frac{2m}{\ell(\ell+1)}\Omega. \quad (7.5)$$

The associated GW frequencies appearing in Eq. (7.1) are then  $f_0 = 2\omega_0/(2\pi)$ , or

$$f_0 = \frac{1}{\pi}(m - \kappa)\Omega, \quad (7.6)$$

with  $\kappa = 2m/\ell(\ell+1)$  in the Newtonian limit. For simplicity, in this work we will assume barotropic neutron stars, so that  $|m| = \ell$ , and focus on  $(\ell, m) = (2, 2)$ ; within the Newtonian framework one then has  $\kappa = 2/3$ .

As shown in [172], in a relativistic treatment of slowly rotating stars, the resonance frequency can differ significantly from the Newtonian value. In that work, numerical values for  $\kappa$  were computed for relativistic neutron stars described by a variety of tabulated EOSs, and a fitting formula was obtained for the function  $\kappa(C)$ , with  $C = m/R$  the compactness, where  $R$  is a neutron star's radius. However, in this work we are interested in the imprint of resonant r-modes on GW emission, where it is more convenient to have  $\kappa$  as function of the dimensionless neutron star tidal deformability  $\Lambda$ , since this is a parameter that enters directly into the waveform.

With this in mind, for each value of  $\kappa$  reported in [172] (Table II), we computed  $\Lambda$  for each EOS and compactness listed. This was done using the TOV solver available in LALSuite [108]. As seen in Fig. 7.1, there is a clear dependence of  $\kappa$  on the logarithm of  $\Lambda$ . Using a least-squares fitting method, we find that the functional dependence is approximated well by the universal relation

$$\kappa = 0.3668 + 0.0498 \log(\Lambda) - 0.0025 \log^2(\Lambda), \quad (7.7)$$

with fitting residuals at the  $\mathcal{O}(1\%)$  level.

### 7.2.2 Universal relation for the r-mode overlap

Next we turn to the r-mode overlap. In the Newtonian approximation one has [168]

$$\bar{I}^r = \sqrt{\frac{1}{m^5} \int_0^R \rho r^6 dr}, \quad (7.8)$$

where  $\rho$  is the density of the neutron star,  $m$  its mass, and  $R$  its radius. In [168], a universal relation was obtained for the Newtonian  $\bar{I}^r$  as function of  $\Lambda$ . In this work we

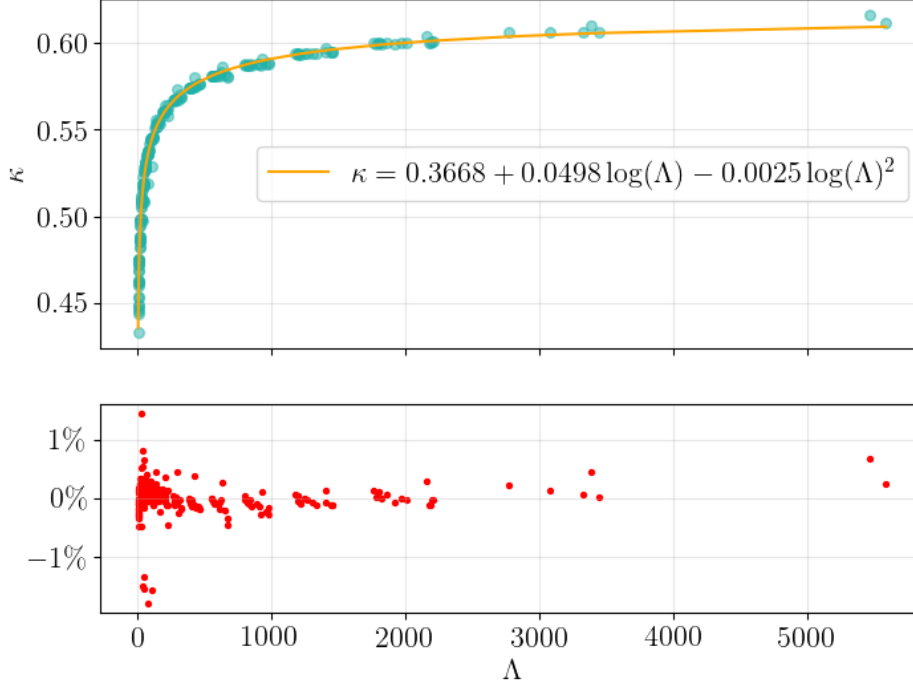


Figure 7.1: Top panel: values of  $\kappa$  and corresponding tidal deformabilities  $\Lambda$  computed for a variety of EOSs and compactnesses listed in [172] (green dots), and the fit for  $\kappa(\Lambda)$  of Eq. 7.7. Bottom panel: fitting residuals.

instead follow the relativistic description in Eq. (5.70), where the following expression was found:

$$\bar{I}^r = \sqrt{\frac{15}{4\pi}(\Sigma_{\text{stat}} - \Sigma_{\text{irr}})}. \quad (7.9)$$

Here  $\Sigma_{\text{stat}}$  and  $\Sigma_{\text{irr}}$  are dimensionless static and irrotational magnetic Love numbers, respectively. Universal relations for these quantities as function of  $\Lambda$  were given in Eq. (6.35). Together with Eq. (7.9), these yield a relation for  $\bar{I}^r(\Lambda)$ .

## 7.3 Setup of the analyses

In this section we describe the waveform model used, the Fisher matrix formalism for obtaining a multivariate Gaussian approximation of likelihoods, the parameterization used for reconstructing EOSs, and our framework for performing such reconstructions using multiple GW detections.

### 7.3.1 Waveform model

We will focus on the inspiral, and use an analytic, frequency domain waveform following the stationary phase approximation [245], which takes the general form

$$\tilde{h}(f) = \mathcal{A} f^{-7/6} e^{i\Psi(f)}. \quad (7.10)$$

Here  $\mathcal{A}$  collects parameters appearing in the amplitude: masses, sky position, orientation of the orbital plane, and luminosity distance to the source. The phase  $\Psi(f)$  can be written as

$$\Psi(f) = \Psi_{\text{PP}}(f) + \Psi_{\text{SO}}(f) + \Psi_{\text{T}}(f) + \Psi_r(f), \quad (7.11)$$

where  $\Psi_{\text{PP}}$  has point particle contributions up to 3.5 post-Newtonian (PN) order, and  $\Psi_{\text{SO}}$  contains spin-orbit effects at 1.5PN; we consider spin-spin effects to be negligible in the case of binary neutron stars.  $\Psi_{\text{T}}$  contains tidal effects at 5PN and 6PN orders [36]. Finally,  $\Psi_r$  is as given in Eq. (7.1); it depends on the r-mode induced phase shifts  $\Delta\Phi_i$ ,  $i = 1, 2$  of Eq. (7.2), which in turn depend on spin tilt angles  $\psi_1, \psi_2$  through Eq. 7.3. As shown in [168] (see their Appendix A), spin precession has a negligible effect during resonance, and in the usual case of simple precession [246],  $\psi_1$  and  $\psi_2$  can be considered approximately constant throughout the inspiral process.

Without the r-mode contribution, the phase depends on the 8 free parameters

$$\vec{\theta}_{nr} = (t_c, \phi_c, m_1, m_2, \tilde{\Lambda}, \delta\tilde{\Lambda}, \chi_{sz}, \chi_{az}), \quad (7.12)$$

whereas with r-modes included, the free parameters are

$$\vec{\theta}_r = (t_c, \phi_c, m_1, m_2, \tilde{\Lambda}, \delta\tilde{\Lambda}, \Omega_1, \Omega_2, \psi_1, \psi_2). \quad (7.13)$$

Here  $t_c$  and  $\phi_c$  are respectively the time and phase of coalescence;  $m_i$ ,  $i = 1, 2$  the component masses;  $\chi_{sz} = (\chi_{1z} + \chi_{2z})/2$  and  $\chi_{az} = (\chi_{1z} - \chi_{2z})/2$  respectively the symmetric and antisymmetric dimensionless spins, with  $\chi_{1z}$  and  $\chi_{2z}$  the spin components in the direction of orbital angular momentum;  $\Omega_i$  the spin angular frequencies of the neutron stars; and  $\psi_i$  the angles between the dimensionless spins and the orbital angular momentum. We note that in the detector frame, the component masses  $m_{1,2}^{\text{det}}$  that directly enter the waveform are redshifted with respect to the source frame masses  $m_{1,2}$ : one has  $m_{1,2}^{\text{det}} = (1+z)m_{1,2}$ , with  $z$  the redshift. With a global network of third-generation (3G) observatories, for BNS signals the luminosity distance can be measured to  $\mathcal{O}(1\%)$  accuracy for the loudest sources [247], and with a cosmological model (e.g. from Planck [248]), distance can be converted to redshift. We will assume that other 3G observatories will be operational at the same time as ET, so that for the high-SNR sources considered below, the distance uncertainties will be sufficiently small that uncertainties on redshift can be neglected in the conversion between source frame and detector frame masses. (In principle we could then also have included tidal information from these other observatories in our analyses, but the aim of this chapter is to specifically assess ET's ability to extract EOS information from the GW phase.) Finally,  $\tilde{\Lambda}$  and  $\delta\tilde{\Lambda}$  are related to the individual neutron stars' tidal deformability parameters ( $\Lambda_1, \Lambda_2$ ) through [249]

$$\begin{aligned} \tilde{\Lambda} = & \frac{8}{3} \left[ (1 + 7\eta - 31\eta^2)(\Lambda_1 + \Lambda_2) \right. \\ & \left. + \sqrt{1 - 4\eta}(1 + 9\eta - 11\eta^2)(\Lambda_1 - \Lambda_2) \right], \end{aligned} \quad (7.14)$$

$$\begin{aligned} \delta\tilde{\Lambda} = & \frac{1}{2} \left[ \sqrt{1 - 4\eta} \left( 1 - \frac{13272}{1319}\eta + \frac{8944}{1319}\eta^2 \right) (\Lambda_1 + \Lambda_2) \right. \\ & \left. + \left( 1 - \frac{15910}{1319}\eta + \frac{32850}{1319}\eta^2 + \frac{3380}{1319}\eta^3 \right) (\Lambda_1 - \Lambda_2) \right], \end{aligned} \quad (7.15)$$

where  $\eta = m_1 m_2 / (m_1 + m_2)^2$  is the symmetric mass ratio.

When comparing the cases with and without r-modes, we can use that

$$\chi_{iz} = \bar{I}_i \Omega_i m_i \cos(\psi_i) \quad (7.16)$$

for  $i = 1, 2$ . Here  $\bar{I}_i$  are normalized moments of inertia, for which one has the universal relation [226]

$$\begin{aligned} \log \bar{I} = & 1.47 + 8.17 \times 10^{-2} \log(\Lambda) + 1.49 \times 10^{-2} \log^2(\Lambda) \\ & + 2.87 \times 10^{-4} \log^3(\Lambda) - 3.64 \times 10^{-5} \log^4(\Lambda). \end{aligned} \quad (7.17)$$

### 7.3.2 Spectral parametrization of the EOS

For the EOS we will use the so-called spectral parameterization in terms of the adiabatic index  $\Gamma(p)$ , defined as [250, 251]

$$\Gamma(p) = \frac{\epsilon + p}{p} \frac{dp}{d\epsilon}, \quad (7.18)$$

where  $\epsilon$  is energy density and  $p$  is pressure. The EOS  $\epsilon(p)$  is obtained from the adiabatic index by writing the above equation as

$$\frac{d\epsilon}{dp} = \frac{\epsilon(p) + p}{p\Gamma(p)}, \quad (7.19)$$

or

$$\epsilon(p) = \frac{\epsilon_0}{\mu(p)} + \frac{1}{\mu(p)} \int_{p_0}^p \frac{\mu(p')}{\Gamma(p')} dp', \quad (7.20)$$

where

$$\mu(p) = \exp \left( - \int_{p_0}^p \frac{1}{p' \Gamma(p')} dp' \right), \quad (7.21)$$

with  $\epsilon_0 = \epsilon(p_0)$  a constant of integration. The EOS  $\epsilon(p)$  can in principle be solved for arbitrary adiabatic index  $\Gamma(p)$ , but here we will spectrally decompose it in terms of a set of polynomial basis functions,

$$\Gamma(p) = \exp \left( \sum_{k=0}^n \gamma_k x^k \right), \quad (7.22)$$

where  $x = \log(p/p_0)$  is a dimensionless pressure variable,  $p_0$  is some reference pressure, and values of  $n$  up to 3 tend to allow for accurate representations of a variety of EOSs [251].

For given coefficients  $\gamma_k$  in Eq. (7.22), the TOV solver available in LALSuite [108] numerically performs the integrals in Eqs. (7.21) and (7.20) to obtain  $\epsilon(p)$  and rest mass density  $\rho(p)$ , which is inverted to arrive at  $p(\rho)$ . The reference pressure  $p_0$ , also called the stitching pressure, is fixed to  $5.3716 \times 10^{32}$  dyne cm<sup>-2</sup>; below this pressure, the EOS called SLY [252] is stitched on. The coefficients  $\gamma_k$ ,  $k = 0, \dots, 3$  are given uniform priors

with ranges  $\gamma_0 \in [0.2, 2.0]$ ,  $\gamma_1 \in [-1.6, 1.7]$ ,  $\gamma_2 \in [-0.6, 0.6]$ , and  $\gamma_3 \in [-0.02, 0.02]$ . The speed of sound  $v_s = \sqrt{dp/d\epsilon}$  is restricted to  $v_s < 1.1c$ , where the 10% leeway is to allow for imperfect parameterization. We also require that EOSs lead to a maximum neutron star mass greater than  $1.97 M_\odot$  [253]. Finally, the adiabatic index is confined to  $\Gamma(p) \in [0.6, 4.5]$  [118].

### 7.3.3 Analysis framework

Let  $\theta^a$  be the components of the parameter vector  $\vec{\theta}$ , which in our case will be either the one from Eq. (7.12) or (7.13), depending on whether or not r-modes are taken into account. For GW events with sufficiently high SNR and assuming stationary, Gaussian noise, the likelihood function for the signal parameters  $\theta^a$  will approximately take the form of a multivariate Gaussian centered on the true values  $\hat{\theta}^a$  [254, 255]. Defining  $\Delta\theta^a = \theta^a - \hat{\theta}^a$ , the likelihood is given by Eq. (2.32)

$$L(\Delta\theta^a) = \mathcal{N} e^{-\frac{1}{2}\Gamma_{ab}\Delta\theta^a\Delta\theta^b}. \quad (7.23)$$

Strictly speaking, Eq. (7.23) pertains to signals  $\tilde{h}(f)$  as seen in a *single* detector, while the baseline design for Einstein Telescope assumes three V-shaped detectors arranged in a triangle [95, 96]. In principle one would then have to project the gravitational wave polarizations  $\tilde{h}_+(f)$ ,  $\tilde{h}_\times(f)$  onto each of the three detectors using the appropriate antenna pattern functions, construct a separate Fisher matrix for each detector, and take the sum of these to obtain the final Fisher matrix. In this work we will consider sources from a catalog constructed as in [127], with SNRs computed for a triangular ET. However, since here we will mainly be interested in information coming from the phasing, for our purposes it will suffice to compute a single Fisher matrix with the ET-D PSD [96] for an L-shaped detector, and with the SNRs set to the values obtained from the triangular ET. In Eq. (2.16) we take the lower frequency cut-off  $f_{\text{low}}$  to be 5 Hz. For  $f_{\text{high}}$  we choose the nominal frequency of the innermost stable circular orbit (ISCO):  $f_{\text{high}} = 1/(6^{3/2}\pi(1+z)M)$ . We note that for stiff EOSs, the two neutron stars might touch before ISCO is reached [242], but the effect of this for the purposes of EOS measurements is marginal [249]. Finally, we point out that the information about mass in the ISCO frequency enters only weakly, through the upper integration limit in the inner product and not through derivatives with respect to mass acting on some window function on the waveform (see [256] for a discussion). In a more realistic setting, additional information would be gained from the frequency where the transition to merger occurs, and indeed from the merger and post-merger parts of the signal themselves [257].

Since we are interested in how well one can measure the EOS with BNS inspiral signals, we need to choose a “true” EOS, which we take to be FPS [258], with  $(\gamma_0, \gamma_1, \gamma_2, \gamma_3) = (1.1561, -0.0468, 0.0081, -0.0010)$ . Given a choice of masses  $m_1, m_2$ , we let the true values of the tidal deformabilities be  $\Lambda_1 = \Lambda_{\text{FPS}}(m_1)$ ,  $\Lambda_2 = \Lambda_{\text{FPS}}(m_2)$ , where  $\Lambda_{\text{FPS}}(m)$  is the dependence set by the given EOS.

The main question in this work is how well ET will be able to determine the EOS, i.e., with what accuracy the EOS parameters  $\vec{E} \equiv (\gamma_0, \gamma_1, \gamma_2, \gamma_3)$  will be measured. To this end, consider the posterior probability density function  $p(\vec{E}, \vec{\theta}|d, \mathcal{H}, \mathcal{I})$ , where  $\vec{\theta}$  denotes the parameters in (7.12) or (7.13) *except* for  $\tilde{\Lambda}$  and  $\delta\tilde{\Lambda}$ , which can be calculated from

$\vec{E}$  together with  $m_1, m_2$ ; other than that,  $d$  denotes the data for a given signal,  $\mathcal{H}$  a waveform model, and  $\mathcal{I}$  any background information we may possess. Bayes' theorem tells us that

$$p(\vec{E}, \vec{\theta}' | d, \mathcal{H}, \mathcal{I}) = \frac{p(d | \vec{E}, \vec{\theta}', \mathcal{H}, \mathcal{I}) p(\vec{E}, \vec{\theta}' | \mathcal{H}, \mathcal{I})}{p(d | \mathcal{H}, \mathcal{I})}, \quad (7.24)$$

where  $p(\vec{E}, \vec{\theta}' | \mathcal{H}, \mathcal{I})$  is the prior probability density for  $\vec{E}$  and  $\vec{\theta}'$ ,  $p(d | \vec{E}, \vec{\theta}', \mathcal{H}, \mathcal{I})$  the likelihood, and  $p(d | \mathcal{H}, \mathcal{I})$  the evidence, which is set by the requirement that the posterior probability density be normalized. Clearly  $p(d | \vec{E}, \vec{\theta}', \mathcal{H}, \mathcal{I})$  is not quite the same as the likelihood  $L(\Delta\theta^a)$  obtained from the Fisher matrix in Eq. (7.23), but given true values  $\hat{\theta}^a$  for the parameters entering the waveform, it is possible to relate the two by writing

$$\begin{aligned} L(\Delta\theta^a) &= p(d | \vec{\theta}', \mathcal{H}, \mathcal{I}) \\ &= p(d | \{\tilde{\Lambda}_{\vec{E}}(m_1, m_2), \delta\tilde{\Lambda}_{\vec{E}}(m_1, m_2), \vec{\theta}'\}, \mathcal{H}, \mathcal{I}) \\ &= p(d | \{\vec{E}, \vec{\theta}'\}, \mathcal{H}, \mathcal{I}), \end{aligned} \quad (7.25)$$

where in the second line,  $\tilde{\Lambda}_{\vec{E}}(m_1, m_2)$  and  $\delta\tilde{\Lambda}_{\vec{E}}(m_1, m_2)$  are the  $\tilde{\Lambda}$  and  $\delta\tilde{\Lambda}$  obtained from the component masses for an EOS with the given parameters  $\vec{E}$ , and the likelihood in the last line is the one appearing in Eq. (7.24).

The way we will proceed is then as follows. Using the Fisher matrix we compute the likelihood of Eq. (7.23), and with the identification of Eq. (7.25) this is turned into a likelihood in terms of the EOS parameters  $\vec{E}$  and waveform parameters  $\vec{\theta}'$ . We initially choose flat priors on all of the individual parameters. Following [259], in the space of the  $\vec{E}$  we perform a principal component analysis to construct a rotated coordinate system that is better tailored to the problem at hand. The likelihood obtained in Eq. (7.25) is then sampled using PyMultiNest [260] with the priors from the previous subsection, which leads to the posterior density in Eq. (7.24). By integrating out the  $\vec{\theta}'$ , this gives us a posterior density for the  $\vec{E}$ ,  $p(\vec{E} | d, \mathcal{H}, \mathcal{I})$ .<sup>1</sup> So far we have focused on a single signal, but given a catalog of detected signals  $d_1, d_2, \dots, d_N$ , information from all of them can be combined to obtain [241]

$$p(\vec{E} | d_1, d_2, \dots, d_N, \mathcal{H}, \mathcal{I}) = p(\vec{E} | \mathcal{H}, \mathcal{I})^{1-N} \prod_{n=1}^N p(\vec{E} | d_n, \mathcal{H}, \mathcal{I}),$$

where in practice the posteriors in the product are Gaussian kernel density estimates of the ones obtained directly with PyMultiNest. Through the TOV solver of LALSuite [108], the above combined posterior distribution for  $\vec{E}$  leads to a distribution over equations of state  $p(\rho)$ .

Sources are picked from a catalog constructed as in [127]. For binary neutron stars this assumes uniformly distributed source frame component masses, where for the primary mass  $m_1 \in [1 M_\odot, M_{\max}]$  and for the secondary mass  $m_2 \in [1 M_\odot, m_1]$ ; here we take  $M_{\max}$

<sup>1</sup>In principle we could have set  $\tilde{\Lambda} = \tilde{\Lambda}_{\vec{E}}(m_1, m_2)$  and  $\delta\tilde{\Lambda} = \delta\tilde{\Lambda}_{\vec{E}}(m_1, m_2)$  directly in the Fisher matrix, and obtained 1-sigma uncertainties on the components of  $\vec{E}$  from the covariance matrix in the usual way [254, 255]. However, introducing too many additional parameters can lead to ill-conditioned Fisher matrices, which will cause problems with numerical inversion.



to be the maximum mass supported by our reference EOS, which is  $M_{\text{max}} = 2.03 M_{\odot}$ . As explained in Sec. 7.3.1, we will assume that for the highest-SNR sources, distances can be measured with sufficient accuracy that uncertainties on redshift can be neglected in the conversion between source frame masses and detector frame masses. The sources were distributed over comoving distance according to a particular prediction for the merger rate as a function of redshift; for details we refer to the original paper [127]. ET is likely to see tens of thousands of BNSs per year, but it is reasonable to expect that most of the information will come from the loudest sources [243]. Hence we consider the 20 loudest sources in the catalog, which have SNRs between 154 and 368. The angles between the spin vectors and the orbital angular momentum are taken to be uniform on the sphere. The rotation angular frequencies of the neutron stars are initially taken to be uniform in the intervals  $\Omega_i \in [0, 2\pi \times 45]$  Hz,  $i = 1, 2$ . This is motivated by the fact that radio observations of the known pulsars in binary neutron stars yield rotation frequencies that appear randomly scattered between 0.36 and 44 Hz [261]; we are not aware of theoretical predictions for the underlying distribution. However, to get an idea of how results change if the range of spin frequencies stretches to higher values, we will also perform an analysis in which all rotation frequencies from the previous one have been multiplied by 3. Given these ranges for the  $\Omega_i$  and the assumed detector lower frequency cut-off of  $f_{\text{low}} = 5$  Hz, there is a small chance for the r-mode GW frequency  $f_0$  in Eq. (7.6) to be below  $f_{\text{low}}$  for one or both neutron stars in a binary, but this will not be the case for any of the simulated sources considered here. We will perform our analyses with r-modes included, in which case the free parameters are the ones in Eq. (7.13), and without r-modes, in which case the free parameters are the ones in (7.12), with the values for  $\chi_{1z}$  and  $\chi_{2z}$  set according to Eq. (7.16).

## 7.4 Results

We are now ready to assess the accuracy with which ET will be able to reconstruct the EOS of dense nuclear matter. However, in order to check the validity of our method, we first compare results for a simulated GW170817-like source seen in Advanced LIGO with those that were obtained in reality for GW170817. Then we turn to ET and perform an analysis on the 20 loud sources mentioned above, with or without r-modes included.

### 7.4.1 Analysis of a GW170817-like signal

Let us consider a signal with properties similar to that of GW170817, the binary neutron star signal discovered with LIGO and Virgo in 2017 [5]. Looking at maximum-likelihood parameter values obtained in [117], we take  $(m_1, m_2) = (1.44, 1.27) M_{\odot}$ ,  $\chi_{1z} = 0.022$ , and  $\chi_{2z} = 0.0081$ . The SNR is set to 32.4, and for the Fisher matrix we take the PSD to be the one for LIGO Livingston at the time of the detection, setting  $f_{\text{low}} = 23$  Hz and  $f_{\text{high}} = 1625.36$  Hz. The effects of r-modes are not included, since they would have had no impact in this case. Given that we do not know what is the true equation of state, we consider the same EOS as in the rest of this chapter (namely FPS), which for the given masses yields  $(\Lambda_1, \Lambda_2) = (387.0, 872.2)$ .

With the formalism described in the previous section, the above parameters lead to a



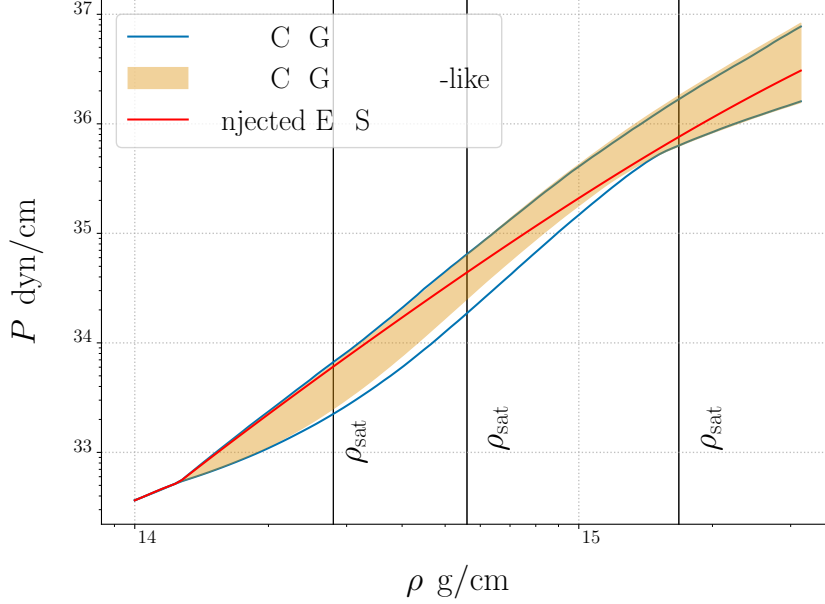


Figure 7.2: Shown is pressure versus density for a GW170817-like signal whose EOS is FPS (the red curve), with a 90% credible region (orange). This is compared with the 90% credible region that was actually obtained for GW170817 (black curves) [118]. Vertical lines indicate a few multiples of the nuclear saturation density,  $\rho_{\text{sat}}$ .

“measurement” of  $p(\rho)$ . Fig. 7.2 shows the underlying  $p(\rho)$  together with a 90% credible region. This is compared with the 90% credible region for  $p(\rho)$  that was actually obtained for this event [118]. Though but a sanity check, the qualitative similarity lends confidence to our methodology.

#### 7.4.2 EOS reconstruction with Einstein Telescope

Next we turn to ET. Fig 7.3 shows the posteriors for the EOS parameters from the 20 loudest sources combined, with r-modes and without r-modes. As expected, we find that the posteriors are more constrained with r-modes than without r-modes. Fig. 7.4 shows the EOS recovery with only the loudest source, the 5 loudest sources, and the 20 loudest sources in our simulated catalog. An improvement in measurement accuracy with increasing number of sources is clearly in evidence. We also note the narrowing of the 90% credible region near twice the nuclear saturation density,  $\rho = 2\rho_{\text{sat}}$ , this being the approximate average density for most of the neutron stars in our BNSs, given the EOS we picked. At  $2\rho_{\text{sat}}$  and for 20 sources, the width of the 90% credible interval for the pressure is  $2.48 \times 10^{33}$  dyn/cm<sup>2</sup>, to be compared with  $3.84 \times 10^{34}$  dyn/cm<sup>2</sup> for our simulated GW170817 as seen by Advanced LIGO. At other densities, ET improves somewhat less on the results for GW170817; the widths  $\Delta P_{90\%}(\rho)$  of the 90% credible intervals for pressure at a few different values for density are shown in Table 7.1, for different numbers of sources in ET, with and without r-modes. Note how at  $2\rho_{\text{sat}}$ , a single loud source in ET improves the pressure estimation by a factor of  $\sim 3$  over GW170817,

but when combining information from 20 sources the improvement is by a factor of  $\sim 15$  with r-modes included (and a factor of  $\sim 11$  without r-modes). Still at  $2\rho_{\text{sat}}$ , the gain from r-modes reaches 36%.

In Table I we also show results at  $6\rho_{\text{sat}}$ , for which a caveat applies. During inspiral, densities up to the central densities of the individual neutron stars are probed, which go up to 3 to 4 times nuclear saturation density (see e.g. [262]); thus, the measurement of the EOS parameters  $\vec{E}$  takes place in a density regime roughly bounded from above by the latter. The spectral representation is known to faithfully represent, over a wide density range, a large number of EOSs, each having particular values of  $\vec{E}$  associated with them [251]. Hence one might be tempted to view results for pressure at  $6\rho_{\text{sat}}$  as being reliably set by the posteriors for the  $\vec{E}$ , regardless of what density regime the latter were obtained from. However, it should be stressed that the spectral representation does not follow from fundamental considerations, and in particular the EOS chosen by nature may not be consistent with it. Thus, results at  $6\rho_{\text{sat}}$  should only be viewed as illustrative.

Sources	$\Delta P_{90\%}(\rho_{\text{sat}})$ [dyn/cm <sup>2</sup> ]	$\Delta P_{90\%}(2\rho_{\text{sat}})$ [dyn/cm <sup>2</sup> ]	$\Delta P_{90\%}(6\rho_{\text{sat}})$ [dyn/cm <sup>2</sup> ]
GW170817-like	$3.85 \times 10^{33}$	$3.84 \times 10^{34}$	$1.18 \times 10^{36}$
ET, 1 source	$2.63 \times 10^{33}$ ( $3.07 \times 10^{33}$ )	$1.25 \times 10^{34}$ ( $1.36 \times 10^{34}$ )	$1.34 \times 10^{36}$ ( $1.33 \times 10^{36}$ )
ET, 5 sources	$2.24 \times 10^{33}$ ( $2.59 \times 10^{33}$ )	$6.13 \times 10^{33}$ ( $7.74 \times 10^{33}$ )	$6.97 \times 10^{35}$ ( $7.24 \times 10^{35}$ )
ET, 10 sources	$7.80 \times 10^{32}$ ( $1.59 \times 10^{33}$ )	$2.88 \times 10^{33}$ ( $4.40 \times 10^{33}$ )	$3.33 \times 10^{35}$ ( $4.20 \times 10^{35}$ )
ET, 20 sources	$6.12 \times 10^{32}$ ( $1.07 \times 10^{33}$ )	$2.48 \times 10^{33}$ ( $3.38 \times 10^{33}$ )	$2.93 \times 10^{35}$ ( $3.48 \times 10^{35}$ )

Table 7.1: The widths of the 90% credible intervals for the pressure at different densities, for our GW170817-like analysis, and for ET with different numbers of sources. In the case of ET, the numbers in brackets are without r-modes.

To gain insight into the effect of the (unknown) range of spin frequencies that neutron stars in binaries may have, we redo the analysis with all spin frequencies in the previous one multiplied by a factor 3. The results are shown in Table 7.2 and in Fig. 7.6, 7.7, 7.8. We see that the numbers as well figures come out rather similar. On the one hand, looking at Eq. (7.2) for the size of the phase shifts induced by r-modes, we see that these depend on the spin frequencies  $\Omega_i$ ,  $i = 1, 2$  through  $\Omega_i^{2/3}$ , so that naively one may have expected a greater effect from r-modes compared to the previous analysis. However, Eq. (7.1) also involves step functions that modify the gravitational wave phase starting from the resonance frequencies  $f_0^{(i)}$ ; if the latter are higher, then the imprint of the resonances is present in a smaller frequency interval, over which a smaller fraction of SNR is accumulated; note also that most of the SNR comes from the low-frequency regime. These two effects act in opposite directions in terms of measurement accuracy, which

presumably explains why the measurement accuracy on the EOS remains qualitatively the same.

Sources	$\Delta P_{90\%}(\rho_{\text{sat}})$ [dyn/cm <sup>2</sup> ]	$\Delta P_{90\%}(2\rho_{\text{sat}})$ [dyn/cm <sup>2</sup> ]	$\Delta P_{90\%}(6\rho_{\text{sat}})$ [dyn/cm <sup>2</sup> ]
ET, 1 source	$2.63 \times 10^{33}$ ( $3.02 \times 10^{33}$ )	$1.24 \times 10^{34}$ ( $1.33 \times 10^{34}$ )	$1.33 \times 10^{36}$ ( $1.29 \times 10^{36}$ )
ET, 5 sources	$2.29 \times 10^{33}$ ( $2.44 \times 10^{33}$ )	$6.84 \times 10^{33}$ ( $7.17 \times 10^{33}$ )	$7.12 \times 10^{35}$ ( $7.19 \times 10^{35}$ )
ET, 10 sources	$7.92 \times 10^{32}$ ( $1.53 \times 10^{33}$ )	$2.96 \times 10^{33}$ ( $4.44 \times 10^{33}$ )	$3.34 \times 10^{35}$ ( $4.26 \times 10^{35}$ )
ET, all sources	$6.32 \times 10^{32}$ ( $1.08 \times 10^{33}$ )	$2.50 \times 10^{33}$ ( $3.52 \times 10^{33}$ )	$2.84 \times 10^{35}$ ( $3.50 \times 10^{35}$ )

Table 7.2: Similar results to the ones in Table 7.1, but for an analysis in which the neutron star rotation frequencies were taken to be larger by a factor 3.

Thus, more advanced GW observatories will dramatically improve our knowledge of the EOS, both through increased sensitivity and by seeing a larger number of sources. The largest improvement happens near densities that actually occur in neutron stars. In Fig. 7.5 we show the accuracy in the measurement of pressure at  $\rho = 2\rho_{\text{sat}}$ , with and without r-modes. The benefit of seeing r-modes is clearly in evidence. Note how in both cases, most of the measurement accuracy and precision comes from combining information from the  $\sim 10$  loudest sources.

## 7.5 Summary and conclusions

We have investigated how well one will be able to determine the equation of state of neutron stars with Einstein Telescope, given that this observatory will detect tens of BNS inspirals per year for which the SNR will be in the hundreds. In doing so we have taken into account the effect of resonant r-modes, which provides additional information about the EOS. The latter were treated fully relativistically, both in terms of the resonance frequency and the r-mode overlap; for the former we introduced a new universal relation linking it to the neutron star tidal deformability, and for the latter we utilized the recent treatment in [237]. A reference EOS was chosen, and general EOSs were represented in terms of the so-called spectral parameterization. Simulations were performed based on the Fisher approximation of the likelihood; when identifying the tidal deformabilities  $\Lambda_i$  with the ones obtained from an EOS with *a priori* unknown parameters  $\vec{E}$ , sampling the likelihood leads to a PDF for  $\vec{E}$ . From this one can reconstruct the EOS in terms of pressure as a function of density. We tested our formalism on a simulated GW170817-like source, and found the accuracy of our  $p(\rho)$  reconstruction to be similar to what was obtained in reality. We then turned to ET, and focused on the 20 loudest sources in

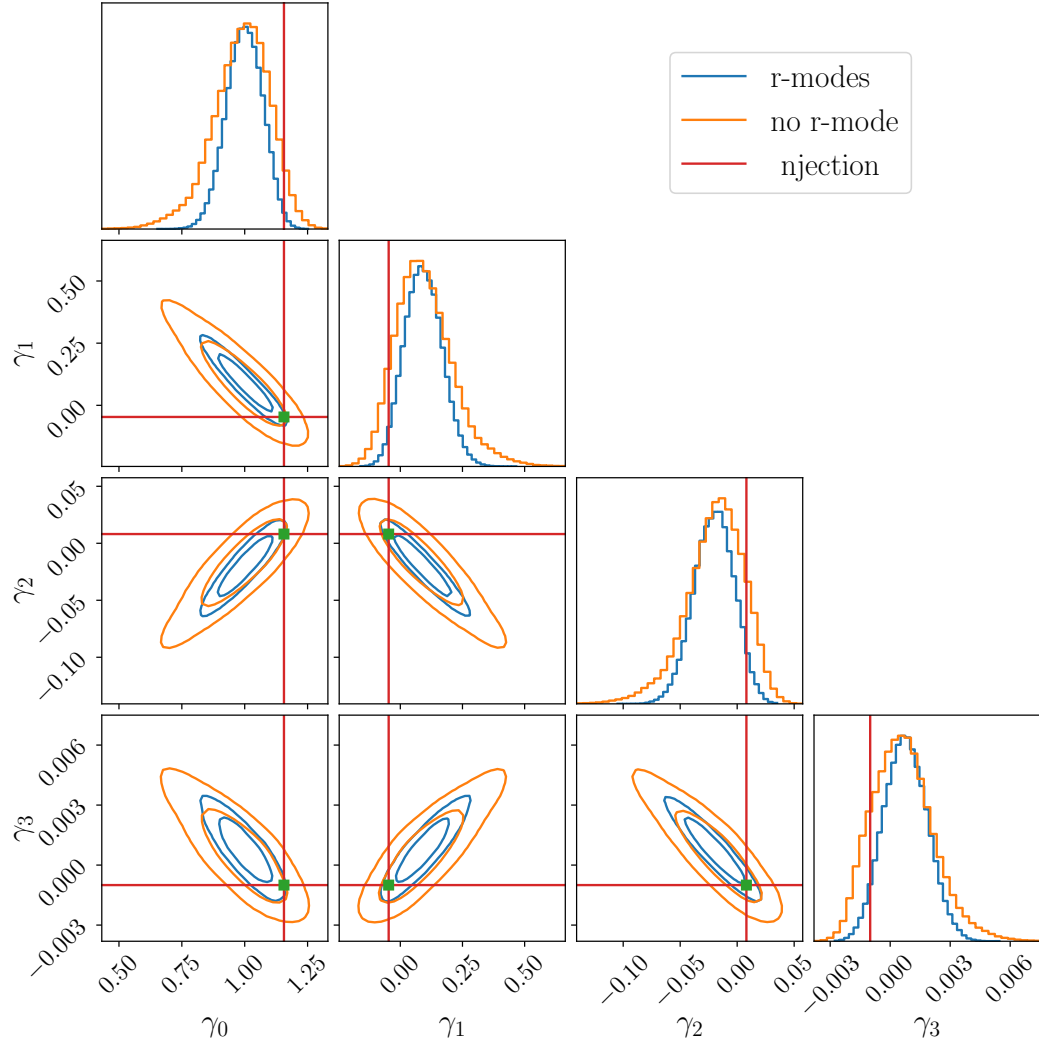


Figure 7.3: Combined posterior probability distributions for the EOS parameters from the 20 loudest sources in ET, the red shows the injected EOS parameters. EOS parameters are more constrained, when r-modes are included than without r-modes.

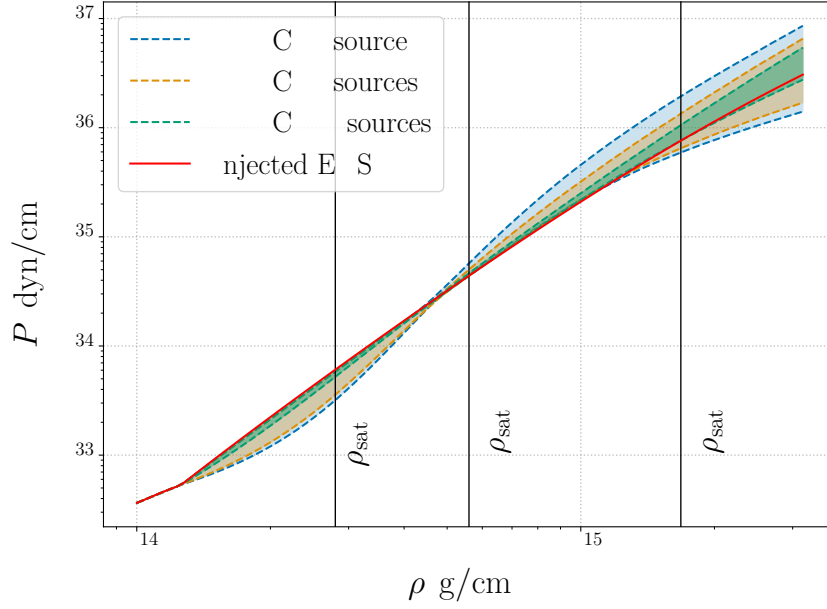


Figure 7.4: 90% credible regions for pressure versus density from the loudest source, the 5 loudest sources, and the 20 loudest sources in ET, in the case where r-modes are included.

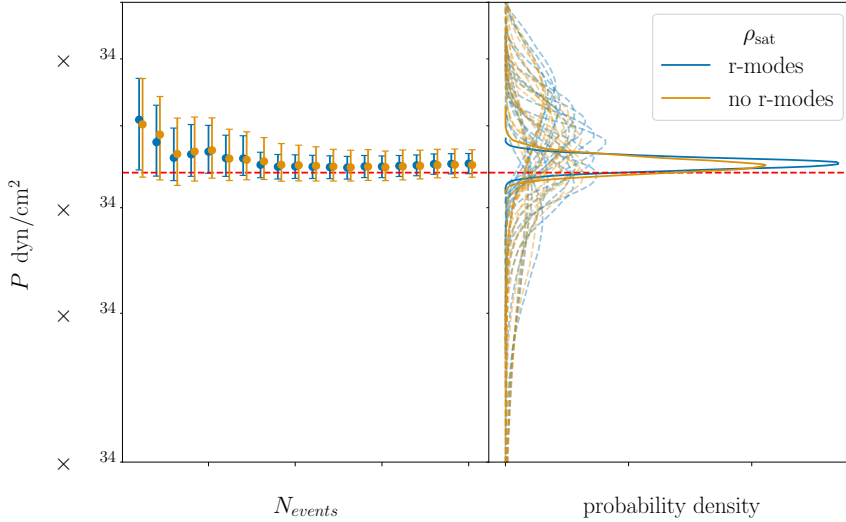


Figure 7.5: Left panel: The improvement in the measurement of pressure at twice the nuclear saturation density; shown is the evolution of medians (the dots) and 90% credible intervals when going from 1 source to 20 sources, where the blue includes r-modes while the orange does not. From left to right, sources are being added in order of decreasing SNR. Right: The individual and combined probability distributions for pressure.

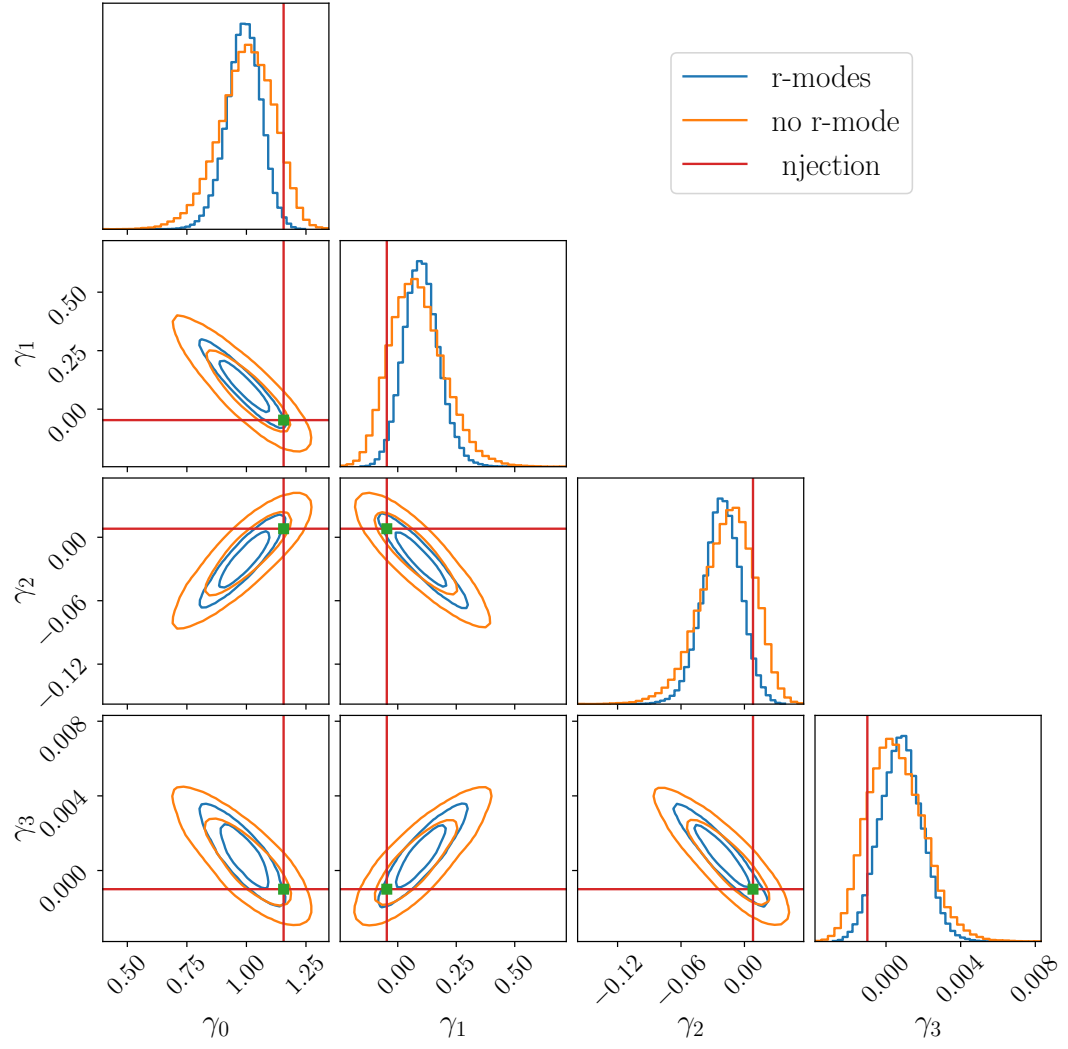


Figure 7.6: Similar plot as the Fig. 7.3, but for an analysis in which the neutron star rotation frequencies were taken to be larger by a factor 3.

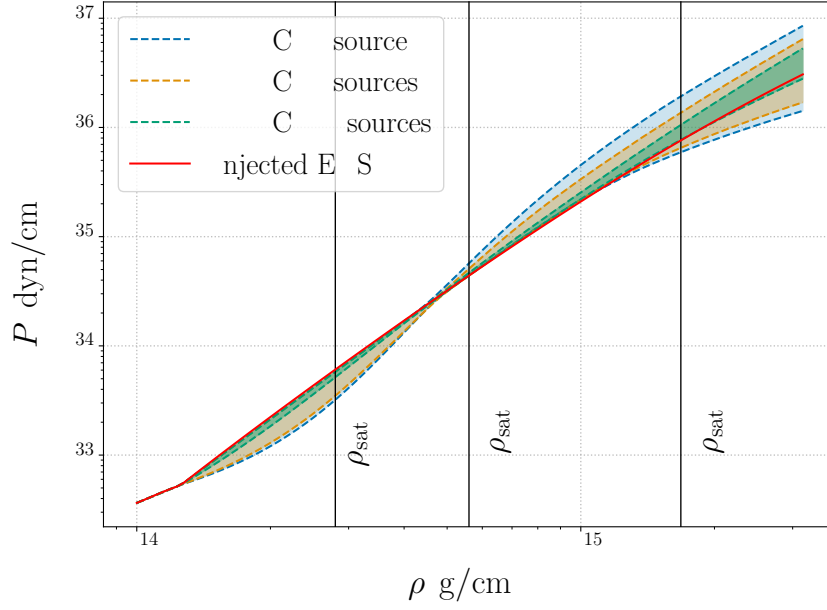


Figure 7.7: Similar plot as the Fig. 7.4, but for an analysis in which the neutron star rotation frequencies were taken to be larger by a factor 3.

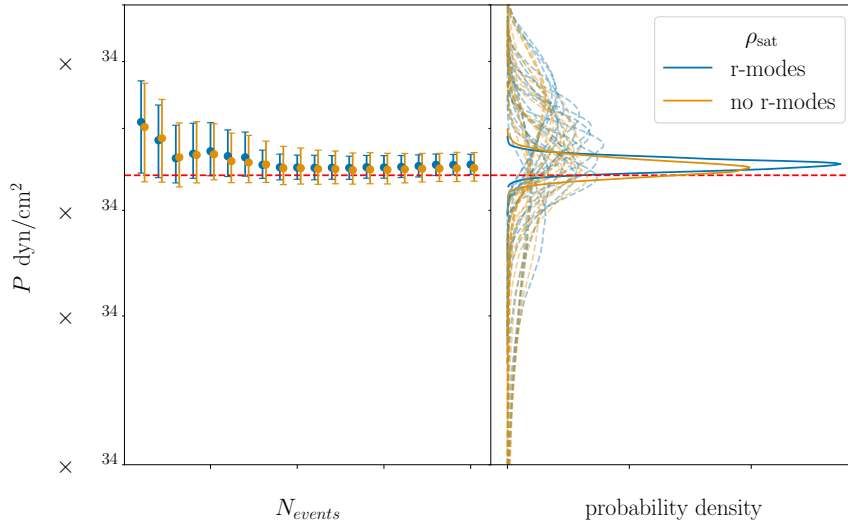


Figure 7.8: Similar plot as the Fig. 7.4, but for an analysis in which the neutron star rotation frequencies were taken to be larger by a factor 3.

a simulated “catalog” with realistic assumptions for the merger rate as a function of redshift.

The estimates arrived at in this chapter are necessarily somewhat crude, due to the approximations made, and especially the limitations of the Fisher matrix formalism [263]. We only aimed to give a rough sense of how accurately ET would be able to pin down the EOS; however, the comparison we made for GW170817 between results from our formalism and actual EOS measurements lends confidence to the reliability of our predictions.

As expected, ET will dramatically improve our knowledge of the EOS compared with what was gleaned from GW170817. In terms of  $p(\rho)$ , the main improvement comes at densities around twice the nuclear saturation density, since this is the typical average density of a neutron star. At that density, ET with 20 loud sources will improve pressure measurements by a factor  $\sim 15$  over GW170817. We found that most of the information will come from the  $\sim 10$  loudest sources.

We also saw that the inclusion of r-modes leads to an improvement in our ability to measure the EOS, at the 50% level in terms of pressure at twice saturation density. This may seem small compared to what is suggested by [168] for a single source, but in that work, an optimistic scenario was assumed where the source had an extremely large SNR (of  $\sim 1500$ ), and values for the angles  $\psi_1, \psi_2$  between the spins and the orbital angular momentum were chosen so as to nearly maximize the effect of r-modes on the gravitational waveform. By contrast, our sources had SNRs between 154 and 368, and randomly chosen angles  $\psi_i$ .

In this work we only considered information about the EOS coming from the inspiral part of the signal. However, ET will also have access to the merger and post-merger [264], which will lead to further improvements in the measurement of the EOS. Assessing the effect of the latter is left for future work.

Here we have assessed the likely improvement in EOS measurements in terms of parameter estimation. However, another avenue is *hypothesis ranking* between proposed equations of state [241, 242], as was investigated in the context of Einstein Telescope in Ref. [265], also for 20 loud sources. Though the results take a different form and can not easily be compared with ours, both analyses highlight the benefits that third-generation gravitational wave observatories will bring in probing the properties of dense nuclear matter.





## Summary and conclusions

The first direct detection of gravitational waves from a binary black hole (GW150914) by the two Advanced LIGO detectors strengthened the foundation of the theory of general relativity as the theory of gravity [4]. The detection of gravitational waves has opened a window to regions of our Universe that are inaccessible to astronomical observation and has started a new era of gravitational wave astronomy. In this thesis, we have explored the existence of dark charges as dark matter candidates in binary black holes. We have modeled the gravitomagnetic tidal effects for binary neutron stars and have studied their effect on the measurability of tidal parameters for binary neutron stars. We also make predictions about the reconstruction of the neutron star equation of state through a catalog of binary neutron star coalescences using electric tidal effects and r-modes for the Einstein Telescope.

### Dark charges on binary black holes

Gravitational waves from binary black holes are modelled by general relativity but they also allow to explore beyond general relativity. We explored the modification of gravitational waves from binary black holes due to minicharged dark matter associated with a hidden  $U(1)$  symmetry, in such a way that the inspiral dynamics of binary black holes can be described by Einstein-Maxwell theory. In particular, the inspiral part of the phasing of the precessing-spin IMRPhenomPv2 inspiral-merger-ringdown waveform was modified to include the effect of such charges up to 1PN order. With this waveform model, we set up and tested a Bayesian framework to discover, or constrain, dark charges on binary black holes using gravitational waves. Then, we applied it to selected binary black hole signals from the second Gravitational Wave Transient Catalog (GWTC-2), namely those with low masses so that most of the signal-to-noise ratio is in the inspiral regime. We found no evidence for charges on the black holes, and placed typical  $1\text{-}\sigma$  bounds on the charge-to-mass ratios of  $|q_i/m_i| \lesssim 0.2 - 0.3$ .

## Modelling of dynamical gravitomagnetic tides for slowly rotating neutron stars

Gravitomagnetic quasi-normal modes of neutron stars are resonantly excited by tidal effects during a binary inspiral, leading to a potentially measurable effect in the gravitational-wave signal. We developed the fully relativistic effective action for gravitomagnetic tidal effects for slowly rotating neutron stars. We constructed the leading order terms in the action using symmetry principle and power counting rules, where the undetermined coefficients in the action encodes the information about neutron-star structure. We showed that the most important coefficients in the action match to the magnetic Love numbers and mode frequencies of the neutron star, showing that both kinds of magnetic Love numbers have physical relevance. We also discussed several interesting dynamical consequences and unusual features compared to the gravitoelectric case, including the frequency-domain response function and time-domain Love operator. Our results provide the foundation for deriving precision predictions of gravitomagnetic effects, and the nuclear physics they encode, for gravitational-wave astronomy.

## Effect of dynamical gravitomagnetic tides on measurability of tidal parameters for binary neutron stars

Gravitational waves (GWs) from binary neutron stars (NSs) have opened unique opportunities to constrain the nuclear equation of state by measuring tidal effects associated with the excitation of characteristic modes of the NSs. This includes gravitomagnetic modes associated with the Coriolis effect, whose frequencies are proportional to the NS's spin frequency, and for which the spin orientation determines the subclass of modes that are predominantly excited. We advanced the GW models by incorporating more realistic descriptions of resonant and adiabatic gravitomagnetic tidal effects for slowly rotating neutron stars in the known results of Fourier-domain GW phasing. We performed a data analysis to study of the impact of gravitomagnetic effects on the measurements of tidal parameters with third-generation GW detectors. We found several quantitative insights and demonstrated that gravitomagnetic tides can be important to avoid biases in the inferred  $\tilde{\Lambda}$  and lead to a peaked distribution in  $\delta\tilde{\Lambda}$ , which is flat and thus uninformative when neglecting gravitomagnetic effects. Our results substantiate the importance of dynamical gravitomagnetic tidal effects for measurements with third-generation detectors.

## Determining the neutron stars equation of state using tidal effects and r-mode (gravitomagnetic $\ell = m = 2$ mode)

Third-generation gravitational wave (GW) observatories such as Einstein Telescope (ET) and Cosmic Explorer (CE) will be ideal instruments to probe the structure of neutron stars through the GWs they emit when undergoing binary coalescence. We investigated how well one will be able to determine the equation of state of neutron stars with Einstein Telescope, given that this observatory will detect tens of BNS inspirals per year for which the SNR will be in the hundreds. We used the GW model which included gravitoelectric tidal effect and resonant gravitomagnetic mode  $\ell = m = 2$  known as r-modes. We found that the ability to observe resonant r-modes would have a noticeable impact

on the neutron star equation of state measurements with ET.

Current gravitational wave detectors have already had a significant impact on testing general relativity, searching for dark charges and neutron star equation of state. However, with next-generation detectors such as Einstein Telescope, Cosmic explorer, and LISA will open many new opportunities and high precision studies to gain insight about dark charges and neutron star equation of state. These advanced detectors will enable us to observe greater diversity of events and larger fraction of the universe. These observations will provide new information about the universe and its astrophysical phenomena to discover new physics.



# Appendix A

## Appendix

### A.1 Useful formulas

Let us collect here some useful formulas from the symmetric-tracefree tensor formalism, see, e.g., Refs. [113, 266, 267]. One can change from a symmetric-tracefree tensor basis (indices  $s_1 \dots s_\ell$ ) to a spherical-harmonic basis labeled by  $(\ell, m)$  using the symbol  $\mathcal{Y}_{s_1 \dots s_\ell}^{\ell m}$ , as in

$$Y_{\ell m}(\theta, \phi) = \mathcal{Y}_{s_1 s_2 \dots s_\ell}^{\ell m} n^{s_1} n^{s_2} \dots n^{s_\ell}, \quad (\text{A.1})$$

where  $n^i = x^i/r$  is the unit radial vector. Here, the ordinary spherical harmonics  $Y^{\ell m}(\theta, \varphi)$  depend on the polar and azimuthal angles  $(\theta, \varphi)$ . The following holds,

$$N_\ell^2 \mathcal{Y}_{s_1 \dots s_\ell}^{*\ell m'} \mathcal{Y}_{s_1 \dots s_\ell}^{\ell m} = \delta_{m'm}, \quad (\text{A.2})$$

where  $N_\ell = \sqrt{4\pi\ell!/(2\ell+1)!!}$ . Furthermore, Eq. (2.26) of Ref. [113] leads to

$$e_z^i \epsilon_{ijk} N_\ell^2 \mathcal{Y}_{j s_1 \dots s_{\ell-1}}^{*\ell m'} \mathcal{Y}_{k s_1 \dots s_{\ell-1}}^{\ell m} = \frac{im}{\ell} \delta_{m'm}, \quad (\text{A.3})$$

where  $\mathbf{e}_z = (0, 0, 1)$ .

A very useful integral formula is Eq. (2.3) in Ref. [113],

$$\int d\Omega n_{i_1} \dots n_{i_{2\ell}} = \frac{N_\ell^2}{\ell!} (\delta_{i_1 i_2} \delta_{i_3 i_4} \dots \delta_{i_{2\ell-1} i_{2\ell}} + \dots), \quad (\text{A.4})$$

where the sum runs over all combinations of indices, and the integral is zero for an odd number of  $\mathbf{n}$ -vectors in the integrand. For instance,

$$\int d\Omega n^i n^j n^k n^\ell = \frac{4\pi}{15} (\delta_{ij} \delta_{kl} + \delta_{ik} \delta_{jl} + \delta_{il} \delta_{jk}). \quad (\text{A.5})$$

From the general integral formula, one can derive an extension of Eqs. (2.5), (2.6) of Ref. [113]: for any two symmetric-tracefree tensors  $A_{s_1 \dots s_\ell}$ ,  $B_{s_1 \dots s_{\ell'}}$  with  $\ell \geq \ell'$  the follow-

ing holds,

$$\begin{aligned}
 & \int d\Omega n^i n^j A_{s_1 \dots s_\ell} n^{s_1} \dots n^{s_\ell} B_{r_1 \dots r_{\ell'}} n^{r_1} \dots n^{r_{\ell'}} \\
 &= \frac{N_{\ell+1}^2}{(\ell+1)} \left[ \delta_{ij} A_{s_1 \dots s_\ell} B_{s_1 \dots s_\ell} \right. \\
 &\quad \left. + 2\ell A_{s_1 \dots s_{\ell-1}(i} B_{j)s_1 \dots s_{\ell-1}} \right] \quad \text{if } \ell = \ell', \quad (\text{A.6a}) \\
 &= N_\ell^2 A_{ijs_1 \dots s_{\ell'}} B_{s_1 \dots s_{\ell'}} \quad \text{if } \ell = \ell' + 2, \quad (\text{A.6b}) \\
 &= 0 \quad \text{else.} \quad (\text{A.6c})
 \end{aligned}$$

The symmetric-tracefree property of  $A$ ,  $B$  is crucial here, which means any two same indices (a trace) give zero, e.g.,  $A_{\dots i \dots i \dots} = 0$ .

The magnetic vector spherical harmonics  $\mathbf{Y}_B^{\ell m}$  play an important role in Chapter 5. They are defined as

$$\mathbf{Y}_{\ell m}^B(\theta, \varphi) = \frac{1}{\sqrt{\ell(\ell+1)}} \mathbf{x} \times \nabla Y^{\ell m}, \quad (\text{A.7})$$

or more explicitly in components as

$$Y_{\ell m}^{Bi}(\theta, \varphi) = \frac{\sqrt{\ell}}{\sqrt{\ell+1}} \epsilon^{ijk} n^j \mathcal{Y}_{ks_1 \dots s_{\ell-1}}^{\ell m} n^{s_1} \dots n^{s_{\ell-1}}. \quad (\text{A.8})$$

The prefactor is chosen to satisfy the normalization

$$\int d\Omega \mathbf{Y}_{\ell' m'}^{B*} \cdot \mathbf{Y}_{\ell m}^B = \delta_{\ell' \ell} \delta_{m' m}. \quad (\text{A.9})$$

This can be shown with the help of Eq. (A.2), recalling that the  $\mathcal{Y}_{s_1 \dots s_\ell}^{\ell m}$  are symmetric tracefree in the indices  $s_i$ , and the relation

$$\begin{aligned}
 \int d\Omega Y_{\ell' m'}^{B* i} Y_{\ell m}^{B j} &= \frac{N_\ell^2 \delta_{\ell' \ell}}{\ell+1} \mathcal{Y}_{as_1 \dots s_{\ell-1}}^{* \ell m'} \mathcal{Y}_{bs_1 \dots s_{\ell-1}}^{\ell m} \\
 &\times [\ell \delta_{ij} \delta_{ab} - (\ell-1) \delta_{ia} \delta_{jb} - \ell \delta_{ib} \delta_{ja}], \quad (\text{A.10})
 \end{aligned}$$

which in turn follows from Eq. (A.6), where one shifts  $\ell \rightarrow \ell-1$  and identifies  $A_{s_1 \dots s_{\ell-1}}^{k, \ell m} = \mathcal{Y}_{ks_1 \dots s_{\ell-1}}^{\ell m}$ , and similar for  $B_{s_1 \dots s_{\ell'-1}}^{k, \ell' m'}$ .

## A.2 Tensor Virial theorem

Using conservation of energy momentum tensor Eq. (1.14),

$$T_{,\nu}^{\mu\nu} = 0, \quad \Rightarrow T_{,0}^{\mu 0} + T_{,i}^{\mu i} = 0. \quad (\text{A.11})$$

Integrating over the source volume and applying Gauss's theorem,

$$\int T_{,0}^{\mu 0} dV + \int T_{,i}^{\mu i} dV = 0, \quad \Rightarrow \frac{\partial}{\partial t} \int T^{\mu 0} dV + \int T^{\mu i} dS_i = 0. \quad (\text{A.12})$$

On the surface  $T^{\mu\nu} = 0$ , therefore

$$\frac{\partial}{\partial t} \int T^{\mu 0} dV = 0 \Rightarrow \int T^{\mu 0} dV = \text{constant}. \quad (\text{A.13})$$

Let us consider, From Eq. (A.11), multiplying by  $x^k$  and integrating over the volume,

$$\frac{\partial}{\partial t} \int T^{\mu 0} x^k dx^3 + \int \frac{\partial T^{\mu i}}{\partial x^i} x^k dx^3 = 0, \quad (\text{A.14})$$

$$\frac{\partial}{\partial t} \int T^{\mu 0} x^k dx^3 + \int \frac{\partial (T^{\mu i} x^k)}{\partial x^i} dx^3 - \int T^{\mu i} \frac{\partial x^k}{\partial x^i} dx^3 = 0, \quad (\text{A.15})$$

$$\frac{\partial}{\partial t} \int T^{\mu 0} x^k dx^3 + \int T^{\mu i} x^k dS_i - \int T^{\mu k} dx^3 = 0, \quad (\text{A.16})$$

where we have used integration by parts and Gauss's theorem. Since on the surface  $T^{\mu\nu} = 0$ , therefore

$$\frac{\partial}{\partial t} \int T^{\mu 0} x^k dx^3 = \int T^{\mu k} dx^3. \quad (\text{A.17})$$

Since  $T^{\mu k}$  is symmetric in  $\mu$  and  $k$ , Eq. (A.17) can be written as

$$\frac{\partial}{\partial t} \int T^{k 0} x^\mu dx^3 = \int T^{k \mu} dx^3. \quad (\text{A.18})$$

Adding Eq. (A.17) and (A.18) together gives,

$$\frac{\partial}{\partial t} \int T^{\mu 0} x^k dx^3 + \frac{\partial}{\partial t} \int T^{k 0} x^\mu dx^3 = \int T^{\mu k} dx^3 + \int T^{k \mu} dx^3, \quad (\text{A.19})$$

which can be simplified as,

$$\frac{\partial}{\partial t} \int (T^{\mu 0} x^k + T^{k 0} x^\mu) dx^3 = 2 \int T^{\mu k} dx^3. \quad (\text{A.20})$$

Consider the  $t$  component of Eq. (A.11),

$$T_{,0}^{00} + T_{,i}^{0i} = 0. \quad (\text{A.21})$$

Let us multiply it by  $x^k x^\mu$  and integrate over volume

$$\frac{\partial}{\partial t} \int T^{00} x^k x^\mu dx^3 + \int \frac{\partial T^{0i}}{\partial x^i} x^k x^\mu dx^3 = 0, \quad (\text{A.22})$$

$$\frac{\partial}{\partial t} \int T^{00} x^k x^\mu dx^3 + \left[ \int \frac{\partial (T^{0i} x^k x^\mu)}{\partial x^i} dx^3 - \int \left( T^{0i} \frac{\partial x^k}{\partial x^i} x^\mu + T^{0i} \frac{\partial x^\mu}{\partial x^i} x^k \right) dx^3 \right] = 0, \quad (\text{A.23})$$

$$\frac{\partial}{\partial t} \int T^{00} x^k x^\mu dx^3 + \int T^{0i} x^k x^\mu dS_i - \int (T^{0k} x^\mu + T^{0\mu} x^k) dx^3 = 0, \quad (\text{A.24})$$



where we have used integration by parts and Gauss's theorem. As before the surface integral vanishes,

$$\frac{\partial}{\partial t} \int T^{00} x^k x^\mu dx^3 = \int (T^{0k} x^\mu + T^{0\mu} x^k) dx^3. \quad (\text{A.25})$$

Let us differentiate Eq. (A.25) with respect to  $t$ ,

$$\frac{\partial^2}{\partial t^2} \int T^{00} x^k x^\mu dx^3 = \frac{\partial}{\partial t} \int (T^{0k} x^\mu + T^{0\mu} x^k) dx^3. \quad (\text{A.26})$$

Inserting Eq. (A.20) in to Eq. (A.26) gives,

$$2 \int T^{\mu k} dx^3 = \frac{\partial^2}{\partial t^2} \int T^{00} x^k x^\mu dx^3. \quad (\text{A.27})$$

### A.3 PN coefficients of the phase in Einstein-Maxwell theory

The PN coefficients in the phase Eq. (4.3) are given by [147]

$$\begin{aligned} \rho_0^{\text{QD}} = & -\frac{G_{12}}{4096\nu} \left\{ \frac{5}{168} \left( 336f_E - 672f_\gamma - f_{1/r^2}^T - f_{v^2/r}^T - f_{v^4}^T \right) \left[ 2 \left( \frac{q_1}{m_1} - \frac{q_2}{m_2} \right)^2 \right] \right. \\ & \left. - 96 + 10(f_{1/r}^V + f_{v^2}^V) + 40f_\gamma \left( \frac{q_1}{m_1} - \frac{q_2}{m_2} \right)^2 + 16 \left( X_2 \frac{q_1}{m_1} + X_1 \frac{q_2}{m_2} \right)^2 \right\}, \end{aligned} \quad (\text{A.28})$$

$$\begin{aligned} \rho_2^{\text{QD}} = & -\frac{5G_{12}}{1548288\nu} \left\{ -32256f_E + \left[ 48 - 20f_E \left( \frac{q_1}{m_1} - \frac{q_2}{m_2} \right)^2 \right] \left( 672f_\gamma + f_{1/r^2}^T + f_{v^2/r}^T + f_{v^4}^T \right) \right. \\ & + \frac{5}{224} \left[ 2 \left( \frac{q_1}{m_1} - \frac{q_2}{m_2} \right)^2 \right] \left( 672f_\gamma + f_{1/r^2}^T + f_{v^2/r}^T + f_{v^4}^T \right)^2 - \left( 672f_\gamma + f_{1/r^2}^T + f_{v^2/r}^T + f_{v^4}^T - 336f_E \right) \\ & \left. \times \left[ 10(f_{1/r}^V + f_{v^2}^V) + 40f_\gamma \left( \frac{q_1}{m_1} - \frac{q_2}{m_2} \right)^2 + 16 \left( X_2 \frac{q_1}{m_1} + X_1 \frac{q_2}{m_2} \right)^2 \right] \right\}. \end{aligned} \quad (\text{A.29})$$

where the coefficients  $f_E$  and  $f_\gamma$  are defined as

$$f_E = \frac{-1}{3G_{12}^2} \left[ G_{12}^2 \left( \frac{1+\nu}{4} + \frac{3}{1 - \frac{q_1 q_2}{M\mu}} \right) - 1 - X_1 \frac{q_2^2}{M\mu} - X_2 \frac{q_1^2}{M\mu} + 2 \frac{q_1 q_2}{M\mu} \right], \quad (\text{A.30})$$

$$f_\gamma \equiv \frac{1}{6G_{12}^2} \left[ G_{12}^2 (1 - 2\nu) + 3G_{12} + 2 + 2 \frac{q_2^2}{M\mu} X_1 + 2 \frac{q_1^2}{M\mu} X_2 - 4 \frac{q_1 q_2}{M\mu} \right]. \quad (\text{A.31})$$

The coefficients due to the vector flux are given by,

$$\begin{aligned}
f_{v^2}^V &= \frac{2}{5} \left( X_2^2 \frac{q_1}{m_1} - X_1^2 \frac{q_2}{m_2} \right) \left( \frac{q_1}{m_1} - \frac{q_2}{m_2} \right) + \frac{2}{M} (X_1 - X_2) (q_1 + q_2) \left( \frac{q_1}{m_1} - \frac{q_2}{m_2} \right) \\
&\quad + \frac{1}{1 - \frac{q_1 q_2}{M\mu}} \left( \frac{q_1}{m_1} - \frac{q_2}{m_2} \right)^2 \left( 2 + 6\nu + \frac{q_1 q_2}{M\mu} (1 - 6\nu) \right), \\
f_{\dot{r}^2}^V &= - \left( \frac{q_1}{m_1} - \frac{q_2}{m_2} \right)^2 \left[ 3\nu + \frac{(X_1 - X_2) (q_1 + q_2)}{M \left( \frac{q_1}{m_1} - \frac{q_2}{m_2} \right)} + \frac{8 - 4\nu - 2 \frac{q_1 q_2}{M\mu} (1 - 2\nu)}{1 - \frac{q_1 q_2}{M\mu}} \right], \\
f_{1/r}^V &= -2 \left( \frac{q_1}{m_1} - \frac{q_2}{m_2} \right)^2 \left[ 2\nu + \frac{2}{5} \frac{X_2^2 q_1 / m_1 - X_1^2 q_2 / m_2}{q_1 / m_1 - q_2 / m_2} - \frac{q_1 q_2}{M\mu} \frac{5}{\left( 1 - \frac{q_1 q_2}{M\mu} \right)^2} \right. \\
&\quad \left. + \frac{(X_1 - X_2) (q_1 + q_2)}{M \left( \frac{q_1}{m_1} - \frac{q_2}{m_2} \right)} + \frac{4 + X_2 \frac{q_1^2}{M\mu} + X_1 \frac{q_2^2}{M\mu}}{\left( 1 - \frac{q_1 q_2}{M\mu} \right)^2} \right].
\end{aligned} \tag{A.32}$$

and the ones due to the tensor flux are given by

$$\begin{aligned}
f_{v^4}^T &= \left[ \frac{785 - 281 \frac{q_1 q_2}{M\mu}}{1 - \frac{q_1 q_2}{M\mu}} - 852\nu \right] \\
f_{v^2 \dot{r}^2}^T &= -2 \left[ \frac{1487 - 563 \frac{q_1 q_2}{M\mu}}{1 - \frac{q_1 q_2}{M\mu}} - 1392\nu \right], \\
f_{\dot{r}^4}^T &= 3 \left[ \frac{687 - 267 \frac{q_1 q_2}{M\mu}}{1 - \frac{q_1 q_2}{M\mu}} - 620\nu \right], \\
f_{1/r^2}^T &= 16(1 - 4\nu),
\end{aligned} \tag{A.33}$$

$$\begin{aligned}
f_{v^2/r}^T &= - \frac{8}{\left( 1 - \frac{q_1 q_2}{M\mu} \right)^2} \left[ 20(17 - \nu) + 84 \frac{q_1^2}{M\mu} X_2 + 84 \frac{q_2^2}{M\mu} X_1 + \frac{q_1^2 q_2^2}{M^2 \mu^2} (67 - 20\nu) - \frac{q_1 q_2}{M\mu} (491 - 40\nu) \right], \\
f_{\dot{r}^2/r}^T &= \frac{8}{\left( 1 - \frac{q_1 q_2}{M\mu} \right)^2} \left[ (367 - 15\nu) + 84 \frac{q_1^2}{M\mu} X_2 + 84 \frac{q_2^2}{M\mu} X_1 + \frac{q_1^2 q_2^2}{M^2 \mu^2} (73 - 15\nu) - \frac{2q_1 q_2}{M\mu} (262 - 15\nu) \right].
\end{aligned} \tag{A.34}$$

# Public summary

---

Our story begins back in ancient Greek times, when philosophers like Aristotle pondered about the motion of objects in the heavens and on earth. Aristotle believed that the natural state of an object is to be at rest and objects fell to the ground because they were trying to reach their natural place, which was the center of the universe.

This view held for many centuries, until Galileo formulated the law of inertia, which states that an object at rest will remain at rest and an object in motion will remain in motion with a constant velocity unless acted upon by an external force. He also discovered the law of falling bodies, which states that all objects fall to the ground with the same acceleration regardless of their weight.

Building upon Galileo's work, Newton developed a mathematical theory of gravity that could explain the motion of planets around the Sun. He also showed that the same gravitational force that causes an apple to fall from a tree is responsible for keeping the planets in orbit around the Sun. But Newton's theory had certain limitations, cause and effect in this theory were instantaneous which is not compatible with special theory of relativity and it couldn't explain the slight wobbling of Mercury's orbit. This led to the development of Einstein's theory of general relativity.

In 1915, Albert Einstein introduced the theory of general relativity, which describes gravity as a curvature of spacetime. Massive objects distort the spacetime curvature which affects the motion of other objects in the vicinity. In other words, the geometry of spacetime is not flat but rather curved in the presence of matter. In 1916, Albert Einstein predicted the existence of gravitational waves from his theory of general relativity. But, he did not believe they existed as these waves were obtained by linearization of general relativity and not from full nonlinear theory of general relativity. It was not until around 1962 that the mathematicians Ivor Robinson and Andrzej Trautman found explicit wave solutions to the full nonlinear theory of general relativity, which established the existence of gravitational waves. In 1974, the first indirect evidence of gravitational waves comes from discovery of a binary neutron star system known as Hulse–Taylor binary. In 1994, the construction of the Laser Interferometer Gravitational-Wave Observatory (LIGO) began for direct detection of gravitational waves.

In 2015, the Advanced Laser Interferometer Gravitational-wave Observatory made the first direct detection of gravitational waves signal from a binary black hole. The signal from this event matched the prediction of general relativity. This signal is referred to as GW150914, which was emitted by a binary black hole with masses of  $M_{\text{sun}}$  and  $29 M_{\text{sun}}$  at a distance of 1.4 billion lightyears. The radiated energy from the gravitational wave event GW150914 was estimated to be 3 solar masses, which is equivalent to the energy released by the conversion of 3 times the mass of the Sun into pure energy according to Einstein's famous equation  $E = mc^2$ .

In 2017, the first gravitational wave signal from a binary neutron star merger, GW170817, was detected by both Advanced LIGO and Advanced Virgo. From this merger, a gamma ray burst was detected by the Fermi Gamma-ray Space Telescope and the INTErnational Gamma-Ray Astrophysics Laboratory (INTEGRAL) spacecraft which initiated a

new era of multi-messenger astronomy.

## Neutron star matter

Neutron stars are the most densest objects in our universe which are formed in supernova explosions. This makes neutron stars ideal astrophysical laboratories for testing theories of dense matter physics. A typical neutron star has a mass of the order of 1.4 solar masses and a radius of 12 km. The matter inside a neutron star is characterised by the relation between pressure and density, known as the neutron star equation of state. Equation of states of neutron stars are modelled by various theories in nuclear physics and quantum chromodynamics.

A neutron star in a binary system is deformed due to tidal forces of its companion, either a neutron star or a black hole. This effect is similar to what happens here on Earth when the moon's gravity raises the ocean tides. Internal oscillations of the neutron star arise when the companion's tidal force varies at a frequency close to the star's characteristic frequency. This is like a bridge oscillating when a band marches at a pace matching its frequency. The amount of tidal deformation and the characteristic frequency depend on the equation of state of the neutron star matter. Any tidal response of the star leaves a distinct imprint on the gravitational waves emitted by the binary. Thus, gravitational waves will reveal unique information about the exotic interior of the neutron stars.

There are two types of tidal effects: gravitoelectric and gravitomagnetic. Gravitoelectric are leading order tidal effects while gravitomagnetic are next to leading order tidal effects. In this thesis, we modelled the gravitomagnetic tides for a binary neutron stars and their effect on the gravitational waves signal. We used this model to understand the effect of gravitomagnetic tides on measuring the equation of state of neutron stars using third-generation gravitational wave observatories such as Einstein Telescope and Cosmic Explorer.

## Dark Charges

Most of the matter in the Universe is made of dark matter which cannot be directly observed. It is called "dark" because it does not interact with light or other forms of electromagnetic radiation. Its presence can be inferred from its gravitational effects on visible matter, such as galaxies and clusters of galaxies. Over the years, many candidates of dark matter have been proposed, one of them being dark charges. These are reminiscent of electrons, but their charge-to-mass ratio is smaller. They can accumulate on binary black holes through various astrophysical process. In this thesis, we explored the possibility of detecting dark charges using gravitational waves from binary black holes.

# Openbare samenvatting

---

Ons verhaal begint in de Griekse oudheid, toen filosofen als Aristoteles nadachten over de beweging van voorwerpen in de hemel en op aarde. Aristoteles geloofde dat de natuurlijke staat van een voorwerp in rust is en dat voorwerpen op de grond vielen omdat zij probeerden hun natuurlijke plaats, het centrum van het universum, te bereiken.

Deze opvatting hield vele eeuwen stand, totdat Galileo de wet van de traagheid formuleerde, die stelt een object dat in rust is, in rust blijft en een object in beweging met een constante snelheid blijft bewegen, tenzij er een externe kracht op inwerkt. Hij ontdekte ook de wet van de vallende lichamen, die stelt dat alle voorwerpen met dezelfde versnelling op de grond vallen, ongeacht hun gewicht.

Voortbouwend op het werk van Galileo ontwikkelde Newton een wiskundige theorie van de zwaartekracht die de beweging van planeten rond de zon kon verklaren. Hij toonde ook aan dat dezelfde zwaartekracht die ervoor zorgt dat een appel van de boom valt, verantwoordelijk is om de planeten in een baan rond de zon te houden. Maar Newtons theorie had bepaalde beperkingen: oorzaak en gevolg waren in deze theorie ogenblikkelijk, wat niet verenigbaar is met de speciale relativiteitstheorie, en ze kon lichte schommeling van de baan van Mercurius niet verklaren. Dit leidde tot de ontwikkeling van Einsteins algemene relativiteitstheorie.

In 1915 introduceerde Albert Einstein de algemene relativiteitstheorie, die de zwaartekracht beschrijft als een kromming van de ruimtetijd. Massieve objecten vervormen de kromming van de ruimtetijd, wat de beweging van andere objecten in de buurt beïnvloedt. Met andere woorden, de geometrie van de ruimtetijd is niet vlak, maar gekromd in aanwezigheid van materie. In 1916 voorspelde Albert Einstein het bestaan van gravitatiegolven vanuit zijn algemene relativiteitstheorie. Maar hij geloofde niet dat ze bestonden omdat deze golven werden verkregen door linearisatie van algemene relativiteit en niet door volledige niet-lineaire algemene relativiteitstheorie. Pas rond 1962 vonden de wiskundigen Ivor Robinson en Andrzej Trautman expliciete golfoplossingen voor de volledige niet-lineaire algemene relativiteitstheorie, die het bestaan van gravitatiegolven vaststelden. In 1974 komt het eerste indirecte bewijs van gravitatiegolven van de ontdekking van een binair neutronenster systeem dat bekend staat als Hulse-Taylor binair. In 1994 begon de bouw van het Laser Interferometer Gravitational-Wave Observatory (LIGO) voor de directe detectie van gravitatiegolven.

In 2015 deed het Advanced LIGO de eerste directe detectie van zwaartekrachtsgolven, een signaal van een binair zwart gat. Het signaal van deze gebeurtenis kwam overeen met de voorspelling van de algemene relativiteit. Dit signaal wordt GW150914 genoemd en werd uitgezonden door een binair zwart gat met een massa van  $M_{\odot}$  en  $29 M_{\odot}$  op een afstand van 1,4 miljard lichtjaar. De uitgestraalde energie van het zwaartekrachtgolfgebeuren GW150914 werd geschat op ongeveer 3 zonsmassa's, wat overeenkomt met de energie die vrijkomt bij de omzetting van 3 keer de massa van de zon in zuivere energie volgens Einsteins beroemde vergelijking  $E = mc^2$ .

In 2017 werd het eerste zwaartekrachtgolfsignaal van een binaire neutronensterfusie, GW170817, gedetecteerd door zowel Advanced LIGO als Advanced Virgo. Uit deze

fusie werd een gammastraaluitbarsting gedetecteerd door de Fermi Gamma-ray Space Telescope en het INTErnational Gamma-Ray Astrophysics Laboratory (INTEGRAL) ruimtevaartuig, waarmee een nieuw tijdperk van multi-messenger astronomie werd ingeluid.

## Neutronenster-materie

Neutronensterren zijn de meest dichte objecten in ons heelal, die worden gevormd bij supernova-explosies. Dit maakt neutronensterren tot ideale astrofysische laboratoria voor het testen van theorieën over de fysica van dichte materie. Typische neutronensterren hebben een massa in de orde van grootte van 1,4 zonsmassa's en een straal van 12 km. De materie in een neutronenster wordt gekenmerkt door de relatie tussen druk en dichtheid, die bekend staat als de toestandsvergelijking. De toestandsvergelijking van neutronensterren wordt gemodelleerd door verschillende theorieën uit de kernfysica en de kwantumchromodynamica. Ze kan worden onderzocht door binaire neutronensterren te laten fuseren en de getijden te meten.

Een neutronenster in een binair systeem wordt vervormd door getijdenkrachten van zijn begeleider, een neutronenster of een zwart gat. Dit effect is vergelijkbaar met wat hier op aarde gebeurt wanneer de zwaartekracht van de maan de getijden van de oceanen doet toenemen. Op dezelfde manier vervormt de neutronenster in reactie zijn begeleider. De interne trillingen van de neutronenster ontstaan wanneer de getijdenkracht van de begeleider varieert met een frequentie die dicht bij de karakteristieke frequentie van de ster ligt. Dit is als een brug die oscilleert wanneer een band marcheert met een frequentie die overeenkomt met zijn frequentie. De hoeveelheid getijdevervorming en de karakteristieke frequentie zijn afhankelijk van de toestandsvergelijking van de materie van de neutronenster. Elke getijdenreactie van de ster laat een duidelijke afdruk achter op de zwaartekrachtgolven die de binaire ster uitzendt. Gravitatiegolven zullen dus unieke informatie onthullen over het exotische inwendige van neutronensterren.

Er zijn twee soorten getijde-effecten: gravitoelectische en gravitomagnetische. Gravitoelectische zijn getijde-effecten van de eerste orde, terwijl gravitomagnetische naast hogere-orde getijde-effecten zijn. In dit proefschrift hebben we de gravitomagnetische getijden gemodelleerd voor een binaire neutronenster en het effect daarvan op het zwaartekrachtsgolvensignaal van een binaire neutronenster. We hebben dit model gebruikt om het effect van gravitomagnetische getijden op het meten van de toestandsvergelijking van neutronensterren met detectoren van de derde generatie (zoals Einstein Telescope en Cosmic Explorer) te begrijpen.

## Donkere ladingen

De meeste materie in het heelal bestaat uit donkere materie die niet rechtstreeks kan worden waargenomen. Het wordt "donker" genoemd omdat het niet reageert met licht of andere vormen van elektromagnetische straling. Zijn aanwezigheid kan worden afgeleid uit zijn gravitatie-effecten op zichtbare materie, zoals sterrenstelsels en clusters van sterrenstelsels. In de loop der jaren zijn vele kandidaten voor donkere materie voorgesteld, waarvan er één bekend staat als donkere ladingen. doet denken aan elektronen, maar

met een kleinere verhouding van lading tot massa. Deze donkere ladingen kunnen door verschillende astrofysische processen op binaire zwarte gaten worden geaccumuleerd. In dit proefschrift onderzochten we de mogelijkheid om donkere ladingen te detecteren met behulp van gravitatiegolven van binaire zwarte gaten.

# Curriculum Vitae

---

## Personal Information

Name: Pawan Kumar Gupta  
Nationality: Indian  
Birth Data: 25th of July 1994  
Email: p.gupta@nikhef.nl p.k.gupta@uu.nl

## Education

2019-2023: Ph.D. in PHYSICS  
Nikhef & GRASP, Utrecht University; Prof. dr. C. Van Den Broeck  
and Dr. Tanja Hinderer  
2013-2018: Integrated M.Sc. in PHYSICS  
UM- DAE Centre for Excellence in Basic Sciences, Mumbai

## Publications

**Pawan Kumar Gupta**, “Binary dynamics from Einstein-Maxwell theory at second post-Newtonian order using effective field theory,” [arXiv:2205.11591](#) (2022).

**Pawan Kumar Gupta**, Jan Steinhoff, Tanja Hinderer, “Relativistic effective action of dynamical gravitomagnetic tides for slowly rotating neutron stars,” [Phys. Rev. Research 3, 013147](#) (2021).

**Pawan Kumar Gupta**, Jan Steinhoff, Tanja Hinderer, “Effect of dynamical gravitomagnetic tides on measurability of tidal parameters for binary neutron star using gravitational waves,” [arXiv:2302.11274](#) (2023).

**Pawan Kumar Gupta**, Anna Puecher, Peter T.H. Pang, Justin Janquart, Gideon Koekoek, Chris Van Den Broeck, “Determining the equation of state of neutron stars with Einstein Telescope using tidal effects and r-mode excitations from a population of binary inspirals,” [arXiv:2205.01182](#) (2022).

**Pawan Kumar Gupta**, Thomas F.M. Spieksma, Peter T.H. Pang, Gideon Koekoek, Chris Van Den Broeck, “Bounding dark charges on binary black holes using gravitational waves,” [Phys. Rev. D 104, 063041](#) (2021).

Andrey A. Shoom, **Pawan K. Gupta**, Badri Krishnan, Alex B. Nielsen, Collin D. Capano, “Testing GR with the Gravitational Wave Inspiral Signal GW170817,” [arXiv:2105.02191v1](#) (2021).





# Bibliography

- [1] Albert Einstein. “Näherungsweise Integration der Feldgleichungen der Gravitation”. In: *Sitzungsberichte der Königl. Preussischen Akademie der Wissenschaften* (Jan. 1916), pp. 688–696.
- [2] J. H. Taylor, L. A. Fowler, and P. M. McCulloch. “Measurements of general relativistic effects in the binary pulsar PSR 1913+16”. In: *Nature* 277 (1979), pp. 437–440. DOI: [10.1038/277437a0](https://doi.org/10.1038/277437a0).
- [3] J. Aasi et al. “Advanced LIGO”. In: *Class. Quant. Grav.* 32 (2015), p. 074001. DOI: [10.1088/0264-9381/32/7/074001](https://doi.org/10.1088/0264-9381/32/7/074001). arXiv: [1411.4547](https://arxiv.org/abs/1411.4547) [gr-qc].
- [4] B. P. Abbott et al. “Observation of Gravitational Waves from a Binary Black Hole Merger”. In: *Phys. Rev. Lett.* 116 (6 Feb. 2016), p. 061102. DOI: [10.1103/PhysRevLett.116.061102](https://doi.org/10.1103/PhysRevLett.116.061102). URL: <https://link.aps.org/doi/10.1103/PhysRevLett.116.061102>.
- [5] B. P. Abbott et al. “GW170817: Observation of Gravitational Waves from a Binary Neutron Star Inspiral”. In: *Phys. Rev. Lett.* 119.16 (2017), p. 161101. DOI: [10.1103/PhysRevLett.119.161101](https://doi.org/10.1103/PhysRevLett.119.161101). arXiv: [1710.05832](https://arxiv.org/abs/1710.05832) [gr-qc].
- [6] F. Acernese et al. “Advanced Virgo: a second-generation interferometric gravitational wave detector”. In: *Class. Quant. Grav.* 32.2 (2015), p. 024001. DOI: [10.1088/0264-9381/32/2/024001](https://doi.org/10.1088/0264-9381/32/2/024001). arXiv: [1408.3978](https://arxiv.org/abs/1408.3978) [gr-qc].
- [7] B. P. Abbott et al. “Tests of general relativity with GW150914”. In: *Phys. Rev. Lett.* 116.22 (2016). [Erratum: *Phys. Rev. Lett.* 121, 129902 (2018)], p. 221101. DOI: [10.1103/PhysRevLett.116.221101](https://doi.org/10.1103/PhysRevLett.116.221101). arXiv: [1602.03841](https://arxiv.org/abs/1602.03841) [gr-qc].
- [8] B. P. Abbott et al. “Binary Black Hole Population Properties Inferred from the First and Second Observing Runs of Advanced LIGO and Advanced Virgo”. In: *Astrophys. J. Lett.* 882.2 (2019), p. L24. DOI: [10.3847/2041-8213/ab3800](https://doi.org/10.3847/2041-8213/ab3800). arXiv: [1811.12940](https://arxiv.org/abs/1811.12940) [astro-ph.HE].
- [9] B. P. Abbott et al. “Tests of General Relativity with GW170817”. In: *Phys. Rev. Lett.* 123.1 (2019), p. 011102. DOI: [10.1103/PhysRevLett.123.011102](https://doi.org/10.1103/PhysRevLett.123.011102). arXiv: [1811.00364](https://arxiv.org/abs/1811.00364) [gr-qc].
- [10] B. P. Abbott et al. “Tests of General Relativity with the Binary Black Hole Signals from the LIGO-Virgo Catalog GWTC-1”. In: *Phys. Rev. D* 100.10 (2019), p. 104036. DOI: [10.1103/PhysRevD.100.104036](https://doi.org/10.1103/PhysRevD.100.104036). arXiv: [1903.04467](https://arxiv.org/abs/1903.04467) [gr-qc].

- [11] R. Abbott et al. “Tests of general relativity with binary black holes from the second LIGO-Virgo gravitational-wave transient catalog”. In: *Phys. Rev. D* 103.12 (2021), p. 122002. DOI: [10.1103/PhysRevD.103.122002](https://doi.org/10.1103/PhysRevD.103.122002). arXiv: [2010.14529](https://arxiv.org/abs/2010.14529) [gr-qc].
- [12] Katherine Garrett and Gintaras Duda. “Dark Matter: A Primer”. In: *Adv. Astron.* 2011 (2011), p. 968283. DOI: [10.1155/2011/968283](https://doi.org/10.1155/2011/968283). arXiv: [1006.2483](https://arxiv.org/abs/1006.2483) [hep-ph].
- [13] Stefano Profumo, Leonardo Giani, and Oliver F. Piattella. “An Introduction to Particle Dark Matter”. In: *Universe* 5.10 (2019), p. 213. DOI: [10.3390/universe5100213](https://doi.org/10.3390/universe5100213). arXiv: [1910.05610](https://arxiv.org/abs/1910.05610) [hep-ph].
- [14] Nicolás Bernal et al. “The Dawn of FIMP Dark Matter: A Review of Models and Constraints”. In: *Int. J. Mod. Phys. A* 32.27 (2017), p. 1730023. DOI: [10.1142/S0217751X1730023X](https://doi.org/10.1142/S0217751X1730023X). arXiv: [1706.07442](https://arxiv.org/abs/1706.07442) [hep-ph].
- [15] A. Arbey and F. Mahmoudi. “Dark matter and the early Universe: a review”. In: *Prog. Part. Nucl. Phys.* 119 (2021), p. 103865. DOI: [10.1016/j.ppnp.2021.103865](https://doi.org/10.1016/j.ppnp.2021.103865). arXiv: [2104.11488](https://arxiv.org/abs/2104.11488) [hep-ph].
- [16] F. Zwicky. “Republication of: The redshift of extragalactic nebulae”. In: *General Relativity and Gravitation* 41.1 (Jan. 2009), pp. 207–224. DOI: [10.1007/s10714-008-0707-4](https://doi.org/10.1007/s10714-008-0707-4).
- [17] Vera C. Rubin and Jr. Ford W. Kent. “Rotation of the Andromeda Nebula from a Spectroscopic Survey of Emission Regions”. In: *apj* 159 (Feb. 1970), p. 379. DOI: [10.1086/150317](https://doi.org/10.1086/150317).
- [18] Douglas Clowe, Anthony Gonzalez, and Maxim Markevitch. “Weak-Lensing Mass Reconstruction of the Interacting Cluster 1E 0657-558: Direct Evidence for the Existence of Dark Matter”. In: *apj* 604.2 (Apr. 2004), pp. 596–603. DOI: [10.1086/381970](https://doi.org/10.1086/381970). arXiv: [astro-ph/0312273](https://arxiv.org/abs/astro-ph/0312273) [astro-ph].
- [19] P. A. R. Ade et al. “Planck 2015 results. XIII. Cosmological parameters”. In: *Astron. Astrophys.* 594 (2016), A13. DOI: [10.1051/0004-6361/201525830](https://doi.org/10.1051/0004-6361/201525830). arXiv: [1502.01589](https://arxiv.org/abs/1502.01589) [astro-ph.CO].
- [20] Jonathan L. Feng. “Dark Matter Candidates from Particle Physics and Methods of Detection”. In: *Ann. Rev. Astron. Astrophys.* 48 (2010), pp. 495–545. DOI: [10.1146/annurev-astro-082708-101659](https://doi.org/10.1146/annurev-astro-082708-101659). arXiv: [1003.0904](https://arxiv.org/abs/1003.0904) [astro-ph.CO].
- [21] Lars Bergstrom. “Dark Matter Candidates”. In: *New J. Phys.* 11 (2009), p. 105006. DOI: [10.1088/1367-2630/11/10/105006](https://doi.org/10.1088/1367-2630/11/10/105006). arXiv: [0903.4849](https://arxiv.org/abs/0903.4849) [hep-ph].
- [22] G. Aad et al. “Search for dark matter produced in association with a dark Higgs boson decaying into  $W^+W^-$  in the one-lepton final state at  $\sqrt{s}=13$  TeV using 139 fb $^{-1}$  of  $pp$  collisions recorded with the ATLAS detector”. In: *JHEP* 07 (2023), p. 116. DOI: [10.1007/JHEP07\(2023\)116](https://doi.org/10.1007/JHEP07(2023)116). arXiv: [2211.07175](https://arxiv.org/abs/2211.07175) [hep-ex].
- [23] E. Aprile et al. “Projected WIMP sensitivity of the XENONnT dark matter experiment”. In: *JCAP* 11 (2020), p. 031. DOI: [10.1088/1475-7516/2020/11/031](https://doi.org/10.1088/1475-7516/2020/11/031). arXiv: [2007.08796](https://arxiv.org/abs/2007.08796) [physics.ins-det].
- [24] Jonathan L. Feng et al. “Hidden Charged Dark Matter”. In: *JCAP* 07 (2009), p. 004. DOI: [10.1088/1475-7516/2009/07/004](https://doi.org/10.1088/1475-7516/2009/07/004). arXiv: [0905.3039](https://arxiv.org/abs/0905.3039) [hep-ph].

- [25] A. De Rujula, S. L. Glashow, and U. Sarid. “CHARGED DARK MATTER”. In: *Nucl. Phys. B* 333 (1990), pp. 173–194. DOI: [10.1016/0550-3213\(90\)90227-5](https://doi.org/10.1016/0550-3213(90)90227-5).
- [26] B.P. Abbott et al. “GW170817: Measurements of neutron star radii and equation of state”. In: *Phys. Rev. Lett.* 121.16 (2018), p. 161101. DOI: [10.1103/PhysRevLett.121.161101](https://doi.org/10.1103/PhysRevLett.121.161101). arXiv: [1805.11581](https://arxiv.org/abs/1805.11581) [gr-qc].
- [27] B. P. Abbott et al. “Properties of the binary neutron star merger GW170817”. In: *Phys. Rev. X* 9.1 (2019), p. 011001. DOI: [10.1103/PhysRevX.9.011001](https://doi.org/10.1103/PhysRevX.9.011001). arXiv: [1805.11579](https://arxiv.org/abs/1805.11579) [gr-qc].
- [28] B. P. Abbott et al. “Constraining the  $p$ -Mode- $g$ -Mode Tidal Instability with GW170817”. In: *Phys. Rev. Lett.* 122.6 (2019), p. 061104. DOI: [10.1103/PhysRevLett.122.061104](https://doi.org/10.1103/PhysRevLett.122.061104). arXiv: [1808.08676](https://arxiv.org/abs/1808.08676) [astro-ph.HE].
- [29] Benjamin P. Abbott et al. “GW170817: Observation of Gravitational Waves from a Binary Neutron Star Inspiral”. In: *Phys. Rev. Lett.* 119.16 (2017), p. 161101. DOI: [10.1103/PhysRevLett.119.161101](https://doi.org/10.1103/PhysRevLett.119.161101). arXiv: [1710.05832](https://arxiv.org/abs/1710.05832) [gr-qc].
- [30] B. P. Abbott et al. “GW190425: Observation of a Compact Binary Coalescence with Total Mass  $\sim 3.4M_{\odot}$ ”. In: (2020). arXiv: [2001.01761](https://arxiv.org/abs/2001.01761) [astro-ph.HE].
- [31] R. Abbott et al. “GW190814: Gravitational Waves from the Coalescence of a 23 Solar Mass Black Hole with a 2.6 Solar Mass Compact Object”. In: *Astrophys. J. Lett.* 896.2 (2020), p. L44. DOI: [10.3847/2041-8213/ab960f](https://doi.org/10.3847/2041-8213/ab960f). arXiv: [2006.12611](https://arxiv.org/abs/2006.12611) [astro-ph.HE].
- [32] The Nuclear Physics European Collaboration Committee. *NuPECC long range plan on Perspectives in Nuclear Physics*. 2017. URL: <http://www.nupecc.org/pub/lrp17/lrp2017.pdf>.
- [33] Ani Aprahamian et al. “Reaching for the horizon: The 2015 long range plan for nuclear science”. In: (2015).
- [34] Eanna E. Flanagan and Tanja Hinderer. “Constraining neutron star tidal Love numbers with gravitational wave detectors”. In: *Phys. Rev. D* 77 (2008), p. 021502. DOI: [10.1103/PhysRevD.77.021502](https://doi.org/10.1103/PhysRevD.77.021502). arXiv: [0709.1915](https://arxiv.org/abs/0709.1915) [astro-ph].
- [35] Tanja Hinderer et al. “Tidal deformability of neutron stars with realistic equations of state and their gravitational wave signatures in binary inspiral”. In: *Phys. Rev. D* 81 (2010), p. 123016. DOI: [10.1103/PhysRevD.81.123016](https://doi.org/10.1103/PhysRevD.81.123016). arXiv: [0911.3535](https://arxiv.org/abs/0911.3535) [astro-ph.HE].
- [36] Justin Vines, Eanna E. Flanagan, and Tanja Hinderer. “Post-1-Newtonian tidal effects in the gravitational waveform from binary inspirals”. In: *Phys. Rev. D* 83 (2011), p. 084051. DOI: [10.1103/PhysRevD.83.084051](https://doi.org/10.1103/PhysRevD.83.084051). arXiv: [1101.1673](https://arxiv.org/abs/1101.1673) [gr-qc].
- [37] Dong Lai and Yanqin Wu. “Resonant Tidal Excitations of Inertial Modes in Coalescing Neutron Star Binaries”. In: *Phys. Rev. D* 74 (2006), p. 024007. DOI: [10.1103/PhysRevD.74.024007](https://doi.org/10.1103/PhysRevD.74.024007). arXiv: [astro-ph/0604163](https://arxiv.org/abs/astro-ph/0604163).
- [38] Eanna E. Flanagan and Etienne Racine. “Gravitomagnetic resonant excitation of Rossby modes in coalescing neutron star binaries”. In: *Phys. Rev. D* 75 (2007), p. 044001. DOI: [10.1103/PhysRevD.75.044001](https://doi.org/10.1103/PhysRevD.75.044001). arXiv: [gr-qc/0601029](https://arxiv.org/abs/gr-qc/0601029).

- [39] Nils Andersson. *Gravitational-Wave Astronomy: Exploring the Dark Side of the Universe*. 2019. DOI: [10.1093/oso/9780198568032.001.0001/oso-9780198568032](https://doi.org/10.1093/oso/9780198568032.001.0001/oso-9780198568032).
- [40] K. D. Kokkotas and B. F. Schutz. “W-modes - A new family of normal modes of pulsating relativistic stars”. In: *mnras* 255 (Mar. 1992), pp. 119–128. DOI: [10.1093/mnras/255.1.119](https://doi.org/10.1093/mnras/255.1.119).
- [41] Kostas D. Kokkotas and Bernd G. Schmidt. “Quasinormal modes of stars and black holes”. In: *Living Rev. Rel.* 2 (1999), p. 2. DOI: [10.12942/lrr-1999-2](https://doi.org/10.12942/lrr-1999-2). arXiv: [gr-qc/9909058](https://arxiv.org/abs/gr-qc/9909058).
- [42] Caio F. B. Macedo et al. “Astrophysical signatures of boson stars: quasinormal modes and inspiral resonances”. In: *Phys. Rev. D* 88.6 (2013), p. 064046. DOI: [10.1103/PhysRevD.88.064046](https://doi.org/10.1103/PhysRevD.88.064046). arXiv: [1307.4812 \[gr-qc\]](https://arxiv.org/abs/1307.4812).
- [43] B. P. Abbott et al. “Search for Post-merger Gravitational Waves from the Remnant of the Binary Neutron Star Merger GW170817”. In: *Astrophys. J. Lett.* 851.1 (2017), p. L16. DOI: [10.3847/2041-8213/aa9a35](https://doi.org/10.3847/2041-8213/aa9a35). arXiv: [1710.09320 \[astro-ph.HE\]](https://arxiv.org/abs/1710.09320).
- [44] Bernard F. Schutz. *A FIRST COURSE IN GENERAL RELATIVITY*. Cambridge, UK: Cambridge Univ. Pr., 1985.
- [45] Michele Maggiore. *Gravitational Waves. Vol. 1: Theory and Experiments*. Oxford Master Series in Physics. Oxford University Press, 2007. ISBN: 978-0-19-857074-5, 978-0-19-852074-0.
- [46] Javier M. Antelis and Claudia Moreno. “Obtaining gravitational waves from inspiral binary systems using LIGO data”. In: *Eur. Phys. J. Plus* 132.1 (2017). [Erratum: *Eur.Phys.J.Plus* 132, 103 (2017)], p. 10. DOI: [10.1140/epjp/i2017-11283-5](https://doi.org/10.1140/epjp/i2017-11283-5). arXiv: [1610.03567 \[astro-ph.IM\]](https://arxiv.org/abs/1610.03567).
- [47] Luc Blanchet. “Gravitational radiation from postNewtonian sources and inspiraling compact binaries”. In: *Living Rev. Rel.* 5 (2002), p. 3. DOI: [10.12942/lrr-2002-3](https://doi.org/10.12942/lrr-2002-3). arXiv: [gr-qc/0202016](https://arxiv.org/abs/gr-qc/0202016).
- [48] Serge Droz et al. “Gravitational waves from inspiraling compact binaries: Validity of the stationary-phase approximation to the Fourier transform”. In: *Phys. Rev. D* 59 (12 May 1999), p. 124016. DOI: [10.1103/PhysRevD.59.124016](https://doi.org/10.1103/PhysRevD.59.124016). URL: <https://link.aps.org/doi/10.1103/PhysRevD.59.124016>.
- [49] Thibault Damour, Piotr Jaranowski, and Gerhard Schaefel. “Dimensional regularization of the gravitational interaction of point masses”. In: *Phys. Lett.* B513 (2001), pp. 147–155. DOI: [10.1016/S0370-2693\(01\)00642-6](https://doi.org/10.1016/S0370-2693(01)00642-6). arXiv: [gr-qc/0105038 \[gr-qc\]](https://arxiv.org/abs/gr-qc/0105038).
- [50] Alessandra Buonanno et al. “Comparison of post-Newtonian templates for compact binary inspiral signals in gravitational-wave detectors”. In: *Phys. Rev. D* 80 (2009), p. 084043. DOI: [10.1103/PhysRevD.80.084043](https://doi.org/10.1103/PhysRevD.80.084043). arXiv: [0907.0700 \[gr-qc\]](https://arxiv.org/abs/0907.0700).
- [51] Luc Blanchet and Bala R. Iyer. “Hadamard regularization of the third post-Newtonian gravitational wave generation of two point masses”. In: *Phys. Rev. D* 71 (2005), p. 024004. DOI: [10.1103/PhysRevD.71.024004](https://doi.org/10.1103/PhysRevD.71.024004). arXiv: [gr-qc/0409094](https://arxiv.org/abs/gr-qc/0409094).

- [52] Luc Blanchet et al. “Gravitational wave inspiral of compact binary systems to 7/2 postNewtonian order”. In: *Phys. Rev. D* 65 (2002). [Erratum: Phys.Rev.D 71, 129902 (2005)], p. 061501. DOI: [10.1103/PhysRevD.71.129902](https://doi.org/10.1103/PhysRevD.71.129902). arXiv: [gr-qc/0105099](https://arxiv.org/abs/gr-qc/0105099).
- [53] Luc Blanchet, Bala R. Iyer, and Benoit Joguet. “Gravitational waves from inspiralling compact binaries: Energy flux to third postNewtonian order”. In: *Phys. Rev. D* 65 (2002). [Erratum: Phys.Rev.D 71, 129903 (2005)], p. 064005. DOI: [10.1103/PhysRevD.65.064005](https://doi.org/10.1103/PhysRevD.65.064005). arXiv: [gr-qc/0105098](https://arxiv.org/abs/gr-qc/0105098).
- [54] Yousuke Itoh and Toshifumi Futamase. “New derivation of a third postNewtonian equation of motion for relativistic compact binaries without ambiguity”. In: *Phys. Rev. D* 68 (2003), p. 121501. DOI: [10.1103/PhysRevD.68.121501](https://doi.org/10.1103/PhysRevD.68.121501). arXiv: [gr-qc/0310028](https://arxiv.org/abs/gr-qc/0310028).
- [55] Luc Blanchet and Bala R. Iyer. “Third postNewtonian dynamics of compact binaries: Equations of motion in the center-of-mass frame”. In: *Class. Quant. Grav.* 20 (2003), p. 755. DOI: [10.1088/0264-9381/20/4/309](https://doi.org/10.1088/0264-9381/20/4/309). arXiv: [gr-qc/0209089](https://arxiv.org/abs/gr-qc/0209089).
- [56] Vanessa C. de Andrade, Luc Blanchet, and Guillaume Faye. “Third postNewtonian dynamics of compact binaries: Noetherian conserved quantities and equivalence between the harmonic coordinate and ADM Hamiltonian formalisms”. In: *Class. Quant. Grav.* 18 (2001), pp. 753–778. DOI: [10.1088/0264-9381/18/5/301](https://doi.org/10.1088/0264-9381/18/5/301). arXiv: [gr-qc/0011063](https://arxiv.org/abs/gr-qc/0011063).
- [57] Luc Blanchet et al. “Dimensional regularization of the third post-Newtonian gravitational wave generation from two point masses”. In: *Phys. Rev. D* 71 (2005), p. 124004. DOI: [10.1103/PhysRevD.71.124004](https://doi.org/10.1103/PhysRevD.71.124004). arXiv: [gr-qc/0503044](https://arxiv.org/abs/gr-qc/0503044).
- [58] Thibault Damour, Piotr Jaranowski, and Gerhard Schafer. “Equivalence between the ADM-Hamiltonian and the harmonic coordinates approaches to the third post-Newtonian dynamics of compact binaries”. In: *Phys. Rev. D* 63 (2001). [Erratum: Phys.Rev.D 66, 029901 (2002)], p. 044021. DOI: [10.1103/PhysRevD.63.044021](https://doi.org/10.1103/PhysRevD.63.044021). arXiv: [gr-qc/0010040](https://arxiv.org/abs/gr-qc/0010040).
- [59] Luc Blanchet et al. “Gravitational radiation from inspiralling compact binaries completed at the third post-Newtonian order”. In: *Phys. Rev. Lett.* 93 (2004), p. 091101. DOI: [10.1103/PhysRevLett.93.091101](https://doi.org/10.1103/PhysRevLett.93.091101). arXiv: [gr-qc/0406012](https://arxiv.org/abs/gr-qc/0406012).
- [60] Luc Blanchet, Thibault Damour, and Gilles Esposito-Farese. “Dimensional regularization of the third postNewtonian dynamics of point particles in harmonic coordinates”. In: *Phys. Rev. D* 69 (2004), p. 124007. DOI: [10.1103/PhysRevD.69.124007](https://doi.org/10.1103/PhysRevD.69.124007). arXiv: [gr-qc/0311052](https://arxiv.org/abs/gr-qc/0311052).
- [61] K. G. Arun et al. “Parameter estimation of inspiralling compact binaries using 3.5 post-Newtonian gravitational wave phasing: The Non-spinning case”. In: *Phys. Rev. D* 71 (2005). [Erratum: Phys.Rev.D 72, 069903 (2005)], p. 084008. DOI: [10.1103/PhysRevD.71.084008](https://doi.org/10.1103/PhysRevD.71.084008). arXiv: [gr-qc/0411146](https://arxiv.org/abs/gr-qc/0411146).
- [62] Alessandra Buonanno, Gregory B. Cook, and Frans Pretorius. “Inspiral, merger and ring-down of equal-mass black-hole binaries”. In: *Phys. Rev. D* 75 (2007), p. 124018. DOI: [10.1103/PhysRevD.75.124018](https://doi.org/10.1103/PhysRevD.75.124018). arXiv: [gr-qc/0610122](https://arxiv.org/abs/gr-qc/0610122).



- [63] Chad Hanna et al. “A method for estimating time-frequency characteristics of compact binary mergers to improve searches for inspiral, merger and ring-down phases separately”. In: *Class. Quant. Grav.* 26 (2009), p. 015009. DOI: [10.1088/0264-9381/26/1/015009](https://doi.org/10.1088/0264-9381/26/1/015009). arXiv: [0801.4297](https://arxiv.org/abs/0801.4297) [gr-qc].
- [64] L E Kidder, C M Will, and A G Wiseman. “Innermost stable orbits for coalescing binary systems of compact objects”. In: *Classical and Quantum Gravity* 9.9 (Sept. 1992), p. L125. DOI: [10.1088/0264-9381/9/9/004](https://doi.org/10.1088/0264-9381/9/9/004). URL: <https://dx.doi.org/10.1088/0264-9381/9/9/004>.
- [65] Luc Blanchet. “Innermost circular orbit of binary black holes at the third post-Newtonian approximation”. In: *Phys. Rev. D* 65 (2002), p. 124009. DOI: [10.1103/PhysRevD.65.124009](https://doi.org/10.1103/PhysRevD.65.124009). arXiv: [gr-qc/0112056](https://arxiv.org/abs/gr-qc/0112056).
- [66] Lawrence E. Kidder, Clifford M. Will, and Alan G. Wiseman. “Spin effects in the inspiral of coalescing compact binaries”. In: *Phys. Rev. D* 47.10 (1993), R4183–R4187. DOI: [10.1103/PhysRevD.47.R4183](https://doi.org/10.1103/PhysRevD.47.R4183). arXiv: [gr-qc/9211025](https://arxiv.org/abs/gr-qc/9211025).
- [67] K. G. Arun et al. “Higher-order spin effects in the amplitude and phase of gravitational waveforms emitted by inspiraling compact binaries: Ready-to-use gravitational waveforms”. In: *Phys. Rev. D* 79 (2009). [Erratum: *Phys.Rev.D* 84, 049901 (2011)], p. 104023. DOI: [10.1103/PhysRevD.79.104023](https://doi.org/10.1103/PhysRevD.79.104023). arXiv: [0810.5336](https://arxiv.org/abs/0810.5336) [gr-qc].
- [68] Luc Blanchet, Alessandra Buonanno, and Guillaume Faye. “Tail-induced spin-orbit effect in the gravitational radiation of compact binaries”. In: *Phys. Rev. D* 84 (2011), p. 064041. DOI: [10.1103/PhysRevD.84.064041](https://doi.org/10.1103/PhysRevD.84.064041). arXiv: [1104.5659](https://arxiv.org/abs/1104.5659) [gr-qc].
- [69] Balazs Mikoczi, Matyas Vasuth, and Laszlo A. Gergely. “Self-interaction spin effects in inspiralling compact binaries”. In: *Phys. Rev. D* 71 (2005), p. 124043. DOI: [10.1103/PhysRevD.71.124043](https://doi.org/10.1103/PhysRevD.71.124043). arXiv: [astro-ph/0504538](https://arxiv.org/abs/astro-ph/0504538).
- [70] Mark Hannam et al. “Simple Model of Complete Precessing Black-Hole-Binary Gravitational Waveforms”. In: *Phys. Rev. Lett.* 113 (15 Oct. 2014), p. 151101. DOI: [10.1103/PhysRevLett.113.151101](https://doi.org/10.1103/PhysRevLett.113.151101). URL: <https://link.aps.org/doi/10.1103/PhysRevLett.113.151101>.
- [71] Sascha Husa et al. “Frequency-domain gravitational waves from nonprecessing black-hole binaries. I. New numerical waveforms and anatomy of the signal”. In: *Phys. Rev. D* 93 (4 Feb. 2016), p. 044006. DOI: [10.1103/PhysRevD.93.044006](https://doi.org/10.1103/PhysRevD.93.044006). URL: <https://link.aps.org/doi/10.1103/PhysRevD.93.044006>.
- [72] Sebastian Khan et al. “Frequency-domain gravitational waves from nonprecessing black-hole binaries. II. A phenomenological model for the advanced detector era”. In: *Phys. Rev. D* 93 (4 Feb. 2016), p. 044007. DOI: [10.1103/PhysRevD.93.044007](https://doi.org/10.1103/PhysRevD.93.044007). URL: <https://link.aps.org/doi/10.1103/PhysRevD.93.044007>.
- [73] Patricia Schmidt, Mark Hannam, and Sascha Husa. “Towards models of gravitational waveforms from generic binaries: A simple approximate mapping between precessing and non-precessing inspiral signals”. In: *Phys. Rev. D* 86 (2012), p. 104063. DOI: [10.1103/PhysRevD.86.104063](https://doi.org/10.1103/PhysRevD.86.104063). arXiv: [1207.3088](https://arxiv.org/abs/1207.3088) [gr-qc].

- [74] P. Ajith. “Addressing the spin question in gravitational-wave searches: Waveform templates for inspiralling compact binaries with nonprecessing spins”. In: *Phys. Rev. D* 84 (2011), p. 084037. DOI: [10.1103/PhysRevD.84.084037](https://doi.org/10.1103/PhysRevD.84.084037). arXiv: [1107.1267](https://arxiv.org/abs/1107.1267) [gr-qc].
- [75] L. Santamaria et al. “Matching post-Newtonian and numerical relativity waveforms: systematic errors and a new phenomenological model for non-precessing black hole binaries”. In: *Phys. Rev. D* 82 (2010), p. 064016. DOI: [10.1103/PhysRevD.82.064016](https://doi.org/10.1103/PhysRevD.82.064016). arXiv: [1005.3306](https://arxiv.org/abs/1005.3306) [gr-qc].
- [76] Curt Cutler and Eanna E. Flanagan. “Gravitational waves from merging compact binaries: How accurately can one extract the binary’s parameters from the inspiral wave form?” In: *Phys. Rev. D* 49 (1994), pp. 2658–2697. DOI: [10.1103/PhysRevD.49.2658](https://doi.org/10.1103/PhysRevD.49.2658). arXiv: [gr-qc/9402014](https://arxiv.org/abs/gr-qc/9402014).
- [77] Eric Poisson and Clifford M. Will. “Gravitational waves from inspiraling compact binaries: Parameter estimation using second postNewtonian wave forms”. In: *Phys. Rev. D* 52 (1995), pp. 848–855. DOI: [10.1103/PhysRevD.52.848](https://doi.org/10.1103/PhysRevD.52.848). arXiv: [gr-qc/9502040](https://arxiv.org/abs/gr-qc/9502040).
- [78] Michael Pürrer et al. “Testing the validity of the single-spin approximation in inspiral-merger-ringdown waveforms”. In: *Phys. Rev. D* 88 (2013), p. 064007. DOI: [10.1103/PhysRevD.88.064007](https://doi.org/10.1103/PhysRevD.88.064007). arXiv: [1306.2320](https://arxiv.org/abs/1306.2320) [gr-qc].
- [79] Sebastian Khan et al. “Frequency-domain gravitational waves from nonprecessing black-hole binaries. II. A phenomenological model for the advanced detector era”. In: *Phys. Rev. D* 93.4 (2016), p. 044007. DOI: [10.1103/PhysRevD.93.044007](https://doi.org/10.1103/PhysRevD.93.044007). arXiv: [1508.07253](https://arxiv.org/abs/1508.07253) [gr-qc].
- [80] <https://gracedb.ligo.org/superevents/public/03/>.
- [81] B.P. Abbott et al. “Observation of Gravitational Waves from a Binary Black Hole Merger”. In: *Phys. Rev. Lett.* 116.6 (2016), p. 061102. DOI: [10.1103/PhysRevLett.116.061102](https://doi.org/10.1103/PhysRevLett.116.061102). arXiv: [1602.03837](https://arxiv.org/abs/1602.03837) [gr-qc].
- [82] B. P. Abbott et al. “GW151226: Observation of Gravitational Waves from a 22-Solar-Mass Binary Black Hole Coalescence”. In: *Phys. Rev. Lett.* 116.24 (2016), p. 241103. DOI: [10.1103/PhysRevLett.116.241103](https://doi.org/10.1103/PhysRevLett.116.241103). arXiv: [1606.04855](https://arxiv.org/abs/1606.04855) [gr-qc].
- [83] B. P. Abbott et al. “Binary Black Hole Mergers in the first Advanced LIGO Observing Run”. In: *Phys. Rev. X* 6.4 (2016). [Erratum: *Phys. Rev. X* 8, 039903 (2018)], p. 041015. DOI: [10.1103/PhysRevX.6.041015](https://doi.org/10.1103/PhysRevX.6.041015). arXiv: [1606.04856](https://arxiv.org/abs/1606.04856) [gr-qc].
- [84] B. P. Abbott et al. “GWTC-1: A Gravitational-Wave Transient Catalog of Compact Binary Mergers Observed by LIGO and Virgo during the First and Second Observing Runs”. In: *Phys. Rev. X* 9.3 (2019), p. 031040. DOI: [10.1103/PhysRevX.9.031040](https://doi.org/10.1103/PhysRevX.9.031040). arXiv: [1811.12907](https://arxiv.org/abs/1811.12907) [astro-ph.HE].
- [85] R. Abbott et al. “GWTC-2: Compact Binary Coalescences Observed by LIGO and Virgo During the First Half of the Third Observing Run”. In: (Oct. 2020). arXiv: [2010.14527](https://arxiv.org/abs/2010.14527) [gr-qc].



- [86] R. Abbott et al. “GWTC-3: Compact Binary Coalescences Observed by LIGO and Virgo During the Second Part of the Third Observing Run”. In: (Nov. 2021). arXiv: [2111.03606 \[gr-qc\]](#).
- [87] R. Abbott et al. “Observation of Gravitational Waves from Two Neutron Star–Black Hole Coalescences”. In: *Astrophys. J. Lett.* 915.1 (2021), p. L5. DOI: [10.3847/2041-8213/ac082e](#). arXiv: [2106.15163 \[astro-ph.HE\]](#).
- [88] Jonathan L. Feng and Jason Kumar. “The WIMPlless Miracle: Dark-Matter Particles without Weak-Scale Masses or Weak Interactions”. In: *Phys. Rev. Lett.* 101 (2008), p. 231301. DOI: [10.1103/PhysRevLett.101.231301](#). arXiv: [0803.4196 \[hep-ph\]](#).
- [89] Jason Arakawa and Tim M. P. Tait. “Is a Miracle-less WIMP Ruled out?” In: *SciPost Phys.* 11.2 (2021), p. 019. DOI: [10.21468/SciPostPhys.11.2.019](#). arXiv: [2101.11031 \[hep-ph\]](#).
- [90] Sanjeev Dhurandhar and Sanjit Mitra. *General relativity and gravitational waves : essentials of theory and practice / Sanjeev Dhurandhar, Sanjit Mitra*. eng. UNITEXT for physics. Cham: Springer, 2022. ISBN: 3030923347.
- [91] The LIGO Scientific Collaboration et al. “Advanced LIGO”. In: *Classical and Quantum Gravity* 32.7 (Mar. 2015), p. 074001. DOI: [10.1088/0264-9381/32/7/074001](#). URL: <https://dx.doi.org/10.1088/0264-9381/32/7/074001>.
- [92] Gregory M Harry and (for the LIGO Scientific Collaboration). “Advanced LIGO: the next generation of gravitational wave detectors”. In: *Classical and Quantum Gravity* 27.8 (Apr. 2010), p. 084006. DOI: [10.1088/0264-9381/27/8/084006](#). URL: <https://dx.doi.org/10.1088/0264-9381/27/8/084006>.
- [93] Yoichi Aso et al. “Interferometer design of the KAGRA gravitational wave detector”. In: *Phys. Rev.* D88.4 (2013), p. 043007. DOI: [10.1103/PhysRevD.88.043007](#). arXiv: [1306.6747 \[gr-qc\]](#).
- [94] C. S. Unnikrishnan. “IndIGO and LIGO-India: Scope and plans for gravitational wave research and precision metrology in India”. In: *Int. J. Mod. Phys. D* 22 (2013), p. 1341010. DOI: [10.1142/S0218271813410101](#). arXiv: [1510.06059 \[physics.ins-det\]](#).
- [95] M. Punturo et al. “The third generation of gravitational wave observatories and their science reach”. In: *Class. Quant. Grav.* 27 (2010). Ed. by Zsuzsa Marka and Szabolcs Marka, p. 084007. DOI: [10.1088/0264-9381/27/8/084007](#).
- [96] S. Hild et al. “Sensitivity Studies for Third-Generation Gravitational Wave Observatories”. In: *Class. Quant. Grav.* 28 (2011), p. 094013. DOI: [10.1088/0264-9381/28/9/094013](#). arXiv: [1012.0908 \[gr-qc\]](#).
- [97] Benjamin P Abbott et al. “Exploring the Sensitivity of Next Generation Gravitational Wave Detectors”. In: *Class. Quant. Grav.* 34.4 (2017), p. 044001. DOI: [10.1088/1361-6382/aa51f4](#). arXiv: [1607.08697 \[astro-ph.IM\]](#).
- [98] David Reitze et al. “Cosmic Explorer: The U.S. Contribution to Gravitational-Wave Astronomy beyond LIGO”. In: *Bull. Am. Astron. Soc.* 51 (July 2019), p. 035. arXiv: [1907.04833 \[astro-ph.IM\]](#).

- [99] Pau Amaro-Seoane et al. *Laser Interferometer Space Antenna*. 2017. arXiv: [1702.00786 \[astro-ph.IM\]](#).
- [100] F. Acernese et al. “Advanced Virgo: a second-generation interferometric gravitational wave detector”. In: *Class. Quant. Grav.* 32.2 (2015), p. 024001. DOI: [10.1088/0264-9381/32/2/024001](#). arXiv: [1408.3978 \[gr-qc\]](#).
- [101] J. Aasi et al. “Advanced LIGO”. In: *Class. Quant. Grav.* 32 (2015), p. 074001. DOI: [10.1088/0264-9381/32/7/074001](#). arXiv: [1411.4547 \[gr-qc\]](#).
- [102] Tyson B. Littenberg and Neil J. Cornish. “Bayesian inference for spectral estimation of gravitational wave detector noise”. In: *Phys. Rev. D* 91 (8 Apr. 2015), p. 084034. DOI: [10.1103/PhysRevD.91.084034](#). URL: <https://link.aps.org/doi/10.1103/PhysRevD.91.084034>.
- [103] Benjamin P Abbott et al. “A guide to LIGO–Virgo detector noise and extraction of transient gravitational-wave signals”. In: *Class. Quant. Grav.* 37.5 (2020), p. 055002. DOI: [10.1088/1361-6382/ab685e](#). arXiv: [1908.11170 \[gr-qc\]](#).
- [104] Eric Thrane and Colm Talbot. “An introduction to Bayesian inference in gravitational-wave astronomy: Parameter estimation, model selection, and hierarchical models”. In: *Publications of the Astronomical Society of Australia* 36 (2019). DOI: [10.1017/pasa.2019.2](#). URL: <https://doi.org/10.1017/pasa.2019.2>.
- [105] John Skilling. “Nested sampling for general Bayesian computation”. In: *Bayesian Analysis* 1.4 (2006), pp. 833–859. DOI: [10.1214/06-BA127](#). URL: <https://doi.org/10.1214/06-BA127>.
- [106] F. Feroz et al. “Importance Nested Sampling and the MultiNest Algorithm”. In: *Open J. Astrophys.* 2.1 (2019), p. 10. DOI: [10.21105/astro.1306.2144](#). arXiv: [1306.2144 \[astro-ph.IM\]](#).
- [107] P. Haensel, A. Y. Potekhin, and D. G. Yakovlev. *Neutron stars 1: Equation of state and structure*. Vol. 326. New York, USA: Springer, 2007. DOI: [10.1007/978-0-387-47301-7](#).
- [108] LIGO Scientific Collaboration. *LIGO Algorithm Library - LALSuite*. free software (GPL). 2018. DOI: [10.7935/GT1W-FZ16](#).
- [109] Tanja Hinderer. “Tidal Love numbers of neutron stars”. In: *Astrophys. J.* 677 (2008), pp. 1216–1220. DOI: [10.1086/533487](#). arXiv: [0711.2420 \[astro-ph\]](#).
- [110] Thibault Damour, Alessandro Nagar, and Loic Villain. “Measurability of the tidal polarizability of neutron stars in late-inspiral gravitational-wave signals”. In: *Phys. Rev. D* 85 (2012), p. 123007. DOI: [10.1103/PhysRevD.85.123007](#). arXiv: [1203.4352 \[gr-qc\]](#).
- [111] Quentin Henry, Guillaume Faye, and Luc Blanchet. “Tidal effects in the gravitational-wave phase evolution of compact binary systems to next-to-next-to-leading post-Newtonian order”. In: *Phys. Rev. D* 102.4 (2020), p. 044033. DOI: [10.1103/PhysRevD.102.044033](#). arXiv: [2005.13367 \[gr-qc\]](#).
- [112] S. Chandrasekhar. “A General Variational Principle Governing the Radial and the Non-Radial Oscillations of Gaseous Masses.” In: *apj* 139 (Feb. 1964), p. 664. DOI: [10.1086/147792](#).

- [113] K. S. Thorne. “Multipole Expansions of Gravitational Radiation”. In: *Rev. Mod. Phys.* 52 (1980), pp. 299–339. DOI: [10.1103/RevModPhys.52.299](https://doi.org/10.1103/RevModPhys.52.299).
- [114] Piotr T. Chrusciel, Joao Lopes Costa, and Markus Heusler. “Stationary Black Holes: Uniqueness and Beyond”. In: *Living Rev. Rel.* 15 (2012), p. 7. DOI: [10.12942/lrr-2012-7](https://doi.org/10.12942/lrr-2012-7). arXiv: [1205.6112](https://arxiv.org/abs/1205.6112) [gr-qc].
- [115] Kent Yagi and Nicolas Yunes. “I-Love-Q Relations in Neutron Stars and their Applications to Astrophysics, Gravitational Waves and Fundamental Physics”. In: *Phys. Rev. D* 88.2 (2013), p. 023009. DOI: [10.1103/PhysRevD.88.023009](https://doi.org/10.1103/PhysRevD.88.023009). arXiv: [1303.1528](https://arxiv.org/abs/1303.1528) [gr-qc].
- [116] Kent Yagi and Nicolás Yunes. “Approximate Universal Relations for Neutron Stars and Quark Stars”. In: *Phys. Rept.* 681 (2017), pp. 1–72. DOI: [10.1016/j.physrep.2017.03.002](https://doi.org/10.1016/j.physrep.2017.03.002). arXiv: [1608.02582](https://arxiv.org/abs/1608.02582) [gr-qc].
- [117] B. P. Abbott et al. “Properties of the binary neutron star merger GW170817”. In: *Phys. Rev. X* 9.1 (2019), p. 011001. DOI: [10.1103/PhysRevX.9.011001](https://doi.org/10.1103/PhysRevX.9.011001). arXiv: [1805.11579](https://arxiv.org/abs/1805.11579) [gr-qc].
- [118] B. P. Abbott et al. “GW170817: Measurements of neutron star radii and equation of state”. In: *Phys. Rev. Lett.* 121.16 (2018), p. 161101. DOI: [10.1103/PhysRevLett.121.161101](https://doi.org/10.1103/PhysRevLett.121.161101). arXiv: [1805.11581](https://arxiv.org/abs/1805.11581) [gr-qc].
- [119] M. Soares-Santos et al. “The Electromagnetic Counterpart of the Binary Neutron Star Merger LIGO/Virgo GW170817. I. Discovery of the Optical Counterpart Using the Dark Energy Camera”. In: *Astrophys. J. Lett.* 848.2 (2017), p. L16. DOI: [10.3847/2041-8213/aa9059](https://doi.org/10.3847/2041-8213/aa9059). arXiv: [1710.05459](https://arxiv.org/abs/1710.05459) [astro-ph.HE].
- [120] P. S. Cowperthwaite et al. “The Electromagnetic Counterpart of the Binary Neutron Star Merger LIGO/Virgo GW170817. II. UV, Optical, and Near-infrared Light Curves and Comparison to Kilonova Models”. In: *Astrophys. J. Lett.* 848.2 (2017), p. L17. DOI: [10.3847/2041-8213/aa8fc7](https://doi.org/10.3847/2041-8213/aa8fc7). arXiv: [1710.05840](https://arxiv.org/abs/1710.05840) [astro-ph.HE].
- [121] B. P. Abbott et al. “Gravitational Waves and Gamma-rays from a Binary Neutron Star Merger: GW170817 and GRB 170817A”. In: *Astrophys. J. Lett.* 848.2 (2017), p. L13. DOI: [10.3847/2041-8213/aa920c](https://doi.org/10.3847/2041-8213/aa920c). arXiv: [1710.05834](https://arxiv.org/abs/1710.05834) [astro-ph.HE].
- [122] Tim Dietrich, Tanja Hinderer, and Anuradha Samajdar. “Interpreting Binary Neutron Star Mergers: Describing the Binary Neutron Star Dynamics, Modelling Gravitational Waveforms, and Analyzing Detections”. In: *Gen. Rel. Grav.* 53.3 (2021), p. 27. DOI: [10.1007/s10714-020-02751-6](https://doi.org/10.1007/s10714-020-02751-6). arXiv: [2004.02527](https://arxiv.org/abs/2004.02527) [gr-qc].
- [123] B. P. Abbott et al. “Prospects for observing and localizing gravitational-wave transients with Advanced LIGO, Advanced Virgo and KAGRA”. In: *Living Rev. Rel.* 21.1 (2018), p. 3. DOI: [10.1007/s41114-020-00026-9](https://doi.org/10.1007/s41114-020-00026-9). arXiv: [1304.0670](https://arxiv.org/abs/1304.0670) [gr-qc].
- [124] Michele Maggiore et al. “Science Case for the Einstein Telescope”. In: *JCAP* 03 (2020), p. 050. DOI: [10.1088/1475-7516/2020/03/050](https://doi.org/10.1088/1475-7516/2020/03/050). arXiv: [1912.02622](https://arxiv.org/abs/1912.02622) [astro-ph.CO].
- [125] B. S. Sathyaprakash et al. “Extreme Gravity and Fundamental Physics”. In: (Mar. 2019). arXiv: [1903.09221](https://arxiv.org/abs/1903.09221) [astro-ph.HE].

- [126] Vicky Kalogera et al. “The Next Generation Global Gravitational Wave Observatory: The Science Book”. In: (Nov. 2021). arXiv: [2111.06990 \[gr-qc\]](#).
- [127] Anuradha Samajdar et al. “Biases in parameter estimation from overlapping gravitational-wave signals in the third-generation detector era”. In: *Phys. Rev. D* 104.4 (2021), p. 044003. DOI: [10.1103/PhysRevD.104.044003](#). arXiv: [2102.07544 \[gr-qc\]](#).
- [128] Matthew Evans et al. “A Horizon Study for Cosmic Explorer: Science, Observatories, and Community”. In: (Sept. 2021). arXiv: [2109.09882 \[astro-ph.IM\]](#).
- [129] Vitor Cardoso et al. “Black holes and gravitational waves in models of minicharged dark matter”. In: *JCAP* 05 (2016). [Erratum: *JCAP* 04, E01 (2020)], p. 054. DOI: [10.1088/1475-7516/2016/05/054](#). arXiv: [1604.07845 \[hep-ph\]](#).
- [130] Robert M. Wald. “Black hole in a uniform magnetic field”. In: *Phys. Rev. D* 10 (1974), pp. 1680–1685. DOI: [10.1103/PhysRevD.10.1680](#).
- [131] D. M. Eardley and W. H. Press. “Astrophysical processes near black holes”. In: *Ann. Rev. Astron. Astrophys.* 13 (1975), pp. 381–422. DOI: [10.1146/annurev.aa.13.090175.002121](#).
- [132] Bob Holdom. “Two  $U(1)$ ’s and Epsilon Charge Shifts”. In: *Phys. Lett. B* 166 (1986), pp. 196–198. DOI: [10.1016/0370-2693\(86\)91377-8](#).
- [133] Kris Sigurdson et al. “Dark-matter electric and magnetic dipole moments”. In: *Phys. Rev. D* 70 (2004). [Erratum: *Phys.Rev.D* 73, 089903 (2006)], p. 083501. DOI: [10.1103/PhysRevD.70.083501](#). arXiv: [astro-ph/0406355](#).
- [134] Sacha Davidson and Michael E. Peskin. “Astrophysical bounds on millicharged particles in models with a paraphoton”. In: *Phys. Rev. D* 49 (1994), pp. 2114–2117. DOI: [10.1103/PhysRevD.49.2114](#). arXiv: [hep-ph/9310288](#).
- [135] Sacha Davidson, Steen Hannestad, and Georg Raffelt. “Updated bounds on millicharged particles”. In: *JHEP* 05 (2000), p. 003. DOI: [10.1088/1126-6708/2000/05/003](#). arXiv: [hep-ph/0001179](#).
- [136] Samuel D. McDermott, Hai-Bo Yu, and Kathryn M. Zurek. “Turning off the Lights: How Dark is Dark Matter?” In: *Phys. Rev. D* 83 (2011), p. 063509. DOI: [10.1103/PhysRevD.83.063509](#). arXiv: [1011.2907 \[hep-ph\]](#).
- [137] S. L. Dubovsky, D. S. Gorbunov, and G. I. Rubtsov. “Narrowing the window for millicharged particles by CMB anisotropy”. In: *JETP Lett.* 79 (2004), pp. 1–5. DOI: [10.1134/1.1675909](#). arXiv: [hep-ph/0311189](#).
- [138] A. D. Dolgov et al. “Constraints on millicharged particles from Planck data”. In: *Phys. Rev. D* 88.11 (2013), p. 117701. DOI: [10.1103/PhysRevD.88.117701](#). arXiv: [1310.2376 \[hep-ph\]](#).
- [139] Holger Gies, Joerg Jaeckel, and Andreas Ringwald. “Polarized Light Propagating in a Magnetic Field as a Probe of Millicharged Fermions”. In: *Phys. Rev. Lett.* 97 (2006), p. 140402. DOI: [10.1103/PhysRevLett.97.140402](#). arXiv: [hep-ph/0607118](#).

- [140] H. Gies, J. Jaeckel, and A. Ringwald. “Accelerator Cavities as a Probe of Millicharged Particles”. In: *Europhys. Lett.* 76 (2006), pp. 794–800. DOI: [10.1209/epl/i2006-10356-5](https://doi.org/10.1209/epl/i2006-10356-5). arXiv: [hep-ph/0608238](https://arxiv.org/abs/hep-ph/0608238).
- [141] C. Burrage et al. “Late time CMB anisotropies constrain mini-charged particles”. In: *JCAP* 11 (2009), p. 002. DOI: [10.1088/1475-7516/2009/11/002](https://doi.org/10.1088/1475-7516/2009/11/002). arXiv: [0909.0649](https://arxiv.org/abs/0909.0649) [[astro-ph.CO](#)].
- [142] Markus Ahlers. “The Hubble diagram as a probe of mini-charged particles”. In: *Phys. Rev. D* 80 (2009), p. 023513. DOI: [10.1103/PhysRevD.80.023513](https://doi.org/10.1103/PhysRevD.80.023513). arXiv: [0904.0998](https://arxiv.org/abs/0904.0998) [[hep-ph](#)].
- [143] Andrew Haas et al. “Looking for milli-charged particles with a new experiment at the LHC”. In: *Phys. Lett. B* 746 (2015), pp. 117–120. DOI: [10.1016/j.physletb.2015.04.062](https://doi.org/10.1016/j.physletb.2015.04.062). arXiv: [1410.6816](https://arxiv.org/abs/1410.6816) [[hep-ph](#)].
- [144] Austin Ball et al. “A Letter of Intent to Install a milli-charged Particle Detector at LHC P5”. In: (July 2016). arXiv: [1607.04669](https://arxiv.org/abs/1607.04669) [[physics.ins-det](#)].
- [145] Kenji Kadota, Toyokazu Sekiguchi, and Hiroyuki Tashiro. “A new constraint on millicharged dark matter from galaxy clusters”. In: (Feb. 2016). arXiv: [1602.04009](https://arxiv.org/abs/1602.04009) [[astro-ph.CO](#)].
- [146] Enrico Barausse, Nicolás Yunes, and Katie Chamberlain. “Theory-Agnostic Constraints on Black-Hole Dipole Radiation with Multiband Gravitational-Wave Astrophysics”. In: *Phys. Rev. Lett.* 116.24 (2016), p. 241104. DOI: [10.1103/PhysRevLett.116.241104](https://doi.org/10.1103/PhysRevLett.116.241104). arXiv: [1603.04075](https://arxiv.org/abs/1603.04075) [[gr-qc](#)].
- [147] Mohammed Khalil et al. “Hairy binary black holes in Einstein-Maxwell-dilaton theory and their effective-one-body description”. In: *Phys. Rev. D* 98.10 (2018), p. 104010. DOI: [10.1103/PhysRevD.98.104010](https://doi.org/10.1103/PhysRevD.98.104010). arXiv: [1809.03109](https://arxiv.org/abs/1809.03109) [[gr-qc](#)].
- [148] Paolo Pani, Emanuele Berti, and Leonardo Gualtieri. “Gravitoelectromagnetic Perturbations of Kerr-Newman Black Holes: Stability and Isospectrality in the Slow-Rotation Limit”. In: *Phys. Rev. Lett.* 110.24 (2013), p. 241103. DOI: [10.1103/PhysRevLett.110.241103](https://doi.org/10.1103/PhysRevLett.110.241103). arXiv: [1304.1160](https://arxiv.org/abs/1304.1160) [[gr-qc](#)].
- [149] Paolo Pani, Emanuele Berti, and Leonardo Gualtieri. “Scalar, Electromagnetic and Gravitational Perturbations of Kerr-Newman Black Holes in the Slow-Rotation Limit”. In: *Phys. Rev. D* 88 (2013), p. 064048. DOI: [10.1103/PhysRevD.88.064048](https://doi.org/10.1103/PhysRevD.88.064048). arXiv: [1307.7315](https://arxiv.org/abs/1307.7315) [[gr-qc](#)].
- [150] Miguel Zilhão et al. “Testing the nonlinear stability of Kerr-Newman black holes”. In: *Phys. Rev. D* 90.12 (2014), p. 124088. DOI: [10.1103/PhysRevD.90.124088](https://doi.org/10.1103/PhysRevD.90.124088). arXiv: [1410.0694](https://arxiv.org/abs/1410.0694) [[gr-qc](#)].
- [151] Zachary Mark et al. “Quasinormal modes of weakly charged Kerr-Newman space-times”. In: *Phys. Rev. D* 91.4 (2015), p. 044025. DOI: [10.1103/PhysRevD.91.044025](https://doi.org/10.1103/PhysRevD.91.044025). arXiv: [1409.5800](https://arxiv.org/abs/1409.5800) [[gr-qc](#)].
- [152] Oscar J. C. Dias, Mahdi Godazgar, and Jorge E. Santos. “Linear Mode Stability of the Kerr-Newman Black Hole and Its Quasinormal Modes”. In: *Phys. Rev. Lett.* 114.15 (2015), p. 151101. DOI: [10.1103/PhysRevLett.114.151101](https://doi.org/10.1103/PhysRevLett.114.151101). arXiv: [1501.04625](https://arxiv.org/abs/1501.04625) [[gr-qc](#)].



- [153] Patricia Schmidt, Frank Ohme, and Mark Hannam. “Towards models of gravitational waveforms from generic binaries II: Modelling precession effects with a single effective precession parameter”. In: *Phys. Rev. D* 91.2 (2015), p. 024043. DOI: [10.1103/PhysRevD.91.024043](https://doi.org/10.1103/PhysRevD.91.024043). arXiv: [1408.1810](https://arxiv.org/abs/1408.1810) [gr-qc].
- [154] R. Abbott et al. “GW190412: Observation of a Binary-Black-Hole Coalescence with Asymmetric Masses”. In: *Phys. Rev. D* 102.4 (2020), p. 043015. DOI: [10.1103/PhysRevD.102.043015](https://doi.org/10.1103/PhysRevD.102.043015). arXiv: [2004.08342](https://arxiv.org/abs/2004.08342) [astro-ph.HE].
- [155] D. J. A. McKechn, C. Robinson, and B. S. Sathyaprakash. “A tapering window for time-domain templates and simulated signals in the detection of gravitational waves from coalescing compact binaries”. In: *Class. Quant. Grav.* 27 (2010), p. 084020. DOI: [10.1088/0264-9381/27/8/084020](https://doi.org/10.1088/0264-9381/27/8/084020). arXiv: [1003.2939](https://arxiv.org/abs/1003.2939) [gr-qc].
- [156] J. Veitch et al. “Parameter estimation for compact binaries with ground-based gravitational-wave observations using the LALInference software library”. In: *Phys. Rev. D* 91.4 (2015), p. 042003. DOI: [10.1103/PhysRevD.91.042003](https://doi.org/10.1103/PhysRevD.91.042003). arXiv: [1409.7215](https://arxiv.org/abs/1409.7215) [gr-qc].
- [157] E T. Newman et al. “Metric of a Rotating, Charged Mass”. In: *J. Math. Phys.* 6 (1965), pp. 918–919. DOI: [10.1063/1.1704351](https://doi.org/10.1063/1.1704351).
- [158] J. Provost, G. Berthomieu, and A. Rocca. “Low Frequency Oscillations of a Slowly Rotating Star - Quasi Toroidal Modes”. In: *aap* 94 (Jan. 1981), p. 126.
- [159] Wynn C. G. Ho and Dong Lai. “Resonant tidal excitations of rotating neutron stars in coalescing binaries”. In: *Mon. Not. Roy. Astron. Soc.* 308 (1999), p. 153. DOI: [10.1046/j.1365-8711.1999.02703.x](https://doi.org/10.1046/j.1365-8711.1999.02703.x). arXiv: [astro-ph/9812116](https://arxiv.org/abs/astro-ph/9812116) [astro-ph].
- [160] A. Katrin Schenk et al. “Nonlinear mode coupling in rotating stars and the r mode instability in neutron stars”. In: *Phys. Rev. D* 65 (2002), p. 024001. DOI: [10.1103/PhysRevD.65.024001](https://doi.org/10.1103/PhysRevD.65.024001). arXiv: [gr-qc/0101092](https://arxiv.org/abs/gr-qc/0101092) [gr-qc].
- [161] Keith H. Lockitch and John L. Friedman. “Where are the r modes of isentropic stars?” In: *Astrophys. J.* 521 (1999), p. 764. DOI: [10.1086/307580](https://doi.org/10.1086/307580). arXiv: [gr-qc/9812019](https://arxiv.org/abs/gr-qc/9812019) [gr-qc].
- [162] John L. Friedman and Sharon M. Morsink. “Axial instability of rotating relativistic stars”. In: *Astrophys. J.* 502 (1998), pp. 714–720. DOI: [10.1086/305920](https://doi.org/10.1086/305920). arXiv: [gr-qc/9706073](https://arxiv.org/abs/gr-qc/9706073) [gr-qc].
- [163] Nils Andersson. “A New class of unstable modes of rotating relativistic stars”. In: *Astrophys. J.* 502 (1998), pp. 708–713. DOI: [10.1086/305919](https://doi.org/10.1086/305919). arXiv: [gr-qc/9706075](https://arxiv.org/abs/gr-qc/9706075) [gr-qc].
- [164] Kostas D. Kokkotas and Kai Schwenzer. “R-mode astronomy”. In: *Eur. Phys. J. A* 52.2 (2016), p. 38. DOI: [10.1140/epja/i2016-16038-9](https://doi.org/10.1140/epja/i2016-16038-9). arXiv: [1510.07051](https://arxiv.org/abs/1510.07051) [gr-qc].
- [165] Eric Poisson. “Gravitomagnetic tidal resonance in neutron-star binary inspirals”. In: *Phys. Rev. D* 101.10 (2020), p. 104028. DOI: [10.1103/PhysRevD.101.104028](https://doi.org/10.1103/PhysRevD.101.104028). arXiv: [2003.10427](https://arxiv.org/abs/2003.10427) [gr-qc].

- [166] Eric Poisson. “Gravitomagnetic Love tensor of a slowly rotating body: post-Newtonian theory”. In: *Phys. Rev. D* 102.6 (2020), p. 064059. DOI: [10.1103/PhysRevD.102.064059](https://doi.org/10.1103/PhysRevD.102.064059). arXiv: [2007.01678](https://arxiv.org/abs/2007.01678) [gr-qc].
- [167] Eric Poisson and Cyann Buisson. “Tidal driving of inertial modes of Maclaurin spheroids”. In: *Phys. Rev. D* 102.10 (2020), p. 104005. DOI: [10.1103/PhysRevD.102.104005](https://doi.org/10.1103/PhysRevD.102.104005). arXiv: [2007.03050](https://arxiv.org/abs/2007.03050) [gr-qc].
- [168] Sizheng Ma, Hang Yu, and Yanbei Chen. “Revisiting the tidal excitation of Rossby modes in coalescing binary systems”. In: (2020). arXiv: [2010.03066](https://arxiv.org/abs/2010.03066) [gr-qc].
- [169] Bala Iyer et al. *LIGO-India, Proposal of the Consortium for Indian Initiative in Gravitational-wave Observations*. LIGO Document M1100296-v2. 2011. URL: <https://dcc.ligo.org/LIGO-M1100296/public>.
- [170] Wenrui Xu and Dong Lai. “Resonant Tidal Excitation of Oscillation Modes in Merging Binary Neutron Stars: Inertial-Gravity Modes”. In: *Phys. Rev. D* 96.8 (2017), p. 083005. DOI: [10.1103/PhysRevD.96.083005](https://doi.org/10.1103/PhysRevD.96.083005). arXiv: [1708.01839](https://arxiv.org/abs/1708.01839) [astro-ph.HE].
- [171] Nils Andersson and Kostas D. Kokkotas. “The R mode instability in rotating neutron stars”. In: *Int. J. Mod. Phys. D* 10 (2001), pp. 381–442. DOI: [10.1142/S0218271801001062](https://doi.org/10.1142/S0218271801001062). arXiv: [gr-qc/0010102](https://arxiv.org/abs/gr-qc/0010102) [gr-qc].
- [172] Ashikuzzaman Idrisy, Benjamin J. Owen, and David I. Jones. “R-mode frequencies of slowly rotating relativistic neutron stars with realistic equations of state”. In: *Phys. Rev. D* 91.2 (2015), p. 024001. DOI: [10.1103/PhysRevD.91.024001](https://doi.org/10.1103/PhysRevD.91.024001). arXiv: [1410.7360](https://arxiv.org/abs/1410.7360) [gr-qc].
- [173] Umin Lee and Shijun Yoshida. “R-modes of neutron stars with the superfluid core”. In: *Astrophys. J.* 586 (2003), p. 403. DOI: [10.1086/367617](https://doi.org/10.1086/367617). arXiv: [astro-ph/0211580](https://arxiv.org/abs/astro-ph/0211580) [astro-ph].
- [174] Thibault Damour and Alessandro Nagar. “Relativistic tidal properties of neutron stars”. In: *Phys. Rev. D* 80 (2009), p. 084035. DOI: [10.1103/PhysRevD.80.084035](https://doi.org/10.1103/PhysRevD.80.084035). arXiv: [0906.0096](https://arxiv.org/abs/0906.0096) [gr-qc].
- [175] Taylor Binnington and Eric Poisson. “Relativistic theory of tidal Love numbers”. In: *Phys. Rev. D* 80 (2009), p. 084018. DOI: [10.1103/PhysRevD.80.084018](https://doi.org/10.1103/PhysRevD.80.084018). arXiv: [0906.1366](https://arxiv.org/abs/0906.1366) [gr-qc].
- [176] Philippe Landry and Eric Poisson. “Gravitomagnetic response of an irrotational body to an applied tidal field”. In: *Phys. Rev. D* 91.10 (2015), p. 104026. DOI: [10.1103/PhysRevD.91.104026](https://doi.org/10.1103/PhysRevD.91.104026). arXiv: [1504.06606](https://arxiv.org/abs/1504.06606) [gr-qc].
- [177] Philippe Landry and Eric Poisson. “Dynamical response to a stationary tidal field”. In: *Phys. Rev. D* 92.12 (2015), p. 124041. DOI: [10.1103/PhysRevD.92.124041](https://doi.org/10.1103/PhysRevD.92.124041). arXiv: [1510.09170](https://arxiv.org/abs/1510.09170) [gr-qc].
- [178] Eric Poisson and Jean Doucot. “Gravitomagnetic tidal currents in rotating neutron stars”. In: *Phys. Rev. D* 95.4 (2017), p. 044023. DOI: [10.1103/PhysRevD.95.044023](https://doi.org/10.1103/PhysRevD.95.044023). arXiv: [1612.04255](https://arxiv.org/abs/1612.04255) [gr-qc].

- [179] Paolo Pani et al. “Magnetic tidal Love numbers clarified”. In: *Phys. Rev. D* 98.12 (2018), p. 124023. DOI: [10.1103/PhysRevD.98.124023](https://doi.org/10.1103/PhysRevD.98.124023). arXiv: [1810.01094](https://arxiv.org/abs/1810.01094) [gr-qc].
- [180] Barak Kol and Michael Smolkin. “Non-Relativistic Gravitation: From Newton to Einstein and Back”. In: *Class. Quant. Grav.* 25 (2008), p. 145011. DOI: [10.1088/0264-9381/25/14/145011](https://doi.org/10.1088/0264-9381/25/14/145011). arXiv: [0712.4116](https://arxiv.org/abs/0712.4116) [hep-th].
- [181] Thibault Damour, Michael Soffel, and Chong-ming Xu. “General relativistic celestial mechanics. 1. Method and definition of reference systems”. In: *Phys. Rev. D* 43 (1991), pp. 3273–3307. DOI: [10.1103/PhysRevD.43.3273](https://doi.org/10.1103/PhysRevD.43.3273).
- [182] Jeff D. Kaplan, David A. Nichols, and Kip S. Thorne. “Post-Newtonian Approximation in Maxwell-Like Form”. In: *Phys. Rev. D* 80 (2009), p. 124014. DOI: [10.1103/PhysRevD.80.124014](https://doi.org/10.1103/PhysRevD.80.124014). arXiv: [0808.2510](https://arxiv.org/abs/0808.2510) [gr-qc].
- [183] J. L. Friedman and B. F. Schutz. “Lagrangian perturbation theory of nonrelativistic fluids.” In: *apj* 221 (May 1978), pp. 937–957. DOI: [10.1086/156098](https://doi.org/10.1086/156098).
- [184] Walter D. Goldberger and Ira Z. Rothstein. “An Effective field theory of gravity for extended objects”. In: *Phys. Rev. D* 73 (2006), p. 104029. DOI: [10.1103/PhysRevD.73.104029](https://doi.org/10.1103/PhysRevD.73.104029). arXiv: [hep-th/0409156](https://arxiv.org/abs/hep-th/0409156) [hep-th].
- [185] Walter D. Goldberger. “Les Houches lectures on effective field theories and gravitational radiation”. In: *Les Houches Summer School - Session 86: Particle Physics and Cosmology: The Fabric of Spacetime Les Houches, France, July 31-August 25, 2006*. 2007. arXiv: [hep-ph/0701129](https://arxiv.org/abs/hep-ph/0701129) [hep-ph].
- [186] Stefano Foffa and Riccardo Sturani. “Effective field theory methods to model compact binaries”. In: *Class. Quant. Grav.* 31.4 (2014), p. 043001. DOI: [10.1088/0264-9381/31/4/043001](https://doi.org/10.1088/0264-9381/31/4/043001). arXiv: [1309.3474](https://arxiv.org/abs/1309.3474) [gr-qc].
- [187] Ira Z. Rothstein. “Progress in effective field theory approach to the binary inspiral problem”. In: *Gen. Rel. Grav.* 46 (2014), p. 1726. DOI: [10.1007/s10714-014-1726-y](https://doi.org/10.1007/s10714-014-1726-y).
- [188] Rafael A. Porto. “The effective field theorist’s approach to gravitational dynamics”. In: *Phys. Rept.* 633 (2016), pp. 1–104. DOI: [10.1016/j.physrep.2016.04.003](https://doi.org/10.1016/j.physrep.2016.04.003). arXiv: [1601.04914](https://arxiv.org/abs/1601.04914) [hep-th].
- [189] Michèle Levi. “Effective Field Theories of Post-Newtonian Gravity: A comprehensive review”. In: *Rept. Prog. Phys.* 83.7 (2020), p. 075901. DOI: [10.1088/1361-6633/ab12bc](https://doi.org/10.1088/1361-6633/ab12bc). arXiv: [1807.01699](https://arxiv.org/abs/1807.01699) [hep-th].
- [190] Walter D. Goldberger and Ira Z. Rothstein. “Dissipative effects in the worldline approach to black hole dynamics”. In: *Phys. Rev. D* 73 (2006), p. 104030. DOI: [10.1103/PhysRevD.73.104030](https://doi.org/10.1103/PhysRevD.73.104030). arXiv: [hep-th/0511133](https://arxiv.org/abs/hep-th/0511133) [hep-th].
- [191] Jan Steinhoff et al. “Dynamical Tides in General Relativity: Effective Action and Effective-One-Body Hamiltonian”. In: *Phys. Rev. D* 94.10 (2016), p. 104028. DOI: [10.1103/PhysRevD.94.104028](https://doi.org/10.1103/PhysRevD.94.104028). arXiv: [1608.01907](https://arxiv.org/abs/1608.01907) [gr-qc].
- [192] Rafael A. Porto. “Post-Newtonian corrections to the motion of spinning bodies in NRGR”. In: *Phys. Rev. D* 73 (2006), p. 104031. DOI: [10.1103/PhysRevD.73.104031](https://doi.org/10.1103/PhysRevD.73.104031). arXiv: [gr-qc/0511061](https://arxiv.org/abs/gr-qc/0511061) [gr-qc].



- [193] Michele Levi. “Next to Leading Order gravitational Spin-Orbit coupling in an Effective Field Theory approach”. In: *Phys. Rev.* D82 (2010), p. 104004. DOI: [10.1103/PhysRevD.82.104004](#). arXiv: [1006.4139 \[gr-qc\]](#).
- [194] Michele Levi and Jan Steinhoff. “Spinning gravitating objects in the effective field theory in the post-Newtonian scheme”. In: *JHEP* 09 (2015), p. 219. DOI: [10.1007/JHEP09\(2015\)219](#). arXiv: [1501.04956 \[gr-qc\]](#).
- [195] Rafael A. Porto. “Absorption effects due to spin in the worldline approach to black hole dynamics”. In: *Phys. Rev.* D77 (2008), p. 064026. DOI: [10.1103/PhysRevD.77.064026](#). arXiv: [0710.5150 \[hep-th\]](#).
- [196] Solomon Endlich and Riccardo Penco. “Effective field theory approach to tidal dynamics of spinning astrophysical systems”. In: *Phys. Rev.* D93.6 (2016), p. 064021. DOI: [10.1103/PhysRevD.93.064021](#). arXiv: [1510.08889 \[gr-qc\]](#).
- [197] Gregor Kälin and Rafael A. Porto. “Post-Minkowskian Effective Field Theory for Conservative Binary Dynamics”. In: *JHEP* 11 (2020), p. 106. DOI: [10.1007/JHEP11\(2020\)106](#). arXiv: [2006.01184 \[hep-th\]](#).
- [198] Gregor Kälin, Zhengwen Liu, and Rafael A. Porto. “Conservative Tidal Effects in Compact Binary Systems to Next-to-Leading Post-Minkowskian Order”. In: *Phys. Rev.* D102 (2020), p. 124025. DOI: [10.1103/PhysRevD.102.124025](#). arXiv: [2008.06047 \[hep-th\]](#).
- [199] Donato Bini, Thibault Damour, and Andrea Geralico. “Scattering of tidally interacting bodies in post-Minkowskian gravity”. In: *Phys. Rev.* D101.4 (2020), p. 044039. DOI: [10.1103/PhysRevD.101.044039](#). arXiv: [2001.00352 \[gr-qc\]](#).
- [200] Clifford Cheung and Mikhail P. Solon. “Tidal Effects in the Post-Minkowskian Expansion”. In: *Phys. Rev. Lett.* 125.19 (2020), p. 191601. DOI: [10.1103/PhysRevLett.125.191601](#). arXiv: [2006.06665 \[hep-th\]](#).
- [201] Kays Haddad and Andreas Helset. “Tidal effects in quantum field theory”. In: *JHEP* 12 (2020), p. 024. DOI: [10.1007/JHEP12\(2020\)024](#). arXiv: [2008.04920 \[hep-th\]](#).
- [202] Clifford Cheung, Nabha Shah, and Mikhail P. Solon. “Mining the Geodesic Equation for Scattering Data”. In: *Phys. Rev.* D103.2 (2021), p. 024030. DOI: [10.1103/PhysRevD.103.024030](#). arXiv: [2010.08568 \[hep-th\]](#).
- [203] Zvi Bern et al. “Leading Nonlinear Tidal Effects and Scattering Amplitudes”. In: (2020). arXiv: [2010.08559 \[hep-th\]](#).
- [204] Michele Levi and Jan Steinhoff. “EFTofPNG: A package for high precision computation with the Effective Field Theory of Post-Newtonian Gravity”. In: *Class. Quant. Grav.* 34.24 (2017), p. 244001. DOI: [10.1088/1361-6382/aa941e](#). arXiv: [1705.06309 \[gr-qc\]](#).
- [205] Donato Bini, Thibault Damour, and Guillaume Faye. “Effective action approach to higher-order relativistic tidal interactions in binary systems and their effective one body description”. In: *Phys. Rev.* D85 (2012), p. 124034. DOI: [10.1103/PhysRevD.85.124034](#). arXiv: [1202.3565 \[gr-qc\]](#).

- [206] Batoul Banihashemi and Justin Vines. “Gravitomagnetic tidal effects in gravitational waves from neutron star binaries”. In: *Phys. Rev. D* 101.6 (2020), p. 064003. DOI: [10.1103/PhysRevD.101.064003](https://doi.org/10.1103/PhysRevD.101.064003). arXiv: [1805.07266 \[gr-qc\]](https://arxiv.org/abs/1805.07266).
- [207] Quentin Henry, Guillaume Faye, and Luc Blanchet. “Tidal effects in the equations of motion of compact binary systems to next-to-next-to-leading post-Newtonian order”. In: *Phys. Rev. D* 101.6 (2020), p. 064047. DOI: [10.1103/PhysRevD.101.064047](https://doi.org/10.1103/PhysRevD.101.064047). arXiv: [1912.01920 \[gr-qc\]](https://arxiv.org/abs/1912.01920).
- [208] Quentin Henry, Guillaume Faye, and Luc Blanchet. “Hamiltonian for tidal interactions in compact binary systems to next-to-next-to-leading post-Newtonian order”. In: *Phys. Rev. D* 102.12 (2020), p. 124074. DOI: [10.1103/PhysRevD.102.124074](https://doi.org/10.1103/PhysRevD.102.124074). arXiv: [2009.12332 \[gr-qc\]](https://arxiv.org/abs/2009.12332).
- [209] Walter D. Goldberger and Andreas Ross. “Gravitational radiative corrections from effective field theory”. In: *Phys. Rev. D* 81 (2010), p. 124015. DOI: [10.1103/PhysRevD.81.124015](https://doi.org/10.1103/PhysRevD.81.124015). arXiv: [0912.4254 \[gr-qc\]](https://arxiv.org/abs/0912.4254).
- [210] Walter D. Goldberger, Andreas Ross, and Ira Z. Rothstein. “Black hole mass dynamics and renormalization group evolution”. In: *Phys. Rev. D* 89.12 (2014), p. 124033. DOI: [10.1103/PhysRevD.89.124033](https://doi.org/10.1103/PhysRevD.89.124033). arXiv: [1211.6095 \[hep-th\]](https://arxiv.org/abs/1211.6095).
- [211] Solomon Endlich and Riccardo Penco. “A Modern Approach to Superradiance”. In: *JHEP* 05 (2017), p. 052. DOI: [10.1007/JHEP05\(2017\)052](https://doi.org/10.1007/JHEP05(2017)052). arXiv: [1609.06723 \[hep-th\]](https://arxiv.org/abs/1609.06723).
- [212] Chad R. Galley and Manuel Tiglio. “Radiation reaction and gravitational waves in the effective field theory approach”. In: *Phys. Rev. D* 79 (2009), p. 124027. DOI: [10.1103/PhysRevD.79.124027](https://doi.org/10.1103/PhysRevD.79.124027). arXiv: [0903.1122 \[gr-qc\]](https://arxiv.org/abs/0903.1122).
- [213] Chad R. Galley. “Classical Mechanics of Nonconservative Systems”. In: *Phys. Rev. Lett.* 110.17 (2013), p. 174301. DOI: [10.1103/PhysRevLett.110.174301](https://doi.org/10.1103/PhysRevLett.110.174301). arXiv: [1210.2745 \[gr-qc\]](https://arxiv.org/abs/1210.2745).
- [214] Thibault Damour and Gerhard Schafer. “Redefinition of position variables and the reduction of higher order Lagrangians”. In: *J. Math. Phys.* 32 (1991), pp. 127–134. DOI: [10.1063/1.529135](https://doi.org/10.1063/1.529135).
- [215] James B. Hartle. “Slowly Rotating Relativistic Stars. I. Equations of Structure”. In: *apj* 150 (Dec. 1967), p. 1005. DOI: [10.1086/149400](https://doi.org/10.1086/149400).
- [216] Eric Poisson. “Gravitational waves from inspiraling compact binaries: The Quadrupole moment term”. In: *Phys. Rev. D* 57 (1998), pp. 5287–5290. DOI: [10.1103/PhysRevD.57.5287](https://doi.org/10.1103/PhysRevD.57.5287). arXiv: [gr-qc/9709032 \[gr-qc\]](https://arxiv.org/abs/gr-qc/9709032).
- [217] William G. Laarakkers and Eric Poisson. “Quadrupole moments of rotating neutron stars”. In: *Astrophys. J.* 512 (1999), pp. 282–287. DOI: [10.1086/306732](https://doi.org/10.1086/306732). arXiv: [gr-qc/9709033 \[gr-qc\]](https://arxiv.org/abs/gr-qc/9709033).
- [218] Sayan Chakrabarti, T rence Delsate, and Jan Steinhoff. “New perspectives on neutron star and black hole spectroscopy and dynamic tides”. In: (2013). arXiv: [1304.2228 \[gr-qc\]](https://arxiv.org/abs/1304.2228).

- [219] Tanja Hinderer et al. “Effects of neutron-star dynamic tides on gravitational waveforms within the effective-one-body approach”. In: *Phys. Rev. Lett.* 116.18 (2016), p. 181101. DOI: [10.1103/PhysRevLett.116.181101](https://doi.org/10.1103/PhysRevLett.116.181101). arXiv: [1602.00599](https://arxiv.org/abs/1602.00599) [gr-qc].
- [220] Elena M. Kantor, Mikhail E. Gusakov, and Vasiliy A. Dommes. “Constraining neutron superfluidity with  $r$ -mode physics”. In: *Phys. Rev. Lett.* 125.15 (2020), p. 151101. DOI: [10.1103/PhysRevLett.125.151101](https://doi.org/10.1103/PhysRevLett.125.151101). arXiv: [2009.12553](https://arxiv.org/abs/2009.12553) [astro-ph.HE].
- [221] Samuel E. Gralla. “On the Ambiguity in Relativistic Tidal Deformability”. In: *Class. Quant. Grav.* 35.8 (2018), p. 085002. DOI: [10.1088/1361-6382/aab186](https://doi.org/10.1088/1361-6382/aab186). arXiv: [1710.11096](https://arxiv.org/abs/1710.11096) [gr-qc].
- [222] T  rence Delsate. “I-Love relations for irrotational stars”. In: *Phys. Rev.* D92.12 (2015), p. 124001. DOI: [10.1103/PhysRevD.92.124001](https://doi.org/10.1103/PhysRevD.92.124001). arXiv: [1504.07335](https://arxiv.org/abs/1504.07335) [gr-qc].
- [223] J  r  mie Gagnon-Bischoff et al. “Extended I-Love relations for slowly rotating neutron stars”. In: *Phys. Rev.* D97.6 (2018), p. 064042. DOI: [10.1103/PhysRevD.97.064042](https://doi.org/10.1103/PhysRevD.97.064042). arXiv: [1711.05694](https://arxiv.org/abs/1711.05694) [gr-qc].
- [224] Paolo Pani, Leonardo Gualtieri, and Valeria Ferrari. “Tidal Love numbers of a slowly spinning neutron star”. In: *Phys. Rev.* D92.12 (2015), p. 124003. DOI: [10.1103/PhysRevD.92.124003](https://doi.org/10.1103/PhysRevD.92.124003). arXiv: [1509.02171](https://arxiv.org/abs/1509.02171) [gr-qc].
- [225] Xisco Jim  nez Forteza et al. “Impact of high-order tidal terms on binary neutron-star waveforms”. In: *Phys. Rev.* D98.12 (2018), p. 124014. DOI: [10.1103/PhysRevD.98.124014](https://doi.org/10.1103/PhysRevD.98.124014). arXiv: [1807.08016](https://arxiv.org/abs/1807.08016) [gr-qc].
- [226] Kent Yagi and Nicolas Yunes. “I-Love-Q”. In: *Science* 341 (2013), pp. 365–368. DOI: [10.1126/science.1236462](https://doi.org/10.1126/science.1236462). arXiv: [1302.4499](https://arxiv.org/abs/1302.4499) [gr-qc].
- [227] Sayan Chakrabarti, T  rence Delsate, and Jan Steinhoff. “Effective action and linear response of compact objects in Newtonian gravity”. In: *Phys. Rev.* D88 (2013), p. 084038. DOI: [10.1103/PhysRevD.88.084038](https://doi.org/10.1103/PhysRevD.88.084038). arXiv: [1306.5820](https://arxiv.org/abs/1306.5820) [gr-qc].
- [228] Alexandre Le Tiec and Marc Casals. “Spinning Black Holes Fall in Love”. In: (2020). arXiv: [2007.00214](https://arxiv.org/abs/2007.00214) [gr-qc].
- [229] L. D. Landau and E. M. Lifshitz. *Mechanics, Third Edition: Volume 1 (Course of Theoretical Physics)*. Butterworth-Heinemann, Jan. 1976. ISBN: 0750628960. URL: <http://www.worldcat.org/isbn/0750628960>.
- [230] Shijun Yoshida and Umin Lee. “ $r$  modes in relativistic superfluid stars”. In: *Phys. Rev.* D67 (2003), p. 124019. DOI: [10.1103/PhysRevD.67.124019](https://doi.org/10.1103/PhysRevD.67.124019). arXiv: [gr-qc/0304073](https://arxiv.org/abs/gr-qc/0304073) [gr-qc].
- [231] Geraint Pratten, Patricia Schmidt, and Natalie Williams. “Impact of Dynamical Tides on the Reconstruction of the Neutron Star Equation of State”. In: *Phys. Rev. Lett.* 129.8 (2022), p. 081102. DOI: [10.1103/PhysRevLett.129.081102](https://doi.org/10.1103/PhysRevLett.129.081102). arXiv: [2109.07566](https://arxiv.org/abs/2109.07566) [astro-ph.HE].
- [232] Hang Yu and Nevin N. Weinberg. “Dynamical tides in coalescing superfluid neutron star binaries with hyperon cores and their detectability with third generation gravitational-wave detectors”. In: *Mon. Not. Roy. Astron. Soc.* 470.1 (2017), pp. 350–360. DOI: [10.1093/mnras/stx1188](https://doi.org/10.1093/mnras/stx1188). arXiv: [1705.04700](https://arxiv.org/abs/1705.04700) [astro-ph.HE].

- [233] Miquel Miravet-Tenés et al. “Prospects for the inference of inertial modes from hypermassive neutron stars with future gravitational-wave detectors”. In: (Feb. 2023). arXiv: [2302.04553 \[gr-qc\]](#).
- [234] Xisco Jiménez Forteza et al. “Impact of high-order tidal terms on binary neutron-star waveforms”. In: *Phys. Rev. D* 98.12 (2018), p. 124014. DOI: [10.1103/PhysRevD.98.124014](#). arXiv: [1807.08016 \[gr-qc\]](#).
- [235] Sarp Akcay et al. “Effective-one-body multipolar waveform for tidally interacting binary neutron stars up to merger”. In: *Phys. Rev. D* 99.4 (2019), p. 044051. DOI: [10.1103/PhysRevD.99.044051](#). arXiv: [1812.02744 \[gr-qc\]](#).
- [236] Kent Yagi. “Multipole Love Relations”. In: *Phys. Rev. D* 89.4 (2014). [Erratum: *Phys.Rev.D* 96, 129904 (2017), Erratum: *Phys.Rev.D* 97, 129901 (2018)], p. 043011. DOI: [10.1103/PhysRevD.89.043011](#). arXiv: [1311.0872 \[gr-qc\]](#).
- [237] Pawan Kumar Gupta, Jan Steinhoff, and Tanja Hinderer. “Relativistic effective action of dynamical gravitomagnetic tides for slowly rotating neutron stars”. In: *Phys. Rev. Res.* 3.1 (2021), p. 013147. DOI: [10.1103/PhysRevResearch.3.013147](#). arXiv: [2011.03508 \[gr-qc\]](#).
- [238] Lawrence E. Kidder. “Coalescing binary systems of compact objects to postNewtonian 5/2 order. 5. Spin effects”. In: *Phys. Rev. D* 52 (1995), pp. 821–847. DOI: [10.1103/PhysRevD.52.821](#). arXiv: [gr-qc/9506022 \[gr-qc\]](#).
- [239] Kip S. Thorne. “Multipole expansions of gravitational radiation”. In: *Reviews of Modern Physics* 52.2 (Apr. 1980), pp. 299–340. DOI: [10.1103/RevModPhys.52.299](#).
- [240] Tim Dietrich, Sebastiano Bernuzzi, and Wolfgang Tichy. “Closed-form tidal approximants for binary neutron star gravitational waveforms constructed from high-resolution numerical relativity simulations”. In: *Phys. Rev. D* 96 (12 Dec. 2017), p. 121501. DOI: [10.1103/PhysRevD.96.121501](#). URL: <https://link.aps.org/doi/10.1103/PhysRevD.96.121501>.
- [241] Walter Del Pozzo et al. “Demonstrating the feasibility of probing the neutron star equation of state with second-generation gravitational wave detectors”. In: *Phys. Rev. Lett.* 111.7 (2013), p. 071101. DOI: [10.1103/PhysRevLett.111.071101](#). arXiv: [1307.8338 \[gr-qc\]](#).
- [242] Michalis Agathos et al. “Constraining the neutron star equation of state with gravitational wave signals from coalescing binary neutron stars”. In: *Phys. Rev. D* 92.2 (2015), p. 023012. DOI: [10.1103/PhysRevD.92.023012](#). arXiv: [1503.05405 \[gr-qc\]](#).
- [243] Benjamin D. Lackey and Leslie Wade. “Reconstructing the neutron-star equation of state with gravitational-wave detectors from a realistic population of inspiralling binary neutron stars”. In: *Phys. Rev. D* 91.4 (2015), p. 043002. DOI: [10.1103/PhysRevD.91.043002](#). arXiv: [1410.8866 \[gr-qc\]](#).

- [244] Benjamin P Abbott et al. “Model comparison from LIGO–Virgo data on GW170817’s binary components and consequences for the merger remnant”. In: *Class. Quant. Grav.* 37.4 (2020), p. 045006. DOI: [10.1088/1361-6382/ab5f7c](https://doi.org/10.1088/1361-6382/ab5f7c). arXiv: [1908.01012](https://arxiv.org/abs/1908.01012) [gr-qc].
- [245] B. S. Sathyaprakash and S. V. Dhurandhar. “Choice of filters for the detection of gravitational waves from coalescing binaries”. In: *Phys. Rev. D* 44 (1991), pp. 3819–3834. DOI: [10.1103/PhysRevD.44.3819](https://doi.org/10.1103/PhysRevD.44.3819).
- [246] Theocharis A. Apostolatos et al. “Spin-induced orbital precession and its modulation of the gravitational waveforms from merging binaries”. In: *Phys. Rev. D* 49 (12 June 1994), pp. 6274–6297. DOI: [10.1103/PhysRevD.49.6274](https://doi.org/10.1103/PhysRevD.49.6274). URL: <https://link.aps.org/doi/10.1103/PhysRevD.49.6274>.
- [247] Wen Zhao and Linqing Wen. “Localization accuracy of compact binary coalescences detected by the third-generation gravitational-wave detectors and implication for cosmology”. In: *Phys. Rev. D* 97.6 (2018), p. 064031. DOI: [10.1103/PhysRevD.97.064031](https://doi.org/10.1103/PhysRevD.97.064031). arXiv: [1710.05325](https://arxiv.org/abs/1710.05325) [astro-ph.CO].
- [248] P.A.R. Ade et al. “Planck 2013 results. XVI. Cosmological parameters”. In: *Astron. Astrophys.* 571 (2014), A16. DOI: [10.1051/0004-6361/201321591](https://doi.org/10.1051/0004-6361/201321591). arXiv: [1303.5076](https://arxiv.org/abs/1303.5076) [astro-ph.CO].
- [249] Leslie Wade et al. “Systematic and statistical errors in a bayesian approach to the estimation of the neutron-star equation of state using advanced gravitational wave detectors”. In: *Phys. Rev. D* 89.10 (2014), p. 103012. DOI: [10.1103/PhysRevD.89.103012](https://doi.org/10.1103/PhysRevD.89.103012). arXiv: [1402.5156](https://arxiv.org/abs/1402.5156) [gr-qc].
- [250] P. S. Koliogiannis and Ch. C. Moustakidis. “Constraints on the equation of state from the stability condition of neutron stars”. In: *Astrophys. Space Sci.* 364.3 (2019), p. 52. DOI: [10.1007/s10509-019-3539-7](https://doi.org/10.1007/s10509-019-3539-7). arXiv: [1806.09999](https://arxiv.org/abs/1806.09999) [nucl-th].
- [251] Lee Lindblom. “Spectral Representations of Neutron-Star Equations of State”. In: *Phys. Rev. D* 82 (2010), p. 103011. DOI: [10.1103/PhysRevD.82.103011](https://doi.org/10.1103/PhysRevD.82.103011). arXiv: [1009.0738](https://arxiv.org/abs/1009.0738) [astro-ph.HE].
- [252] F. Douchin and P. Haensel. “A unified equation of state of dense matter and neutron star structure”. In: *Astron. Astrophys.* 380 (2001), p. 151. DOI: [10.1051/0004-6361:20011402](https://doi.org/10.1051/0004-6361:20011402). arXiv: [astro-ph/0111092](https://arxiv.org/abs/astro-ph/0111092).
- [253] M. Coleman Miller, Cecilia Chirenti, and Frederick K. Lamb. “Constraining the equation of state of high-density cold matter using nuclear and astronomical measurements”. In: (Apr. 2019). DOI: [10.3847/1538-4357/ab4ef9](https://doi.org/10.3847/1538-4357/ab4ef9). arXiv: [1904.08907](https://arxiv.org/abs/1904.08907) [astro-ph.HE].
- [254] Lee Samuel Finn and David F. Chernoff. “Observing binary inspiral in gravitational radiation: One interferometer”. In: *Phys. Rev. D* 47 (1993), pp. 2198–2219. DOI: [10.1103/PhysRevD.47.2198](https://doi.org/10.1103/PhysRevD.47.2198). arXiv: [gr-qc/9301003](https://arxiv.org/abs/gr-qc/9301003).
- [255] Lee S. Finn. “Detection, measurement, and gravitational radiation”. In: *Phys. Rev. D* 46 (12 Dec. 1992), pp. 5236–5249. DOI: [10.1103/PhysRevD.46.5236](https://doi.org/10.1103/PhysRevD.46.5236). URL: <https://link.aps.org/doi/10.1103/PhysRevD.46.5236>.



- [256] Ilya Mandel et al. “Parameter estimation on compact binary coalescences with abruptly terminating gravitational waveforms”. In: *Class. Quant. Grav.* 31 (2014), p. 155005. DOI: [10.1088/0264-9381/31/15/155005](https://doi.org/10.1088/0264-9381/31/15/155005). arXiv: [1404.2382](https://arxiv.org/abs/1404.2382) [gr-qc].
- [257] Anna Puecher et al. “Unraveling information about supranuclear-dense matter from the complete binary neutron star coalescence process using future gravitational-wave detector networks”. In: (Oct. 2022). arXiv: [2210.09259](https://arxiv.org/abs/2210.09259) [gr-qc].
- [258] B. Friedman and V. R. Pandharipande. “Hot and cold, nuclear and neutron matter”. In: *Nucl. Phys. A* 361 (1981), pp. 502–520. DOI: [10.1016/0375-9474\(81\)90649-7](https://doi.org/10.1016/0375-9474(81)90649-7).
- [259] Daniel Wysocki et al. “Inferring the neutron star equation of state simultaneously with the population of merging neutron stars”. In: (Jan. 2020). arXiv: [2001.01747](https://arxiv.org/abs/2001.01747) [gr-qc].
- [260] J. Buchner et al. “X-ray spectral modelling of the AGN obscuring region in the CDFS: Bayesian model selection and catalogue”. In: *Astron. Astrophys.* 564 (2014), A125. DOI: [10.1051/0004-6361/201322971](https://doi.org/10.1051/0004-6361/201322971). arXiv: [1402.0004](https://arxiv.org/abs/1402.0004) [astro-ph.HE].
- [261] D. R. Lorimer. “Binary and Millisecond Pulsars”. In: *Living Rev. Rel.* 11 (2008), p. 8. DOI: [10.12942/lrr-2008-8](https://doi.org/10.12942/lrr-2008-8). arXiv: [0811.0762](https://arxiv.org/abs/0811.0762) [astro-ph].
- [262] Peter T. H. Pang et al. “NMMA: A nuclear-physics and multi-messenger astrophysics framework to analyze binary neutron star mergers”. In: (May 2022). arXiv: [2205.08513](https://arxiv.org/abs/2205.08513) [astro-ph.HE].
- [263] Michele Vallisneri. “Use and abuse of the Fisher information matrix in the assessment of gravitational-wave parameter-estimation prospects”. In: *Phys. Rev. D* 77 (2008), p. 042001. DOI: [10.1103/PhysRevD.77.042001](https://doi.org/10.1103/PhysRevD.77.042001). arXiv: [gr-qc/0703086](https://arxiv.org/abs/gr-qc/0703086).
- [264] Joshua A. Faber and Frederic A. Rasio. “Binary Neutron Star Mergers”. In: *Living Rev. Rel.* 15 (2012), p. 8. DOI: [10.12942/lrr-2012-8](https://doi.org/10.12942/lrr-2012-8). arXiv: [1204.3858](https://arxiv.org/abs/1204.3858) [gr-qc].
- [265] Costantino Pacilio et al. “Ranking Love Numbers for the Neutron Star Equation of State: The Need for Third-Generation Detectors”. In: *Phys. Rev. Lett.* 128.10 (2022), p. 101101. DOI: [10.1103/PhysRevLett.128.101101](https://doi.org/10.1103/PhysRevLett.128.101101). arXiv: [2104.10035](https://arxiv.org/abs/2104.10035) [gr-qc].
- [266] T. Damour and Bala R. Iyer. “Multipole analysis for electromagnetism and linearized gravity with irreducible cartesian tensors”. In: *Phys. Rev. D* 43 (1991), pp. 3259–3272. DOI: [10.1103/PhysRevD.43.3259](https://doi.org/10.1103/PhysRevD.43.3259).
- [267] Luc Blanchet and Thibault Damour. “Radiative gravitational fields in general relativity I. general structure of the field outside the source”. In: *Phil. Trans. Roy. Soc. Lond.* A320 (1986), pp. 379–430. DOI: [10.1098/rsta.1986.0125](https://doi.org/10.1098/rsta.1986.0125).

